

# Contents

<b>Resum</b>	<b>i</b>
<b>Acknowledgements</b>	<b>i</b>
<b>Introduction</b>	<b>1</b>
<b>1 Standard Model Higgs Boson Physics</b>	<b>5</b>
1.1 The Standard Model . . . . .	5
1.1.1 Electromagnetic Interaction . . . . .	7
1.1.2 Strong Interaction . . . . .	9
1.1.3 Electroweak Interaction . . . . .	11
1.2 Electroweak Symmetry Breaking . . . . .	12
1.2.1 Spontaneous Symmetry Breaking . . . . .	13
1.2.2 The Higgs Mechanism . . . . .	14
1.3 SM Higgs Boson Decays . . . . .	18
1.3.1 Higgs Boson Decay to Fermions . . . . .	18
1.3.2 Higgs Boson Decays to Vector Bosons . . . . .	19
1.3.3 Two Gluon Decay . . . . .	20
1.4 SM Higgs Boson Production at Tevatron . . . . .	20
1.4.1 Gluon Fusion . . . . .	20
1.4.2 Vector Boson Associated Production . . . . .	21
1.4.3 Vector Boson Fusion . . . . .	21
1.4.4 $Ht\bar{t}$ , $Hb\bar{b}$ Production . . . . .	22
1.5 Theoretical Limits on the Higgs Boson Mass . . . . .	22
1.5.1 Upper Bound: <i>Triviality</i> . . . . .	23
1.5.2 Lower Bound: <i>Vacuum Stability</i> . . . . .	23
1.6 Experimental Limits on the Higgs Boson Mass . . . . .	24
1.6.1 Indirect Searches . . . . .	24
1.6.2 LEP Direct Searches . . . . .	25
1.6.3 CDF Direct Searches . . . . .	26
<b>2 The Apparatus</b>	<b>35</b>
2.1 Fermilab Accelerator Complex . . . . .	35
2.1.1 The Proton Cycle . . . . .	36

2.1.2	The Antiproton Cycle . . . . .	38
2.2	The Collider Detector at Fermilab . . . . .	39
2.2.1	CDF Kinematical Variables and Reference System . . . . .	39
2.2.2	Cherenkov Luminosity Monitor . . . . .	41
2.2.3	Tracking System . . . . .	42
2.2.4	Time of Flight Detector . . . . .	46
2.2.5	Magnet . . . . .	46
2.2.6	Calorimetry . . . . .	47
2.2.7	Muon System . . . . .	47
<b>3</b>	<b>The Intermediate Silicon Layers Detector</b>	<b>51</b>
3.1	Silicon Detectors in High Energy Physics . . . . .	51
3.1.1	Energy Loss of High Energy Charged Particles in Silicon . . . . .	51
3.1.2	Silicon Properties and the p-n Junction . . . . .	53
3.1.3	The p-n Junction . . . . .	54
3.1.4	Leakage Current . . . . .	56
3.1.5	Silicon Resistivity and Junction Capacitance . . . . .	57
3.1.6	Noise . . . . .	59
3.1.7	Processing . . . . .	60
3.1.8	Double Sided Silicon Microstrip Detectors with Integrated Cou- pling Capacitors . . . . .	61
3.1.9	Breakdown Phenomena . . . . .	64
3.2	The ISL Detector . . . . .	65
3.2.1	Silicon Sensors . . . . .	65
3.2.2	ISL Ladder . . . . .	66
3.2.3	Read-out Electronics . . . . .	67
3.2.4	Hybrids . . . . .	69
3.2.5	ISL Data Acquisition System . . . . .	71
3.2.6	Space Frame . . . . .	71
3.2.7	Radiation Hardness . . . . .	73
3.2.8	ISL Radiation Length . . . . .	77
<b>4</b>	<b>ISL Ladder Electrical Characterization Tests</b>	<b>79</b>
4.1	Components . . . . .	80
4.2	DAQ During Production . . . . .	81
4.3	Preliminary Tests . . . . .	82
4.3.1	Sensor Tests . . . . .	83
4.3.2	Hybrid Tests . . . . .	85
4.4	ISL Ladder Assembly and Construction Procedures . . . . .	86
4.4.1	Assembly . . . . .	87
4.5	Ladder Functionality Tests . . . . .	88
4.5.1	Defective Channel Removal . . . . .	89
4.5.2	Operational Bias Voltage . . . . .	92

4.6	Burn-in Tests . . . . .	93
4.6.1	ISL Ladder Burn-in . . . . .	94
4.6.2	SVX II Ladder Burn-in . . . . .	94
4.7	Laser Tests . . . . .	98
4.7.1	Laser Diagnostics . . . . .	101
4.7.2	Charge Collection Efficiency and Rise Time Measurements . .	102
4.8	ISL Ladder Signal to Noise Measurements . . . . .	103
4.8.1	$\beta$ -source Test Setup . . . . .	103
4.8.2	Clustering Algorithm . . . . .	105
4.8.3	$S/N$ Measurement . . . . .	107
4.8.4	Bandwidth Optimization . . . . .	109
4.9	ISL Ladder Grading . . . . .	109
4.10	Final Assembly . . . . .	110
4.11	Summary . . . . .	111
<b>5</b>	<b>The CDF Trigger System</b>	<b>113</b>
5.1	Introduction . . . . .	113
5.2	Level 1 Trigger . . . . .	116
5.2.1	Calorimetric Objects . . . . .	116
5.2.2	Tracking Objects . . . . .	117
5.2.3	Muon Objects . . . . .	118
5.2.4	Global Decision . . . . .	118
5.3	Level 2 Trigger . . . . .	119
5.3.1	Calorimetric Clustering . . . . .	119
5.3.2	$\sum E_T$ and $\cancel{E}_T$ . . . . .	120
5.3.3	Muons . . . . .	120
5.3.4	Electrons . . . . .	121
5.3.5	Silicon Vertex Trigger . . . . .	121
5.4	Level 3 Trigger . . . . .	122
5.5	Event Reconstruction . . . . .	124
5.5.1	Jet Reconstruction . . . . .	124
5.5.2	Missing $E_T$ Measurement . . . . .	127
5.5.3	Track Reconstruction . . . . .	127
5.5.4	Primary Vertex Identification . . . . .	129
5.5.5	b-Jet Identification . . . . .	130
<b>6</b>	<b>Trigger Rate and Efficiency Calculation</b>	<b>133</b>
6.1	Rate Calculation . . . . .	133
6.2	Correction for Multiple Interactions . . . . .	134
6.3	Data Samples for Rate Estimation . . . . .	135
6.4	Signal Trigger Efficiency . . . . .	136
6.5	Run-II Luminosity Extrapolation . . . . .	136

<b>7</b>	<b>Design of a Dedicated Trigger for <math>H + W/Z \rightarrow b\bar{b}jj</math> Searches</b>	<b>139</b>
7.1	Motivation . . . . .	139
7.2	Trigger Strategy . . . . .	140
7.3	Trigger Rate and Efficiency Calculation . . . . .	142
7.4	Level 1 Trigger Rates and Efficiencies . . . . .	142
7.4.1	Single Trigger Tower . . . . .	143
7.4.2	Global $\sum E_T$ Trigger . . . . .	144
7.5	Level 2 Trigger Rates and Efficiencies . . . . .	147
7.5.1	Calorimetric Selection . . . . .	147
7.5.2	SVT Selection . . . . .	153
7.5.3	Level 2 Trigger Rate Control . . . . .	159
7.5.4	Multiple Interactions Dependence . . . . .	160
7.5.5	Run-II Extrapolation . . . . .	160
7.6	Level 3 Trigger . . . . .	163
7.7	b-Tag Rates . . . . .	164
7.8	Run-II <i>versus</i> Run-I Improvement and Trigger Cuts Summary . . . .	167
<b>8</b>	<b>Design of a Dedicated Trigger for <math>H + Z \rightarrow b\bar{b}\nu\bar{\nu}</math> Searches</b>	<b>171</b>
8.1	Motivation . . . . .	171
8.2	Trigger Rate and Efficiency Calculation . . . . .	173
8.3	Level 1 Trigger Rates and Efficiencies . . . . .	173
8.4	Level 2 Trigger Rates and Efficiencies . . . . .	175
8.4.1	Trigger Requirements . . . . .	175
8.5	Level 3 Trigger . . . . .	180
8.6	$\cancel{E}_T$ Trigger Turn-On . . . . .	181
8.7	b-Tag Rates . . . . .	183
8.8	Conclusions and Trigger Cuts Summary . . . . .	184
<b>9</b>	<b>SM Higgs Boson Discovery Reach</b>	<b>187</b>
9.1	$H + W/Z \rightarrow b\bar{b}jj$ Channel . . . . .	188
9.2	$H + Z \rightarrow b\bar{b}\nu\bar{\nu}$ Channel . . . . .	189
9.3	Run-II Analysis for the $H + W/Z \rightarrow b\bar{b}jj$ Channel . . . . .	190
9.3.1	Signal Monte Carlo Simulation . . . . .	190
9.3.2	Backgrounds . . . . .	190
9.3.3	Kinematical Selection . . . . .	195
9.3.4	Counting Experiment . . . . .	204
9.4	Extrapolation of Run-I Searches . . . . .	205
	<b>Conclusions</b>	<b>209</b>
<b>A</b>	<b>ISL Sensors Specifications</b>	<b>213</b>
A.1	Hamamatsu Sensors Electrical Specifications . . . . .	213
A.2	Hamamatsu Sensors Mechanical Specifications . . . . .	215
A.3	Radiation Damage Specifications for Pilot Hamamatsu Sensors . . . .	216

---

A.4	Micron Sensors Specifications . . . . .	217
<b>B</b>	<b>DAQ During Production</b>	<b>219</b>
B.1	System Overview . . . . .	219
B.2	DAQ Personal Computer and Low Level Software . . . . .	220
B.3	MUX/FIFO Board . . . . .	222
B.4	Burn-in Test High Level Software . . . . .	230
	B.4.1 Software Architecture . . . . .	231
	B.4.2 Burn-In Data Readout and Online Monitoring . . . . .	231
	B.4.3 Binary Data Format . . . . .	233
B.5	Modifications for the Laser Test Station . . . . .	234
B.6	Modifications for the $\beta$ Source Test Setup . . . . .	235



# Resum

## Antecedents

Al nivell actual de coneixements tots els fenòmens experimentals no gravitacionals relatius a la física de partícules elementals poden ser explicats en el marc del denominat *Model Standard* [1, 2, 14].

El *Model Standard* és una teoria quàntica del camp a la que se li aplica el principi d'invariància respecte a transformacions de calibració, conegut també com a principi d'invariància *gauge*. Aquest principi permet explicar les diverses interaccions entre partícules com degudes a l'acció de camps intermediaris amb l'emissió i absorció de partícules portadores de la interacció, denominades bosons *gauge*. En particular, el principi d'invariància *gauge* exigeix que la massa d'aquestes partícules siga igual a zero, fet que es troba en contradicció amb les dades experimentals. Així, per a la interacció electrodèbil existeix una abrumadora evidència de que tres dels seus bosons *gauge* ( $W^\pm$  i  $Z^0$ ) posseeixen masses respectivament iguals a  $80 \text{ GeV}/c^2$  i  $91 \text{ GeV}/c^2$  [20]. En el marc del *Model Standard* la hipòtesi més senzilla per explicar aquest fenomen és l'anomenat mecanisme de Higgs [22]. El mecanisme de Higgs consisteix en l'introducció d'un nou camp escalar complexe, el camp de Higgs, la particularitat del qual resideix en què, si bé amb la seua introducció el lagrangianà que descriu l'interacció continua essent invariant respecte a les transformacions *gauge*, l'estat fonamental no ho és, amb un valor mitjà distint de zero que permet explicar l'existència de massa no tan sols per als bosons *gauge*, sino també per a la resta de les partícules. Aquesta situació en la que el lagrangianà de l'interacció presenta una simetria que no es conserva per a l'estat fonamental es coneguda com *ruptura espontànea de la simetria* [21] i es dona també en altres camps de la física, com ara a la física de l'estat sòlid per als materials ferromagnètics [24]. Una conseqüència immediata del mecanisme de Higgs es l'existència d'una nova partícula elemental, el bosó de Higgs. La teoria no permet preveure la seua massa pero els seus modes de producció i les seues interaccions amb altres partícules estan ben definits i poden ser calculats. Fins a la dada, no hi ha evidència experimental de la seua existència. El mecanisme de Higgs no és una conseqüència necessària del *Model Standard*, però el seu descobriment suposaria un èxit fonamental de la teoria física i de la nostra capacitat de comprensió dels fenòmens de la naturalesa.

Als darrers anys la búsqueda del bosó de Higgs ha estat objecte d'un intens

esforç de recerca en diversos experiments situats als acceleradors de partícules més avançants. Així, a l'accelerador *Large Electron-Positron Collider* al Laboratori Europeu de Física d'Altes Energies i Partícules (Suïssa) l'estudi de col·lisions electró positró a energies de centre de masses de l'ordre de 200 GeV ha permès establir un límit inferior en la massa del Higgs de 114.1 GeV/ $c^2$ , amb indicacions de senyal per a una hipotètica massa de 115.6 GeV/ $c^2$  [32]. Diverses consideracions teòriques estableixen un límit superior de l'ordre de 1 TeV [29]. L'ús de dades provinents de mesures de precisió de diversos paràmetres de l'interacció electrodèbil semblen indicar que el bosó de Higgs podria trobar-se a l'extrem inferior d'aquest interval [31].

A l'accelerador Tevatron (Fermi National Laboratory, Batavia, USA) [38] on es produeixen col·lisions protó antiprotó a energies de centre de masses de l'ordre de 2 TeV, el rang de masses per a la búsqueda del bosó de Higgs s'esté fins als  $\sim 200$  GeV/ $c^2$ . A aquestes energies els modes de producció més abundants per al bosó de Higgs són la fusió gluònica  $gg \rightarrow H$  ( $\sigma = 1 - 0.1$  pb) i la producció associada amb un bosó vectorial  $V = W^\pm, Z$  ( $\sigma = 0.38 - 0.02$  pb) [8]. Per a masses per baix dels 140 GeV/ $c^2$ , on el bosó de Higgs es desintegra principalment en un parell de *beauty* quark i antiquark  $b\bar{b}$  (BR 0.76 - 0.44) la producció mitjançant la fusió gluònica és practicament impossible de detectar degut al fons de parells de  $b\bar{b}$  quarks produïts directament per l'interacció forta. Per a la producció associada el senyal generat per la desintegració del bosó vectorial ( $W \rightarrow q\bar{q}', l\bar{\nu}$ ;  $Z \rightarrow q\bar{q}, \bar{l}l, \nu\bar{\nu}$ ) subministra un criteri que permet discriminar eficientment el senyal del fons, al mateix temps que l'identificació dels dos *jets* b provinents de la hadronització del quark b (*jets* b) i originats en la desintegració del bosó de Higgs, permeten reconstruir la seua massa invariant sense ambigüitats. Per a masses per damunt dels 140 GeV/ $c^2$  la secció eficaç de producció disminueix aproximadament en un ordre de magnitud per a tots els modes de producció. No obstant això, en aquesta regió de masses els canals de desintegració del bosó de Higgs predominants són  $H \rightarrow WW^*$  i  $H \rightarrow ZZ^*$  els quals proporcionen un senyal molt clar quan els bosons vectorials es desintegren en leptons [13].

Durant el període operacional de Tevatron conegut com *Run-I* (1992-1995) al detector *Collider Detector at Fermilab* (CDF) [10] es va efectuar una búsqueda exhaustiva de la producció associada del bosó de Higgs fins masses de l'ordre de  $M_H \leq 130$  GeV/ $c^2$  utilitzant  $109 \text{ pb}^{-1}$  de lluminositat integrada. En aquest mode de producció la desintegració del bosó vectorial determina la topologia del senyal: dos *jets* més un leptó més energia transversa perduda ( $H \rightarrow b\bar{b}, W \rightarrow l\bar{\nu}$ ) [34], quatre *jets* ( $H \rightarrow b\bar{b}, W/Z \rightarrow q\bar{q}'$ ) [114], dos *jets* més energia transversa perduda ( $H \rightarrow b\bar{b}, Z \rightarrow \nu\bar{\nu}$ ) [33] i dos *jets* més dos leptons ( $H \rightarrow b\bar{b}, Z \rightarrow \bar{l}l$ ) [36]. L'anàlisi de les dades no va mostrar cap evidència de senyal i, combinant tots els canals, es va poder establir un límit superior a la secció eficaç de producció  $\sigma(p\bar{p} \rightarrow W/ZH) \times BR(H \rightarrow b\bar{b})$  d'aproximadament 8 pb [37]. Aquest límit és aproximadament un ordre de magnitud superior al valor predit per la teoria.

Per al nou període operacional denominat *Run-II* (2002-2005) s'espera aconseguir

una lluminositat integrada de  $15 \text{ fb}^{-1}$  que representa un augment d'un factor 140 respecte al Run-I. Tota l'electrònica de lectura del detector ha hagut de ser substituïda per adaptar-la al nou interval de col·lisió entre els protons i antiprotons, que al Run-II és de 132 ns (3500 ns al Run-I) [10]. Entre altres millores ha estat construït un nou sistema de detecció de traces de partícules carregades basat en detectors de silici de microbandes i dotat d'una major acceptància geomètrica [11]. L'àrea activa total d'aquest nou sistema ha estat augmentada dels  $0.7 \text{ m}^2$  del Run-I fins als  $1.8 \text{ m}^2$  del Run-II. Des de la part més interna fins a la més externa aquest nou sistema consta de tres detectors: el *Layer00*, el SVX-II i l'*Intermediate Silicon Layers* (ISL). El *Layer00*, consistent en un ultra-lleuger detector d'una sola cara resistent a la radiació i situat a molt baix radius (1.6 cm), té com a finalitat millorar la resolució en paràmetre d'impacte per traces amb baix moment transvers. El següent detector és el detector de vèrtexs SVX-II. Amb una longitud total de 90 cm i cinc capes de silici de doble cara, permetrà duplicar l'acceptància geomètrica respecte al Run-I. Inmediatament després del SVX-II, a una distància radial de 20 cm, es troba el ISL. Amb una longitud total de  $\approx 2 \text{ m}$ , aquest detector està la reconstrucció de traces (i per tant la capacitat d'identificar *jets* deguts al quark b) des d'una pseudorapiditat màxima de  $|\eta| \leq 1$  assolida al Run-I fins a pseudorapiditats de  $|\eta| \leq 2$ . L'addició de coordenades stereo al SVX II i l'ISL permetrà la reconstrucció tridimensional de les traces incrementant l'eficiència d'identificació de *jets* b i disminuint al mateix temps el percentatge de falses identificacions.

El sistema de *trigger* de CDF també ha estat substancialment millorat. La innovació més significativa consisteix en la introducció de nous processadors a segon nivell expresament dissenyats per a la reconstrucció de traces amb qualitat similar als algorismes *offline* [96], el que permet la detecció a nivell de *trigger* de *jets* b.

Estudis preliminars realitzats amb una simulació simplificada del detector CDF [13] indiquen que l'existència del bosó de Higgs prodria ser exclosa a un nivell de certesa del 95% per a masses fins als  $180 \text{ GeV}/c^2$ . Amb la lluminositat programada de  $15 \text{ fb}^{-1}$  es preveu que es pugui observar evidència de senyal al nivell de  $3\sigma$  per a una part significativa d'aquesta regió. No obstant, per a una observació al nivell de  $5\sigma$  és necessària una major lluminositat.

## Objectius

Aquesta tesi està dedicada a l'estudi i millorament de la sensibilitat del detector CDF en la recerca del bosó de Higgs al Run-II. En col·lisions protó antiprotó amb altes lluminositats instantànies, factors de rebuig a nivell de *trigger* de l'ordre de  $10^{12}$  són necessaris per tal de poder adquirir dades amb unes característiques idònies per a la recerca del bosó de Higgs. L'autor d'aquesta tesi ha estudiat i optimitzat *triggers* per a la recerca del bosó de Higgs als casos en els que els *triggers* estàndards del Run-I eren inadequats. En la recerca del bosó de Higgs la capacitat d'identificar *jets* provinents de la hadronització del quark b és fonamental, i exigeix un òptim

funcionament dels detectors de silici que permeta la reconstrucció de les traces de les partícules carregades amb la necessària resolució. El sistema de detecció de traces de silici de CDF consta de més de 700,000 canals de lectura que han de ser cuidadosament comprovats abans de la seua instal·lació al detector. L'autor d'aquesta tesi ha desenvolupat un sistema complet per al test de les característiques elèctriques i funcionals dels diversos detectors que componen el ISL durant la seua construcció als laboratoris de l'Istituto Nazionale di Fisica Nucleare (Pisa, Itàlia) així com, en col·laboració amb la Universitat de Rutgers (New Jersey, USA), el disseny i implementació del *burn-in* test de tots els components del detector SVX II durant la seua construcció a les instal·lacions del Fermi National Laboratory.

## Producció i Tests de Caracterització Elèctrica del Detector ISL

El detector ISL esta provist a la regió central ( $|\eta| \leq 1$ ) d'una capa de detectors de silici situada a un radi de 23 cm i a cadascuna de les parts anterior i posterior ( $1 \leq |\eta| \leq 2$ ) de dues capes situades a un radi de 20 i 29 cm respectivament. La unitat bàsica de l'ISL és la *ladder*. Cada *ladder* consta de tres sensors de silici de microbandes de doble cara consecutivament microsoldats. A la part superior les microbandes són paraleles a l'eix  $z$  del feix de protons i antiprotons, mentre que a la cara inferior estan disposades en un petit angle ( $1.2^\circ$ ) per tal de mesurar la coordenada stereo. En un dels extrems s'afegeix l'hibrid que conté l'electrònica de lectura, duta a terme amb el xip SVX-III [45].

Les *ladders* de l'ISL són construïdes en tres etapes: producció dels híbrids i dels sensors de silici, l'assemblatge de la *ladder* i l'assemblatge dels mòduls formats emparellant dues *ladders*. Per a construir una *ladder* els tres sensors de silici i un híbrid de lectura són encolats damunt d'un suport de fibra de carboni.

Els sensors, els híbrids i els suports de fibra de carboni son rebuts ja comprovats pels fabricants. A les instal·lacions del laboratori s'assemblen les *ladders*, s'instrumenten i després d'una sèrie de tests finals són enviades al Fermi National Laboratory per a la seua instal·lació en el suport general de l'ISL.

Per a aquesta tesi ha estat dissenyat un sistema d'adquisició de dades, electrònica de lectura i programari per la manipulació de les dades per al test i caracterització elèctrica de les *ladders* en cadascuna de les etapes de llur construcció. Els tests consistien en la comprovació de la funcionalitat de cadascun dels canals de lectura (pedestals, nivel de soroll i guany), la detecció de defectes als capacitadors d'acoplament (*pin-holes*) produïts durant el proces de micro-soldadura, la detecció d'acoplaments elèctrics anòmals, tests amb llum de laser infraroig on la il·luminació de cadascuna de les microbandes permet comprobar el funcionament de tota la cadena de lectura, i un *burn-in* test de 72 hores de durada amb la finalitat de detectar defectes intrínsecs que solen apareixer en les primeres hores de funcionament dels detectors. Posteriorment als tests de producció, cada *ladder* era classificada segons

la ocupància de canals necessària per assolir una certa eficiència (98%) de senyal. Per a un nombre reduït de *ladders* s'han realitzat diversos estudis de caracterització del senyal *versus* soroll amb un sorgent de raigs  $\beta$ .

## Estudi d'un Trigger per al Procés $H + W/Z \rightarrow b\bar{b}jj$

Al Run-I la búsqueda a CDF del bosó de Higgs al canal multijet de la producció associada  $H + W/Z \rightarrow b\bar{b}jj$  va patir d'una reduïda sensibilitat degut a un deficient disseny del *trigger*, que rebutjava fins a un 75% dels esdeveniments de senyal ( $M_H = 120 \text{ GeV}/c^2$ ). Per a la selecció d'estats finals amb quatre o més *jets* al Run-I l'únic *trigger* adient era el *multijets trigger* amb els requirements:

**Trigger de Nivell 1:**  $\sum E_T \geq 120 \text{ GeV}$

**Trigger de Nivell 2:**  $N_{clus}(E_T^{clus} \geq 15 \text{ GeV}) \geq 4$ , and  $\sum E_T^{clus} \geq 125 \text{ GeV}$

Aquest *trigger* fou optimitzat per a la búsqueda i posterior observació de la producció de parells top anti-top quan ambdós quarks es desintegren hadrònicament  $t\bar{t} \rightarrow W^-W^+b\bar{b} \rightarrow jjjjbb$ . Degut a la major massa del top quark i a la major multiplicitat de *jets* a l'estat final, el requirements d'aquest trigger resulten ser massa restrictius per al canal  $H + W/Z \rightarrow b\bar{b}jj$ .

Per al Run-II es proposa un nou *trigger* amb uns requeriments menys restrictius:

**Trigger de Nivell 1:** Single trigger tower  $E_T^{tow} \geq 10 \text{ GeV}$

**Trigger de Nivell 2:**  $N_{clus}(E_T^{clus} \geq 10 \text{ GeV}) \geq 3$ , and  $\sum E_T^{clus} \geq 90 \text{ GeV}$

Amb aquest nou disseny del *trigger* l'eficiència per al senyal s'incrementa per un factor  $\sim 3$  per a les diverses masses del bosó de Higgs (Taula 1).

Selecció	$M_H (\text{GeV}/c^2)$				
	110	115	120	125	130
Només Calorimetria $N_{clus}(E_T^{clus} \geq 10) \geq 3$ $\sum E_T^{clus} \geq 90 \text{ GeV}$	$73.4 \pm 0.4\%$	$76.4 \pm 0.4\%$	$78.1 \pm 0.2\%$	$80.8 \pm 0.4\%$	$82.4 \pm 0.6\%$
Calorimetria + $\geq 1$ traça de SVT $ d_0  \geq 100 \mu\text{m}$	$36.9 \pm 0.4\%$	$37.7 \pm 0.4\%$	$39.7 \pm 0.4\%$	$41.3 \pm 0.4\%$	$42.3 \pm 0.7\%$
Calorimetria + $\geq 2$ traces de SVT: $ d_0  \geq 100 \mu\text{m}$ $ d_1  \geq 80 \mu\text{m}$	$28.7 \pm 0.4\%$	$29.2 \pm 0.5\%$	$30.6 \pm 0.2\%$	$32.3 \pm 0.5\%$	$33.2 \pm 0.7\%$

Table 1: Eficiències de senyal per al segon nivell de *trigger* per a diverses masses del bosó de Higgs.

El factor limitatiu de qualsevol *trigger* és la freqüència que resulta de l'adquisició d'esdeveniments produïts pels processos de fons. Amb el nou sistema de trigger de

CDF la màxima amplaria de banda a nivell 1 és de 50 kHz, mentre que a nivell 2 és de 300 Hz. Un *trigger* dedicat a un canal específic pot ocupar només al voltant del  $\sim 5\%$  del total de la banda. Per al nostre estudi la freqüència de *trigger* ha estat calculada emprant dades reals del Run-I amb secció eficaç coneguda. Per al nostre *trigger* a nivell 2 la freqüència de *trigger* resulta ser 15 Hz ( $= 1 \cdot 10^{32} \text{ cm}^{-2} \text{ s}^{-1}$ , Taula 2), completament acceptable pel sistema d'adquisició de dades.

Selecció (JET20)	Freqüència (Hz)	$\sigma_T$ (nb)	rebuig
Només calorimetria $N_{clus}(E_T^{clus} \geq 10) \geq 3$ $\sum E_T^{clus} \geq 90 \text{ GeV}$	$17.1 \pm 0.6$	$171 \pm 6$	1
Calorimetria + $\geq 1$ traça de SVT $ d_0  \geq 100 \mu\text{m}$	$3.3 \pm 0.1$	$33 \pm 1$	$5.2 \pm 0.2$
Calorimetria + $\geq 2$ traces de SVT $ d_0  \geq 100 \mu\text{m},  d_1  \geq 80 \mu\text{m}$	$1.08 \pm 0.04$	$10.8 \pm 0.4$	$16 \pm 1$

Table 2: Freqüència, secció eficaç i factors de rebuig per al nivell 2 de *trigger*. Els factors de rebuig estan calculats respecte als esdeveniments que superen els requeriments calorimètrics.

Al nivell 3 de *trigger* la màxima freqüència permesa al nostre cas és de 1-2 Hz. És necessari doncs un factor  $\sim 7.5$  de rebuig addicional. Al nou sistema de *trigger* de CDF és possible reconstruir traces de partícules carregades a nivell 2 amb qualitat similar a la subministrada pels algorismes *offline* amb el *Silicon Vertex Trigger* (SVT) [96]. Fins a masses de  $140 \text{ GeV}/c^2$ , el bosó de Higgs es desintegra principalment en parells de *beauty* quark anti-quark. El moment transvers dels hadrons b és gran en comparació amb la massa del mateix b quark. Aquesta circumstància, juntament amb la llarga vida mitjana dels hadrons b ( $\tau = 1.549 \pm 0.20 \text{ ps}$  [91]) resulta en una gran longitud mitjana de desintegració i per tant en la presència de vertexs secundaris juntament amb la presència de traces amb llargs paràmetre d'impacte. En aquesta tesi proposem l'ús addicional de la informació subministrada per l'SVT requerint la presència de traces amb paràmetre d'impacte per damunt d'un cert llindar, requeriment que permet seleccionar b jets i rebutjar jets produïts en l'hadronització de gluons o quarks lleugers. Els nostres estudis mostren que requerint al menys dos traces amb parametre d'impacte  $d_0 \geq 100 \mu\text{m}$  i  $d_1 \geq 80 \mu\text{m}$  s'aconsegueix un factor de rebuig del fons de  $\sim 7.5$ , amb eficiències per al senyal del  $\sim 40\%$  (Taules 1 i 2).

La recerca del bosó de Higgs fins a masses de  $\sim 140 \text{ GeV}/c^2$  es basa principalment en el requeriment de dos *jets* identificats com a *jets* b, el que permet reconstruir la seua massa invariant sense ambigüitats. A CDF un dels algorismes més estudiats per a la identificació de jets b es basa en la detecció de vertexs secundaris a l'interior

dels *jets*. És d'esperar doncs que la selecció a nivell de *trigger* d'esdeveniments amb traces amb llarg parametre d'impacte resulte en una mostra on l'eficiència per a la identificació de *jets* b siga particularment alta. La Taula 3 mostra l'eficiència de detecció d'un o dos *jets* b en mostres del procés  $H + W/Z \rightarrow b\bar{b}jj$  que satisfan les condicions del nou i del *multijets trigger* del Run-I.

Selecció de Trigger	$M_H = 120 \text{ GeV}/c^2$		
	Freqüència de <i>jets</i> b (%)		$\epsilon_{\text{trigger}}$ (%)
	Un <i>jet</i> b	Dos <i>jet</i> b	
<b>Run-I</b> $N_{\text{cl}}(E_T^{\text{cl}} \geq 15 \text{ GeV}) \geq 4$ $\Sigma E_T^{\text{cl}} \geq 125 \text{ GeV}$	$40.3 \pm 0.1$	$12.6 \pm 0.4$	$24.6 \pm 0.4$
<b>Run-II</b> Calorimetria Nivell 2: $N_{\text{clus}}(E_T^{\text{cl}} \geq 10 \text{ GeV}) \geq 3$ , $\Sigma E_T^{\text{cl}} \geq 90 \text{ GeV}$	$44.7 \pm 0.1$	$12.8 \pm 0.2$	$78.1 \pm 0.2$
Calorimetry Nivell 2 + $\geq 2$ SVT tracks $ d_0  \geq 100,  d_1  \geq 80 \mu\text{m}$	$80.7 \pm 0.1$	$27.7 \pm 0.1$	$39.9 \pm 0.3$

Table 3: Eficiència d'identificació d'un o dos *jets* b i eficiència de *trigger* ( $\epsilon_{\text{trigger}}$ ) per al senyal ( $M_H = 120 \text{ GeV}/c^2$ ) per al *trigger multijet* del Run-I i per cadascun dels requeriments del nou *trigger*.

L'eficiència total per a esdeveniments que satisfan les condicions de *trigger* i on a més els dos *jets* provinents de la desintegració del bosó de Higgs poden ser identificats com a *jets* b és  $0.393 \times 0.277 = 0.108$ . Aquesta xifra ha de ser comparada amb la corresponent al Run-I, que és  $.126 \times 0.246 = 0.03$ , és a dir, amb el nou *trigger* s'obté un millorament d'aproximadament un factor 3.

Al Run-I l'anàlisi del canal  $H + W/Z \rightarrow b\bar{b}jj$  va permetre establir un límit superior a la producció associada del bosó de Higgs competitiu amb els obtinguts en altres canals, malgrat l'enorme fons degut a la producció multijets de QCD. Els processos de fons considerats varen ser la producció multijet de quarks b mitjançant processos de QCD, la producció de parells  $t\bar{t}$ , la producció d'un bosó vectorial amb parells  $b\bar{b}$  o  $c\bar{c}$ , producció de *single top* quark i la producció de dibosons WW o ZZ. Els talls requerits consistien en el *trigger multijets* del Run-I, quatre o més *jets* amb energia transversa  $E_T \geq 15 \text{ GeV}$ , al menys dos *jets* identificats com a *jets* b i un tall al moment transversal del sistema format pels dos *jets* b de  $p_T(b\bar{b}) \geq 50 \text{ GeV}/c$ . Analitzant l'espectre de massa invariant del sistema format pels dos *jets* b es va establir un límit superior a la secció eficaç de producció del bosó de Higgs  $\sigma \times BR(H \rightarrow b\bar{b})$  de 18 pb ( $M_H = 120 \text{ GeV}/c^2$ ) a un nivell de certesa del 95% [121]. El valor predit per la teoria per a la secció eficaç en el marc del *Model Standard* és de 0.20 pb [8].

A aquesta tesi hem extrapolat aquest límit a les condicions del Run-II tenint en compte les eficiències del nou trigger i l'increment per un factor 1400 de la lluminositat integrada. En absència de senyal, el valor de la secció eficaç d'exclusió a un nivell de certesa del 95% varia amb la lluminositat integrada i amb les eficiències

pel senyal i el fons de la forma

$$\sigma_{95\%}^{II} \sim \sigma_{95\%}^I \cdot \sqrt{\frac{\epsilon_{II}^{back}}{\epsilon_I^{back}}} \cdot \frac{\epsilon_I^{sig}}{\epsilon_{II}^{sig}} \cdot \sqrt{\frac{\mathcal{L}^I}{\mathcal{L}^{II}}} \quad (1)$$

A la nostra anàlisi els processos de fons considerats han estat els mateixos que a l'anàlisi del Run-I. Pel que respecta a l'eficiència de la selecció, tant per al fons com per al senyal, els talls considerats han estat: els requisits de *trigger*, quatre o més jets amb  $E_T^{jets} \geq 15$  GeV, la suma de l'energia transversa de tots els *jets* amb  $E_T^{jet} \geq 15$  GeV igual o major que 140 GeV, al menys dos *jets* identificats com a *jets b* i requerint que la massa invariant corresponent al bosó vectorial siga igual o major a 90 GeV/ $c^2$ . Tenint en compte aquests talls i la eficiència del nou *trigger*, juntament amb l'augment de la lluminositat integrada, trobem que la sensibilitat de CDF al Run-II en aquest canal pot incrementar-se per un factor 20, poguent excloure seccions eficaces de producció fins als 0.70 pb [ $M_H = 120$  GeV/ $c^2$ ] (Figura 1).

## Estudi d'un *Trigger* per al Procés $H + Z \rightarrow b\bar{b}\nu\bar{\nu}$

La recerca del bosó de Higgs en el canal  $H + Z \rightarrow b\bar{b}\nu\bar{\nu}$  es va realitzar al Run-I de CDF amb un *trigger* que requeria a nivell 2 energia transversa perduda major de 35 GeV. Al Run-II, degut a l'increment per un factor 10 de la lluminositat instantània ( $\mathcal{L} = 1 \cdot 10^{32}$  cm<sup>-2</sup>s<sup>-1</sup>), el llinar en l'energia transversa perduda deu ser incrementat fins als 45 GeV per tal d'obtindre freqüències de *trigger* acceptables, amb una considerable pèrdua d'eficiència (Taula 4).

Selecció	Massa del bosó d'Higgs ( GeV/ $c^2$ )				
	110	115	120	125	130
<b>Inclusiu</b> $\cancel{E}_T \geq 35$ GeV	60.4 $\pm$ 0.9	61.6 $\pm$ 0.9	62.9 $\pm$ 0.9	63.7 $\pm$ 0.9	64.7 $\pm$ 0.9
$\cancel{E}_T \geq 15$ GeV $E_T^{clus} \geq 20$ GeV	85.4 $\pm$ 0.9	86.6 $\pm$ 0.9	86.9 $\pm$ 0.3	88.7 $\pm$ 0.9	84.7 $\pm$ 0.9
$\cancel{E}_T \geq 15$ GeV + $E_T^{clus} \geq 20$ GeV 1 SVT, $ d_0  \geq 100 \mu\text{m}$	51.3 $\pm$ 0.6	52.0 $\pm$ 0.6	52.6 $\pm$ 0.6	55.1 $\pm$ 0.6	51.4 $\pm$ 0.6
$\cancel{E}_T \geq 15$ GeV + $E_T^{clus} \geq 20$ GeV + 1 SVT, $ d_0  \geq 100 \mu\text{m}$ 1 SVT, $ d_1  \geq 80 \mu\text{m}$	38.2 $\pm$ 0.5	38.6 $\pm$ 0.5	39.2 $\pm$ 0.7	40.9 $\pm$ 0.5	38.2 $\pm$ 0.5

Table 4: Eficiències de *trigger* per a diferents seleccions de *trigger*

Per al Run-II a aquesta tesi hem estudiat l'optimització d'aquest *trigger* emprant el SVT a segon nivell. Requerint al menys dos traces amb parametre d'impacte

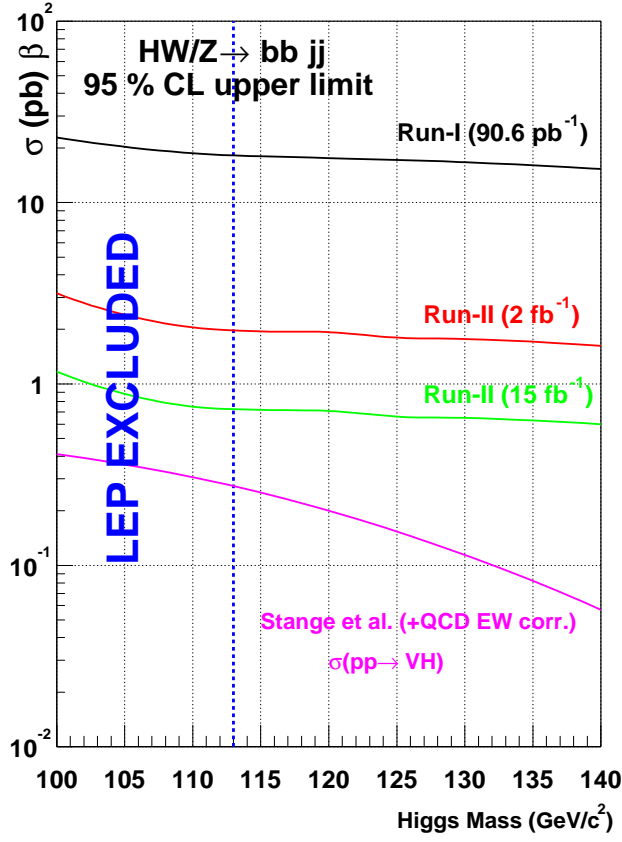


Figure 1: Extrapolació per al Run-II dels límits d'exclusió a un nivell de certesa del 95% per a  $\sigma(p\bar{p} \rightarrow HW/Z) \cdot \beta$ , on  $\beta = BR(H \rightarrow b\bar{b})$ .

$d_0 \geq 100 \mu\text{m}$  i  $d_1 \geq 80 \mu\text{m}$  és possible reduir el llinar d'energia transversa perduda fins a 15 GeV amb freqüències de *trigger* acceptables (Taules 5 i 6).

La Taula 6 mostra les eficiències de *trigger* per a esdeveniments  $H + Z \rightarrow b\bar{b}\nu\bar{\nu}$  amb el nou *trigger* i amb el *trigger* estàndard proposat pel Run-II. Hom pot veure que les eficiències del *trigger* estàndard són més altes que amb el nou *trigger*. Ara bé, la búsqueda del bosó de Higgs en aquest canal requereix necessàriament que dos *jets* siguin identificats com a *jets* b, juntament amb un cert llinar en l'energia transversa perduda. En aquest cas l'eficiència rellevant és l'eficiència combinada de *trigger* més l'eficiència d'identificació de dos *jets* b. Degut a la correlació existent entre els requeriments de traces amb llarg paràmetre d'impacte i el funcionament dels algorismes d'identificació de *jets* b, hom pot veure que aquesta eficiència combinada és per als esdeveniments que satisfan el nou *trigger*  $= 0.181 \times 0.392 = 0.07$  (Taula 6), mentre que pel *trigger* estàndard és  $= 0.089 \times 0.507 = 0.45$ , és a dir, un millorament per un factor 1.6.

	$\sigma_T$ (nb)	Freqüència (Hz)	Factor de rebuig
<b>Inclusiu</b> $\cancel{E}_T \geq 35$ GeV	$77 \pm 1$	$7.7 \pm 0.7$	$97 \pm 2$
$\cancel{E}_T \geq 15$ GeV $E_T^{clus} \geq 20$ GeV	$2344 \pm 7$	$234.4 \pm 0.7$	$3.2 \pm 0.1$
$\cancel{E}_T \geq 15$ GeV + $E_T^{clus} \geq 20$ GeV 1 SVT, $ d_0  \geq 100 \mu\text{m}$	$280 \pm 3$	$28.0 \pm 0.3$	$26.8 \pm 0.3$
$\cancel{E}_T \geq 15$ GeV + $E_T^{clus} \geq 20$ GeV 1 SVT, $ d_0  \geq 100 \mu\text{m}$ 1 SVT, $ d_1  \geq 80 \mu\text{m}$	$58 \pm 6$	$5.8 \pm 0.6$	$129 \pm 3$

Table 5: Freqüència de *trigger* ( $\mathcal{L} = 1 \cdot 10^{32} \text{ cm}^{-2} \text{ s}^{-1}$ ), secció eficaç ( $\sigma_T$ ) de *trigger* i factor de rebuig.

Selecció de Trigger	Freqüència de <i>jets</i> b(%)		$\epsilon_{\text{trigger}}$ (%)
	Un <i>jet</i> b	Dos <i>jet</i> b	
<b>Incl.</b> $\cancel{E}_T \cancel{E}_T^{trg} \geq 35$ GeV $\cancel{E}_T^{off} \geq 45$ GeV	$40.4 \pm 0.1$	$8.9 \pm 0.4$	$50.7 \pm 0.5$
<b>Run-II</b> Nivell 2 Calorimetria: $\cancel{E}_T^{trg} > 15$ GeV	$40.0 \pm 0.7$	$8.9 \pm 0.3$	$86.9 \pm 0.3$
Nivell 2 Calorimetria + $\geq 2$ traces de SVT, $ d_0  \geq 100 \mu\text{m}$ , $ d_1  \geq 80 \mu\text{m}$	$67.9 \pm 0.1$	$18.1 \pm 0.1$	$39.2 \pm 0.7$

Table 6: Eficiència d'identificació d'un o dos *jets* b i eficiència de *trigger* ( $\epsilon_{\text{trigger}}$ ) per al senyal ( $M_H = 120 \text{ GeV}/c^2$ ). ( $M_H = 120 \text{ GeV}/c^2$ )

## Conclusions

En aquesta tesi hem desenvolupat un sistema per als tests de producció i caracterització elèctrica de les *ladders* del detector ISL construïdes a les instal·lacions del INFN de Pisa (Itàlia). Aquest sistema va permetre el test de més de 150 *ladders* completament instrumentades (la meitat del total de *ladders* de l'ISL,  $\sim 150,000$  canals de lectura) en els terminis previstos (Juny 2001) a un ritme de construcció de dos *ladders* per dia. Així mateix, el test de *burn-in* va ser desenvolupat conjuntament amb el grup de l'Universitat de Rutgers (New Jersey, USA) i aplicat per al test de les *ladders* del detector SVX II al Fermi National Laboratory (USA).

Per a la reserca del bosó de Higgs al Run-II de CDF, hem estudiat i optimitzat dos nous triggers per al canal  $H + W/Z \rightarrow b\bar{b}jj$  i  $H + Z \rightarrow b\bar{b}\nu\bar{\nu}$  respectivament, fent

ús de la nova capacitat de CDF de *trigger* a segon nivell amb traces reconstruïdes amb qualitat *offline*. Per al canal  $H + W/Z \rightarrow b\bar{b}jj$  els nostres estudis mostren que la sensibilitat del detector CDF es pot augmentar per un factor  $\sim 2$ . Per al cas  $H + Z \rightarrow b\bar{b}\nu\bar{\nu}$ , el nou *trigger* permet adquirir dades amb baixos llindars d'energia transversa perduda, malgrat l'augment per un factor 10 de la lluminositat instantània, resultant en un augment de eficiència d'un factor 1.6.



# Acknowledgements

*The thesis is only the beginning*, said to me an American professor one late night at CERN while I was typing the last chapters of this thesis, desperate of endless corrections. It has been a long way. The thesis is the time when, whatever it will be, one acquires his own scientific maturity. One learns from the people around, the supervisor, friends and colleagues and even the enemies, the methods, the discipline, the goals, and the motivation. I have a debt of gratitude with Juan Valls that goes far beyond the technical help. He has been an example of courage, clear mind and enthusiasm. With professor Franco Bedeschi I am in debt for his patience and his comments correcting all my mistakes. There was not any single discussion with him where I have not learned something new about physics. Thanks to all my *bosses*, Aldo Menzione, Antonio Ferrer, Emilio Higón, Giorgio Bellettini and Giorgio Chiarelli. They always trusted me and supported me. Without them this work would simply not exist. Thanks to Simone Donati and Irene Fiori for their immense humanity. To Nail Malakhov for his friendship. To Francesco Palmonari, Giulio Petragnani, Diego Tonelli, Monica D’Onofrio, Andrea Basti, Andrea Moggi and Frabrizio Raffaelli for the nice side of the ISL, and two marvelous years in Tuscany. I will never forget the beauty of this part of the world that a unique person like Carol Ackenheil taught me how to appreciate. Thanks to Flavia Donno for her help with the software, and in general to all the INFN-Pisa staff, specially Clara Scopsi and Oriana Benedetti. To the Silicon Vertex Trigger people, professor Luciano Ristori, Giovanni Punzi, Stefano Belforte, Bill Ashmanksas, Roberto Carosi and Franco Spinella thanks for the opportunity to be witness of a work that I deeply admire. Without Rocio Vilar, Susana Cabrera, Gervasio Gómez, Simona Rolli, Abraham Agallas, Iván Vila, Jonatan Piedra, Mary Anne Cummings and Mario Pérez I could not survive at Fermilab. Thanks to Mario Paolo Giordani for his solidarity and to John Conway for his support.

This thesis is dedicated:

To my parents and sister, the ground that I step every day.

To my grandfather and grandmother, you had no time to wait, *in memoriam*.



# Introduction

In the present time all the experimental phenomena concerning the elementary particles and their non-gravitational interactions can be explained with the so called Standard Model (SM) [1, 2], and so far no deviation from its predictions have been observed.

The SM is a gauge quantum field theory. The gauge invariance of the theory requires masses of the gauge bosons that mediate the electroweak interactions to be zero, in contradiction with the experimental data [3]. Theoretically, the simplest solution in the SM framework is to introduce a complex scalar field [4], the *Higgs* field, which leads to a gauge invariant theory with a spectrum of massive gauge bosons and massive fermions. A consequence of this mechanism [4] is the existence of a new observable scalar particle, the Higgs boson, with unknown mass but fixed couplings to other particles. Direct searches at the LEP [5] experiments have set a lower bound on the mass of  $114.1 \text{ GeV}/c^2$ , with signal hints for a mass hypothesis of  $115.6 \text{ GeV}/c^2$  [5], while several theoretical considerations (*e.g.* the triviality bound [6]) imposes an upper bound of  $\mathcal{O}(1) \text{ TeV}$ . Precision electroweak experiments suggests that the Higgs boson mass may lie at the lower end of this range [7].

In  $p\bar{p}$  collisions at the Tevatron accelerator energies ( $\sqrt{s} = 1.8 - 2.0 \text{ TeV}$ ) the available mass range for Higgs boson searches expands up to  $\approx 200 \text{ GeV}$ . At these energies the two most copious production mechanisms for the SM Higgs boson are the gluon-gluon fusion process  $gg \rightarrow H$  ( $\sigma = 1 - 0.1 \text{ pb}$ ) and the associated production with a vector boson ( $\sigma = 0.38 - 0.02 \text{ pb}$ ) [8]. For masses below  $140 \text{ GeV}/c^2$ , where the Higgs boson predominantly decays to  $b\bar{b}$  (B.R.  $0.76 \div 0.44$ ), the gluon-gluon fusion production mechanism with the subsequent decay of the Higgs boson to  $b\bar{b}$  pairs is very hard to resolve from the overwhelming background of QCD production of  $b\bar{b}$  pairs [13, 113]. In the associated production channel the signature of the vector boson ( $W \rightarrow q\bar{q}', l\bar{\nu}; Z \rightarrow q\bar{q}, \ell\bar{\ell}, \nu\bar{\nu}$ ) provides a simple criteria for signal discrimination, while the identification of the b-jets from the Higgs boson decay allows to reconstruct its invariant mass without ambiguities. For higher Higgs boson masses ( $M_H > 140 \text{ GeV}/c^2$ ) the production cross section decreases by an order of magnitude in all channels. However, in this region the Higgs boson predominant decays modes are  $H \rightarrow WW^*$  and  $H \rightarrow ZZ^*$ , which provide a very clean signature when the vector bosons decay leptonically, and where we can also recover some

channels in the direct production due to the higher production cross section.

In the Run-I of the Tevatron accelerator (1992-1995) the Collider Detector at Fermilab (CDF) has searched for a Higgs boson in the associated production channel in the mass region  $M_H \leq 130 \text{ GeV}/c^2$  with  $109 \text{ pb}^{-1}$  of integrated luminosity. In these channels the decay of the associated vector boson dictates the signal signature: two jets plus lepton plus missing transverse energy ( $H \rightarrow b\bar{b}, W \rightarrow l\bar{\nu}$ ), four jets ( $H \rightarrow b\bar{b}, W/Z \rightarrow q\bar{q}$ ), two jets plus missing energy ( $H \rightarrow b\bar{b}, Z \rightarrow \nu\bar{\nu}$ ) and two jets plus two leptons ( $H \rightarrow b\bar{b}, Z \rightarrow l\bar{l}$ ). No signal evidence was found, and an upper limit on the production cross section  $\sigma(p\bar{p} \rightarrow VH) \times BR(H \rightarrow b\bar{b})$  combining all channels was set to  $\approx 8 \text{ pb}$  [9], approximately an order of magnitude below the theoretically predicted value.

In Run-II (2001-2005,  $\sqrt{s} = 2.0 \text{ TeV}$ ) the expected total integrated luminosity is  $\approx 15 \text{ fb}^{-1}$ , a 150 fold increase respect Run-I. All the detector read-out electronics has been replaced to cope with the new time between bunch crossing of 132 ns (3500 ns in Run-I) [10], and a complete new silicon tracking system has been built with larger geometrical acceptance [11]. The total silicon active area has increased from  $0.7 \text{ m}^2$  in Run-I to  $1.8 \text{ m}^2$  in Run-II. Two new silicon detectors has been added. The Layer 00, a single sided layer of low-mass rad-hard silicon-microstrips, have been placed at very small radius (1.6 cm) to improve the impact parameter resolution, in particular at low transverse momenta. Outside of the SVX-II, at a radial position of  $\approx 20 \text{ cm}$ , the Intermediate Silicon Layers (ISL) detector has been installed. With a total length of  $\approx 2 \text{ m}$  it extends the silicon tracking, and therefore b-jet identification capabilities, from the Run-I range of  $|\eta| \leq 1$  to  $|\eta| \leq 2^1$ . Furthermore, the addition of stereo information will allow three-dimensional track reconstruction with silicon information, and therefore an increased b-jets identification efficiency with a low fake rate. At Level 2 trigger the upgraded CDF detector has the capability to reconstruct silicon tracks with almost offline quality [12], and therefore trigger on secondary vertices produced in the decay of the long-lived B-hadrons, as, *e.g.*, those produced in the  $H \rightarrow b\bar{b}$  decay.

Preliminary studies with a simplified simulation of the upgraded CDF detector [13] indicate that the SM Higgs boson could be excluded at 95% C.L. up to masses of  $180 \text{ GeV}/c^2$ . With the planned  $15 \text{ fb}^{-1}$  evidence for a discovery at the  $3\sigma$  level can be achieved for a significant part of this region. However, more integrated luminosity is needed for a discovery at the  $5\sigma$  level. In this work, we attempt to lower the luminosity needed for the discovery.

This thesis is devoted to the study and enhancement of the CDF sensitivity for Higgs boson searches in Run-II. In  $p\bar{p}$  collisions at high luminosities a trigger rejection factor of  $10^{12}$  must be implemented to be able of acquire data with signatures suitable for Higgs boson searches. The author has studied and optimaized triggers

---

<sup>1</sup>CDF defines the pseudo-rapidity as  $\eta = -\ln(\tan(\theta/2))$ , where  $\theta$  is the production angle with respect to the direction of the proton beam.

for Higgs boson searches in the cases where the usual RUN-I triggers were inadequate. The increase of the CDF potential for Higgs boson searches in Run-II heavily relies in an enhanced capability to identify  $b$ -jets, that can be provided by the second trigger level on secondary vertices with tracks provided by the silicon trackers. A good performance of the silicon trackers is crucial to improve the Higgs discovery potential of CDF in RUN-II. The CDF silicon system consists of more than 700,000 readout channels that must be carefully tested before its insertion in the detector. The author has developed a system for the electrical and functionality tests of the ISL ladders built in the silicon detector facilities of the Istituto Nazionale di Fisica Nucleare, (Pisa, Italy). The system was composed of an automatic laser test station for the assembled ladders, where the author developed all the DAQ software on a personal computer, together with the ladder alignment procedures, software for the micrometric table movement and bias voltage control. Together with the Rutgers University group (New Jersey, USA) and Karlsruhe University group (Germany), the author developed the electronics for the SVX-III chip control and read-out, based on a previous version created at the LBL laboratories for the operation of the SVX-II chip. These read-out electronics were later modified by the author to allow external triggering, and they were used for a  $\beta$ -source test stand. The author implemented also all the software and data handling for the burn-in test of the SVX II detector at the Silicon Laboratories at the Fermi National Laboratory in Batavia, (IL, USA).

The first part of the thesis is dedicated to the procedures and instrumentation developed for ladder testing during construction. The testing was aimed to the detection of silicon sensor damages created during the assembly procedure, the detection of intrinsic weakness present in the sensor and read-out electronics (burn-in test), and the full characterisation of the silicon detector ladders.

The second part of the thesis is devoted to study an optimal design of triggers for Higgs boson searches up to masses of  $140 \text{ GeV}/c^2$ . In two production channels the design of a trigger with high efficiencies and acceptable rates is a concern. For the  $H + W/Z \rightarrow b\bar{b}jj$  channel, the trigger needs in significant improvements respect to the standard Run-I CDF multijet trigger, since it rejected almost 80% of the events for Higgs masses below  $140 \text{ GeV}/c^2$ . In the  $H + Z \rightarrow b\bar{b}\nu\bar{\nu}$  channel keeping a low threshold in the missing transverse energy at trigger level with acceptable rates is a major issue. In both cases we exploit the novel CDF capability to trigger on the impact parameter of reconstructed tracks at trigger level.

Finally, the CDF discovery reach for the Higgs boson in the  $H + W/Z \rightarrow b\bar{b}jj$  channel with these new triggers is studied.

This thesis is structured as follows:

**Chapter 1** gives a brief review of the Higgs mechanism in the Standard Model

and the electroweak symmetry breaking. The Standard Model Higgs boson phenomenology at Tevatron energies is reviewed.

**Chapter 2** describes the upgraded Fermilab laboratory accelerator complex, and the upgraded CDF detector.

**Chapter 3** gives a brief overview of the more relevant aspects of the silicon detectors, and the ISL is described in detail.

**Chapter 4** describes the construction of the ISL ladders, the full custom testing setup (functionality tests, laser test, burn-in test and  $\beta$ -source measurements), and the problems encountered during the ISL ladders construction. The procedures for ladder grading are also discussed.

**Chapter 5** describes the multilevel trigger system of the CDF detector, and the trigger primitives available at each level. The most relevant offline event observables are briefly discussed.

In **Chapter 6** the procedures to estimate the trigger rate and trigger efficiency calculation are described. The particularities of triggering in  $p\bar{p}$  collisions at high luminosities are discussed.

**Chapter 7** and **Chapter 8** are dedicated to study an efficient trigger strategy for the  $H + W/Z \rightarrow b\bar{b}jj$  channel and the  $H + Z \rightarrow b\bar{b}\nu\bar{\nu}$  channels, respectively. Trigger primitives at all levels are defined and trigger rates and trigger efficiencies are calculated.

**Chapter 9** is dedicated to the study of the CDF Run-II Higgs boson discovery potential in the  $H + W/Z \rightarrow b\bar{b}jj$  and  $H + Z \rightarrow b\bar{b}\nu\bar{\nu}$  channels with the discussed triggers. The results of the Tevatron Higgs Working Group are discussed taking into account the new trigger. For the  $H + W/Z \rightarrow b\bar{b}jj$  channel an alternative optimization of the offline cuts is performed, and finally the Run-I limits in this channel are extrapolated to the Run-II scenario.

# Chapter 1

## Standard Model Higgs Boson Physics

Over the last 25 years the *Standard Model* theory of the elementary particles and their non gravitational interactions has succeed explaining all the known experimental phenomena, and no deviations from its predictions have been observed. At the present time the fundamental question about the origin of the masses of the elementary particles remains still open and subject to an intens research effort. Several theoretical approaches have been proposed, but up to date none of them have received experimental confirmation. In the Standard Model framework, the simplest electroweak symmetry breaking mechanism is based on the existence of a single spinless massive particle, called the Higgs boson. The theory does not predict its mass, but its couplings with other particles are well defined and can be calculated. So far there is no experimental evidence about its existence. However, several theoretical arguments strongly indicate that if the Higgs boson exists, it could be discovered with the frontier accelerators already operational like Tevatron (Fermilab, USA), or operational in the near future, as the LHC (CERN, Switzerland).

In this Chapter the most relevant aspects of the spontaneous symmetry breaking mechanism and its application to the Electroweak Sector of the Standard Model (the Higgs mechanism) are treated. The Higgs boson phenomenology at the Tevatron center-of-mass energies is also discussed. Finally, the present status of the Standard Model Higgs boson searches with special emphasis on the Run-I CDF searches is reviewed.

### 1.1 The Standard Model

The Standard Model (SM) is a relativistic quantum field theory of the elementary particles and their interactions [1, 2, 14]. The elementary particles are the point-like constituents of matter with no known substructure up to the present limits of  $10^{-18} - 10^{-19}$  m [23]. There are two types: the fermions and the intermediate interaction particles or gauge bosons. The fermions are particles of spin  $s = \frac{1}{2}$  and are classified into leptons and quarks. The known leptons are the electron ( $e^-$ ),

the muon ( $\mu^-$ ) and the tau-lepton ( $\tau^-$ ), all with electric charge  $Q = -1$ .<sup>1</sup> For each lepton there is also its corresponding neutrino  $\nu_e$ ,  $\nu_\mu$  and  $\nu_\tau$  with  $Q = 0$ . There are six different types of quarks (flavor): u, d, s, c, b and t, which have a fractional electrical charge of  $Q = \frac{2}{3}, -\frac{1}{3}, -\frac{1}{3}, \frac{2}{3}, -\frac{1}{3}$  and  $\frac{2}{3}$  respectively. The quarks have an additional quantum number, the color, which can be of three types and is generically denoted as  $q_i$  ( $i = 1, 2, 3$ ). So far there is not experimental evidence of isolated single quarks. The quarks are assumed to be confined into experimentally observed colorless matter particles, the hadrons. These colorless composite particles are classified into baryons and mesons. The baryons are fermions made of three quarks (*i.e.*, protons and neutrons). The mesons are bosons made of one quark and one antiquark (*i.e.*, the pions). For each particle a corresponding antiparticle exists, with the same mass but opposite quantum numbers. Table 1.1 summarizes the lepton and quark properties.

	Generation		
	1st	2nd	3rd
	1st	2nd	3rd
quarks	<b>up</b> (u) mass: 2 – 8 MeV/ $c^2$ charge: $+\frac{2}{3}$	<b>charm</b> (c) mass: 1.0 – 1.6 GeV/ $c^2$ charge: $+\frac{2}{3}$	<b>top</b> (t) mass: 174 GeV/ $c^2$ charge: $+\frac{2}{3}$
	<b>down</b> (d) mass: 5 – 15 MeV/ $c^2$ charge: $-\frac{1}{3}$	<b>strange</b> (s) mass: 0.1 – 0.3 GeV/ $c^2$ charge: $-\frac{1}{3}$	<b>bottom</b> (b) mass: 4.1 – 4.5 GeV/ $c^2$ charge: $-\frac{1}{3}$
	<b>electron</b> ( $e^-$ ) mass: 0.511 MeV/ $c^2$ charge: $-1$	<b>muon</b> ( $\mu^-$ ) mass: 106 MeV/ $c^2$ charge: $-1$	<b>tau</b> ( $\tau^-$ ) mass: 1.78 GeV/ $c^2$ charge: $-1$
	<b><math>e^-</math> neutrino</b> ( $\nu_e$ ) mass: 0 charge: 0	<b><math>\mu^-</math> neutrino</b> ( $\nu_\mu$ ) mass: 0 charge: 0	<b><math>\tau^-</math> neutrino</b> ( $\nu_\tau$ ) mass: 0 charge: 0

Table 1.1: The fundamental matter particles of the Standard Model in their mass eigenstates [17]. Particles are grouped in *Generations*, ranked according to the increasing mass of the particles<sup>2</sup>. Since quarks are not found in a free state, their masses cannot be determined precisely.

<sup>1</sup>All charges are given in units of the elementary electron charge  $|e|$ .

<sup>2</sup>For each *Generation*, the SM results can be reproduced independently. The LEP experiments (CERN) have shown that the analysis of the  $e^+e^-$  cross section in the  $Z^0$  mass energy region

In the SM the fundamental matter particles are described by relativistic quantum fields. As the physical observables depend on the square of the field's module  $|\Psi|^2$ , it can be demanded the structure of the theory to be invariant under phase transformations of the type [14]:

$$\Psi \rightarrow \Psi' = e^{-i\alpha} \Psi \quad (1.1)$$

called *global Gauge transformations*. One could also explore the implication of requiring the phase of  $\Psi$  in an arbitrary way at each space-time point without affecting the theory. This requirement implies the theory to be invariant under transformations of the type:

$$\Psi(\vec{x}, t) \rightarrow \Psi'(\vec{x}, t) = e^{-i\chi(\vec{x}, t)} \Psi(\vec{x}, t). \quad (1.2)$$

called *local Gauge transformations*.

To keep the fundamental equations of the theory invariant under such transformations, it turns-out that new quantum fields must be introduced [14] leading to new interacting particles, the *gauge bosons*. The fundamental interactions can then be interpreted as an exchange of these *gauge bosons*. Therefore, gauge invariance generates the interaction between the fermions and each interaction is then characterized by a specific gauge symmetry. The interaction *strength* is proportional to a certain constant whose value can not be predicted by the theory. The number and type of gauge transformations which defines the theory is also suggested by the experiments. In general, any theory must obey the causality principle, and must be *renormalizable*, *i.e.*, none of the computed physical observables can take infinite values.<sup>2</sup>

Up to date, three fundamental interactions have been found within the Standard Model, which correspond to three different gauge transformations with their respective symmetries: the  $U(1)_Y$  symmetry which corresponds to the electromagnetic interaction, the  $SU(2)_L$  symmetry for the weak interaction, and the  $SU(3)_C$  symmetry for the strong interaction.

### 1.1.1 Electromagnetic Interaction

The electromagnetic interaction is described by the *Quantum Electrodynamics* gauge theory (QED), developed in the 1940s. QED is based on the  $U(1)$  symmetry, which yields the conservation of the electromagnetic charge  $Q$  and the appearance of one massless gauge boson, the photon ( $\gamma$ ), which describes the interactions among charged particles.

---

is consistent with the SM assumption of three generations [15]. Therefore, any further fermionic generations would need an extension of the SM.

<sup>2</sup>The Standard Model was proof to be renormalizable by 't Hooft in 1971 [18].

The strength of the electromagnetic interaction is given by the coupling constant  $\alpha$ , which in the leading-logarithm approximation can be written as:

$$\alpha(q^2) = \frac{\alpha(\mu^2)}{1 - \frac{\alpha(\mu^2)}{3\pi} \ln\left(\frac{q^2}{\mu^2}\right)} \quad (1.3)$$

where  $q$  is the transferred momentum and  $\mu$  is the energy scale set by the renormalization procedure (Figure 1.1). At  $q^2 = 0$  the coupling constant is the fine structure constant  $\alpha = e^2/4\pi\hbar c = 1/137$ , while at the scale of the  $Z^0$  vector boson mass  $\alpha(M_Z) \approx 1/128$ .

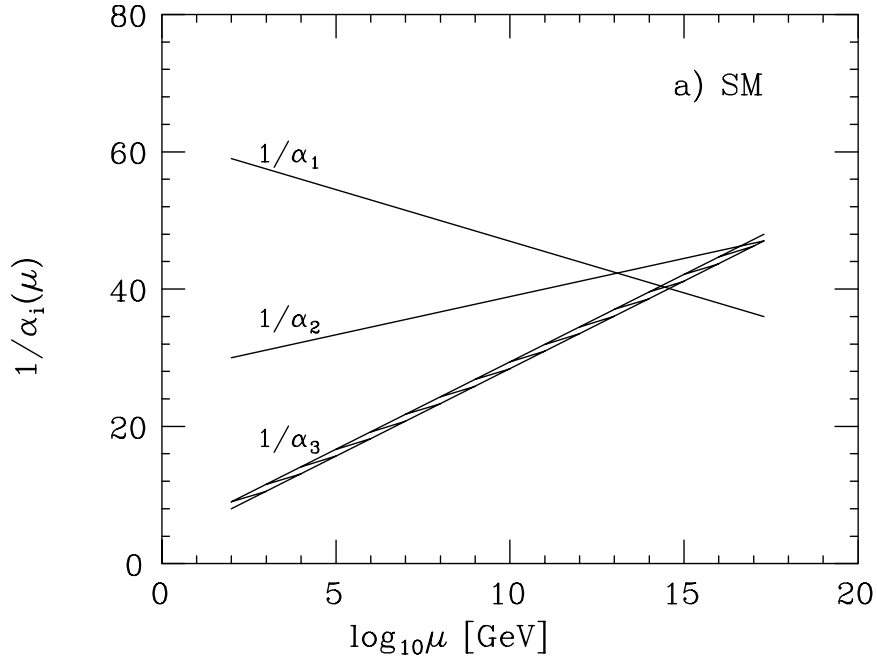


Figure 1.1: Running of the gauge coupling constants at the leading-logarithmic order in the Standard Model [16]. The indexes 1, 2 and 3 refer, respectively, to the electromagnetic, weak and strong interactions.

Since the  $U(1)$  symmetry is the representation of an Abelian group, photons do not carry charge, and thus they are not self-interacting at tree level. Therefore, the electromagnetic interaction is a long range interaction. Table 1.2 summarizes the photon properties.

<b>Boson</b>	Quantum Theory	Quantum Number	Coupling Strength	Range (m)	Mass ( GeV/c <sup>2</sup> )
Photon ( $\gamma$ )	QED	Charge	$\alpha = \frac{e^2}{4\pi\hbar c} = \frac{1}{137}$	$\infty$	0
$Z^0$	Electroweak	Weak Isospin	$G_F m_p^2 \simeq 10^{-5}$	$10^{-18}$	91.2
$W^\pm$					80.2
$H^0$					$\geq 114$
Gluons ( $g_i$ ) $i = 1, \dots, 8$	QCD	Color	$\alpha_s \approx 1$	$10^{-15}$	0
Graviton (G)	(None)	(Mass)	$Gm_p^2 \simeq 6 \times 10^{-39}$	$\infty$	0

Table 1.2: The gauge and Higgs bosons of the Standard Model with their properties and the forces which mediate [17]. The coupling strengths to particles of mass  $m_p$  are given for low-energy interactions ( $q^2 \approx 0$ ). The graviton and Higgs bosons have not yet been observed. The lower bound on the SM Higgs mass is taken from LEP [32].

### 1.1.2 Strong Interaction

The strong interaction is described by *Quantum Chromodynamics* (QCD). QCD is a  $SU(3)$  gauge theory, which leads to eight conserved quantum numbers called *color*, with the corresponding 8 gauge bosons (gluons) that mediate the interaction. Gluons are electrically neutral massless bosons that form an  $SU(3)$  octet. They carry one color and one anti-color charge, and therefore are subject to the color force themselves. The quarks form an  $SU(3)$  color triplet. In QCD the color symmetry is an exact symmetry, which means that QCD calculations are independent of the color of the quarks.

The fact that the gluons carry color (QCD is a non-Abelian theory), and therefore are self interacting, results in a very different behavior of the QCD interaction compared to QED. As two quarks move apart from each other, gluons exchanged between the two quarks interact with each other as well with the quarks, resulting in a linear interaction force which grows with the distance, and therefore in an increasing interaction energy. When the increasing energy density of the color field between the quarks is large enough, another quark anti-quark pair is created from the vacuum. Two separated hadrons are then created (Figure 1.2). This results in quark *confinement*: quarks appear only in bound states forming colorless  $SU(3)$  singlets, as mesons (quark-antiquark pairs  $q\bar{q}$ ) or baryons (quark triples  $qqq$ ). The confinement radius is approximately 1 fm.

As for QED, the QCD coupling constant ( $\alpha_s$ ) is a running coupling constant which also depends on the given scale of the transferred momentum [14]. In the

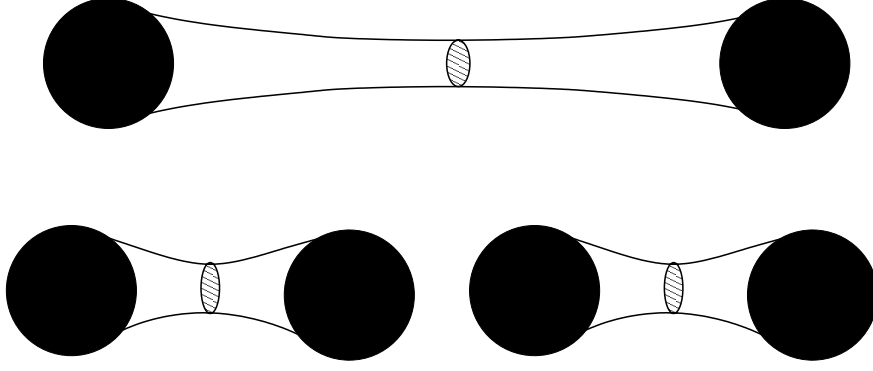


Figure 1.2: Quark confinement. As two quarks move apart from each other, the linear increasing interaction force (represented here by the constant cross section of the *string* between the quarks) increases the interaction energy (upper plot). With high enough interaction energies, the creation of a quark anti-quark pair from vacuum is more energetically favored (bottom plot).

leading-logarithm approximation  $\alpha_s$  is given by:

$$\alpha_s(q^2) = \frac{4\pi}{(11 - \frac{2}{3}N_f(q^2)) \ln(\frac{q^2}{\Lambda^2})} \quad (1.4)$$

where  $N_f$  is the number of quarks flavors with  $m \ll \frac{1}{2}\sqrt{-q^2}$ ,  $q$  the transferred momentum, and  $\Lambda$  is the *QCD* scale parameter, which is the only adjustable parameter of QCD apart from the quark masses. The scale parameter is determined by comparing the QCD predictions to experimental data. Its value depends on the momentum scale, and for most processes the measured value of  $\Lambda$  is  $\sim 200$  MeV/ $c$ .

The behavior of  $\alpha_s$  radically differs from the behavior of the QED coupling constant (Figure 1.1). As  $q$  gets large, the strong coupling constant becomes weaker leaving the quarks unbound. This behavior is called the *asymptotic freedom*. In this region  $\alpha_s$  is small enough to apply perturbative methods as the expansion of Feynman diagrams in series of terms on  $\alpha_s$ . On the contrary, for smaller  $q$  the color force becomes stronger, leading to quark confinement. For the hadronization of the resulting quarks and gluons perturbative methods can not be applied and calculations rely mostly on phenomenological models to describe these processes.

In a high energy proton anti-proton collision the hard scattering part of the interaction (the interaction between single quarks or gluons from each of the colliding protons and anti-protons) occurs with high transferred momentum, and therefore can be calculated perturbatively. For the remaining quarks and gluons, the interactions occur at lower energies where the perturbative methods can not be applied (*hadronisation*), and therefore phenomenological models must be used for this part of the interaction.

### 1.1.3 Electroweak Interaction

The Electroweak Theory combines in a unique interaction the electromagnetic and the weak interactions. Formulated by Weinberg in 1967 and by Salam in 1968, the theory is based in the  $SU(2)_L \times U(1)_Y$  symmetry under global gauge transformations proposed by Glashow in 1961 [19]. The theory is built in two steps. First, global gauge invariance under  $SU(2)$  transformations leads to the conservation of the *weak-isospin* charge  $T$ . A weak-isospin triplet of gauge fields  $\mathbf{W}_\mu^i, i = 1, 2, 3$  is introduced after requiring a Lagrangian invariance under local  $SU(2)$  transformations. The  $SU(2)$  group is non-Abelian, which leads to the self-interaction of these gauge fields. Second, global invariance under the  $U(1)_Y$  transformations leads to the conservation of the *weak-hypercharge*  $Y$ . Local gauge invariance requires the introduction of a weak-hypercharge singlet vector field  $\mathbf{B}_\mu$ .

The electroweak gauge fields can be written as follows [14]:

$$\begin{aligned}\mathbf{W}_\mu^\pm &= \frac{1}{\sqrt{2}}(\mathbf{W}_\mu^1 \mp i\mathbf{W}_\mu^2) \\ \mathbf{Z}_\mu &= \mathbf{W}_\mu^3 \cos \theta_w - \mathbf{B}_\mu \sin \theta_w \\ \mathbf{A}_\mu &= \mathbf{W}_\mu^3 \sin \theta_w + \mathbf{B}_\mu \cos \theta_w\end{aligned}\tag{1.5}$$

where the  $\mathbf{A}_\mu$  field has the form of the electromagnetic interaction in QED and it is identified with the photon, the  $\mathbf{W}_\mu^\pm$  and  $\mathbf{Z}_\mu$  fields are identified as the  $W^\pm$  and  $Z^0$  bosons,<sup>3</sup> and  $\theta_w$  the *Weinberg* angle, that determines the mixing between the third component of the weak-isospin and the weak-hypercharge (the mixing of the weak and electromagnetic interactions).<sup>4</sup>

The weak-hypercharge  $Y$ , the third component of the weak-isospin  $T_3$  and the electrical charge  $Q$  are linearly related by:

$$Q = T_3 + \frac{1}{2}Y.\tag{1.6}$$

Therefore, global and local conservation of weak-isospin and hypercharge imply electrical charge conservation. Since  $U(1)$  is Abelian, none of the gauge bosons carry weak-hypercharge while at the same time the photon does not interact with itself. The  $SU(2)$  group is non-Abelian, thus the weak vector boson fields  $W^\pm$  and  $Z^0$  do carry weak-isospin and, therefore, electrical charge. The three weak-isospin fields have weak-isospin projections  $T_3 = -1, 0, +1$  and hence, from  $Q = T_3$ , there are two charged currents ( $W^\pm$ ) and one neutral current ( $Z^0$ ). The fermion and boson states are given in Table 1.3 together with their quantum numbers.

<sup>3</sup>The  $W^\pm$  and  $Z^0$  bosons were first observed at the CERN  $p\bar{p}$  collider in 1983 [20].

<sup>4</sup>The value for  $\sin \theta_w$  can be measured from many processes. The present world average value is  $\sin^2 \theta_w = 0.2313 \pm 0.0003$  [15].

<sup>7</sup>Under the  $SU(2)$  symmetry, *right handed* transform behaves like singlets, while *left handed* fermions transform like doublets. See [14] for an extensive treatment of the question.

Generation							
<u>Fermions</u>				$T$	$T_3$	$Y$	$Q$
lepton-type (spin $\frac{1}{2}$ )	$(\nu_e)_L$	$(\mu_e)_L$	$(\tau_e)_L$	1/2	+1/2	-1	0
				1/2	-1/2	-1	-1
	$e_R$	$\mu_R$	$\tau_R$	0	0	-2	-1
quark-type (spin $\frac{1}{2}$ )	$(u)_L$	$(c)_L$	$(t)_L$	1/2	+1/2	+1/3	+2/3
				1/2	-1/2	+1/3	-1/3
	$u_R$	$c_R$	$t_R$	0	0	+4/3	+2/3
	$d_R$	$s_R$	$b_R$	0	0	-2/3	-1/3
<u>Bosons</u>							
(spin 1)							
$\gamma$				0	0	0	0
$Z^0$				1	0	0	0
$Z^0$				1	+1	0	+1
$Z^0$				1	-1	0	-1
Higgs (spin 0)	$\Phi = (\phi^+_{\phi^0})$			1/2	+1/2	+1	+1
				1/2	-1/2	+1	0

Table 1.3: The particle properties in the Standard Model for the electroweak interaction. The quantum numbers of *weak-isospin*  $T$ , and its projection  $T_3$ , *weak-hypercharge*  $Y$ , and the electric charge  $Q$ . Indexes  $R$  and  $L$  denote, respectively, *left-handed* and *right-handed* fermions.<sup>7</sup> [17]

## 1.2 Electroweak Symmetry Breaking

The electroweak theory predicts the existence of four physical vector boson eigenstates  $W^\pm$ ,  $Z^0$  and  $\gamma$ , obtained from the rotations of the weak eigenstates. From the symmetry of the Electroweak theory with respect to the rotations on the *weak-isospin* space, one could expect that all the members of the weak-isospin triplet ( $\mathbf{W}^1$ ,  $\mathbf{W}^2$  and  $\mathbf{W}^3$ ) be mass degenerated, while the *weak-isospin* singlet  $\mathbf{B}$  could have some other different mass. However, one linear combination of the  $\mathbf{W}^3$  and  $\mathbf{B}$  fields, the photon (see Equation 1.5), is massless, while other three orthogonal combinations (the  $Z^0$  and  $W^\pm$  bosons) have measured masses of  $\sim 91 \text{ GeV}/c^2$  and  $80 \text{ GeV}/c^2$ , respectively [15].

Naively one could try to make the  $W^\pm$  and  $Z^0$  fields massive by including in the electroweak Lagrangian the terms:

$$m_W^2 W_\mu^\dagger(x) W^\mu(x) + \frac{1}{2} m_Z^2 Z_\mu(x) Z^\mu(x). \quad (1.7)$$

However, introducing in this way the masses causes the Lagrangian density no longer to be invariant under local  $U(1)$  gauge transformations, neither under the  $SU(2)$  gauge transformations.

This situation can be found in other physical systems, like *e.g.*, the ferromagnet materials. For the ferromagnets the Hamiltonian of the iron crystal is invariant under

the rotations in the usual three-dimensional space. However, for temperatures below the Curie temperature, this symmetry is broken. There is a space-preferred direction that breaks the symmetry, the direction of the *spontaneous magnetization* vector. When the temperature is above the Curie temperature, the ferromagnets lose their permanent magnetization, and the symmetry is restored. This phenomena is known as *Spontaneous Symmetry Breaking*. The application of the spontaneous symmetry breaking to the case of gauge invariant theories is the so called *Higgs Mechanism* [22].

### 1.2.1 Spontaneous Symmetry Breaking

A simple definition for the phenomenon of Spontaneous Symmetry Breaking (SBS) is:

*A physical system has a symmetry that is spontaneously broken if the interactions governing the dynamics of the system possess such a symmetry, but the ground system of this system does not* [23].

Note that SBS can take place when the ground state has not an unique solution, but is energy degenerated.

As above mentioned, an illustrative example is the case of an infinitely extended ferromagnet material. Above the Curie temperature the spins of the system are randomly oriented, and as a consequence the average magnetization vanishes:  $\vec{M}_{av} = 0$  (Figure 1.3). The ground state with these disoriented spins is rotationally invariant. For temperatures below the Curie temperature, the spins of the system are all oriented parallel to some particular but arbitrary direction (permanent magnet) and the average magnetization gets a non-zero value  $\vec{M}_{av} \neq 0$  (Figure 1.3). The directions of the spins are arbitrary, and therefore there are infinite possible ground states, each one corresponding to one possible direction and all having the same (minimal) energy. None of these states is rotationally invariant anymore. The system has “chosen” one among the infinite possible non-invariant ground states. The symmetry is broken in the ground state (Figure 1.3). The behavior of this system can be parametrized with a simple mathematical model, where the free energy potential is expressed as a function of the total spontaneous magnetization vector (theory of Ginsburg and Landau [24]). For the ferromagnet above the Curie temperature ( $\vec{M}_{av} = 0$ ), the free energy potential is a symmetric function with respect to the components of  $\vec{M}$  with a single and well defined ground state with  $\vec{M}_{av} = 0$  (Figure 1.3 [c]). For temperatures below the Curie temperature, the potential shows a typical “mexican hat” profile (Figure 1.3 [d]), with an infinite series of different ground states, all of them with  $\vec{M}_{av} \neq 0$ .

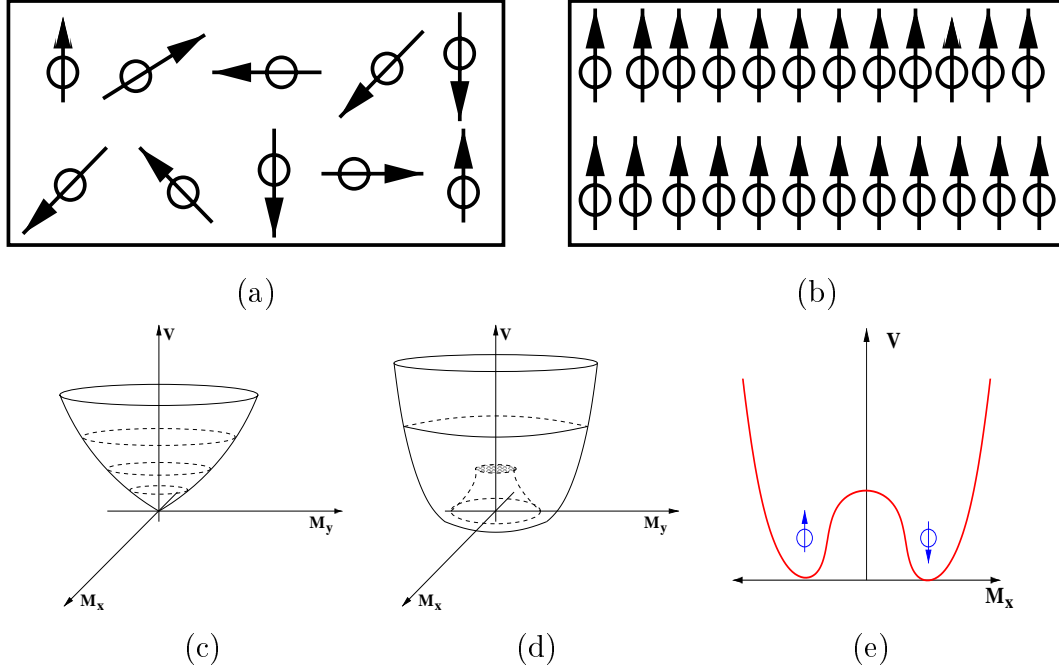


Figure 1.3: Figure (a): schematic representation of the spin orientation in a ferromagnet above the Curie temperature. Figure (b): *idem* for temperatures below the Curie temperature. Figure (c): free energy potential in the symmetric phase above the Curie temperature. Figure (d): free energy potential in the spontaneously broken symmetry phase. Figure (e): transverse section of the free energy potential, where to different positions in the ground state can correspond states with different spontaneous magnetization vector.

### 1.2.2 The Higgs Mechanism

The Higgs Mechanism is the extension of the spontaneous symmetry breaking model to gauge invariant theories [22]. For quantum field theories, the phenomenon of spontaneous symmetry breaking can be formulated in the following way [23]:

*A system is said to possess a symmetry that is spontaneously broken if the Lagrangian describing the dynamics of the system is invariant under these symmetry transformations, but the vacuum of the theory is not.*

The vacuum  $|0\rangle$  is defined as the state where the expectation value of the Hamiltonian  $\langle 0|H|0\rangle$  is minimum. One of the physical implications of this phenomenon is the appearance of massless modes, described by the Goldstone Theorem<sup>5</sup> [25]:

*If a Theory has a global symmetry of the Lagrangian which is not a symmetry*

<sup>5</sup>For the case of the ferromagnet materials described in Section 1.2.1, the equivalent to these massless modes is the appearance of spin waves that connect all the possible ground states.

*of the vacuum, then there must exist one massless boson, scalar or pseudoscalar, associated to each generator which does not annihilate the vacuum and having the same quantum numbers. These modes are referred to as Nambu-Goldstone bosons.*

The Goldstone theorem is valid for theories with spontaneously broken global gauge symmetries, but does not hold for local gauge theories.<sup>6</sup> For gauge invariant theories, the Goldstone theorem must be modified, turning into the so called Higgs mechanism [22]:

*The would-be Goldstone bosons, associated to the global symmetry breaking, do not manifest explicitly in the physical spectrum, but instead they 'combine' with the massless gauge bosons and as a result, once the spectrum of the theory is built up on the asymmetrical vacuum, there appear massive vector particles. The number of vector bosons that acquire a mass is precisely equal to the number of these would-be Goldstone bosons.*

For the case of the electroweak sector of the SM the Higgs Mechanism is implemented in the  $SU(2)_L \times U(1)_Y$  gauge theory to generate the masses of the weak gauge bosons  $W^\pm$  and  $Z$ . Technically this is done introducing 'ad hoc' an additional system that interacts with the gauge sector in a  $SU(2)_L \times U(1)_Y$  gauge invariant manner, and whose self-interactions, introduced also 'ad hoc', must produce the wanted symmetry breaking with three associated equivalent Goldstone bosons, that will combine with the three massless fields of the  $SU(2)_L \times U(1)_Y$  symmetry (see Equation 1.5). By doing this, the introduced field  $\Phi$  must have some *good* properties as:

- $\Phi$  must be a scalar field to preserve Lorentz invariance. At the same time, it must be a complex field, so the Hamiltonian is hermitian.
- It must have non-vanishing weak isospin and hypercharge in order to break the  $SU(2)_L$  and  $U(1)_Y$  symmetry. The most simple way to assign the quantum numbers is choose  $\Phi$  in a way that transforms linearly under the  $SU(2)_L \times U(1)_Y$  transformation, as a single doublet.
- Interactions of  $\Phi$  with the gauge and fermionic sectors must be introduced in a gauge invariant way, and the self-interactions, given by the potential  $V(\Phi)$  must produce the wanted symmetry breaking ( $\langle 0|\Phi|0\rangle \neq 0$ ).
- The interactions in  $V(\Phi)$  must be renormalizable.

Taking into account these requirements, the simplest choice for the system  $\Phi$

---

<sup>6</sup>One example for which the Goldstone theorem is valid is the *chiral symmetry breaking* of the QCD theory [23].

and the Lagrangian of the spontaneous symmetry breaking is [23]:

$$\begin{aligned}\mathcal{L} &= (D_\mu \Phi)^\dagger (D^\mu \Phi) - V(\Phi) \\ V(\Phi) &= -\mu^2 \Phi^\dagger \Phi + \lambda (\Phi^\dagger \Phi)^2; \lambda > 0\end{aligned}\quad (1.8)$$

where,

$$\begin{aligned}\Phi &= \begin{pmatrix} \phi^+ \\ \phi^0 \end{pmatrix} \\ D_\mu \Phi &= (\partial_\mu - \frac{1}{2}ig\vec{\sigma} \cdot \vec{W} - \frac{1}{2}ig'B_\mu)\Phi\end{aligned}\quad (1.9)$$

$\Phi$  is the fundamental complex doublet with hypercharge  $Y(\Phi) = 1$  and  $V(\Phi)$  the simplest renormalizable potential.  $\vec{W}_\mu$  and  $B_\mu$  are, respectively, the gauge fields of the  $SU(2)_L$  and  $U(1)_Y$  symmetries (Equation 1.5), with  $g$  and  $g'$  the corresponding gauge couplings.

Note that for the potential  $V(\Phi)$ , depending on the sign of the mass parameter  $(-\mu^2)$ , there are two possible values of the vacuum  $\langle 0|\Phi|0\rangle$  that minimizes the potential:

1.  $(-\mu^2) > 0$ : The minimum is at:

$$\langle 0|\Phi|0\rangle = 0 \quad (1.10)$$

In this case the vacuum of  $SU(2)_L \times U(1)_Y$  is symmetric and no symmetry breaking occurs. This corresponds to the symmetric phase of the ferromagnet described in Section 1.2.1 (see Figures 1.3 (a) and (c)).

2.  $(-\mu^2) < 0$ : The minimum is at:

$$\langle 0|\Phi|0\rangle = \begin{pmatrix} 0 \\ \frac{v}{\sqrt{2}} \end{pmatrix}; \quad \text{arbitrary } \arg \Phi; \quad v \equiv \sqrt{\frac{\mu^2}{\lambda}} \quad (1.11)$$

In this case there are infinite degenerate vacuum states corresponding to infinite possible states of  $\arg \Phi$ . The breaking of  $SU(2)_L \times U(1)_Y$  occurs once a particular vacuum is chosen. Usually, the simplest choice is taken:

$$\arg \Phi \equiv 0 \quad (1.12)$$

This case corresponds to the asymmetric state of the ferromagnet, described in Section 1.2.1 (Figures 1.3 (b), (c) and (d)).

The full particle spectra and the particle masses are obtained in the following way. The full SM  $SU(2)_L \times U(1)_Y$  invariant Lagrangian can be written in the form:

$$\mathcal{L}_{SM} = \mathcal{L}_f + \mathcal{L}_G + \mathcal{L}_{BS} + \mathcal{L}_{YW} \quad (1.13)$$

where  $\mathcal{L}_f$  and  $\mathcal{L}_G$  are, respectively, the terms describing the fermions and electroweak gauge fields, and  $\mathcal{L}_{BS}$  and  $\mathcal{L}_{YW}$  are the terms introduced for the spontaneous symmetry breaking. The  $\mathcal{L}_{BS}$  has the form:

$$\mathcal{L} = (D_\mu \Phi)^\dagger (D^\mu \Phi) + \mu^2 \Phi^\dagger \Phi - \lambda (\Phi^\dagger \Phi)^2 \quad (1.14)$$

and it will provide the masses for the  $W^\pm$  and  $Z^0$  bosons. The term  $\mathcal{L}_{YW}$  is the Yukawa couplings term

$$\mathcal{L}_{YW} = \lambda_e \bar{l}_L \Phi e_R + \lambda_u \bar{q}_L \tilde{\Phi} u_R + \lambda_d \bar{q}_L \Phi d_R + \text{h.c.} + 2^{\text{nd}} \text{ and } 3^{\text{rd}} \text{ families} \quad (1.15)$$

where

$$\begin{aligned} l_L &= \begin{pmatrix} \nu_L \\ e_L \end{pmatrix}; & q_L &= \begin{pmatrix} u_L \\ d_L \end{pmatrix} \\ \Phi &= \begin{pmatrix} \phi^+ \\ \phi^0 \end{pmatrix}; \tilde{\Phi} &= i\sigma_2 \Phi^* = \begin{pmatrix} \phi_0^* \\ -\phi^- \end{pmatrix}. \end{aligned} \quad (1.16)$$

The Yukawa-coupling Lagrangian term is needed to provide masses to the fermions.

After a series of transformations, consisting basically in the choice of a non symmetric vacuum (Equation 1.11), the parameterization of the fundamental field  $\Phi$  as a “small oscillation” around this vacuum

$$\Phi(x) = \exp \left( i \frac{\vec{\xi}(x) \vec{\sigma}}{v} \right) \begin{pmatrix} 0 \\ \frac{v+H(x)}{\sqrt{2}} \end{pmatrix}, \quad (1.17)$$

and after fixing the gauge to eliminate the unphysical field  $\vec{\xi}(x)$ , the Lagrangian terms  $\mathcal{L}_{SBS}$  and  $\mathcal{L}_{YW}$ , together with the Higgs potential can be written in the form:

$$\begin{aligned} (D_\mu \Phi')^\dagger (D^\mu \Phi') &= \left( \frac{g^2 v^2}{4} \right) W_\mu^+ W^{\mu-} + \frac{1}{2} \left( \frac{(g^2 + g'^2) v^2}{4} \right) Z_\mu Z^\mu + \dots \\ V(\Phi') &= \frac{1}{2} (2\mu^2) H^2 + \dots \\ \mathcal{L}_{YW} &= \left( \lambda_e \frac{v}{\sqrt{2}} \right) \bar{e}'_L e'_R + \left( \lambda_u \frac{v}{\sqrt{2}} \right) \bar{u}'_L u'_R + \left( \lambda_d \frac{v}{\sqrt{2}} \right) \bar{d}'_L d'_R + \dots \end{aligned} \quad (1.18)$$

from where at the tree level we obtain the predictions:

$$\begin{aligned} M_W &= \frac{gv}{2}; M_Z = \frac{\sqrt{g^2 + g'^2} v}{2} \\ M_H &= \sqrt{2} \mu \\ m_e &= \lambda_e \frac{v}{\sqrt{2}}; m_u = \lambda_u \frac{v}{\sqrt{2}}; m_d = \lambda_d \frac{v}{\sqrt{2}}; \dots \end{aligned} \quad (1.19)$$

with  $v = \sqrt{\frac{\mu^2}{\lambda}}$  the vacuum expectation value and  $\lambda$  the Higgs boson self coupling. Note that:

- The interactions of the Higgs boson  $H$  with fermions and with gauge bosons are proportional to the gauge couplings and to the corresponding particle masses:

$$f \bar{f} H : -i \frac{g}{2} \frac{m_f}{M_W} : W_\mu^+ W_\mu^- H : ig M_W g_{\mu\nu} : Z_\mu Z_\nu H : \frac{ig}{c_w} M_Z g_{\mu\nu}$$

- All masses are given in terms of a unique parameter  $v$  (the vacuum expectation<sup>7</sup>) and the couplings  $g, g', \lambda, \lambda_e$ , etc. . .

---

<sup>7</sup> $v$  can be determined experimentally from the  $\mu$  decay measuring the partial width  $\Gamma(\mu \rightarrow \nu_\mu \bar{\nu}_e e)$  at low energies ( $q^2 \ll M_W^2$ ). In the SM one obtains:

$$\frac{G_F}{\sqrt{2}} = \frac{g^2}{8M_W^2} = \frac{1}{2v^2}$$

- The Higgs boson mass  $M_H$  and the Higgs boson self-coupling  $\lambda$  are completely undetermined in the SM. At tree level they are related by  $\lambda = \frac{M_H^2}{2v^2}$ .

### 1.3 SM Higgs Boson Decays

As discussed in Section 1.2.2, the strength of the Higgs boson interactions with SM particles grows with their masses (Equation 1.19). Therefore, the Higgs boson predominantly couples to the heaviest particles:  $W^\pm$  or  $Z$  gauge bosons pairs,  $t\bar{t}$ ,  $b\bar{b}$  quarks, tau leptons,  $c$  quarks, and gluons (the last coupling through quarks loops). The decay into these particles will be dominant if they are kinematically allowed.<sup>8</sup>

Figure 1.4 (a) and Figure 1.4 (b) show, respectively, the total decay width and branching ratios of the Higgs boson as a function of its mass. In the range of interest for Tevatron ( $110 - 200 \text{ GeV}/c^2$ )<sup>9</sup> two regions can be distinguished depending on the predominant decay mode. In the low mass region ( $M_H \leq 140 \text{ GeV}/c^2$  with a total width less than 1 GeV), the predominant decay mode is  $H \rightarrow b\bar{b}$  (85 – 30%) followed by the  $\tau^+\tau^-$  (8 – 3%),  $c\bar{c}$  (3 – 1%) and  $gg$  (7 – 5%) decay modes. For  $M_H \geq 140 \text{ GeV}/c^2$  the  $WW$  decay mode takes over the dominant role, together with the  $ZZ$  decay mode. Around the  $WW$  threshold of  $150 \text{ GeV}/c^2$  where the second  $W$  of the  $WW$  pair becomes on-shell, the  $ZZ$  branching ratio drops down to the level of  $\sim 2\%$ , and reaches again a level of  $\sim 30\%$  above the  $ZZ$  threshold<sup>10</sup>. Note that the great variety of decay modes will dictate different search strategies depending on the mass probe.

#### 1.3.1 Higgs Boson Decay to Fermions

The Higgs boson couples to all fermions with a strength proportional to their masses. Therefore, the coupling to a pair of  $b$  quarks is the strongest.<sup>11</sup>

---

<sup>8</sup>In the lowest order the leptonic decay of SM Higgs boson is given by [26]:

$$\Gamma[H \rightarrow l^+l^-] = \frac{G_F M_H}{4\sqrt{2}\pi} m_l^2 (1 - 4m_l^2/M_H^2)^{3/2}.$$

For the  $\tau$  leptons the branching ratio is  $\sim 10\%$  in the mass range  $115 - 140 \text{ GeV}/c^2$ . For muons it is  $\sim 10^{-4}$ , and for the rest of the leptons the branching ratio is completely negligible.

On the other hand, three-body decay modes may reach the per cent level only for large Higgs masses (1 TeV), and therefore are completely negligible at Tevatron.

<sup>9</sup>The colliding protons and antiprotons are constituted of valence quarks, *sea* quarks and gluons. On average, each of these partons do not carry more than 10% – 15% of the total nucleon momentum.

<sup>10</sup>The  $H \rightarrow \gamma\gamma$  and  $H \rightarrow \gamma Z$  at this mass range are of the order of 0.1%.

<sup>11</sup>The coupling to a pair of  $t$  quarks is even stronger, but at the Tevatron mass range it is not kinematically available.

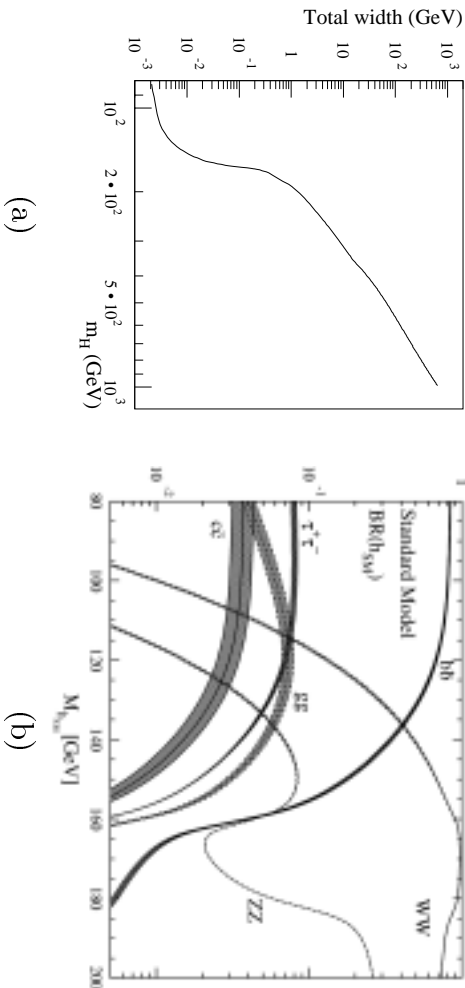


Figure 1.4: (a) total width of the Standard Model Higgs boson as a function of its mass. At Tevatron energies the total width is  $\sim 1$  GeV. Note that for a heavy Higgs boson the width approaches the value of its mass. (b) Branching ratios of the dominant decay modes of the Standard Model Higgs boson [8]. Results include QCD corrections beyond the leading order. The shaded bands represent the variations due to the uncertainties in the input parameters:  $\alpha_s(M_z^2) = 0.120 \pm 0.003$ ,  $\bar{m}_b(M_b) = 4.22 \pm 0.05$  GeV/ $c^2$ ,  $\bar{m}_c(M_c) = 1.22 \pm 0.06$  GeV/ $c^2$ ,  $M_t = 174 \pm 5$  GeV/ $c^2$ .

At tree level the partial width of the fermionic decay is given by [27]:

$$\Gamma_{H \rightarrow f\bar{f}} = \frac{N_c g^2 m_f^2 m_H}{32\pi m_W^2} \left(1 - \frac{4m_f^2}{m_H^2}\right)^{3/2} \quad (1.20)$$

where  $N_c$  is the color factor (3 for quarks, 1 elsewhere). At the Tevatron mass range the QCD corrections are large, leading to a reduction by a factor of two of the  $H \rightarrow b\bar{b}$  decay branching ratio [8]. The remaining uncertainty in the decay width from the  $\mathcal{O}(\alpha_s^3)$  corrections is estimated to be  $\sim 5\%$  [28].

Note that due to the higher mass of the  $\tau$  lepton, this decay mode is stronger than the  $H \rightarrow c\bar{c}$  mode, despite of its color factor enhancement.

### 1.3.2 Higgs Boson Decays to Vector Bosons

At tree level the partial width for the  $H \rightarrow W^-W^+$  and  $H \rightarrow ZZ$  decays are given by [27]:

$$\Gamma_{H \rightarrow ZZ} = \frac{g^2}{128\pi} \frac{m_H^3}{m_Z^2} \sqrt{1 - x_Z} \left(1 - x_Z + \frac{3x_Z^2}{4}\right) \quad (1.21)$$

$$\Gamma_{H \rightarrow WW} = \frac{g^2}{64\pi} \frac{m_H^3}{m_W^2} \sqrt{1 - x_W} \left(1 - x_W + \frac{3x_W^2}{4}\right) \quad (1.22)$$

where:

$$x_Z = 4 \frac{m_Z^2}{m_H^2}, \quad x_W = 4 \frac{m_W^2}{m_H^2}. \quad (1.23)$$

Note that the decay branching ratio  $\Gamma_{H \rightarrow WW}$  is enhanced by a factor of two with respect to the branching ratio  $\Gamma_{H \rightarrow ZZ}$ , due to the different number of identical particles in the final state.

### 1.3.3 Two Gluon Decay

Gluons have no coupling to vector bosons, therefore only the decay through a diagram like the one shown in Figure 1.6 (a) can take place. The two gluons will evolve during fragmentation into a QCD-like di-jet system. Single Higgs production and decay into gluons has also a rate many orders of magnitude below QCD di-jet production. This decay mode has, thus, no interest at Tevatron.<sup>12</sup>

## 1.4 SM Higgs Boson Production at Tevatron

Figure 1.5 shows the cross sections of the most relevant Higgs boson production modes at the Tevatron center of mass energies [8]. Figure 1.6 shows some of the corresponding Feynman diagrams. The results are full NLO QCD-corrected, except for the case  $q\bar{q}, gg \rightarrow Ht\bar{t}, Hq\bar{q}, Hb\bar{b}$ . These corrections coincide with those of the Drell-Yan process and increase the cross section by about 30%. The theoretical uncertainty can be estimated as  $\sim 15\%$  from the scale dependence [8]. The dependence on different sets of parton densities is rather weak and leads to a variation of the production cross section of  $\sim 15\%$ .

### 1.4.1 Gluon Fusion

Gluon fusion is the most copious production mode for the Higgs boson. Cross section values are ranged between  $\sim 1$  pb ( $M_H \sim 120$  GeV/ $c^2$ ) and  $\sim 0.15$  pb ( $M_H \sim 200$  GeV/ $c^2$ ). Gluons do not couple directly to vector bosons. Therefore, the Higgs boson can be produced at higher orders through fermionic loops like the one shown in Figure 1.6 (a). Since Higgs boson couplings depend on the mass of the fermions, the top quark loop contribution dominates. The two-loop QCD corrections enhance the cross section by about 60 – 100% [8].

For Higgs boson masses below 140 GeV/ $c^2$  the predominant decay is  $H \rightarrow b\bar{b}$  (Section 1.3). For this production mode, the final signature is a pair of b-quark jets with a rate many orders of magnitude below the QCD b-quark jet production. For masses above 140 GeV/ $c^2$  the Higgs boson decays predominantly into a pair of gauge bosons  $ZZ$  or  $W^+W^-$ . The high  $E_T$  of the electrons and the  $\cancel{E}_T$  resulting from the

---

<sup>12</sup>Although in a future  $e^+e^-$  collider the  $H \rightarrow gg$  is potentially possible to detect.

W decays are good signatures to separate these processes from other backgrounds [13].

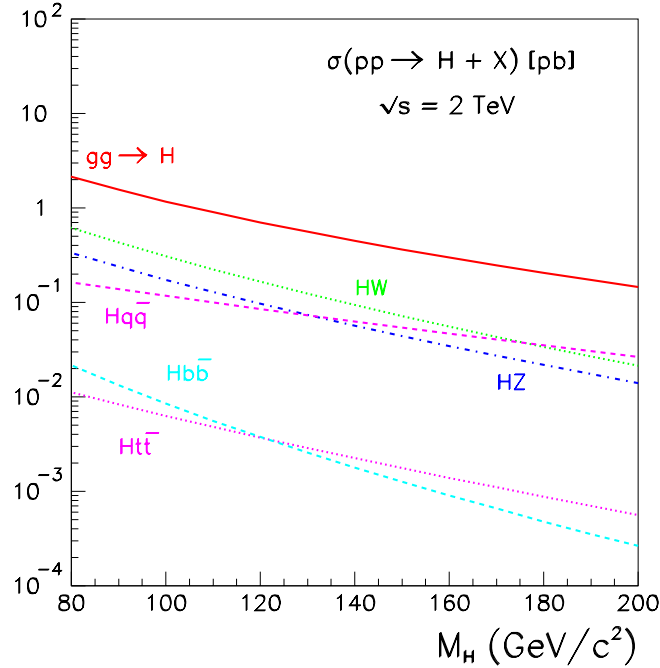


Figure 1.5: Higgs boson production cross sections at the Tevatron ( $\sqrt{s} = 2.0$  TeV) for the various production mechanisms as a function of the Higgs boson mass.

### 1.4.2 Vector Boson Associated Production

The Higgs-strahlung of W, Z bosons  $q\bar{q} \rightarrow W^*/Z^* \rightarrow W/Z + H$  (Figure 1.6 [b]) is the most promising mechanism at Tevatron energies (Section 1.4). The cross section for  $q\bar{q} \rightarrow W^\pm + H$  reaches values of  $0.3 - 0.02$  pb for  $120 \text{ GeV}/c^2 \lesssim M_H \lesssim 200 \text{ GeV}/c^2$ .

### 1.4.3 Vector Boson Fusion

The vector boson fusion process consists on the radiation of vector bosons by the colliding quarks and antiquarks. These vector bosons annihilates to produce a Higgs boson (Figure 1.6 [c]). The resulting Standard Model cross-sections are in the range of  $0.1 - 0.03$  pb for  $120 \text{ GeV}/c^2 \lesssim M_H \lesssim 200 \text{ GeV}/c^2$ . The QCD corrections enhance the cross section by about 10% [13].

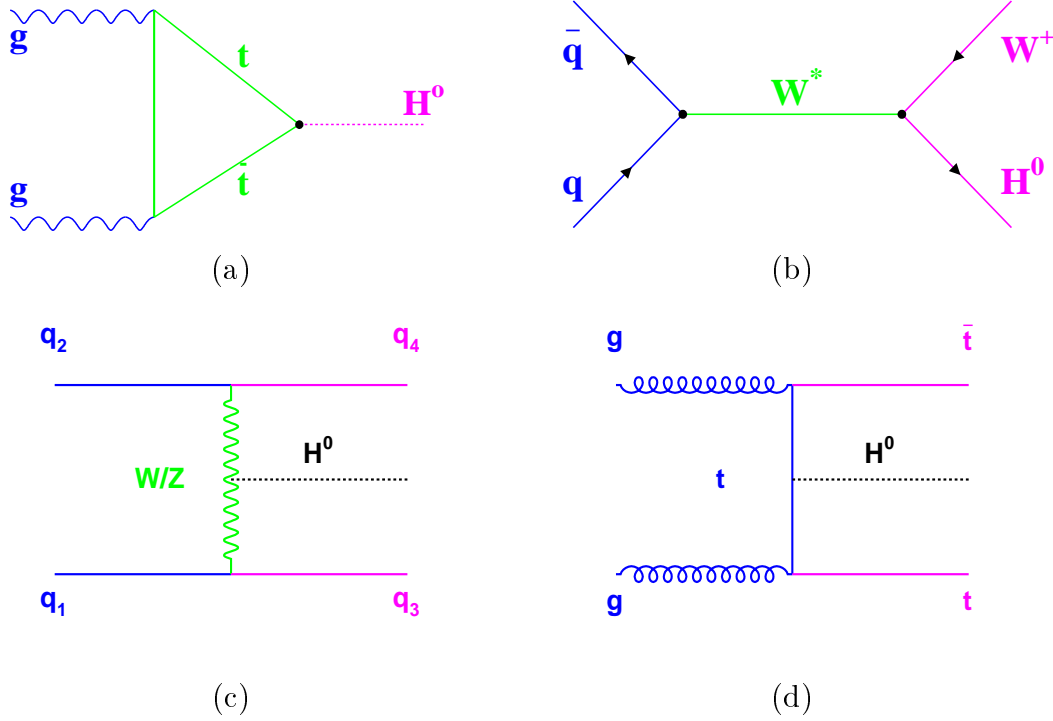


Figure 1.6: Feynman diagrams for the most important Higgs boson production processes at Tevatron ( $\sqrt{s} = 2.0$  TeV): (a) gluon fusion, (b) associated production with a vector boson (W or Z), (c) vector boson fusion, and (d) an example of associated production with a  $t\bar{t}$  pair.

#### 1.4.4 $Ht\bar{t}$ , $Hb\bar{b}$ Production

Figure 1.6 (d) shows the Feynman diagram for the associated production of a Higgs boson together with a pair of heavy flavor quarks  $b\bar{b}$  or  $t\bar{t}$ . At Tevatron energies, the  $q\bar{q}$  annihilation contribution dominates over the  $gg$  fusion for the  $t\bar{t}H$  production, while the situation is the opposite for  $b\bar{b}H$  production. Figure 1.5 shows the cross sections for these processes at leading order. The theoretical uncertainties in this channel are high and need a careful treatment. See Reference [13] for a detailed discussion.

### 1.5 Theoretical Limits on the Higgs Boson Mass

Theoretical considerations based on general consistency arguments of the theory bounds the Higgs boson mass. In this section we briefly describe an upper bound on the Higgs boson mass, the *Triviality* bound,<sup>13</sup> and a lower mass bound derived from

<sup>13</sup>Other upper bounds can be extracted from different general theoretical considerations, such as the *unitarity bound* and the analysis of the  $WW \rightarrow WW$  scattering. See References [14] and

*vacuum stability* considerations. Upper bounds are based on the idea that the theory breaks down if the Higgs boson mass is pushed too far upwards. If the Standard Model has to remain a valid effective theory up to high energy scales  $\Lambda \sim 10^{15}$  GeV and the Higgs mechanism is valid, the Higgs boson mass must lie in a very narrow interval of few hundreds GeV.

### 1.5.1 Upper Bound: *Triviality*

Lets assume a concrete renormalization scheme of the SM parameters<sup>14</sup> and define the renormalized Higgs boson mass parameter as:

$$M_H^2 = 2\lambda_R(v)v^2 \quad (1.24)$$

where:

$$\lambda_R(v) = \frac{\lambda_0}{1 - \frac{3}{2\pi^2}\lambda_0 \log(\frac{v}{\Lambda_{phys}})} \quad (1.25)$$

is the renormalized coupling constant at one-loop level. If we try to remove the cut-off parameter  $\Lambda_{phys}$  by taking the limit  $\Lambda_{phys} \rightarrow \infty$ , while  $\lambda_0$  is kept fixed to a finite value, it turns out that  $\lambda_R \rightarrow 0$  for any finite value of  $v$ , what implies a non interacting theory, *i.e.*, a trivial theory. One could assume then that the theory is valid up to a certain “physical” cut-off  $\Lambda_{phys}$ . Therefore, we must keep all the renormalized masses below the cut-off and, in particular,  $M_H < \Lambda_{phys}$ . By increasing the value of  $\Lambda_{phys}$   $M_H$  decreases, and on the contrary, by lowering  $\Lambda_{phys}$   $M_H$  increases. There is a crossing point where  $M_H \approx \Lambda_{phys}$  which happens to be around 1 TeV [23]. Figure 1.7 shows this upper limit on the Higgs boson mass depending on the value of the  $\Lambda_{phys}$  cut-off parameter. Figure 1.7 also shows that if the Standard Model must be an effective valid theory for energies up to the Planck energy scale ( $\Lambda_{phys} \sim 10^{19}$ ) where all the fundamental interactions should unify (see Figure 1.1), the Higgs boson mass should be  $m_H \lesssim 140$  GeV/ $c^2$ .

### 1.5.2 Lower Bound: *Vacuum Stability*

Once the asymmetric vacuum of the  $SU(2)_L \times U(1)_Y$  theory has been fixed, this vacuum has to be stable with respect to the high order corrections. In principle, quantum corrections could destabilize the asymmetric vacuum and change it to the symmetric one, where the spontaneous symmetry breaking does not take place (see Figure 1.3). By a close analysis of the effective Higgs potential at two-loop level, including the quantum corrections, a relation between the stability conditions and the Higgs boson mass can be derived [30]. Since all the Standard Model parameters are known, this lower bound can be plot as a function of the energy scale  $\Lambda$  (Figure 1.7). Together with the plotted value for the upper bound, Figure 1.7 shows that

---

[29] for a good review of these and other theoretical bounds.

<sup>14</sup>The conclusions do not depend on the particular choice of the renormalization scheme.

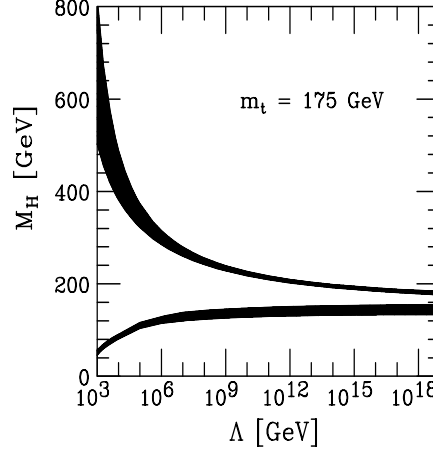


Figure 1.7: Theoretical low and upper bound on the SM Higgs boson mass. The top quark mass is taken to be  $m_t = 175 \text{ GeV}/c^2$  and  $\alpha_s(M_Z) = 0.118$ .

if the SM must be an effective theory up to the Planck energy scale  $\Lambda \simeq 10^{19} \text{ GeV}$ , the Higgs boson mass must lie in a narrow band of few hundred GeV.

## 1.6 Experimental Limits on the Higgs Boson Mass

At present, direct searches for the Higgs boson come from  $e^+e^-$  data collected by four experiments (ALEPH, DELPHI, L3 and OPAL) at the Large Electron Positron (LEP) collider at CERN (Switzerland), and from  $p\bar{p}$  data collected by the CDF experiment at Fermilab. Also, indirect experimental constraints on the Higgs boson mass can be obtained analyzing electroweak precision measurements, assuming the validity of the Standard Model predictions.

### 1.6.1 Indirect Searches

High order corrections to the electroweak observables are in most cases dependent on the Higgs boson mass. As an example, the electroweak parameter  $\rho$ :

$$\rho = \left( \frac{g_Z^2}{M_Z^2} \right) / \left( \frac{g^2}{M_W^2} \right) = \frac{M_W^2}{M_Z^2 \cos^2 \theta_W} \quad (1.26)$$

which measures the relative strength of the charged to neutral currents is in the SM equal to 1. Leading order radiative corrections for  $\rho$  in the large top quark mass

and Higgs boson mass approximation are of the form:

$$\begin{aligned}(\Delta\rho)_t &= \frac{3\sqrt{2}G_F}{16\pi^2}m_t^2 + \dots \\(\Delta\rho)_H &= -3\frac{\sqrt{2}G_F M_W^2}{16\pi^2}\frac{s_W^2}{c_W^2}\left(\log\frac{M_H^2}{M_W^2} - \frac{5}{6}\right) + \dots\end{aligned}\tag{1.27}$$

Note that the high order corrections are more sensitive to the top quark mass (linearly dependence) than to the Higgs boson mass, which grows only as the logarithm of  $M_H^2$ . Due to this weaker dependence, the quantum corrections are not so powerful in limiting the Higgs boson mass as they are for the top quark.

In general, the so called T. Veltman *Screening Theorem* [14] states that, at the one-loop approximation, the Higgs particle corrections to the electroweak observables grow at most, as  $\log M_H$ , with a generic form:

$$g^2\left(\log\frac{M_H^2}{M_W^2} + g^2\frac{M_H^2}{M_W^2} + \dots\right)\tag{1.28}$$

because the other potentially linear corrections  $\frac{M_H^2}{M_W^2}$  are screened by the  $g^2$  small factor.

Precise electroweak measurements performed at LEP and SLD are accurate enough to be sensitive to the mass of the Higgs boson through these radiative corrections [31]. Figure 1.8 shows the likelihood fit on the Higgs boson mass obtained from these corrections with LEP, SLD, UA1 and CDF data [31]. Some of the input parameters are [31]:  $m_Z = 91.1875 \pm 0.0021$  GeV/ $c^2$ ,  $\Gamma_Z = 2.4952 \pm 0.0023$  GeV/ $c^2$  and  $m_W = 80.446 \pm 0.030$  GeV/ $c^2$ . The fit results in a preferred value of  $M_H = 98_{-38}^{+58}$  GeV/ $c^2$  with a 95% confidence level upper limit of  $M_H \leq 212$  GeV/ $c^2$ .

## 1.6.2 LEP Direct Searches

All the LEP experiments have searched for the SM Higgs boson with 2465 pb $^{-1}$  of  $e^-e^+$  data at energies between 189 and 209 GeV [32]. At these energies the SM Higgs boson is expected to be produced mainly in association with a  $Z$  boson through the Higgs-strahlung process,  $e^+e^- \rightarrow HZ$ . At masses around 115 GeV/ $c^2$  the SM Higgs boson is expected to decay mainly into  $b\bar{b}$  quark pairs (74%). The final state topologies used in these searches were determined by these decays and by the decay of the associated  $Z$  boson. LEP experiments have searched in the four-jet final state ( $H \rightarrow b\bar{b}$ ) $q\bar{q}$ , the missing energy final state ( $H \rightarrow b\bar{b}$ ) $\nu\bar{\nu}$ , the leptonic final state ( $H \rightarrow b\bar{b}$ ) $l^+l^-$  ( $l = e, \mu$ ) and the tau lepton final states ( $H \rightarrow b\bar{b}$ ) $\tau^+\tau^-$  and ( $H \rightarrow \tau^+\tau^-$ )( $Z \rightarrow q\bar{q}$ ). Combining the data for all the four experiments in these channels, a lower bound of 114.1 GeV/ $c^2$  has been obtained at the 95% C.L. [32] while signal hints have been observed for Higgs boson mass of 115.6 GeV [32].

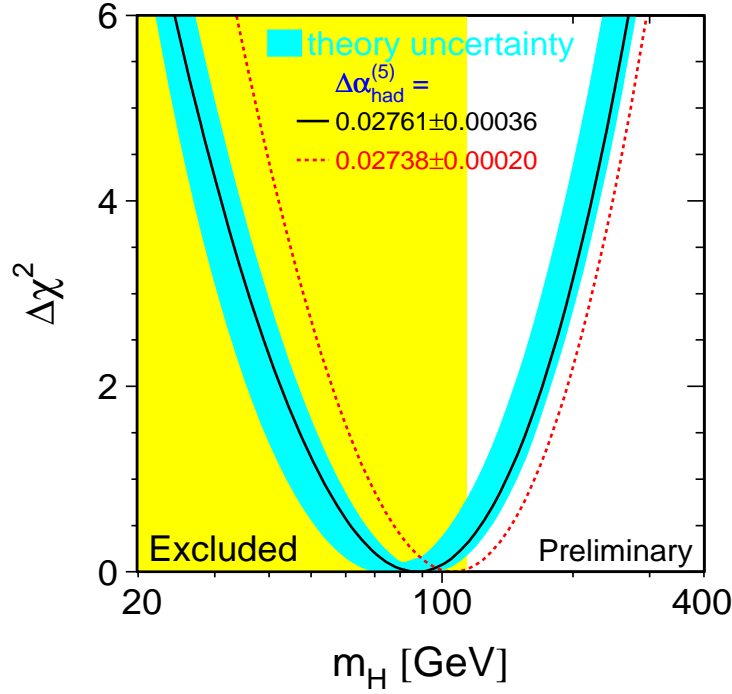


Figure 1.8:  $\Delta\chi^2 = \chi^2 - \chi_{min}^2$  vs.  $m_H$  curve. The line is the result of the fit using all the electroweak precision data available [31]; the band represents an estimate of the theoretical error due to missing higher order corrections. The vertical band shows the 95% C.L. exclusion limit on  $m_H$  from the direct search.

### 1.6.3 CDF Direct Searches

The CDF experiment has searched for a SM Higgs boson in the mass range from 90 to 130  $\text{GeV}/c^2$  with  $106 \text{ pb}^{-1}$  of  $p\bar{p}$  collision data at  $\sqrt{s} = 1.8 \text{ TeV}$ . At these energies, the most copious production mechanism for the Higgs boson is the gluon fusion process ( $gg \rightarrow H$ ,  $\sigma = 1 - 0.1 \text{ pb}$ ) and the associated production with a vector boson ( $\sigma = 0.38 - 0.02 \text{ pb}$ ). The Higgs boson is expected to decay mainly into  $b\bar{b}$  quark pairs (74%), while decays to tau lepton pairs,  $WW^*$ , gluon pairs (7% each), and to  $c\bar{c}$  (4%) are all less important (Section 1.3). For the gluon fusion channel, the predominant Higgs boson decay into  $b\bar{b}$  quark pairs makes it almost impossible to resolve from the huge background of QCD heavy flavor production.

CDF has searched for the Higgs boson decay into  $b\bar{b}$  quark pairs in the associated production mode, where the final topology is determined by the Higgs decay and the decay of the associated vector boson (Table 1.4). The signatures investigated were:

- Two b-jets plus missing energy ( $H \rightarrow b\bar{b}$ ,  $Z \rightarrow \nu\bar{\nu}$ ) [33].
- Two b-jets plus lepton plus missing transverse energy ( $H \rightarrow b\bar{b}$ ,  $W \rightarrow l\bar{\nu}$ ) [34].
- Four jets ( $H \rightarrow b\bar{b}$ ,  $W/Z \rightarrow q\bar{q}$ ) [35].
- Two jets plus two leptons ( $H \rightarrow b\bar{b}$ ,  $Z \rightarrow l\bar{l}$ ) [36].

	BR		BR	$M_H$ (GeV/ $c^2$ )	BR( $H \rightarrow b\bar{b}$ )
$Z \rightarrow$		$W \rightarrow$		100	0.81
$q\bar{q}$	70.0%	$q\bar{q}'$	67.0%	110	0.77
$\nu\bar{\nu}$	19.0%	$l\nu_l$	22.0%	120	0.68
$l^+l^-$ ( $l = e, \mu$ )	6.8%			130	0.53
$\tau^+\tau^-$	3.4%	$\tau\nu_\tau$	11.0%	140	0.34

Table 1.4: Z, W and Higgs boson branching ratios [90].

$M_H$ (GeV/ $c^2$ )	$\sigma_{WH}$ (fb)	$\sigma_{ZH}$ (fb)	Events for $WH \rightarrow l\nu b\bar{b}$	Events for $ZH \rightarrow \nu\bar{\nu} b\bar{b}$	Events for $ZH \rightarrow l\bar{l} b\bar{b}$	Events for $W/ZH \rightarrow jj b\bar{b}$
100	308	173	5.8	2.8	1.0	28
110	224	128	4.0	2.0	0.7	19
120	165	97	2.6	1.3	0.5	13
130	124	74	1.5	0.8	0.3	8
140	94	57	0.8	0.4	0.1	4

Table 1.5: Expected number of events for each of the Higgs boson search signatures with 106 pb $^{-1}$  of integrated luminosity at  $\sqrt{s} = 1.8$  TeV.

Table 1.5 summarizes the expected number of signal events for each of these signatures as a function of the Higgs boson mass. Tables 1.6, 1.7, 1.8 and 1.9 summarize the selection cuts applied on each of these signatures, the selection efficiency and the expected and measured number of background events. Figures 1.9, 1.10, 1.11 and 1.12 shows the dijet mass distribution in the data together with the background expectations for each of these channels.

Figure 1.13 shows the exclusion limits obtained in each of these signatures, together with the combined exclusion limit obtained with a binned likelihood technique [37]. The best exclusion limit is obtained by the  $HZ \rightarrow \nu\bar{\nu} b\bar{b}$ , followed by the fully hadronic decay mode  $HW/Z \rightarrow jj b\bar{b}$ . Combining all channels, the excluded region is an order of magnitude above the SM predicted cross section. This lack of sensitivity is mainly due to the reduced statistics and, in some cases, to a non optimal trigger design. In Run-II, the large increase of the integrated luminosity together with an improved trigger design (the subject of this thesis) will enhance the sensitivity and might lead to an eventual observation of the Higgs signal.

WH $\rightarrow l\nu$ bb					
Single b-jet					
Background	W+1 jet	W+2 jet	W+3 jet	W+ $\geq$ 4 jet	
	QCD	65 $\pm$ 13	22.4 $\pm$ 4.5	4.9 $\pm$ 1.1	1.4 $\pm$ 0.4
	top	2.2 $\pm$ 0.7	7.2 $\pm$ 1.4	11.0 $\pm$ 1.7	11.6 $\pm$ 3.0
	QCD+top	67 $\pm$ 13	30 $\pm$ 5	16 $\pm$ 2	13 $\pm$ 3
Observed	e+jets	36	22	4	5
	$\mu$ + jets	30	14	7	7
Double b-jet					
Background	W+1 jet	W+2 jet	W+3 jet	W+ $\geq$ 4 jet	
	QCD	0	1.6 $\pm$ 0.4	0.3 $\pm$ 0.1	0.15 $\pm$ 0.03
	top	0	1.4 $\pm$ 0.4	3.3 $\pm$ 0.5	5.0 $\pm$ 1.1
	QCD+top	0	3.0 $\pm$ 0.6	3.6 $\pm$ 0.6	5.2 $\pm$ 1.1
Observed	e+jets	0	2	3	2
	$\mu$ + jets	0	4	3	0

Table 1.6: Predicted numbers of tagged W+ $n$  jet events and number of events observed for the WH  $\rightarrow l\nu b\bar{b}$  Higgs search. Results are shown for different data samples requiring a single b-tagged jet and two b-tagged jets. The QCD backgrounds come from Wb $\bar{b}$ , Wc $\bar{c}$  and Wc. Other backgrounds are mistags, top pair production, single top, and other small contribution from b $\bar{b}$  production, diboson (WW or ZZ), Drell-Yan lepton pair production and  $Z \rightarrow \tau^+\tau^-$  decays. The event selection required one central  $|\eta| < 1$  electron or muon with  $E_T \geq 20$  GeV,  $\cancel{E}_T > 20$  GeV, two jets with cone size 0.4,  $E_T > 15$  GeV and  $|\eta| < 2.0$ , where either one or at least two of them are identified as b-quark jets. The double b-tag signal efficiency was found to be  $\approx 0.013$  ( $M_H = 110$  GeV/ $c^2$ ).

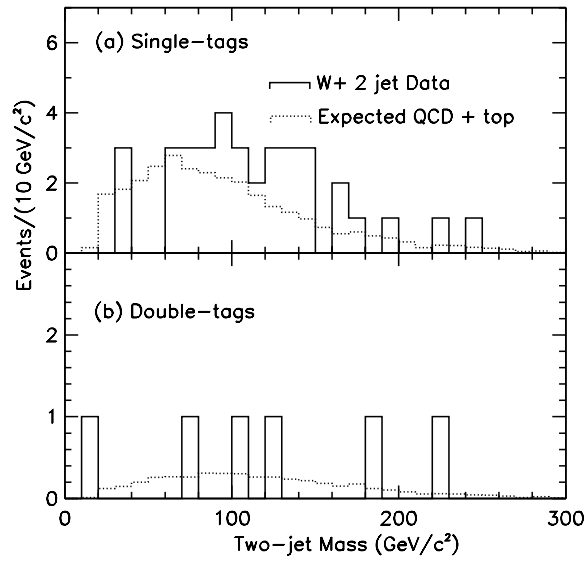


Figure 1.9: The measured dijet invariant mass distribution in the data ( $W + 2$  jet sample) together with the background expectations for the  $HW \rightarrow b\bar{b}\nu l$  search from (a) single tagged events (b) double tagged events.

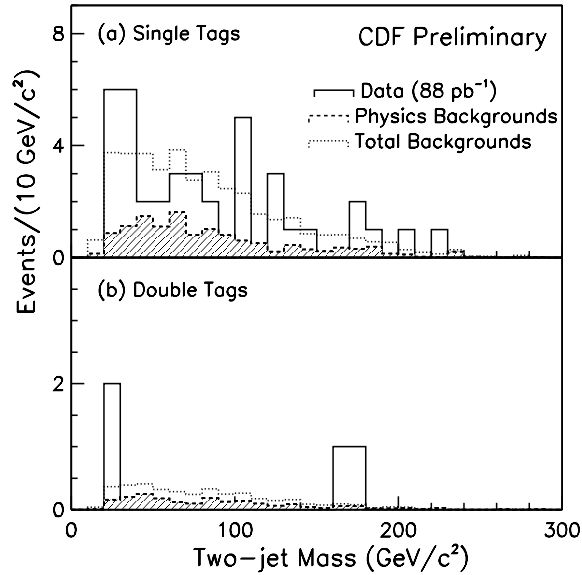


Figure 1.10: The measured dijet invariant mass distribution in the data together with the background expectations for the  $HZ \rightarrow b\bar{b}\nu\bar{\nu}$  search from (a) single tagged events (b) double tagged events.

<b>ZH <math>\rightarrow \nu\bar{\nu}b\bar{b}</math></b>		
Single b-jet		
<b>Background</b>	QCD ( $b\bar{b}$ )	$26 \pm 3$
	W/Z+heavy flavor	$10.1 \pm 2.5$
	Top	$2.4 \pm 0.6$
	WZ and ZZ	$0.45 \pm 0.11$
	<b>Total</b>	$39 \pm 4$
	<b>Observed</b>	40
Double b-jet		
<b>Background</b>	QCD ( $b\bar{b}$ )	$1.9 \pm 0.4$
	W/Z+heavy flavor	$1.0 \pm 0.2$
	Top	$0.8 \pm 0.2$
	WZ and ZZ	$0.17 \pm 0.04$
	<b>Total</b>	$3.9 \pm 0.6$
	<b>Observed</b>	4

Table 1.7: Predicted number of b-tagged events and number of events observed for the  $HZ \rightarrow b\bar{b}\nu\bar{\nu}$  Higgs search. The backgrounds come from QCD heavy flavor production (where the missing energy comes from jet energy mismeasurement),  $Wb\bar{b}$  and  $Zb\bar{b}$ , top pair and diboson production (WZ and ZZ). The event selection required trigger  $\cancel{E}_T > 35$  GeV,  $\cancel{E}_T > 40$  GeV, and 2 or 3 jets with cone size 0.4 ( $E_T > 15$  GeV and  $|\eta| < 2$ ) where at least one is identified as a b-quark jet. The angular separation between the leading jets is required to be  $\Delta\phi_{j1,j2} < 2.6$ , and finally, the separation between any jet and the  $\cancel{E}_T$  direction is required to be  $\Delta\phi_{j,\cancel{E}_T} > 1.0$ . The double b-tagging signal efficiency was estimated to be  $\approx 0.003$  ( $M_H = 110$  GeV/ $c^2$ ).

<b>ZH <math>\rightarrow l\bar{l}b\bar{b}</math></b>		
<b>Background</b>	Z <b><math>b\bar{b}</math></b>	$1.7 \pm 0.7$
	Z+Mistag	$0.65 \pm 0.13$
	Zc $\bar{c}$	$0.32 \pm 0.13$
	WZ and ZZ	$0.19 \pm 0.06$
	Zc $\bar{s}$	$0.17 \pm 0.10$
	Top ( $t\bar{t}$ )	$0.13 \pm 0.04$
	<b>Total</b>	$3.2 \pm 0.7$
	<b>Observed</b>	5

Table 1.8: Predicted number of tagged events and number of events observed for the  $ZH \rightarrow l\bar{l}b\bar{b}$  Higgs search. The event selection required a “tight” central ( $|\eta| < 1$ ) electron or  $\mu$  with  $p_T > 20$  GeV/ $c$ , a “loose” electron or  $\mu$  with  $E_T^e > 10$  GeV and  $p_T^\mu > 10$  GeV/ $c$ ,  $76 < M_{ll} < 106$  GeV,  $\cancel{E}_T < 50$  GeV and two or three jets (reconstructed with cone size of 0.4,  $E_T > 15$  GeV and  $|\eta| < 2.0$ ) where at least one is required to be tagged. The signal efficiency was estimated to be  $\approx 0.0046$  ( $M_H = 110$  GeV/ $c^2$ ).

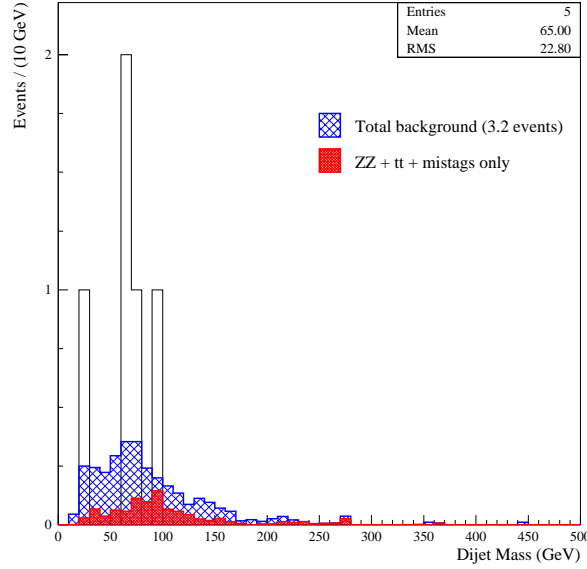


Figure 1.11: Dijet invariant mass distribution for the data and the expected background for the  $ZH \rightarrow l\bar{l}b\bar{b}$  search.

$W/ZH \rightarrow jjb\bar{b}$		
Background	Expected	From Fit to Data
QCD (only data)	–	$474 \pm 27$
Fake double tags	$89 \pm 11$	$83 \pm 11$
Top ( $t\bar{t}$ )	$26 \pm 7$	$22 \pm 7$
Z + jets ( $Z \rightarrow b\bar{b}/c\bar{c}$ ) + jets	$17 \pm 4$	$15 \pm 4$
$Wc\bar{c}, Wb\bar{b}$	$1.2 \pm 0.4$	–
$Zc\bar{c}, Zb\bar{b}$	$0.7 \pm 0.3$	–
<b>Total</b>	–	$596 \pm 30$

Table 1.9: Predicted number of double b-tagged events and number of events observed for the  $W/ZH \rightarrow jjb\bar{b}$  Higgs search. The event selection required four or more jets with cone size 0.4,  $E_T > 15$  GeV and  $|\eta| < 2.1$ . At least 2 among the 4 highest  $E_T$  jets are required to be identified as b-quark jets, and a final cut on  $p_T(b\bar{b}) \geq 50$  GeV/ $c$  was also required. The signal efficiency was estimated to be  $\approx 0.015$  ( $M_H = 110$  GeV/ $c^2$ ).

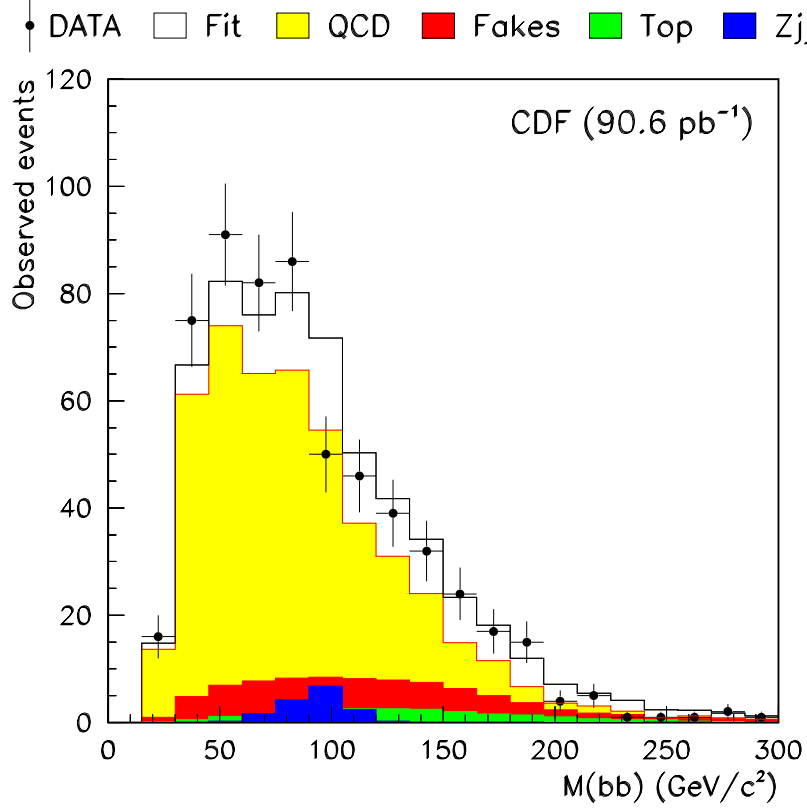


Figure 1.12: Double tag invariant mass distribution for the  $W/ZH \rightarrow jjb\bar{b}$  data compared to the predicted backgrounds for Higgs masses  $M_H \geq 80 \text{ GeV}/c^2$ . The solid line is the sum of all backgrounds (QCD, fakes, top, and Z+jets) and signal contributions as obtained from a fit to the data. The fit yields a zero signal contribution for masses above 80 GeV.

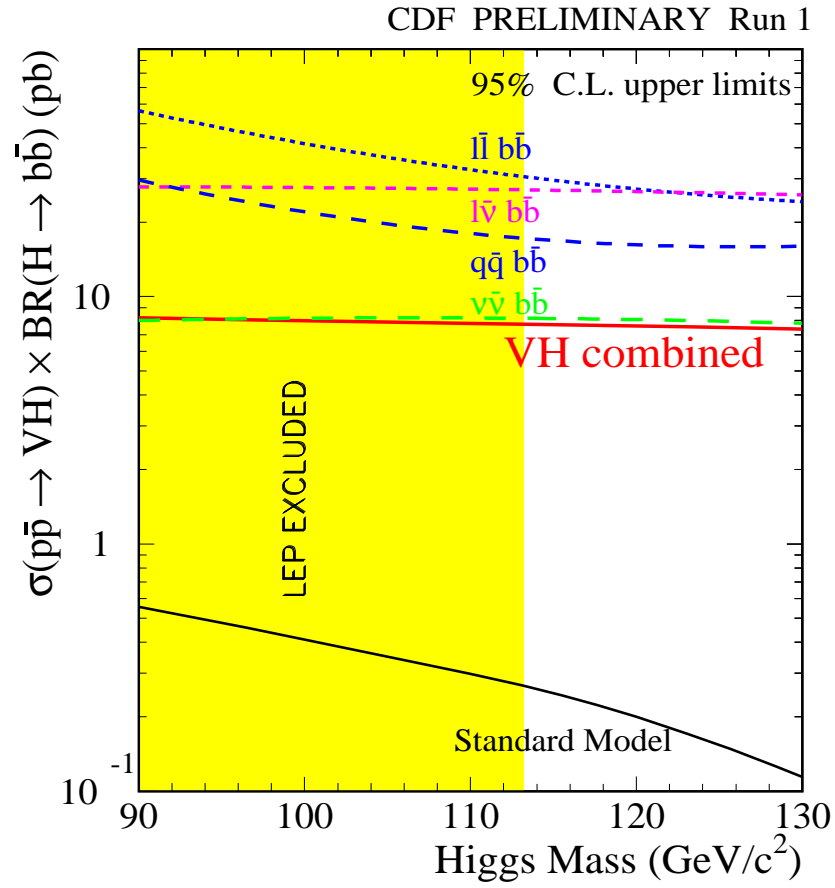


Figure 1.13: Exclusion upper limits at the 95% C.L. set by the individual CDF analysis and the combined result. Black line shows the predicted SM theoretical cross section.



# Chapter 2

## The Apparatus

### 2.1 Fermilab Accelerator Complex

Located near Chicago (Illinois, USA), the Fermilab accelerator complex actually consists of six main accelerators: the Cockcroft-Walton, Linac, Booster, Main Injector, Recycler Ring, and the Tevatron. Two detector facilities are placed at different collisions halls in the Tevatron accelerator for the study of  $p\bar{p}$  collisions at  $\sqrt{s} = 2.0$  TeV. In what concerns the subject of this thesis, three operational periods can be distinguished (Table 2.1): the Run-I (1992-1996)<sup>1</sup>, the starting Run-IIa (2001-2003), and the projected Run-IIb (2004-2007).

Run	Period	Integrated Luminosity
<b>Run Ia:</b>	1992-1993	19 pb <sup>-1</sup>
<b>Run Ib:</b>	1994-1996	90 pb <sup>-1</sup>
<b>Run IIa:</b>	2001-2003	2 fb <sup>-1</sup>
<b>Run IIb:</b>	2004-2007	15 fb <sup>-1</sup>

Table 2.1: CDF operational periods and acquired luminosity in Run-I and the projected Run-II.

In Run-I Tevatron delivered  $p\bar{p}$  collisions at  $\sqrt{s} = 1.8$  TeV. In this period the CDF experiment collected data corresponding to an integrated luminosity of  $109.4 \pm 7.2$  pb<sup>-1</sup>.

For the Run-IIa the goal is to reach an integrated luminosity of 2 fb<sup>-1</sup> in two years [38], with peak luminosities of  $2 \cdot 10^{32}$  cm<sup>-2</sup>s<sup>-1</sup>. For this purpose the Fermilab accelerator complex had undergone several major upgrades and the addition of new accelerators, like the Main Injector and the Recycler. In Run-IIb the goal is to achieve a total integrated luminosity of 15 fb<sup>-1</sup> in four years, with peak luminosities

---

<sup>1</sup>The Run-I is subdivided in two periods: the Run-Ia (1992-1993) and the Run-Ib (1994-1996). Between these two periods several accelerator and detector upgrades were performed.

of  $5 \cdot 10^{32} \text{ cm}^{-2} \text{ s}^{-1}$ . The main factor that limits the increase in luminosity is the availability of antiprotons. Between Run-IIa and Run-IIb an increase on the number of antiprotons by a factor 2-3 is expected with the upgrade of the antiproton source and the improvement of the collection efficiency. Table 2.2 summarizes the expected Tevatron performance. Below we briefly describe the production, acceleration and collision of  $p\bar{p}$  bunches at  $\sqrt{s} = 2.0 \text{ TeV}$  (Figure 2.1).

RUN	Run-Ib	Run-IIa	Run-IIa	Run-IIb
Bunches:	$6 \times 6$	$36 \times 36$	$140 \times 105$	$140 \times 105$
$p$ /bunch	$2.3 \cdot 10^{11}$	$2.7 \cdot 10^{11}$	$2.7 \cdot 10^{11}$	$2.7 \cdot 10^{11}$
$\bar{p}$ /bunch	$5.5 \cdot 10^{10}$	$3.0 \cdot 10^{10}$	$4.4 \cdot 10^{10}$	$1.1 \cdot 10^{11}$
Total $\bar{p}$	$3.3 \cdot 10^{11}$	$1.1 \cdot 10^{12}$	$4.2 \cdot 10^{12}$	$1.1 \cdot 10^{13}$
$\bar{p}$ Production Rate ( $hr^{-1}$ )	$6.0 \cdot 10^{10}$	$1.0 \cdot 10^{11}$	$2.1 \cdot 10^{11}$	$5.2 \cdot 10^{11}$
$p$ emittance ( $mm - rad$ )	$23 \cdot \pi$	$20 \cdot \pi$	$23 \cdot \pi$	$23 \cdot \pi$
$\bar{p}$ emittance ( $mm - rad$ )	$13 \cdot \pi$	$15 \cdot \pi$	$15 \cdot \pi$	$15 \cdot \pi$
$\beta^*$ ( $cm$ )	35	35	35	35
Energy ( GeV )	900	980	980	980
$\bar{p}$ bunches	6	36	105	105
Bunch length (rms, [m])	0.60	0.37	0.37	0.37
Crossing Angle ( $\mu rad$ )	0	0	136	136
Typical Luminosity $\text{cm}^{-2} \text{s}^{-1}$	$0.16 \cdot 10^{31}$	$0.86 \cdot 10^{32}$	$2.1 \cdot 10^{32}$	$5.2 \cdot 10^{32}$
Integrated Luminosity ( $pb^{-1}/\text{week}$ )	3.2	17.3	42	105
Bunch Spacing (ns)	$\sim 3500$	396	132	132
Interactions/crossing	2.5	2.3	1.9	4.8

Table 2.2: Tevatron operational parameters for Run-Ib, Run-IIa and Run-IIb.

### 2.1.1 The Proton Cycle

In the present time is not possible to accelerate protons from thermal energies up to 1 TeV in a single synchrotron accelerator. Radiofrequency cavities electronics, which generate the accelerating fields, can not cope with the rise of the particle's revolution frequency in a single stage. Therefore, the acceleration process is performed in separate accelerators with the appropriate transfer sequence.

The **Cockcroft-Walton** accelerator provides the first stage of acceleration (Figure 2.1). Inside, hydrogen gas is ionized to create negative hydrogen ions. The ions are accelerated by a positive voltage to reach an energy of 750 KeV and transferred to the linear accelerator **Linac**. In the Linac ions are grouped in bunches (each bunch with  $\approx 1.5 \cdot 10^9$  ions) and oscillating electric fields accelerate them up to 400 MeV. At the end of the Linac the ions pass through a thin copper foil which strips the electrons, leaving only bare protons. Linac bunches are then delivered as 20 ms length pulses, with 4000 bunches each, to the next acceleration stage, the Booster. The **Booster** is a synchrotron accelerator of 475 m of circumference where

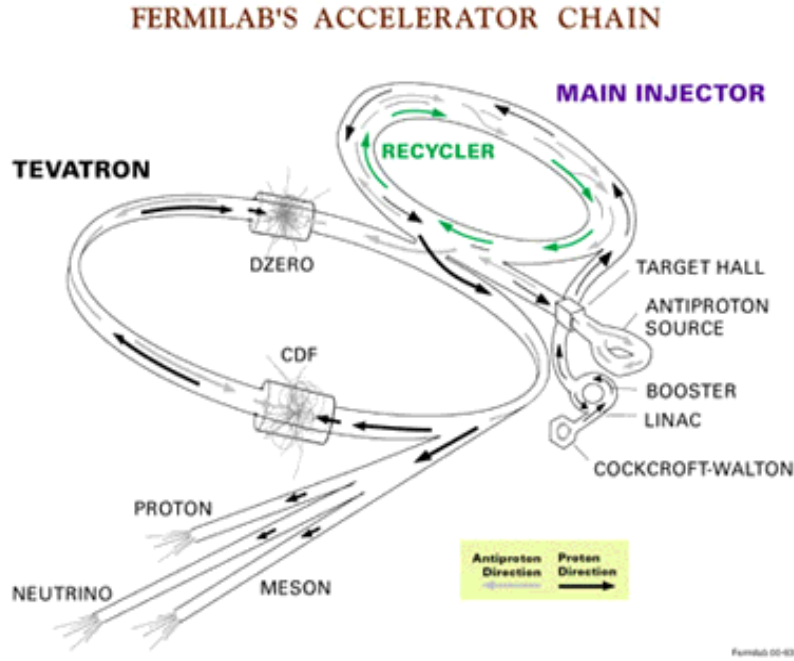


Figure 2.1: General view of the Fermilab accelerator complex [39]. Black arrows show the proton circulation from origin to collisions in both collider detectors and fixed target experiments. Gray arrows show antiproton circulation. Green arrows indicates the antiprotons path in the recycler cycle. Only two detectors in the Tevatron ring are shown.

the protons are accelerated from 400 MeV up to 8 GeV with a revolution frequency rising from 37 MHz to 53 MHz. Since the bunch's revolution period in the Booster is about 2 ms and the Linac pulses have a length of  $\approx 20$  ms, the Booster uses multi-turn injection process to completely transfer each Linac bunch. The **Main Injector** is a 3-km circumference synchrotron accelerator where the protons are accelerated from 8 GeV up to 150 GeV in a 2 s cycle. At each cycle the Main Injector receives 87 bunches from the Booster. Each 5 bunches are merged into 1 and then injected in the Tevatron. The Main Injector is also used for the antiproton cycle, where it serves protons at 120 GeV for the antiproton source, and accelerates the produced antiprotons prior to its injection into the Tevatron<sup>2</sup>. The last accelerator in the chain is the **Tevatron**, an alternating gradient synchrotron with superconducting magnets (4.3° K, 1.8 Tesla). Inside Tevatron, proton and antiproton bunches are accelerated up to energies of 980 GeV, and collisions produced in two different experimental halls. The Tevatron receives 36 bunches (transfers) per cycle from the Main Injector<sup>3</sup> that

<sup>2</sup>The protons and antiprotons rotate inside the same beam pipe in opposite directions.

<sup>3</sup>This corresponds to the  $36 \times 36$  bunch mode, with a bunch time spacing of 396 ns. With a 132 ns bunch time operation, the number of transferred bunches will be 132 for protons and 144 for antiprotons.

are injected into an orbit with an amplitude function<sup>4</sup> of  $\beta^* = 1.7$  m. Before the  $p\bar{p}$  collisions start to occur, the available luminosity is increased<sup>5</sup> by *squeezing* the beam at low  $\beta^* = 0.35$  m with special quadrupoles. Once the Tevatron is completely filled with 36 bunches and the first collisions are produced (the so called *store*), the initial luminosity decreases by 50% in  $\approx 7$  hours.

### 2.1.2 The Antiproton Cycle

The antiproton ( $\bar{p}$ ) production begins with the extraction of protons ( $p$ ) from the Main Injector at 120 GeV. To produce  $\bar{p}$  the extracted  $p$  bunches collide with a nickel target at a rate of 0.6 Hz. The produced  $\bar{p}$  are focused into a beam line with a Lithium lens and filtered with a pulsed magnet to get rid of the secondary particles produced in the nickel target<sup>6</sup>. The  $\bar{p}$  bunches are then moved to the **Debuncher Ring**, where they are merged into a continuous beam and stochastically cooled [40]. In the next step, they are transported to the **Accumulator**, where further cooling is performed. Both the Debuncher Ring and the Accumulator keep the  $\bar{p}$  at a constant energy of 8 GeV. The  $\bar{p}$  stacking rate during Run I was about  $7 \cdot 10^{10} \bar{p}$ /hour; Run-II upgrades will increase this rate by a factor of three to four. When a sufficient number of  $\bar{p}$  (up to  $10^{12}$ ) is available, stacking is suspended; the  $\bar{p}$  are further cooled up to  $\Delta p/p < 10^{-3}$  and then transferred to the Main Injector. In the Main Injector they are accelerated together with the protons up to 150 GeV prior to its injection into the Tevatron.

In the  $\bar{p}$  production cycle the introduction of the **Recycler Ring** will allow to increase the luminosity by a factor 2-3. The Recycler Ring lies above the Main Injector sharing the same tunnel. It acts as a receptacle for  $\bar{p}$  left over at the end of Tevatron Stores. During a Tevatron Store, beam-beam effects lead to an increase in the emittance of the beams<sup>7</sup>. This effect dominates the reduction of the luminosity in the store. The effect is stronger on the  $\bar{p}$  since the  $p$  bunches are, in general, more intense. At the end of a store, which is usually defined by the luminosity having dropped to a few tenths of its initial value, the number of  $\bar{p}$  has only reduced by a factor of two or less. These survivors can be decelerated through the Tevatron and Main Injector and captured in the Recycler. Equipped with stochastic cooling, the Recycler permits the recovery of emittances suitable for reinjection into the Tevatron, and thus results in an effective factor of two enhancement of the number

---

<sup>4</sup>Assuming a beam profile in the phase space  $(x, x')$  ( $x$  is one of the coordinates in the transverse to the beam plane and  $x' = dx/ds$ , where  $s$  is the curvilinear abscissa along the reference orbit) as an ellipse of semiaxes  $\sigma$  and  $\sigma'$ , the *amplitude function*  $\beta$  is defined as the ratio  $\sigma/\sigma'$ .

<sup>5</sup>The Tevatron luminosity is proportional to a form factor  $F$  that depends on the ratio between the bunch longitudinal RMS size,  $\sigma_l$ , and the amplitude function  $\beta^*$  at the interaction point,  $F = F(\sigma_l/\beta^*)$  [38].

<sup>6</sup>For Run-IIb the upgrade of the Lithium lens will increase the collection efficiency, and thus the quantity of available  $\bar{p}$ .

<sup>7</sup>Supposing the profile of the beam in the phase space  $(x, x')$  is an ellipse of semiaxes  $\sigma$  and  $\sigma'$ , the beam *emittance* is the phase volume  $\epsilon = \pi\sigma\sigma'$ .

of available  $\bar{p}$  under normal operation.

## 2.2 The Collider Detector at Fermilab

The Collider Detector at Fermilab (CDF) [10, 41] is a general purpose detector designed to study  $p\bar{p}$  collisions at center of mass energies of 2 TeV. It combines precision charged particle tracking with fast projective calorimetry, time of flight measurement (TOF), and fine grained muon detection. Tracking and TOF systems are contained in a superconducting solenoid, 1.5 m in radius and 4.8 m in length, which generates a 1.4 T magnetic field parallel to the beam axis. Calorimetry and muon systems are all outside the solenoid. The geometrical layout of the detector (Figures 2.2 and 2.3) is symmetric around the beam axis and also has upward-backward symmetry. The actual CDF detector is based in the detector that operated during Run-I [41] with several upgrades. All the read-out electronics have been replaced to accommodate to the new Tevatron bunch time interval of 396 and 132 ns (see Table 2.2). The entire tracking system has been replaced. The drift chamber incorporates more sense wires layers and has smaller drift time to cope with the increased event rate and avoid event pile-up. The silicon system has a larger number of layers, stereo and radial hit detection and an increased geometrical acceptance. A new Time of Flight detector has been added. The Run-I plug calorimeters have been replaced. The muon system has been upgraded and its geometrical acceptance increased. A new detector for luminosity measurement has been implemented.

### 2.2.1 CDF Kinematical Variables and Reference System

The nominal  $p\bar{p}$  interaction point<sup>8</sup> is taken to be the geometrical center of the CDF detector. This point is taken as the origin of a right-handed Cartesian coordinate system. The positive  $z$  direction is the direction of the proton beam, the positive  $y$ -axis points upwards, and the positive  $x$ -axis is pointing out from the center of the Tevatron ring. In the case of a  $p\bar{p}$  collider with unpolarized beams the only preferred axis is the beam direction. Physics processes are hence invariant under rotations around the beam direction, and the polar coordinates system, with the beam direction as the  $z$ -axis, is also a natural choice. In a  $p\bar{p}$  collision, only a fraction of the proton momentum is carried by its constituents (constituents quarks, sea quarks, or gluons), determined by the parton distribution function. As a consequence, the physics interactions have large boosts along the beam direction, and the observed momenta projected into the  $z$  axis do not sum to zero. However, the total momentum in the plane transverse to the beam,  $(p_X, p_Y)$ , is zero. In this plane, the momentum of each particle is represented by its polar coordinates,  $p_T = \sqrt{p_X^2 + p_Y^2}$  and  $\phi$  (the azimuthal angle, measured from the  $x$  axis). The polar angle  $\theta$  is measured starting

---

<sup>8</sup>The  $p\bar{p}$  bunches have a longitudinal dimension of approximately 1 m. The convolution of both yields an interaction region spread of  $\sigma_z = 30$  cm.

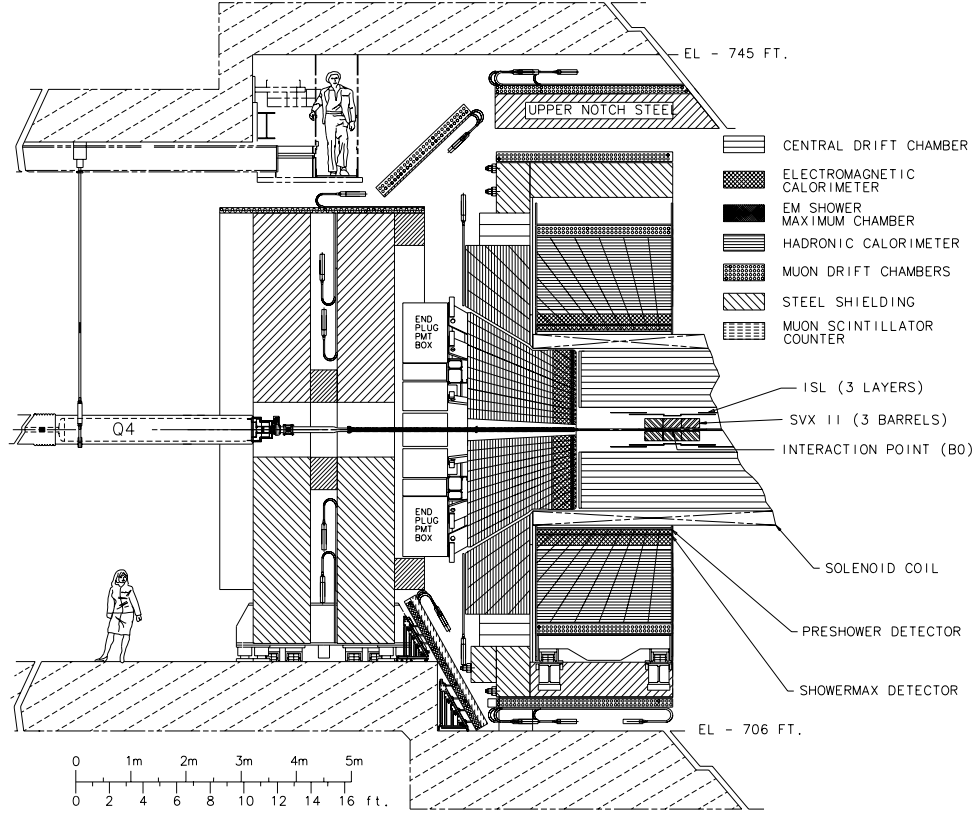


Figure 2.2: Elevation view of one half of the CDF-II detector.

from the positive  $z$  axis. However, the rapidity, defined as:

$$y \equiv \frac{1}{2} \ln \left( \frac{E + p_z}{E - p_z} \right) \quad (2.1)$$

is more useful than the polar angle  $\theta$ : under a boost  $\beta$  in the  $z$  direction the rapidity transforms itself as  $y' = y + \tanh^{-1} \beta$ . Therefore, rapidity shapes of a magnitude  $dN/dy$  are invariant under Lorentz transformations along the  $z$  axis (and thus are the same in both the laboratory frame and in the center-of-mass frame). However, the rapidity depends on the masses of the particles. For ultrarelativistic particles ( $p \gg m$ ) the rapidity can be approximated by the pseudo-rapidity

$$\eta \equiv \frac{1}{2} \ln \left( \frac{p + p_z}{p - p_z} \right) = -\ln \tan \frac{\theta}{2} \quad (2.2)$$

that do not depend in the particle masses.

Therefore, in CDF the energetic hadron collisions are described by the Lorentz-invariant variables  $p_T$ ,  $\phi$  and  $\eta$ . CDF has been designed with approximately cylindrically symmetric layout and roughly uniform segmentation in  $\eta$  and  $\phi$ .

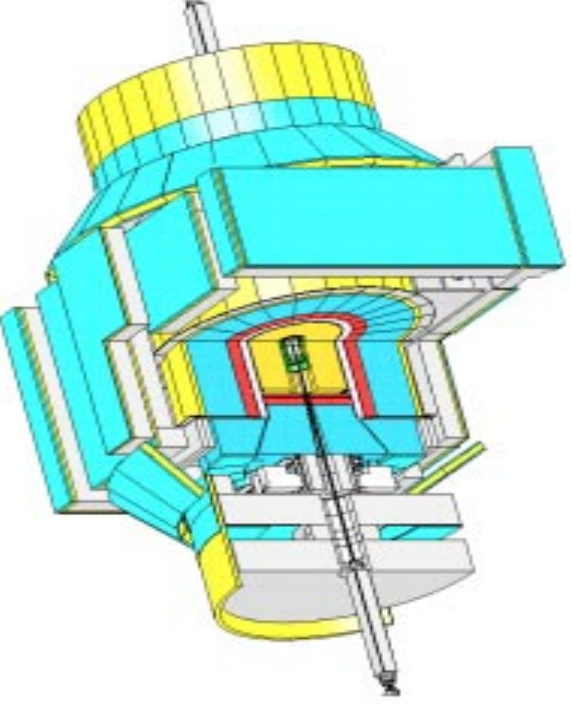


Figure 2.3: Isometric view of the CDF detector .

In the CDF detector (Figure 2.2) particles produced at the interaction point encounter in succession a Beryllium beam pipe, 8 layers of silicon microstrip detectors, a drift chamber, scintillators from a Time of Flight detector, a superconducting solenoid, calorimeters and muon chambers. Below we give a brief description of each of these subdetectors.

### 2.2.2 Cherenkov Luminosity Monitor

The luminosity<sup>9</sup> is measured with the Cherenkov Luminosity Counter (CLC) [42]. The CLC consists of two modules which are located inside the CDF end-plug calorimeters in the forward and backward region, covering a  $3.7 < |\eta| < 4.7$  pseudorapidity range (Figure 2.4). Each CLC detector module consists of 48 thin, long, gas filled, Cherenkov counters. These counters are arranged around the beam-pipe in three concentric layers, with 16 counter each, and pointing to the center of the interaction region. They are built by rolling a 0.1 mm thick sheet of reflective aluminumized mylar (with a 60 nm layer of Al coating) into a conical shape. The cones in the outer two layers (further away from the beam pipe) are about 180 cm long. The inner layers counters are shorter, about 110 cm long. The counters' cross sections range between two and six centimeters in diameter. At the end of the cones, furthest from the interaction region, conical light collectors are placed. Photomultiplier tubes (Hamamatsu R5800Q) are attached to the furthest extreme. They can operate up

---

<sup>9</sup>See Section 6.1 for a definition of luminosity.

to gains of  $2 \cdot 10^6$ . The counters are enclosed in a thin, aluminum, pressure vessel, filled with isobutane at atmospheric pressure.

Luminosity will be measured by counting the number of interactions per bunch crossing. Prompt particles from the  $p\bar{p}$  interactions will cross the full length of the counter and generate a large amplitude photomultiplier signal ( $\sim 100$  photoelectrons). Particles originating from beam-halo interactions or from secondary interactions of prompt particles in the detector material and beam-pipe (secondaries) are softer, and will traverse the counters at larger angles. Their signals are therefore significantly smaller and can be discriminated by using suitable amplitude thresholds (Figure 2.4). The number of particles due to  $p\bar{p}$  interactions and registered by the CLC is proportional to the average number of inelastic  $p\bar{p}$  interactions [42]. Therefore, the average rate of inelastic  $p\bar{p}$  interactions, together with the measured inelastic  $p\bar{p}$  cross section [89] gives a fast and precise measurement of the luminosity.

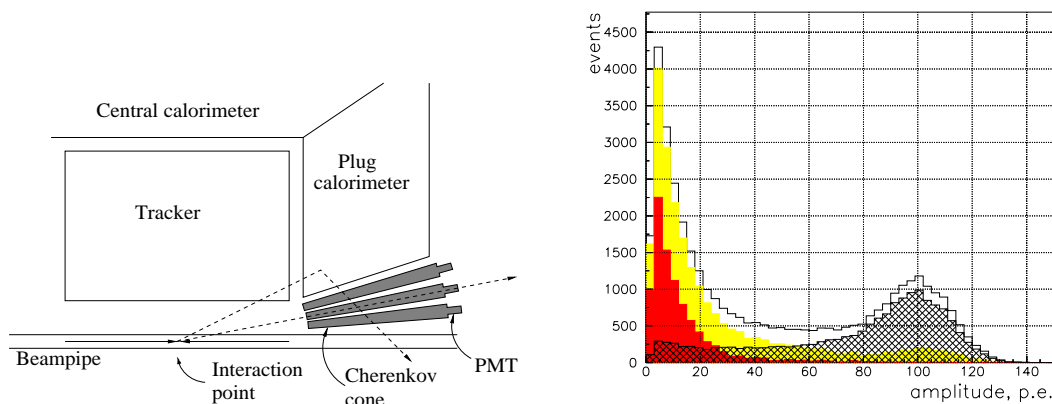


Figure 2.4: Left figure: schematic view of the luminosity monitor inside a quadrant of CDF. Right figure: simulated amplitude distribution in the Cherenkov counter for particles from inelastic  $p\bar{p}$  interactions in the CDF detector. The solid line corresponds to all particles. The hatched histogram to the primary particles, the gray histogram is the contribution from all secondary particles. The contribution from secondaries in the plug calorimeter alone is shown in the black histogram.

### 2.2.3 Tracking System

At CDF, tracking of charged particles is done using four detector systems. From the innermost to the outermost they are: the Layer00, the Silicon Vertex Detector (SVX-II), the Intermediate Silicon Layers Detector (ISL) and the Central Outer Tracker (COT) (Figure 2.5).

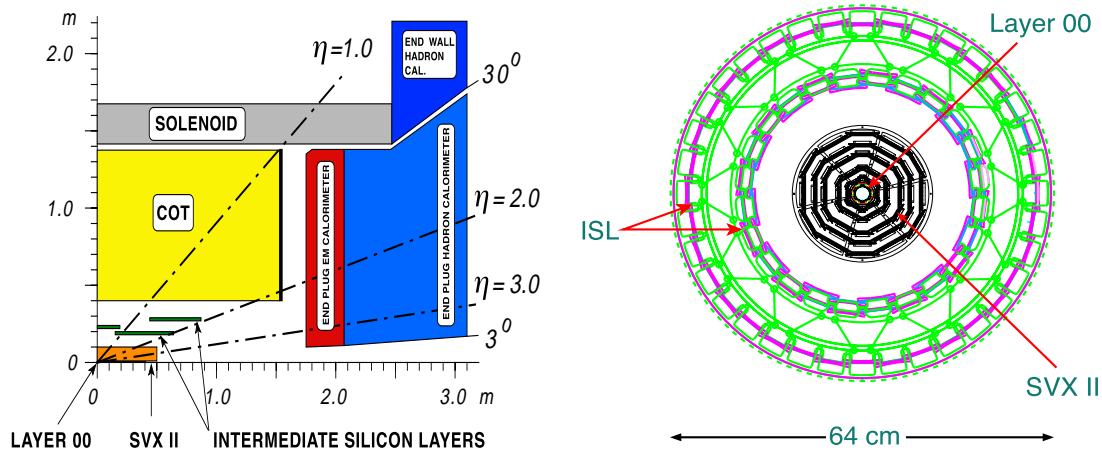


Figure 2.5: Left figure: A cutaway view of one quadrant of the inner portion of the CDF-II detector showing the tracking region surrounded by the solenoid and forward plug calorimeters. Right figure: An end view of the CDF II silicon system including the SVX II cooling bulkheads, the ISL and the support structure.

### Layer 00

The Layer 00 is described in detail in [43]. It is a single sided layer of low-mass silicon-microstrips at very small radius (1.6 cm). The basic readout elements are individual single-sided, axial-strip sensors of  $\approx 10$  cm length. Eight sensors are mounted end to end along the beam pipe. The readout electronics is mounted along the beam pipe at  $|z| > 40$  cm with fine-pitch kapton cables carrying the signals from the sensors to the readout chips. The sensors have an implant pitch of  $25 \mu\text{m}$  with an alternate strip readout, giving a readout pitch of  $50 \mu\text{m}$  and a hit resolution of  $\approx 6 \mu\text{m}$ . The total number of readout channels is  $\approx 16,000$ . At 1.6 cm the expected radiation dose is  $\approx 1 \text{ Mrad}/\text{fb}^{-1}$ ; therefore, radiation-hard silicon is used, similar to the ones designed for the CMS experiment [44]. The readout electronics is basically the same as the ISL and the SVX II: the hybrids are a fairly straightforward adaptation of the ISL hybrids, and the same readout chip, the SVX3 chip [45], is used for the frontend electronics (see Section 3.2.3).

### SVX II

The SVX II [11] is composed of three identical barrels, each 29 cm long, and located symmetrically around the nominal center of the detector. Each barrel is segmented in 12 wedges, each spanning  $30^\circ$  in  $\phi$ . There are 5 layer of silicon sensors per barrel, which are placed radially from 2.45 cm to 10.6 cm. The basic structural unit of the SVX II detector is a ladder, which consist of 4 double-sided silicon microstrip sensors with width and strip multiplicity depending on the layer (Table 2.3). The silicon sensor layout was optimized to handle high radiation levels ( $0.5 \text{ Mrad}/\text{fb}^{-1}$  for the

innermost layer) and short integration times for the readout (132 ns), while keeping good secondary vertex reconstruction and pattern recognition. All the sensors are double-sided and made from n-type high resistivity silicon. Layers 0 (the innermost), 1 and 3 have  $90^\circ$  stereo strips, while for layers 2 and 4 the stereo strip have a small angle ( $\pm 1.2^\circ$ ) (Table 2.3). The nominal thickness is  $300\ \mu\text{m}$  for the  $90^\circ$  stereo sensors and  $275\ \mu\text{m}$  for the small stereo angle. Strips are coupled to the readout electronics through integrated coupling capacitors formed by a thin insulating layer and an aluminum electrode. On the ohmic side, strip isolation is achieved using  $p$ -stops implants (see Section 3.1.8).

The SVX II ladder is readout from both ends through readout chips mounted on electrical hybrids on the surface of the silicon sensors. Support for the ladder is provided by carbon fiber and Rohacell rails. Ladders are aligned on both ends by precision machined beryllium bulkheads. The bulkheads contain integrated cooling channels and are used also as heat sinks for the frontend electronics. The cooling system is designed to keep the silicon temperature at less than  $\sim 15^\circ$  for nominal operating conditions. The total number of read-out channels is about 405,000.

Sensors parameters	Layer 0	Layer 1	Layer 2	Layer 3	Layer 4
Radial Distance (cm)	2.45	4.67	7.02	8.72	10.6
Stereo Angle ( $^\circ$ )	90	90	+1.2	90	-1.2
$r - \phi/z$ readout channels	256/512	384/576	640/640	768/512	896/896
$r - \phi/z$ readout chips	2/2	3/3	5/5	6/4	7/7
$r - \phi/z$ strip pitch ( $\mu\text{m}$ )	60/141	62/125.5	60/60	60/141	65/65
Total width (mm)	17.14	25.59	40.30	47.86	60.17
Total length (mm)	74.3	74.3	74.3	74.3	74.3

Table 2.3: Mechanical specifications of the SVX II sensors.

## ISL

The Intermediate Silicon Layers detector (ISL) [46] has a total active length of 1.9 m. It consists of one layer of microstrip silicon sensors in the central region ( $|\eta| \leq 1$ ) located at radius  $\approx 23$  cm, and two symmetric layers in the forward and backward regions ( $|\eta| \geq 1$ ) located, respectively, at radii  $\approx 20$  cm and  $\approx 29$  cm.

The ISL provides one spacepoint in the central region which improves the linking between SVX II and COT tracks. Its fine granularity helps to resolve ambiguities in dense track environments. Together with the 6 points from the SVX II, the Layer 00 and the COT, the complete tracking system provides high momentum resolution for  $|\eta| < 1$  ( $\sigma_{p_T}/p_T^2 = 9 \cdot 10^{-4} (\text{GeV}/c)^{-1}$  at  $p_T = 10 \text{ GeV}/c$  [10]). In the forward region, where the acceptance of the COT rapidly decreases, the SVX II and ISL detectors constitute a standalone 3D silicon tracker with up to 7 axial and 7 stereo measurement points, extending the tracking capabilities up to  $|\eta| \approx 2$  (Figure 2.5).

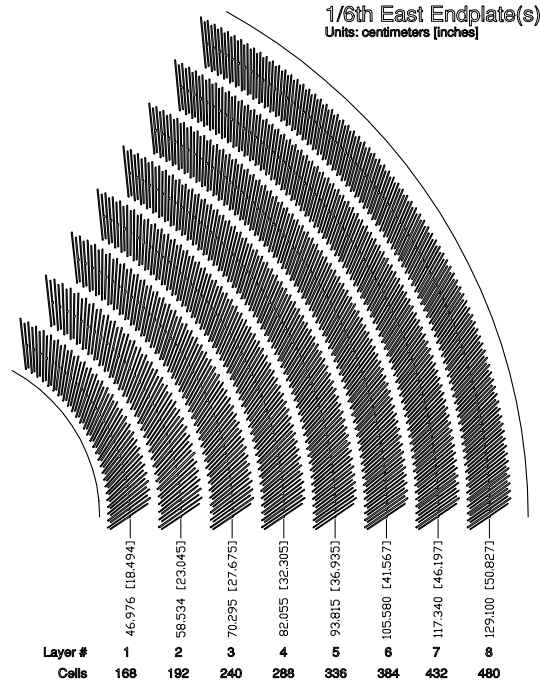


Figure 2.6: COT endplate slots. Sense and field planes are at the clock-wise edge of each slot.

## COT

Outside the silicon detector, but inside the magnetic field, at a distance between 40 and 138 cm from the beam, covering  $|z| < 155$  cm, lies the Central Outer Tracker (COT) [10]. It is a new open-cell drift chamber able to reconstruct tracks in the  $|\eta| < 1$  region with  $p_T \geq 300$  GeV/ $c$ . The COT replaces an older drift chamber, the CTC [47], used in the Run-I, that would have been unable to cope with the expected occupancy and event rate of Run-II due to its larger drift times.

The COT is divided in eight superlayers, each containing twelve layers of sense wires (Figure 2.6). Axial superlayers, in which the wires are parallel to the magnetic field, alternate with superlayers in which the wires have a  $3^\circ$  stereo angle. Each superlayer is divided in identical cells delimited by two field planes. To cope with the Run-II event rate, where events are taken every 132 ns, the COT has been designed with a small cell size  $\approx 1$  cm, four times smaller than the Run-I drift chamber, and is filled with a faster gas. A 50 : 50 mixture of argon and ethane which with a drift field of 1.9 kV/cm provides a drift speed of about  $50 \mu\text{m}/\text{ns}$ . In future, with the 132 ns of bunch crossing, this gas will be replaced by a faster mixture. Wire readout is performed via a custom-built ASD (amplifier, shaper and discriminator) radiation-hard 8-channel chip. They provide continuous measurements without external timing of the signal's leading edge and of the total collected charge. The collected charge is encoded in the output pulse length and used in offline analysis

for  $dE/dx$  particle identification. The signal is carried to TDC boards and then propagated to trigger and readout boards.

### 2.2.4 Time of Flight Detector

The Time-Of-Flight (TOF) detector [43] is an array of scintillator bars placed at the outer edge of the COT, at a radial coordinate of 140 cm. An accurate measurement of a particle's time of flight in the CDF tracking volume can be used quite effectively in particle identification (Figure 2.7). Scintillator bars are about three meters long, matching the COT active volume; their thickness (4 cm) is limited by the space which remained available between the Run-I CTC and magnet. The TOF occupancy is estimated to be 0.1 with 2 superimposed events, and 0.4 with 10 events. The bars have a trapezoidal cross section to minimize cracks in the geometry; the scintillating material is Bicron 408, which has a short rise time and a long (380 cm) attenuation length.

Photomultiplier tubes, attached to both end of each bar, provide time and pulse height measurements. By comparing the two pairs of results, the detector determines the instant in which a particle crossed the scintillator (with an accuracy of about 100 ps) and the  $z$  coordinate of the intersection.

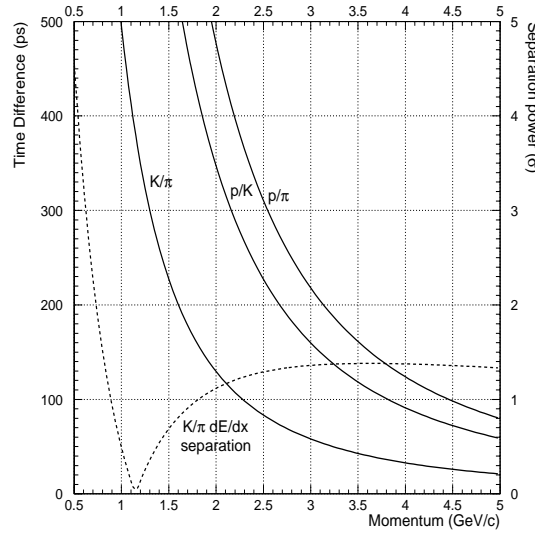


Figure 2.7: Time of flight difference as a function of particle type and momentum. The dashed line indicates the COT  $dE/dX$  separation power for  $K\pi$ .

### 2.2.5 Magnet

The CDF superconducting solenoid provides a uniform magnetic field of up to 1.5 T along the detector axis, over a cylindrical volume of 3.5 m long and 2.8 m in

diameter. The solenoid is built of an Al-stabilized NbTi superconductor, able to withstand currents up to 5000 A, and operating at liquid helium temperature.

### 2.2.6 Calorimetry

The CDF calorimeters [48, 49] are located immediately outside of the solenoid (Figure 2.2). Their coverage is  $2\pi$  in azimuth and  $|\eta| < 3.6$  in pseudo-rapidity. The calorimeters are segmented in pseudorapidity and azimuth to form a projective tower geometry which points back to the geometric center of the detector. The calorimeters are divided into two regions according to their pseudorapidity coverage: the central and the plug. Each region has an electromagnetic calorimeter followed by a hadronic calorimeter. All calorimeters use *shower sampling* to measure particle energy. They are constructed of many layers of dense absorber material (steel or lead) interleaved with active scintillator material sensitive to ionisation. Particles striking the absorber material undergo energy loss through their interaction with nuclei and atomic electrons. The daughter particles also interact with the absorber material giving rise to a *shower* of particles. Showers generate a detectable signal roughly proportional to the number of particles in the shower. Each layer of the active material is said to *sample* the shower. The sum of the signals from all sampling layers is proportional to the energy of the incident particle. The absorber in all hadronic calorimeters is iron and in all electromagnetic calorimeters is lead. Table 2.4 summarizes the coverage, segmentation, thickness and resolution of each of the calorimeters. Proportional chambers with strip and wire readout (CES) [50] are located at a depth of six radiation lengths in the central electromagnetic calorimeter, which approximately corresponds to the shower maximum for electromagnetic showers. The CES provides both the  $z$  and  $r - \phi$  measurements of the shower position. Another wire chamber is placed immediately in front the calorimeter to act as a pre-shower detector (CPR), using the tracker and the solenoid coil as radiators. In Run-I the CPR has proven to be extremely useful in the rejection of electron background. For the plug calorimeter the scintillator tiles of the first layer of the electromagnetic section are made out of 10 mm thick scintillator and are read out by Multi-Anode Photo-multiplier tubes. They will act as a preshower detector. The shower maximum detector is also placed at a depth of approximately six interactions length, but is made of scintillator strips read out by wave-length shifting fibers, with clear fibers carrying the light to Multi-Anode Photo-multipliers.

### 2.2.7 Muon System

The muon system is the outermost component of CDF. The Central MUon system (CMU) [10, 52] consists of four layers of drift chambers located outside the central hadronic calorimeter. The central hadronic calorimeter acts as a hadron absorber for the CMU. Four additional layers of drift chambers located outside the solenoid return yoke and shielded by an extra 0.6 m of steel comprise the Central Muon uPgrade

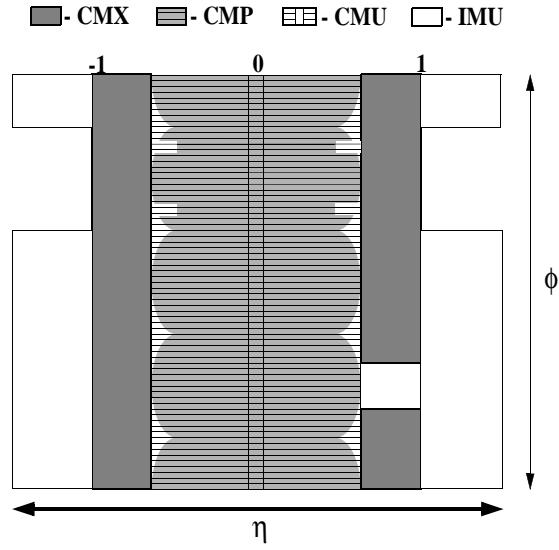
System:	$\eta$ coverage	Thickness	Light yield	Resolution
Electromagnetic				
Central:	$ \eta  < 1.1$	$19X_0, 1\lambda$	$160pe/GeV$	$13.5/\sqrt{E} \oplus 1\%$
Plug:	$1.1 <  \eta  < 3.6$	$21X_0, 1\lambda$	$300pe/GeV$	$16/\sqrt{E} \oplus 1\%$
Hadronic				
Central:	$ \eta  < 1.1$	$4.5\lambda$	$40pe/GeV$	$75\%/\sqrt{E} \oplus 3\%$
Plug:	$1.1 <  \eta  < 3.0$	$7.0\lambda$	$39pe/GeV$	$80\%/\sqrt{E} \oplus 5\%$

Table 2.4: Characteristics of the CDF Run-II calorimeter.

$\eta$ Range:	$\Delta\phi$	$\Delta\eta$
0.0 – 1.1	$15^\circ$	$\sim 0.1$
1.1 – 1.8	$7.5^\circ$	$\sim 0.1$
1.8 – 2.1	$7.5^\circ$	$\sim 0.16$
2.1 – 3.6	$15^\circ$	0.2 – 0.6

Table 2.5: CDF-II calorimeter segmentation.

(CMP). The Central Muon eXtension (CMX) consists of four free-standing conical arches comprising of drift chambers sandwiched between scintillator counters extend the coverage of the CMU and CMP to  $|\eta| < 1$  [53]. For all central muon systems, the muon  $p_T$  is determined from the tracking chamber inside the solenoid. The  $p_T$  of the forward muons  $1 < |\eta| < 1.5$  will be measured with tracks reconstructed using silicon information only. In this region ( $1 < |\eta| < 1.5$ ) a new set of chambers, the Intermediate MUon detector (IMU) [10] has been placed. Table 2.6 summarizes the characteristics of the muon subsystem. Figure 2.8 shows its geometrical acceptance.

Figure 2.8: Location in azimuth  $\phi$  and pseudorapidity  $\eta$  of the muon systems.

	CMU	CMP/CSP	CMX/CSX	IMU
<b><math>\eta</math> coverage:</b>	0 – 0.6	0 – 0.6	0.6 – 1.0	1.0 – 1.5
<b>Drift tubes:</b>				
thickness	2.68 cm	2.5 cm	2.5 cm	2.5 cm
width	6.35 cm	15. cm	15. cm	8.4 cm
length	226 cm	640 cm	180 cm	363 cm
max drif time	0.8 $\mu$ s	1.4 $\mu$ s	1.4 $\mu$ s	0.8 $\mu$ s
tubes	2304	1076	2208	1728
<b>Scintillators:</b>				
thickness	N/A	2.5 cm	1.5 cm	2.5 cm
width	N/A	30 cm	30 – 40 cm	17 cm
length	N/A	320 cm	180 cm	180 cm
# counters	N/A	269	324	864
$\pi^\circ$ int. lengths	5.5	7.8	6.2	6.2 – 20
Min $p_T$ (GeV/c)	1.4	2.2	1.4	1.4 – 2.0
MS resol. ( $cm \cdot GeV$ )	12	15	13	13 – 25

Table 2.6: Parameters of muon detection at CDF. Pion interaction length and the limit on the resolution due to multiple scattering are computed at  $\theta = 90^\circ$  in the central detectors CMU, CMP and CSP; at  $\theta = 55^\circ$  in CMX and CSX; and on the entire  $\theta$  coverage for the IMU.



# Chapter 3

## The Intermediate Silicon Layers Detector

### 3.1 Silicon Detectors in High Energy Physics

Semiconductor detectors were first used in nuclear physics for energy measurements in 1951 [54] and appeared in high energy physics in the 1970s. They were basically reversed polarized p-n junctions operated as ionization chambers. In 1980 the introduction of the planar technique [55] in the production of silicon wafers allowed the segmentation of one side of the p-n junction, where the signals recorded on the segments were used to determine the position of the incident particle. Silicon microstrip detectors are a particular type in which the segments are narrow strips, called microstrips.

#### 3.1.1 Energy Loss of High Energy Charged Particles in Silicon

High energy charged particles traversing crystalline silicon can lose energy either by the excitation of the atomic electrons from the valence to the conduction band or by non-ionizing energy loss (NIEL). The detection of a high energy particle is based on the excitation of the silicon atoms. NIEL losses consists in the displacement of the silicon atoms from the crystal lattice mostly by the process of Coulomb nuclear scattering. For a high energy particle the fraction of energy loss going into the NIEL mechanism is small but the cumulative effects on the detector performance can be severe, and it is one of the causes of the radiation damage in silicon detectors (Section 3.2.7).

The amount of ionization produced per unit length of silicon traversed can be estimated from the linear energy loss given by the Bethe-Bloch formula [56, 57]:

$$-\frac{dE}{dx} = \frac{4\pi n_e Z^2 q^4}{m\beta^2 c^2} \left( \ln \frac{2m\beta^2 \gamma^2 c^2}{I} - \beta^2 - \frac{\delta(\gamma)}{2} \right) \quad (3.1)$$

where  $n_e$  is the electron density per unit volume,  $q$  and  $m$  are the charge and mass of the electron,  $Z$  and  $\beta$  are the charge and velocity of the incident particle,  $I$  is the mean ionization potential for the medium, and  $\delta$  is a correction function which takes into account the dielectric screening in dense material [58]. The most important features of Equation 3.1 are its independence from the mass of the struck particle and its material dependence, which is linear through  $n_e$  and logarithmic through the mean ionization potential.

The energy loss given by the Bethe-Bloch formula (Equation 3.1) exhibits a minimum at energies typically roughly 4 times the rest energy of the particle (Figure 3.1), after which the energy loss remains fairly constant due to the screening of the electrons in the material (Fermi plateau). In this plateau all the particles ionize at an approximately constant rate, regardless of their mass or charge. Particles in the minimum ionizing regime are frequently called *minimum ionizing particles* (MIP). It is clear that most of the ionization is done when the particle slows down and it is almost stopped within the medium.

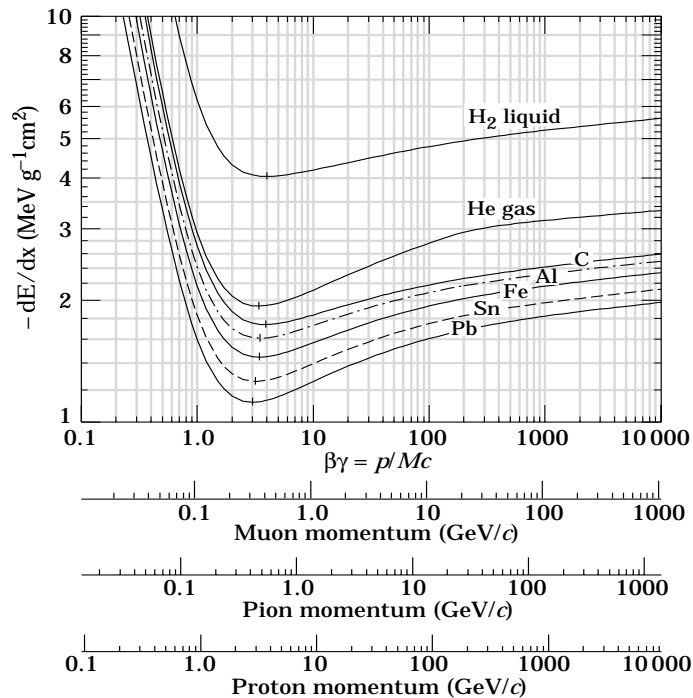


Figure 3.1: Particle energy loss in liquid Hydrogen, Helium, Carbon, Aluminum, Tin and Lead. (From Reference [59])

Silicon detectors have a high energy loss for particles crossing the material due to its high density, what generates large amounts of charge for signal detection. The overall energy loss distributions for MIP consists of an approximately Gaussian core

plus a high tail (the Landau distribution)<sup>1</sup>. The rare collisions with energy transfer greater than approximately 10 KeV generate  $\delta$ -electrons of significant range, which will release electron-hole pairs along their path. This effect may be important in tracking detectors, since it can potentially degradate the spatial precision.

For silicon detectors, unlike gas detectors, there is not multiplication of the primary charge, and the collected signal is only a function of the detector thickness. However, the detector thickness can not be arbitrary large. The bias voltage needed to operate a silicon detector approximately grows as the square of the detector thickness (Section 3.1.3), what makes more difficult its operation. A typical detector thickness is  $\approx 300 \mu\text{m}$ , which yields on average a signal of  $2.4 \cdot 10^4$  electron-hole pairs for minimum ionizing particles crossing the material at normal incidence angle.

Silicon detectors have a very good intrinsic energy resolution. In silicon one electron-hole pair is created for every 3.6 eV released by a particle crossing the medium. In a gaseous detector 30 eV are required to ionize a gas molecule, and in a plastic scintillator coupled to a photomultiplier 300 eV are needed in average to extract an electron from the photocathode.

### 3.1.2 Silicon Properties and the p-n Junction

Silicon is an element of the IV group with 4 electrons on the valence shell. As in any semiconductor material, two electron energy bands can be distinguished [61]: the valence band and the conduction band, separated by a gap that in pure silicon at ambient temperature is 1.1 eV<sup>2</sup> (Table 3.1). Excitation of an electron from the valence band to the conduction band creates a vacancy on the valence band, that behaves itself as a positive charged particle (usually referred as holes). In thermodynamic equilibrium and in absence of impurities the electron (n) and hole densities (p) are equal (*intrinsic material*) and can be calculated as [61]:

$$n = N_c \cdot e^{-\frac{E_c - E_f}{kT}} \quad (3.2)$$

$$p = N_v \cdot e^{-\frac{E_f - E_v}{kT}} \quad (3.3)$$

where  $N_c$  and  $N_v$  are the effective densities of states at the conduction and valence band edge respectively (Table 3.1).  $E_c$ ,  $E_f$  and  $E_v$  are the energies of the conduction band, Fermi level and valence band respectively,  $k$  is the Boltzmann constant, and  $T$  is the absolute temperature.

---

<sup>1</sup>For very thin silicon detectors ( $\sim 1 \mu\text{m}$ ) the overall energy loss distribution does not follow a Landau distribution, but shows clear peaks corresponding to 0, 1, 2 plasmon excitations, followed by a long tail extending to very large energy losses [60]. An efficient tracking detector can not be built with a such active layer. For thickness of  $\sim 300 \mu\text{m}$ , the Landau distribution gives an adequate representation.

<sup>2</sup>Note that the electron-hole generation by particles crossing the silicon is a rather “inefficient” process. The silicon gap between the conduction and the valence band is only 1.1 eV at ambient temperature. Since 3.6 eV are needed to create an electron-hole pair, approximately 2/3 of the energy transferred to the electrons gives rise to phonon generation.

<b>Atomic number:</b>	14	<b>Atomic weight:</b>	28.08
<b>Atoms</b> ( $\text{cm}^{-3}$ ):	$4.99 \cdot 10^{22}$	<b>Density</b> ( $\text{g}/\text{cm}^3$ ):	2.33
<b>Dielectric constant:</b>	11.7	<b>Gap energy</b> (eV):	1.11
<b>Effective states density:</b>		<b>Diffusion const.:</b>	
<b>Conduction band</b> ( $\text{cm}^{-3}$ ):	$2.8 \cdot 10^{19}$	<b>Electrons</b> ( $\text{cm}^2/\text{s}$ ):	34.6
<b>Valence band</b> ( $\text{cm}^{-3}$ ):	$1.04 \cdot 10^{19}$	<b>Holes</b> ( $\text{cm}^2/\text{s}$ ):	12.3
<b>Electron mobility</b> ( $\text{cm}^2/(\text{V} \cdot \text{s})$ ):	1350	<b>Hole mobility</b> ( $\text{cm}^2/(\text{V} \cdot \text{s})$ ):	480
<b>Intrinsic carrier density</b> ( $\text{cm}^{-3}$ ):	$1.45 \cdot 10^{10}$	<b>Intrinsic resistivity</b> ( $\text{k}\Omega\text{cm}$ ):	235
<b>Melting point</b> ( $^{\circ}\text{C}$ ):	1415	<b>Thermal coefficient</b> ( $1/^{\circ}\text{C}$ ):	$2.5 \cdot 10^{-6}$
<b>Breakdown field</b> ( $\text{V}/\mu\text{m}$ ):	30		

Table 3.1: Si physical properties at room temperature.

One important consequence of the thermal equilibrium is the so called *mass action* law, that holds for both intrinsic and extrinsic (with impurities) semiconductors:

$$np = n_i^2 \quad (3.4)$$

where  $n_i$  is the intrinsic concentration of carriers, given by Equations 3.2 and 3.3.

### 3.1.3 The p-n Junction

With pure silicon the intrinsic carrier density is  $n_i = 1.45 \cdot 10^{10} \text{ cm}^{-3}$  at room temperature. A detector made of pure silicon with a surface of  $1 \text{ cm}^2$  and thickness of  $300 \mu\text{m}$  has a total number of free carriers of  $4.5 \cdot 10^8$ , which is four orders of magnitude higher than the expected signal. One way to increase the signal-to-noise ratio is depleting the detector of free carriers through a reverse biased p-n junction. Depleted of free carriers, it behaves like a resistor drawing no current under the applied voltage, but any charge deposited within its volume drifts towards the junction and can be collected.

A p-n junction is a junction of p-type and n-type material (silicon). As stated above, in pure silicon the concentration of holes  $p$  and electrons  $n$  is equal. In p-type silicon the majority carries are holes while in n-type silicon are electrons. p-type silicon is obtained by replacing some of the silicon atoms by atoms from the III group (dopant). Elements from the III group have 3 valence electrons, and to form the 4-valence bond with the surrounding silicon atoms they easily attach an electron from the neighbor atoms, creating a vacancy (hole) that can easily migrate in the crystal. This type of impurity is called an acceptor impurity. Elements of the V group (donors) introduced in pure silicon create n-type silicon. Donors impurities have 5 electrons on the valence shell and easily give one to the conduction band (Figure 3.2).

Figure 3.3 shows a p-n junction, when two semiconductor crystals of p and n-types are put together in thermodynamic equilibrium. At the junction a gradient of electrons and holes densities appears, which results in a diffusive migration of

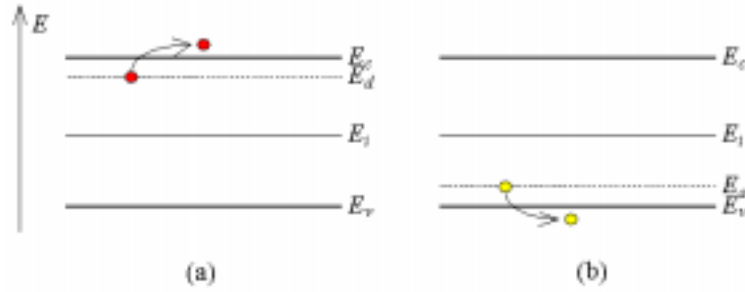


Figure 3.2: Representation of a donor energetic level (left) and an acceptor energetic level (right). The fifth electron of the donor impurities is weakly attached to the impurity atom, which is represented as a level very close to the conduction band, and thus little excitations can transfer it to the conduction band. For the acceptors, with only three valence electrons, a level very close to the valence band is created, and thus low energy electrons from the valence band can easily jump to it, creating the corresponding hole.

majority carriers across the junction. This migration leaves the left-hand region with a net negative charge and the right-hand region with a net positive charge. In this region there is an electric field, but at the same time there are no free carriers. It is called the depletion region.

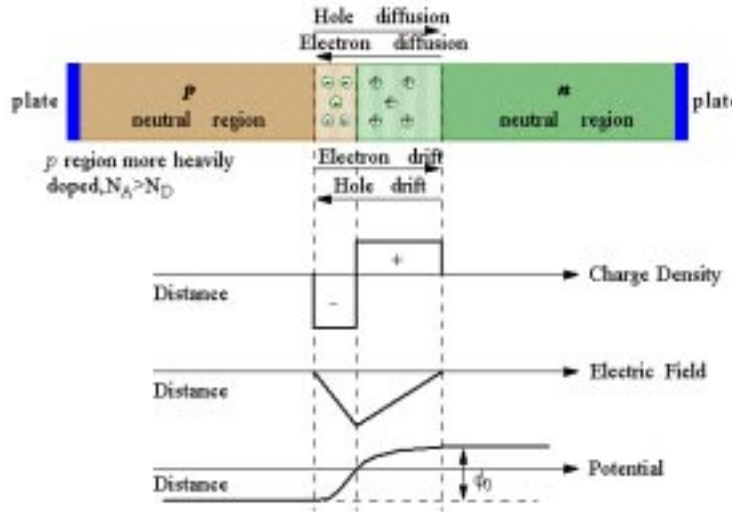


Figure 3.3: The p-n junction. a) Two crystals of opposite type are brought together and a depletion layer is formed on either side of the junction. b) Net space charge density showing zero charge except for a dipole layer at the junction (abrupt junction approximation). c) Electric field distribution. It is maximum at the junction and zero outside the depletion regions. d) The potential distribution within the depletion region.

The initial migration of carriers across the junction sets up a barrier for further migration. At the equilibrium there is not net current flow across the junction, so the barrier's height is self adjusted to avoid the flow of such current. The barrier's

value (the *built-in* potential) depends on the doping of the material. Assuming that the impurities concentration (both for donors in the n-side,  $N_d$ , and acceptors in the p-side,  $N_a$ ) is much higher than the intrinsic carrier concentration ( $N_a, N_d \gg n_i$ ), the value for the built-in potential is given by [61]:

$$V_d = \frac{kT}{q} \ln \frac{N_a \cdot N_d}{n_i^2} \quad (3.5)$$

Usually the built-in potential is of the order of few hundred millivolts.

At this point the depleted zone can be regarded as a detector. The charge created in the depleted zone by a traversing particle could be collected at the junction and read out. Charge created in the undepleted zone recombines with free carriers and is lost. Obviously, with wider depleted zones more charge from the crossing particle can be collected, increasing the amount of signal. The width of the depleted zone can be increased applying an external potential  $V_{bias}$  of the same sign as  $V_d$ . The barrier height would be then  $V_B = V_{bias} + V_d$ . We say that the junction is reverse biased.

The width of the depleted zone in both sides of the junction is a function of the applied bias voltage, as well as the dopant concentration. The width of the depleted region on the p-side and n-side can be expressed in the form [61]:

$$W_p = \sqrt{\frac{2\epsilon V_B}{qN_a(1 + N_a/N_d)}} \quad (\text{p side}) \quad (3.6)$$

$$W_n = \sqrt{\frac{2\epsilon V_B}{qN_d(1 + N_d/N_a)}} \quad (\text{n side}) \quad (3.7)$$

where  $\epsilon$  is the dielectric constant of the material.

Selecting the materials of the p-n junction in a such way that  $N_a \gg N_d$  the depletion region would be very wide on the n-side and shallow on the p-side. This is important because, to avoid problems related to electrons accumulation layers [61], silicon detectors are usually built on n-type silicon wafers, that serves as an active volume while the thin p-type layer is necessary only to deplete the active volume of free carriers.

### 3.1.4 Leakage Current

In p-n junction based detectors the background comes from thermally generated minority carriers. Under equilibrium conditions electron-hole pairs are generated everywhere in the detector. Due to the presence of the electric field in the depleted region, electrons and holes are separated and can not recombine, originating a current, usually referred to as *leakage current*. The leakage current has two sources: the generation current and the diffusion current.<sup>3</sup>

<sup>3</sup>In silicon detectors there is a third important background current, the surface current. Surface currents originate from the traps and defects that appear in the cut border, where the surface is

The generation current,  $j_{gen}$ , is caused by charge generated within the depletion zone. Assuming that the carriers density is very low ( $n, p \ll n_i$ ), the generation current is [61]:

$$j_{gen} = \frac{1}{2}q \frac{n_i}{\tau_0} W \quad (3.8)$$

where  $\tau_0$  is the effective lifetime of minority carriers within the depletion zone. This current is proportional to the width of the depletion zone,  $W$ , which is proportional to  $\sqrt{V_{bias}}$ . There is non explicit dependence on the temperature, but  $n_i$  depends on it exponentially. It is then important to keep the temperature constant for a stable operation of the detector.

The diffusion current,  $j_{diff}$ , comes from charge generated in the neutral silicon and diffusing to the depletion region. In the neutral region outside the depletion zone there is no electric field and electron-hole pairs created there recombine. However, if they are generated in the proximity of the depletion region, they diffuse into it before they recombine. Denoting by  $\tau_n$  and  $\tau_p$  the lifetime of electrons in the p-region and of holes in the n-region, and by  $L_n$  and  $L_p$  the corresponding diffusion length, respectively, the diffusion current densities for the electron and hole components can be expressed as [61]:

$$j_{diff,n} = q \frac{n}{\tau_n} L_n \quad (3.9)$$

$$j_{diff,p} = q \frac{p}{\tau_p} L_p \quad (3.10)$$

When the detector is fully depleted the measured leakage current reaches a plateau (Figure 3.4), where the main contribution to the leakage current comes from the generation current.

From Equations 3.8 and 3.9 we see that to keep the leakage current low the lifetime of minority carriers must be taken into account. Since the lifetime is regulated by generation and recombination processes of undesired impurity atoms, special care must be taken during the processing to keep the crystal clean<sup>4</sup>.

### 3.1.5 Silicon Resistivity and Junction Capacitance

The width of the depleted zone is related to the resistivity of the material. The resistivity is dominated by the concentration of the majority carriers. For n-type

---

heavily damaged. These defects act as source of free carriers that can be injected within the active part of the detector with the increase of the bias voltage. The pioneering work of Kemmer [55] showed that the surface leakage currents can be suppressed by using a passivating silicon dioxide layer.

<sup>4</sup>Impurity atoms create energetic levels in the middle of the forbidden gap [61]. These levels favor the transition of the carriers from the valence band to the conduction band and viceversa, thus increasing the rate of the electron-hole pair generation. In the presence of an electric field, the generated electron-hole pairs will be taken away one from each other suppressing the recombination with an increase of the leakage current.

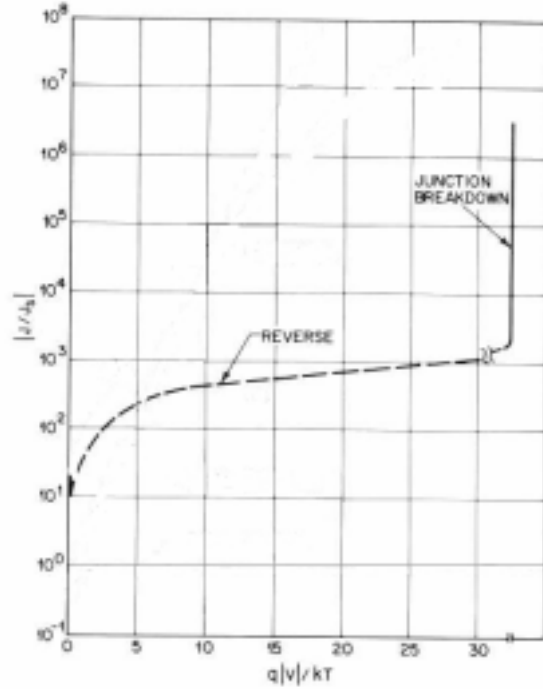


Figure 3.4: Current-voltage characteristic of a reversed biased p-n junction [61]. Current density is normalized with respect to the saturation current density.

material the majority carriers are determined by the concentration of donors  $N_d$ . Therefore, the resistivity can be expressed as [61]:

$$\rho = \frac{1}{q\mu N_d} \quad (3.11)$$

where  $\mu$  is the electron *mobility* [61] (Table 3.1). Substituting in Equation 3.7, we obtain for the width of the depleted region in the n side of the junction the expression:

$$W = \sqrt{2\epsilon\rho\mu V_B} \quad (3.12)$$

One sees that the higher the resistivity of the material, the lower biasing voltage is necessary to fully deplete a given thickness.

When the bias voltage changes, an associated charge appears on either side of the junction. Therefore, we can define a junction capacitance as:

$$C_j = \frac{dQ}{dV_B} = \frac{dQ}{dW} \frac{dW}{dV_B} \quad (3.13)$$

Differentiating Equation 3.7, we obtain:

$$\frac{dW}{dV_B} = \sqrt{\frac{\epsilon}{2qN_d(1 + N_d/N_a)V_B}} \quad (3.14)$$

The charge increment that appears on either side of the junction as a result of the widening of the depletion region is:

$$dQ = q \cdot N_d \cdot dW \quad (3.15)$$

Substituting equations 3.14 and 3.15 into equation 3.13 we obtain:

$$C_j = \sqrt{\frac{q\epsilon N_a N_d}{2(N_a + N_d)V_B}} \quad (3.16)$$

For the case where  $N_a \gg N_d \gg n_i$  this results in:

$$C_j = \sqrt{\frac{\epsilon}{2\mu\rho V_B}} \quad (3.17)$$

We see that the junction capacitance decreases by increasing the biasing voltage.

### 3.1.6 Noise

In silicon tracking detectors there is no charge multiplication, which makes the noise an specially important issue. The electronics and the detector itself contribute to the noise in different ways.

The electronics noise is a sum of a constant term, characteristic for a specific design, and a term which is a function of the detector parameters. To compare the amount of noise with the generated signal, the noise is usually expressed in equivalent noise charge (ENC). Therefore, the readout electronics noise can be expressed as:

$$ENC = A + B \cdot C \quad (3.18)$$

where  $A$  and  $B$  are constants terms which depend on the particular characteristics of the preamplifier, and  $C$  is the input capacitance, that comes mainly from the capacitance of the strip being read out to its neighbors and to the back plane (Figure 3.5). It causes a signal loss and acts as a load capacitance of the preamplifier. The constants  $A$  and  $B$  vary depending on the preamplifier.

Detector noise has two main contributions: one is due to the leakage current flowing through the junction, while the other contribution comes from the resistor biasing the microstrip (see Section 3.1.8). In ENC the contribution from the leakage current (known as shot noise) can be expressed as:

$$ENC = \frac{e}{q} \cdot \sqrt{\frac{qIt_p}{4}} \quad (3.19)$$

where  $e$  is the natural logarithm base,  $q$  is the electron charge,  $I$  is the diode leakage current and  $t_p$  is the peaking time, equal to the time between two samplings.

The contribution from the bias resistor (thermal noise) can be calculated as [61]:

$$ENC = \frac{e}{q} \cdot \sqrt{\frac{T_p \cdot kT}{2R}} \quad (3.20)$$

where  $k$  is the Boltzmann constant,  $T$  the temperature and  $R$  the biasing resistor.

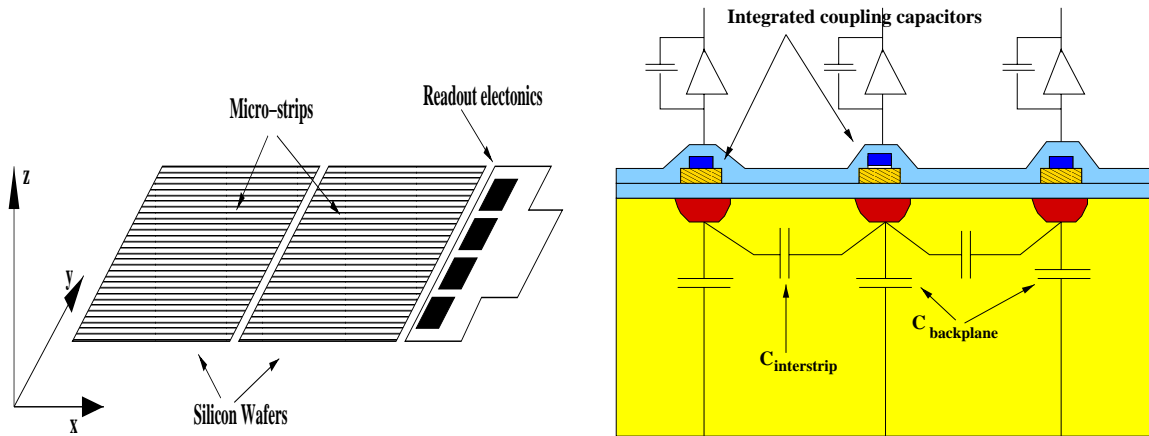


Figure 3.5: Left figure: schematic representation of a microstrip silicon detector. Right figure: first order equivalent scheme of a single sided microstrip detector.

### 3.1.7 Processing

Microstrip silicon detectors are manufactured with the planar process technique, originally developed by the microelectronics industry and actually used in large scale for the production of integrated circuits. Therefore, these techniques are extremely well developed and known [62, 63].

Silicon detectors are fabricated on high resistivity silicon wafers. The process originally described by Kemmer [55] is still the basis for most of the planar silicon detector processes used. Figure 3.6 describes the most important steps in the production of silicon sensors.

Usually the manufacturer receives selected silicon wafers cut into thin disks and polished. The most commonly used wafers are high resistivity n-type silicon (1-10 k $\Omega$ cm), 300  $\mu$ m thick and with lattice orientation  $\langle 111 \rangle$  to maximize the energy loss of the incident particles. Typical wafer size ranges from 4 to 6 inches [64, 65]. A polished surface is necessary for ease of alignment at photolithographic stages. The wafer faces must be parallel and flat to a high precision (30  $\mu$ m), to be able to print the fine geometries required.

Successive placement of patterns of dopant and metallization into and onto a wafer is the basic manufacturing procedure of a semiconductor detector. Photomasks are used to define a pattern. They are usually transparent plates with an opaque film forming the pattern. Plate materials are Quartz, boronsilicate glass or other types of glass. The plate is covered with a film of photoresist and the mask is generated by exposing the areas of the film to ultraviolet light, that when developed can be stripped off using chemicals. The remaining photoresist acts as an etch stop.

First, the wafers are oxidized at 1030° C (Figure 3.6 (b)). The oxide layer (SiO<sub>2</sub>) over the entire wafer acts as the final oxide for some parts of the wafer and also

protects the device from environmental contamination. Oxidation times are of the order of hours. The purpose of this oxide passivation, *i.e.* the growth of a thin silicon dioxide layer on the surface of the silicon wafer, is to terminate the silicon lattice at the surface with a high quality Si-SiO<sub>2</sub> interface, in a way that reduces the density of surface states, and thus suppresses the surface generation currents. With this process low leakage currents ( $\sim 1 \text{ nA/cm}^2$ ) can be obtained with a careful control and minimization of the successive high temperature treatments and maintaining an extreme purity throughout the process.

The desired detector geometrical layout is transferred onto the wafer surface using a photoresist and a mask with the corresponding pattern. In the process the photosensitive resist covering the wafer surface is patterned using the mask to expose parts of it to light, and subsequently etching away the parts of the resist thus selected. In the end the parts of the substrate film that are not protected by the resist are etched away.

In the next step, to produce the p-n junction and other implants in the surface where the oxide passivation layer has been removed in the previous step, impurity atoms are introduced into the lattice via ion implantation. With ion implantation the dopant atoms are ionized, then accelerated in an electric field to form a beam which is directed on the wafer, where the dopant atoms penetrate the silicon to a depth defined by their energy (10-100 KeV).<sup>5</sup> This procedure leads to destructive processes in the lattice of the wafer, that is annealed baking the wafer at temperatures ranging from 800 to 1000°C (Figure 3.6 (d)).

To provide electrical contact to the silicon, metallization of the implanted strips is required because the ultrasonic bonding used to form the interconnections with aluminum or gold wires is possible only on metals. Metallization is performed covering the device with vacuum evaporated metal. The desired metallization pattern on the surface is achieved by lithographic methods.

Finally the wafer is cut into the right size using a fast rotating diamond saw, where the blade can be as thin as 20  $\mu\text{m}$ .

### 3.1.8 Double Sided Silicon Microstrip Detectors with Integrated Coupling Capacitors

A single-sided strip detector measures the position only in one direction, perpendicular to the strips on the detector (Figure 3.5). Using the same detector, a second coordinate can be measured dividing the ohmic back side with n<sup>+</sup> microstrip implants. Comparing with other solutions (gluing together two single sided detectors with different microstrips orientations) this approach has the advantage of the re-

---

<sup>5</sup>There is also another method to introduce dopant impurities in the wafer, via the diffusion of the dopant atoms. In dopant diffusion the wafer surface is either exposed to a gas containing dopant atoms or covered by a film containing dopant atoms. If the temperature of the wafer is high enough, the dopant atoms will diffuse into silicon forming the doped region. Ion implantation is generally preferred because the better control of the process and lower temperatures involved.

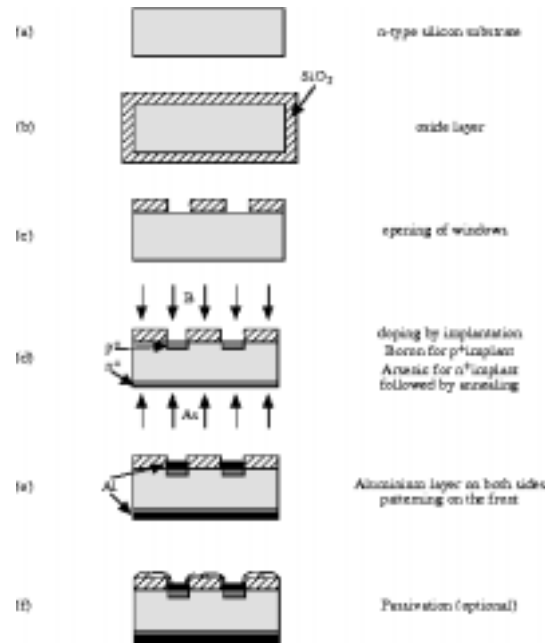


Figure 3.6: An example of detector manufacturing process according to Kemmer [55].

duced amount of material, and therefore less multiple scattering that ultimate improves the tracking resolution. On the other hand, double sided sensors are more difficult to manufacture. The two-sided lithography, alignment and handling of silicon wafers<sup>6</sup> is substantially more complicated and expensive. Another difficulty relates to the low  $\text{n}^+$  interstrip resistance due to an electron accumulation layer under the Si-  $\text{SiO}_2$  interface (Figure 3.8). Due to the positive charge always present in the silicon dioxide at the Si-  $\text{SiO}_2$  interface, the electrostatic attraction between the oxide charge and the electrons in the n-type bulk creates an electron accumulation layer close to the interface. This accumulation layer is so strong that it is practically impossible to make the depletion layer originating from the p-side to extend all the way to the interface on the n-side between the n-type strips. Thus, a conductive electron layer is left on the n-side surface between the strips even at full depletion. This electron accumulation layer connects the n-type strips to each other with a low resistance, destroying the position resolution on the n-side. An effective way to provide an effective strip separation is implanting additional  $\text{p}^+$  strips surrounding each  $\text{n}^+$  strip. In this way the conductive electron layer is broken and the  $\text{n}^+$  strips isolated.

The silicon strip detectors are typically read out using an amplifier with time-dependent filtering. In case the amplifier is connected in DC to the strip, during charge integration the amplifier reads not only the signals from ionizing particles, but also integrates the leakage current of the strip. Variations on the leakage current

<sup>6</sup>For a good review of silicon detectors fabrication techniques, see Reference [61].

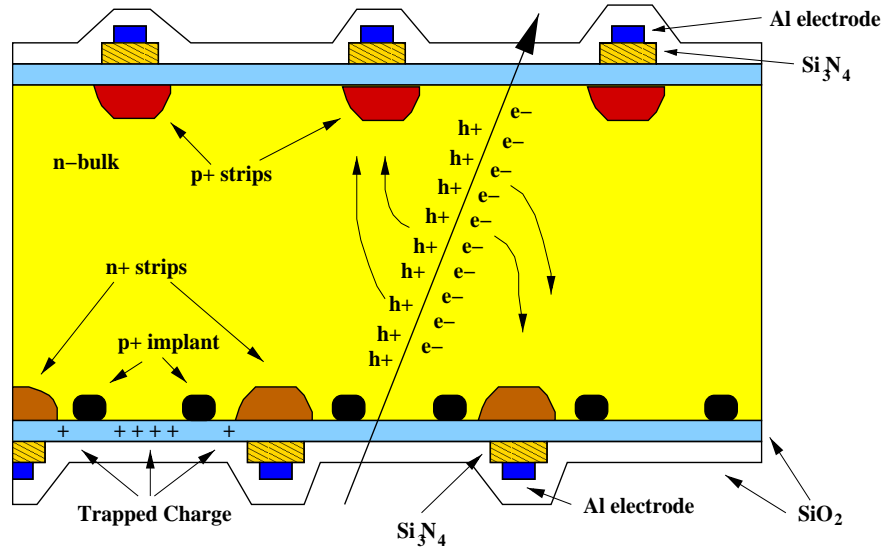


Figure 3.7: Schematic representation of the transverse section of a double sided microstrip detector with integrated coupling capacitors.

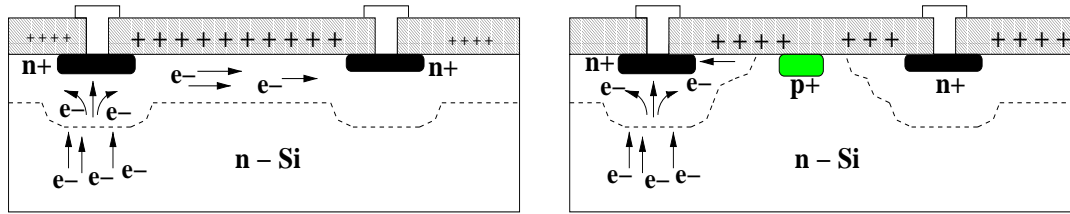


Figure 3.8: Left figure: the positive fixed oxide charge, introduced during the passivation step of detector production, attracts electrons, which form a conductive layer at the Si – SiO<sub>2</sub> interface, connecting the n<sup>+</sup> strips. Right figure: the introduction of intermediate p<sup>+</sup> strips disrupts the electron accumulation layer.

between strips can cause large pedestal variations between read-out channels, which is not convenient for further signal processing. This problem can be avoided by coupling the amplifier inputs to the strips capacitively. The capacitive coupling to the amplifier can be realized integrating the coupling capacitors directly on the detector wafers [66]. The read-out strips (Figure 3.5) can be covered by a thin insulating silicon dioxide layer, on top of which aluminum strips are fabricated. A coupling capacitor is thus formed between the n<sup>+</sup> or p<sup>+</sup> strip and the aluminum strip, the aluminum strips being connected to the readout electronics.

The microstrip bias can be done using polysilicon resistors. The value of the resistors should be high enough to make the time constant for signal spread to neighboring strips through the bias line large compared with the amplifier rise time. On the other hand, the strip leakage currents always cause a voltage drop in the bias

resistor, and the value of the resistors must be such that the variations expected in the leakage currents do not cause too high differences in the individual strip bias voltages.

### 3.1.9 Breakdown Phenomena

When the electric field inside the silicon bulk is increased above a certain value ( $30 \text{ V}/\mu\text{m}$  [61]) called the *breakdown voltage*, the free carriers may gain sufficient kinetic energy in their drift in the electric field to break covalent bonds in the lattice when they collide with them (*impact ionization*). Every carrier creates two or more carriers, which may accelerate and become themselves a cause for avalanching collisions, leading to a multiplication of carriers when the field is large enough. As a first consequence the leakage current together with the noise dramatically increases. The avalanches inside the silicon bulk deform the electrical field creating instabilities. For high enough currents the metal contacts can be severely damaged. For even higher currents, melting of the silicon bulk can occur with irreversible damage. Obviously, in silicon detectors the breakdown voltage must be much higher than the voltage needed to fully deplete the detector volume.

In localized regions of the sensor breakdown avalanches at voltages much lower than the breakdown voltage can take place (microdischarges [67]), specially in the corners of the microstrip implants<sup>7</sup>. Due to the curvature of the junction surface, very high local electric fields can be reached, and the breakdown voltage may be hundred times lower than in the bulk case. When microdischarge appears a sudden increase of the leakage current, together with burst noise (noise of large amplitude) is observed [67]. Technologically, this can be avoided in the metallization of the microstrip, placing the external electrode  $2 \mu\text{m}$  or more stepping back from the edge of the implant.

At the sensor's edge the electric field near the interface of the outer microstrips is almost perpendicular to the interface, creating a high gradient that locally reduces the breakdown voltage. To reduce the electric field at the sensor edge *guard rings* are used (Figure 3.9). Guard rings are implants surrounding the sensor's active area. They are left floating, and thus act as a voltage divider. By increasing the reverse bias, common MOS [61] punch-through conduction is established between the active diode and the guard, self-biasing the floating ring at an intermediate potential with respect to that of both sides of the junction. The depletion region reaches then the floating ring, acting as an equipotential region and spreads the depletion region to a wider area. In this situation the active microstrip has to resist the voltage difference with the ring, and the ring has to resist the remaining part of the applied voltage. The electric field close to the edges is thus decreased, and consequently the

---

<sup>7</sup>Microdischarges can also take place in the silicon bulk, in regions where the silicon resistivity is low, and therefore under bias the local electric field can reach very high values. Usually bulk regions with low resistivity are due to defects or impurities present in the silicon, and are a good criteria to judge about the quality of the used silicon.

avalanche breakdown voltage is increased.

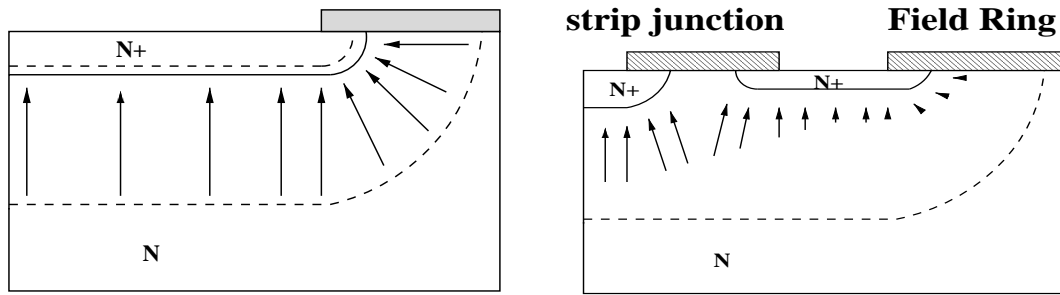


Figure 3.9: Schematic representation of the guard ring structure. Without floating guard ring (left figure) the electric field is higher at the edge of the microstrip implant due to the curvature of the junction surface. The floating guard ring (right figure) reduces the voltage drop, and the field gracefully decreases over a wider region [55].

## 3.2 The ISL Detector

An overall description of the ISL detector as a part of the CDF tracking system is given in Section 2.2.3. Below we describe in more detail the ISL sensors, the read-out electronics, the ISL ladders, and the global ISL mechanical support. We briefly discuss the expected radiation hardness of the silicon sensors and the SVX3 readout chip. The expected radiation length due to the ISL material is also reported.

### 3.2.1 Silicon Sensors

The ISL uses double-sided AC coupled microstrip detectors in high-resistivity n-bulk silicon with single guard ring (see Appendix A). Detectors have been provided by two different manufacturers: Micron Semiconductors Ltd. and Hamamatsu Photonics Cor. Micron has produced sensors with an active area of  $5.7 \times 7.5 \text{ cm}^2$  on 6" wafers [64], that allows the production of two sensors on each wafer. Hamamatsu used 4" high resistivity wafers.<sup>8</sup> Hamamatsu sensors have a slightly smaller area ( $5.7 \times 6.7 \text{ cm}^2$ ), and have been used for the innermost layers of the ISL.

Detectors have 512 strips per side with a pitch of  $112 \mu\text{m}$  on both sides. Micron sensors have the axial strips on the p-implant side and in the n-implant side they have a small stereo angle ( $1.207^\circ$ ). Hamamatsu sensors have the opposite structure. The implant strip width is chosen to be  $22 \mu\text{m}$  and the Al electrode width to be  $16 \mu\text{m}$  for Hamamatsu, and  $18 \mu\text{m}$  and  $14 \mu\text{m}$ , respectively, for Micron. The Al electrode width is made narrower than the implant width to reduce the electric field strength

<sup>8</sup>Hamamatsu does not provide double sided sensors on 6" wafers due to the wafer fragility when flipping the wafers [65].

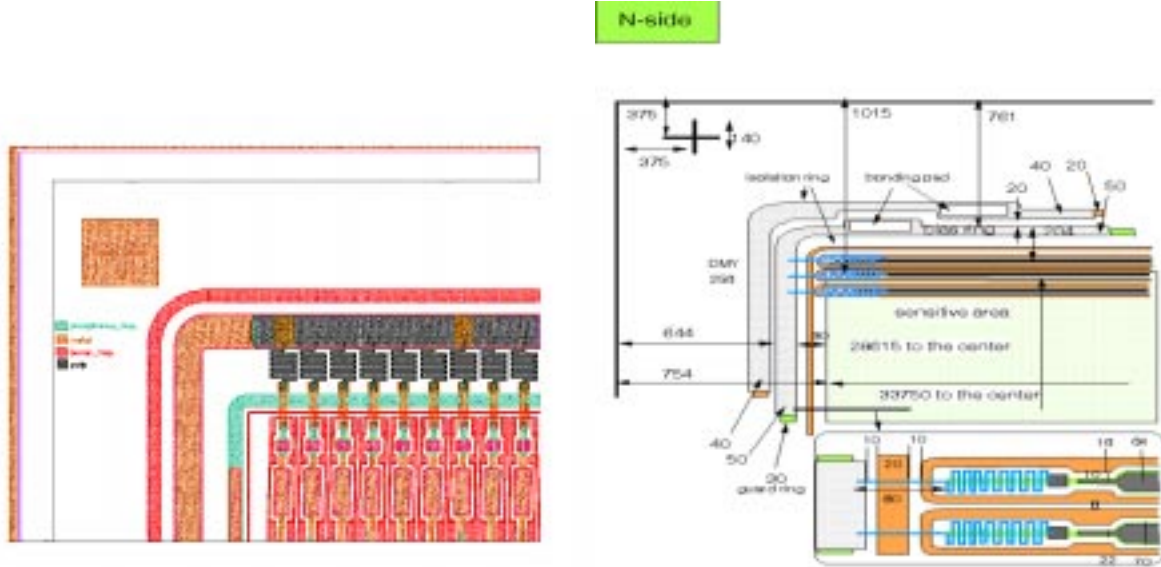


Figure 3.10: Left figure: mask for the n-side of Micron sensors. Right figure: mask for the n-side of Hamamatsu sensors.

through the bulk in the vicinity of the implant strip edges, which causes the micro-discharges [68]. Isolation of n-implant strips is obtained by using the “atoll” scheme with individual p-stops (Figure 3.10) that surrounds the  $n^+$  strips. The distance between different p-stop implants is  $8\text{ }\mu\text{m}$  while that between  $n^+$  and p-stop is set slightly wider,  $10\text{ }\mu\text{m}$ , to take into account possible error in mask alignment. The aim was to cover the gap with p-stop as much as possible, but without an excessively design that could affect the yield. The p-stops are not biased and remain floating. Bias is applied via polysilicon resistors. For the Hamamatsu sensors the resistors on the n-side (Figure 3.10) are designed to snake inside the p-stop implants. Thermal noise contribution from the bias resistors is proportional to  $\sim \sqrt{\frac{kT}{R}}$  (see Section 3.1.6). Thus, to minimize the noise, the goal is to have the highest possible bias resistors the company is able to reliably process. The requested value is about  $4\text{ M}\Omega$ .

The working depletion voltage is  $\approx 40\text{ V}$  with a breakdown voltage of coupling capacitors  $> 120\text{ V}$  to allow an increase of the depletion voltage if needed due to the radiation damage. Since the total ladder length is  $\approx 20\text{ cm}$  (3 detectors are bonded together) the required interstrip capacitance is  $\approx 1.0 - 1.2\text{ pF/cm}$  to keep the total capacitance low.

### 3.2.2 ISL Ladder

The basic ISL unit is the ladder. A ladder is composed of three silicon sensors which are bonded together to form a single electrical unit, and glued on a carbon fiber support (Figure 3.11). The readout hybrid is mounted off the silicon at one end

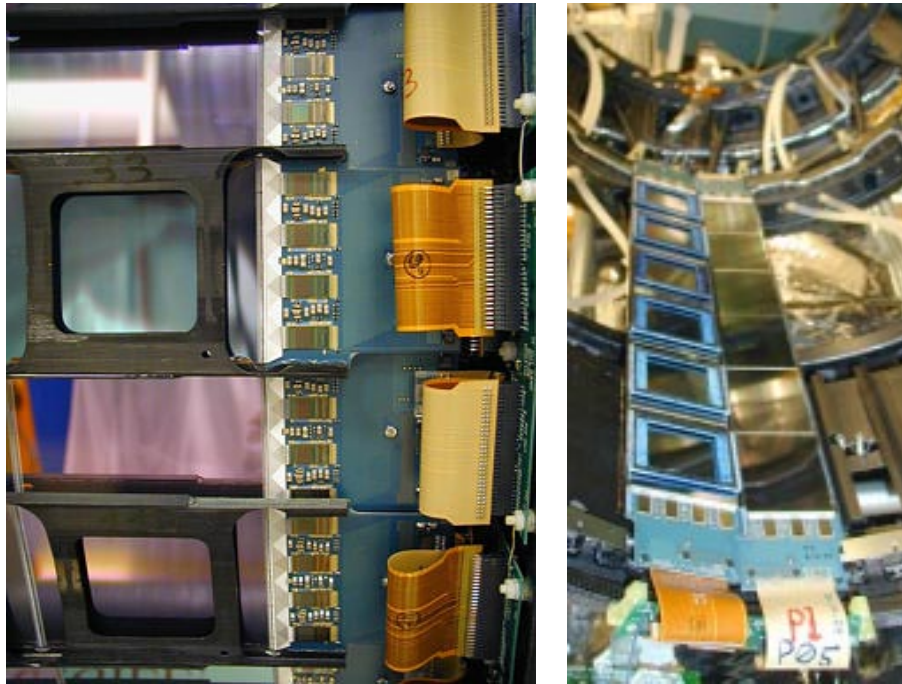


Figure 3.11: Left figure: view of fully assembled ladders installed in the ISL. Right figure: view of fully assembled modules installed in one of the two ISL external barrels.

and glued on the open edge of the support. The three sensors are aligned respect to a precision machined hole on the hybrid bulkhead. The holes on the body of the support (Figure 3.11) are for the assembly jig towers and for the microbonding machine. Full torsional rigidity of the ladder is reached after sensor gluing. To reduce any possible noise due to the electromagnetic coupling between the silicon sensors and the carbon fiber support (antenna effect) in the gluing region, where the two surfaces are separated only by  $\sim 100 \mu\text{m}$  of glue, insulating kapton is inserted between the silicon sensors and the support in the glued region.

Two ladders are paired to form a module ( $\approx 55$  cm long, see Figure 3.11) that is directly mounted on the space frame. In total more than 900 large area double-sided silicon detectors have been mounted on 296 ladders, with a total active area of  $\approx 3.5 \text{ m}^2$  (300,000 channels).

### 3.2.3 Read-out Electronics

The silicon sensors are read out by the SVX3 chip [45], a custom radiation hard integrated circuit (IC) device. It is fabricated in the  $0.8 \mu\text{m}$  bulk CMOS Honeywell process. It has 128 parallel analog inputs and an 8-bit digital output bus. Each channel (Figure 3.12) contains a preamplifier, an analog delay pipeline, an ADC (8 bits), and data sparsification logic. To avoid trigger deadtime, the SVX3 chip has been designed to work in a continuous (deadtimeless) mode, being capable of

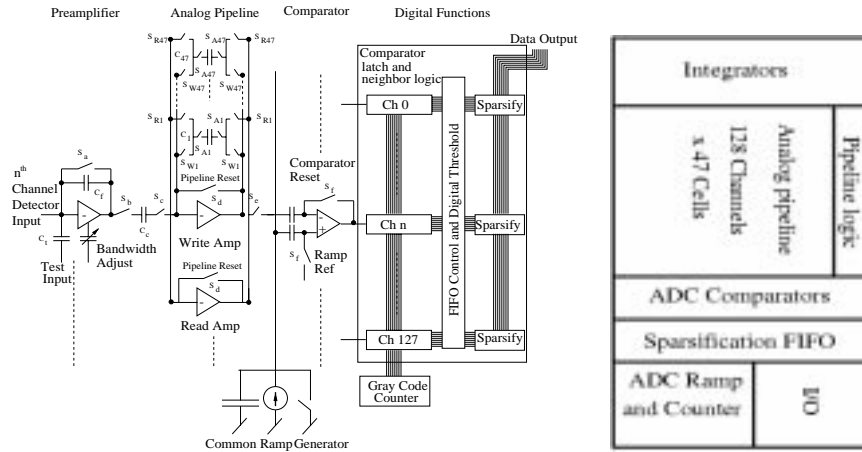


Figure 3.12: Right: SVX3 simplified single channel block diagram. Left: physical layout of the SVX3 chip [70].

performing simultaneously signal acquisition, digitization, and readout. The IC analog and digital parts are placed in the same crystal: the *Front-End* for the analog functions (signal acquisition), and the *Back-end* for the digital functions (signal digitization and readout through the bus).

### Front-End

Every channel contains a charge sensitive preamplifier and an analog storage pipeline. The pipeline is dual ported for simultaneous read and write operation, and consists of a write amplifier, a read amplifier and 47 identical storage cells. The preamplifier can handle strip capacitances ranging from 10 to 35 pF and is able to work with positive or negative signals to handle double-sided detectors. These two parameters are digitally programmable. The total gain is 15 mV/fC, corresponding to a signal of 60 mV for a minimum ionising particle (MIP). The typical noise is  $ENC = 500 + 60 \text{ e/pF rms}$ . Strip's charge is acquired every 132 ns (the Tevatron bunch spacing), and a voltage level proportional to the charge is stored in the one of the cells of the pipeline. Since the Level 1 trigger latency is  $5.5 \mu\text{s}$  (See Section 5.1), 42 bunch-crossing deep pipeline<sup>9</sup> is enough to avoid dead-time at Level 1 trigger. When a Level 1 trigger is issued, a pointer identifies the corresponding cell<sup>10</sup>, this cell is marked and skipped until the contents are transferred to the *Back End*. Up to 4 pipeline cells marked by Level 1 trigger can be queued for digitization and readout. The preamplifier is provided of an input capacitor for calibration purposes.

<sup>9</sup>Indeed, the pipe line is 47 cells deep. 42 cells for the Level 1 trigger latency, 4 for the storage of cells selected by Level 1 trigger until the digitization and readout is initiated in the *Back End*, and one more cell where to store the common pedestal for Dynamical Pedestal Subtraction

<sup>10</sup>The delay between the Level 1 trigger accept signal and the corresponding acquired bunch can be set digitally.

### *Back-End*

In the *Back-End* every channel has its own Wilkinson-type analog to digital converter (ADC)<sup>11</sup> with 8-bit resolution, data sparsification logic, a readout FIFO, and differential output drivers. In the digitization, common mode (pedestal) subtraction in real time, known as Dynamic Pedestal Subtraction (DPS), can be performed.

DPS is implemented by starting a digital counter when a certain number of channel comparators have gone high. This number is referred to as the DPS threshold. If sufficiently many channels do not carry signal, *i.e.*, are at pedestal, the counter will be started somewhere near the pedestal level, setting the zero point of the digital scale at that level. The effect is that the pedestal level will be subtracted from the measured signal.

The motivation for subtracting the pedestal level is that many contributions to noise, for example electromagnetic pickup, can influence all channels on a chip collectively, as common mode noise. In CDF the only way to subtract this noise is to do it on the chip, since pedestal information is lost when data is read out in sparse mode.

Data sparsification logic works by reading out only the digitized charge of channels carrying a digital signal above a sparsification threshold and, optionally, their neighbors. The purpose of sparsification is to keep the readout time down.

### 3.2.4 Hybrids

The ISL hybrid (Figure 3.13) is double sided and hosts eight daisy chained SVX3 chips (four in each side). Since the SVX3 chip has been designed to match the pitch of the SVX II detectors ( $60\ \mu\text{m}$ ), a pitch adapter is mounted on the hybrid to match the ISL pitch ( $112\ \mu\text{m}$ ). The cables connecting the hybrids to the DAQ system are about 1 m long oriented along the  $z$ -axis. To avoid problems in signals amplitude and sincronization, a transceiver chip is mounted on the hybrid.

The hybrid is made on a substrate of Aluminum Nitride (AlN), because of its rather large thermal conductivity that helps the cooling of the sensors [71] (Table 3.2), and its thermal expansion coefficient, very close to the silicon. Each hybrid side has the same number of layers. The basic structure is:

<i>Power plane layer:</i>	gold
<i>Ground plane layer:</i>	gold
<i>First trace layer:</i>	gold
<i>Second trace layer:</i>	gold
<i>Solder pads layer:</i>	mixture of platinum/palladium/gold to resist attack of solder.

For each of these metal layers there are also insulation layers in between and via

---

<sup>11</sup>Typical gain with no input load  $\approx 1/697$  ADC count/electron.

layers to make interconnections. In total, there were 20 layers of artwork<sup>12</sup> per side (total of 40) used in the process. The traces were 100  $\mu\text{m}$  wide with 100  $\mu\text{m}$  of interspace.

AlN	150-170 W/m °C
Al <sub>2</sub> O <sub>3</sub>	35 W/m °C
BeO	250 W/m °C

Table 3.2: Thermal conductivity of materials commonly used for hybrid substrate.

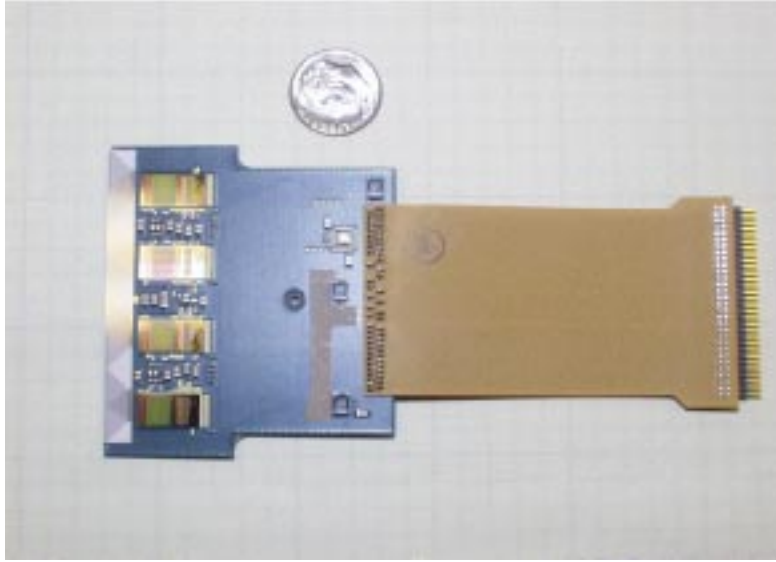


Figure 3.13: Upper side of the ISL hybrid, with the four SVX3 chips hosted and the pitch adapter placed in front of them. The precision machined hole can be seen in the middle of the hybrid. The transceiver chip (in the picture seen in white) is located on the hybrid, near the upper corner of the connection pig-tail (in the picture seen in white). For the scale, a U.S. quarter dollar coin is shown in the picture.

Hybrids were manufactured with the *thick film process*.<sup>13</sup> The design of the circuit is reproduced in a photomask, a thin plastic film with the patterns. A fine metal mesh ( $\sim 250$  wires per cm) is stretched over a metal frame and coated with a photosensitive filler. One screen per artwork layer is required. The screens are exposed to the photomasks and developed. In places where are features the filler

<sup>12</sup>In the microelectronics industry, the artwork refers to the original pattern or configuration produced at an enlarged ratio, from which a circuit product is made, using a technique of photographic reduction to achieve microelectronics scale.

<sup>13</sup>The process is called *thick* because the layers are about 15-30  $\mu\text{m}$  thick each, as opposed to the *thin film process*, where the layers are around 1  $\mu\text{m}$  thick.

goes away. The screen is aligned to the substrate and a special paste is spread on the screen and forced through with a hard rubber squeegee. The paste follows the pattern of the artwork. The paste is a mixture of glass powder, metal powder, and organic binders. For insulator layers the metal powder is not used. This procedure is repeated for every substrate. The parts are then dried at around 150° C to remove the binder and then passed through a furnace on a metal belt. In this furnace they enter various temperature zones up to 850° C. After that they are cooled and the metal and powder hardens. This binds them to the substrate or to the previous layer. This process is repeated over and over until the entire part is built up.

### 3.2.5 ISL Data Acquisition System

The ISL Data Acquisition System (DAQ) is essentially identical to that for the SVX II. It consists (Figure 3.14) of a Port Card (PC), High Density Interconnectors (HDI, Copper/Kapton laminate cables), Dense Optical Interface Modules (DOIM), a Fibre Interface Board (FIB), VME Readout Buffers cards (VRB), and the Silicon Readout Controller (SRC) which communicates with the CDF Trigger Supervisor system (TS).

All of the SVX3 chips from two complete ISL wedges (sectors of 30°) are connected to a Port Card by means of the HDI connectors. The functions of the Port Card are to initialize, generate the control levels and readout the SVX3 chips. It provides regulated power supplies for the analog section of the chip and digital-to-analog converters to generate calibration voltages of the SVX3 chip preamplifier. It also implements the decodification of the FIB commands that are sent to the chips. On the Port Card the digital signals from the chips are converted into optical signals in the DOIM at a rate of 53 MHz, and at each Level 1 trigger accept, the data is sent to one of the FIB boards. The FIB multiplexes the readout data onto a high speed optical link (G-Link) operating at 1.5 GHz. The data are sent to VME Readout Buffer, a VME module that holds the data while the Level 2 trigger decision is made. When a Level 2 trigger accept is received, the data is further sent to the Level 3 trigger at a maximum output rate of 50 Mbytes/sec. The control, timing and execution of all these commands is controlled by the Silicon Readout Controller, that implements the interface with the CDF Trigger Supervisor and the CDF master clock.

### 3.2.6 Space Frame

The ISL Space Frame (SF) is the mechanical structure that defines the location of the ISL detectors. It supports the silicon micro-vertex trackers SVX II, Layer 00, and the beryllium beam pipe. It is described in detail in Reference [69]. The aim of the SF is to provide a stable and stiff supporting structure with high precision features, able to position the ISL detectors within  $\Delta R/R \leq 2.5 \cdot 10^{-4}$  (where  $R$  is the radius from the beam line). A mechanical stability of few microns must be assured over the period

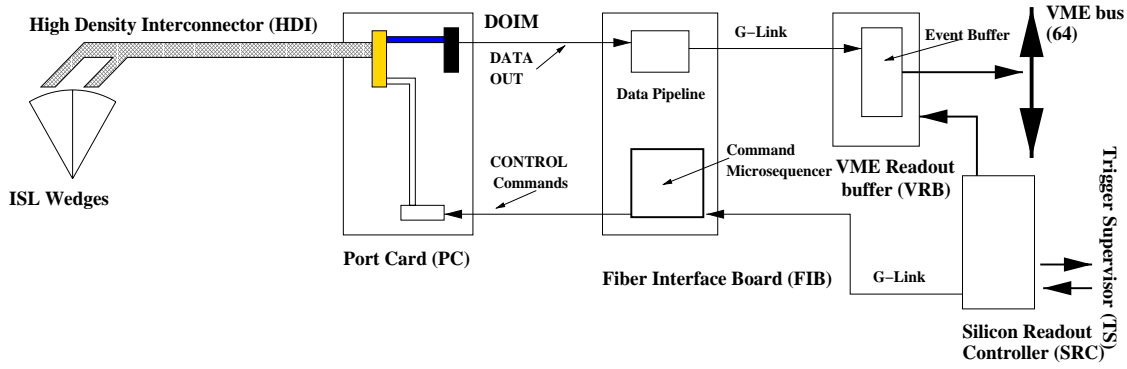


Figure 3.14: Schematic of the ISL data acquisition system.

of one Tevatron fill. The total load of the support is  $\sim 460$  N. The mass of the ISL itself contributes with  $\approx 16$  kg, the SVX II with  $\approx 25$  kg, the Layer 00 with  $\approx 1$  kg, and the beryllium pipe with  $\approx 5$  kg. In addition, thermal gradients of 25 K between the ladders support and the SF structure must not influence the positioning of the ISL ladders. Housing space for cooling services, electronics, cabling and alignment devices is provided without compromising easy access and maintenance. To reduce the total SF mass and avoid secondary interactions with the supporting material, the SF structure has been built with composite carbon fiber (CF), with density  $1.91 \text{ gr/cm}^3$  and 25 cm of radiation length  $X_0$ .

Due to the layout of the ISL the supporting structure is formed by three independent parts. Figures 3.15 and 3.16 show the SF layout. We can distinguish two half SF (each made of four flanges) connected by a central part (spool piece). In the central flanges two layers located at different radii are anchored. All flanges are connected together by struts, and the junction of each strut has been optimized using special CF joints. The SF is externally enclosed by two cylindrical CF shells (1 mm thickness) fastened to the flanges to increase the bending and torsional stiffness of the whole structure.

The flanges are hollow CF ring structures carrying high precision parts that define the ISL layers geometry (ledges). At each flange, the ledges seat at two different radii (external and internal) to allow sensors overlap at the edges. The ledges are rectangular thin beryllium plates (14.5 mm high, 50 mm large and 1 mm thick) with a slot in the middle. The hybrid is attached with a special pin to the ledge. The ledge machining accuracy is guaranteed to be within  $10 \mu\text{m}$  of the nominal value. Aluminum pipes of 4.5 mm diameter are glued to the ledges to provide the necessary cooling system.

Different types of glue have been used. For the flanges assembly, and ledge to flange gluing, epoxy glues with high Young module have been used [69]. For the cooling pipes gluing, an epoxy glue with low Young module have been used to avoid the effect of thermal stresses.

The cooling system has been projected to carry out up to 1.5 kW and keep

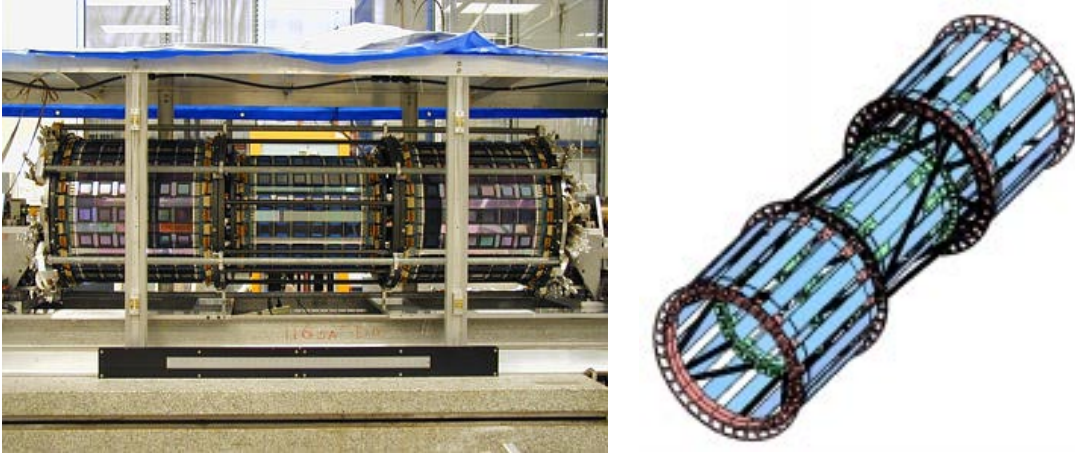


Figure 3.15: Left figure: The fully instrumented ISL detector at the Fermilab Silicon Detector Laboratory previously to its insertion in the CDF detector. Right figure: Isometric view of the ISL detector. Only every second module is shown.

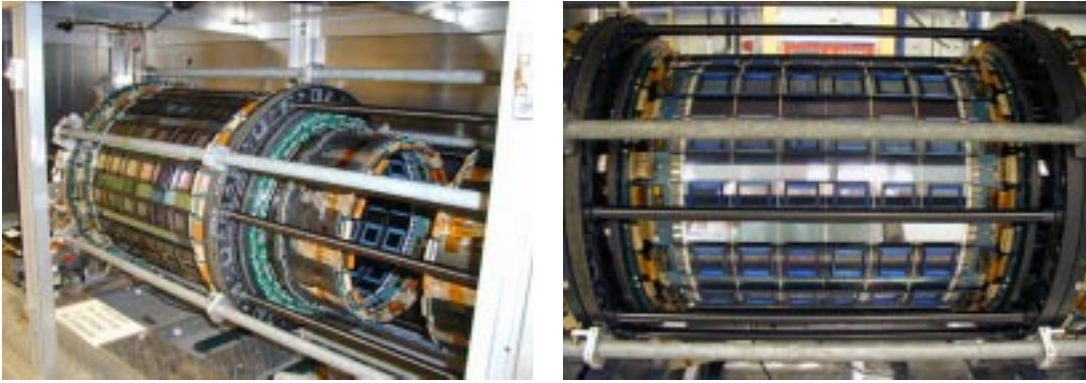


Figure 3.16: View of the ISL detector during the assembly process. Left figure shows the internal layer of the one half of the Space Frame with all the modules installed. Right figure shows the central barrel with all modules mounted.

the silicon sensors temperature below  $20^{\circ}\text{C}$  [69]. A mixture of water and 30% of ethylene glycol flows at 0.6 l/min. The whole system is designed to operate at sub-atmospheric pressures.

### 3.2.7 Radiation Hardness

The ISL sensors are located outside the SVX II detectors, and therefore the flux is modest. At 20 cm of the pipeline, ISL sensors are expected [72] to receive  $5 \times 10^{12}$  protons/cm<sup>2</sup> or 0.15 Mrad after a data collection corresponding to  $30\text{ fb}^{-1}$ .

Radiation can cause damage by two mechanisms. It can break atomic bonds (ionization) creating free charge that can accumulate in electrical insulators, or it can scatter off atomic nuclei giving rise to defects in crystal lattices (the so called

NIEL losses, see Section 3.1.1).

The first type of radiation damage (known also as surface damage) is specially relevant for MOS devices, where the radiation can create surface charge trapped in the dielectric layers of the devices, deteriorating its performance. Due to the interest of the microelectronics industry the surface damage has been intensively studied, and to a certain extent can be controlled by proper design and manufacturing process.

The bulk damage due to NIEL losses is specially relevant for silicon detectors.<sup>14</sup> The defect states create energetic levels in the middle of the gap between the conduction band and the valence band.<sup>15</sup> In the active region of the detector these levels act as a generation-recombination centers, reducing the average lifetime of the charge carriers, and thus increasing the reverse leakage current (see Equation 3.5). In general, the increase of the leakage current increases the shot noise contribution to the readout electronics.

For high enough fluences the bulk type can change. The originally n-type substrate will turn into p-type. This phenomena is known as *type inversion*. The defects created in the crystal lattice due to the recoiling atomic nuclei leads to the creation of vacancy complexes in that act as acceptors, effectively changing the original n-type silicon to p-type. The fluence for which type inversion occurs heavily depends on the initial donor concentration of the substrate. In a period after irradiation a reduction of the bulk acceptors defects occurs. It is the so called *beneficial annealing*. However, in larger time scale, a second phase of the annealing process appears (*reverse annealing*). In the reverse annealing, the concentration of acceptor defects increases with time, at a rate heavily dependent on temperature<sup>16</sup>.

Another effects of the bulk radiation damage are the reduced interstrip isolation, that leads to a loss of precision, and the reduction of charge collection due to charge trapping in the created defects, that decreases the signal amplitude.

ISL sensors response to radiation has been studied exposing them to  $\gamma$  rays from a  $^{60}\text{Co}$  source (surface damage), 63-MeV protons with  $(2 - 8) \times 10^{12}$  fluences (bulk damage), and 8 GeV protons. The total dose was about 0.5 Mrad, well above the expected dose of 0.15 Mrad.

Figure 3.17 shows the  $I$ - $V$  curves of three different quality Hamamatsu sensors before and after irradiation to  $\gamma$  rays and protons. Although the initial  $I$ - $V$  characteristics are different, they are identical after the irradiation with 0.2 Mrad of  $\gamma$  rays. Effects of surface charge accumulation through the  $\gamma$  irradiation dominate over the individual difference observed at pre-irradiation. After  $30 \text{ fb}^{-1}$  of integrated lumi-

---

<sup>14</sup>Bulk ionization damage is not relevant, because the created electron-hole pairs can easily recombine.

<sup>15</sup>n-type materials create energetic levels very near to the bottom of the conduction band, from where electrons can easily “jump” to the conduction band and be charge carriers. For the p-type material additional levels are created very near to the top of the valence band, with the same effect for the holes. Levels at the middle of the gap reduces the effective value of the gap, and therefore facilitates the recombination and creation of new hole-electrons pairs, reducing the charge carrier average lifetime. See Reference [61] for a more detailed explanation.

<sup>16</sup>Saturation can take many years at  $10^\circ \text{C}$  or weeks at room temperature.

nosity ( $5 \times 10^{12}$  protons/cm<sup>2</sup> of neutron equivalent fluence), total leakage currents of the order  $\sim 100 \mu\text{A}$  are considered acceptable [73]. All the three tested sensors met this requirement, and even for thrice higher fluences the leakage current does not exceed  $700 \mu\text{A}$ .

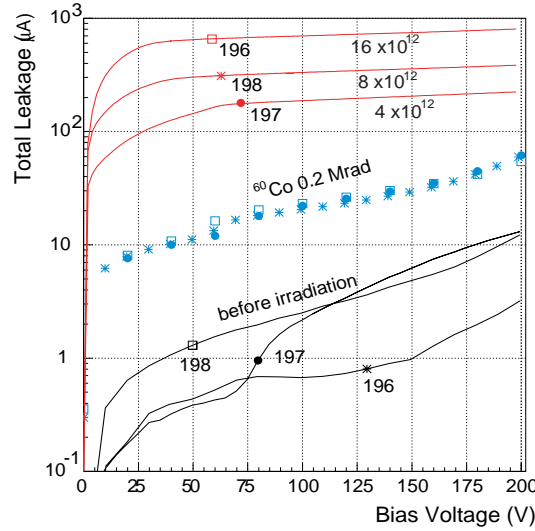


Figure 3.17: From Reference [72].  $I$ - $V$  curves of three Hamamatsu sensors (labeled as 198, 197, and 196) measured before, 3 days after 0.2 Mrad of irradiation with  $^{60}\text{Co}$   $\gamma$  rays, and 4 months after been irradiated with protons at an equivalent neutron fluence of 4, 8, and  $16 \times 10^{12} \text{ cm}^{-2}$ . Sensor 196 is considered good quality sensor. Sensor 197 has one very leaky strip and shows micro-discharges at  $\sim 75 \text{ V}$ . Sensor 198 has some clusters of leaky strips.

The interstrip capacitance is affected by radiation-induced charge accumulation in the oxidation layer. Figure 3.18 shows the p-side interstrip capacitance for Micron sensors measured after  $^{60}\text{Co}$   $\gamma$  irradiation. An increase of roughly a 50% is present on all of the measurement. Such increase can be addressed to the large amount of positive charge trapped on the oxide. The fast annealing of such charge [74] is responsible for the last measurement, performed with one day delay after the 1 Mrad dose, where only a 10% increase is observed. On the  $n$ -side the accumulation layer effectively interconnects the strips, and hence higher bias voltages are necessary to minimize the interstrip capacitance. Figure 3.18 shows the interstrip capacitances on the  $n$ -side and p-side of Hamamatsu sensors. The  $n$ -side bias voltage is effectively shifted by  $\sim 5 \text{ V}$  in the  $n$ -side.

Noise measurements on the Micron proton irradiated sensors are shown in Figure 3.19. The increment is well inside the 10%.

Finally, the dependence of the depletion voltage with proton irradiation was investigated. The depletion voltage initially decreases with proton radiation since the radiation-induced defects acts as donors, and the initial acceptor impurities are

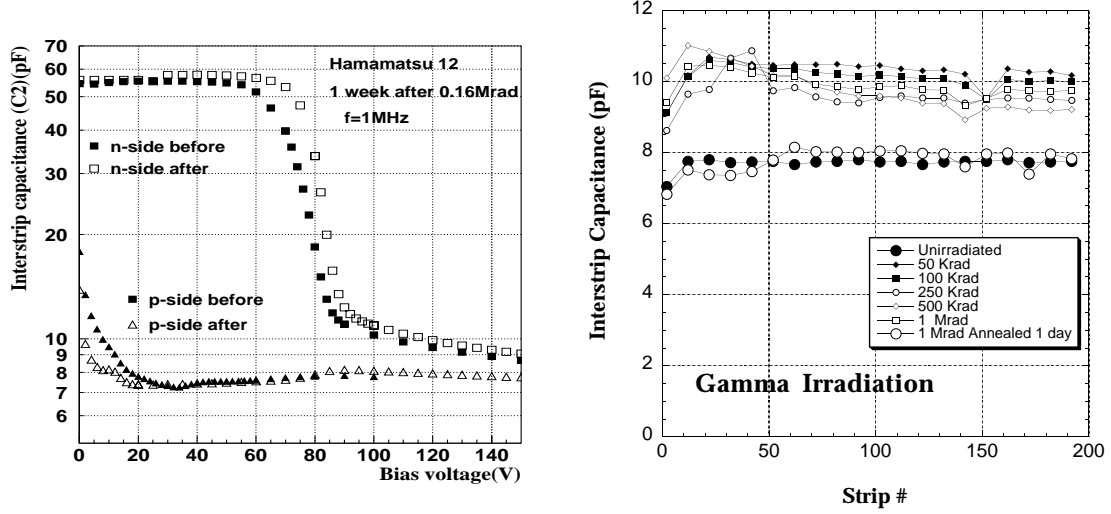


Figure 3.18: From Reference [72, 73]. Left figure: Interstrip capacitance of Hamamatsu sensor measured before and after irradiation of 0.16 Mrad of  $^{60}\text{Co}$   $\gamma$  rays. Right figure: Interstrip capacitance on the p-side of Micron sensors before and after  $\gamma$  rays irradiation.

partially canceled with defects. Above certain radiation level, the initial n-type bulk is inverted into p-type bulk. Figure 3.19 shows the full depletion voltages<sup>17</sup> for Hamamatsu sensors with initial depletion voltage of 80 V. The overlaid curves are predictions of the depletion voltage based in the evolution of the effective impurity concentration with the fluence [75].<sup>18</sup>

The dose that the detectors will face during Run-II data taking is much lower than the used in these studies, and therefore all the observed variations are completely acceptable.

The SVX3 chip was also been tested for radiation hardness exposing it to doses up to 3.5 Mrad of  $^{60}\text{Co}$   $\gamma$  rays [76]. After irradiation the tested chips continued to work at full speed. Only minor changes were observed: a rise in the gain of  $\sim 15\%$  due to a slow-down of the ADC ramp that could require tuning of the pedestal level for the DSP, and an increase of the noise level of  $\sim 20\%$ .

<sup>17</sup>Full depletion voltages are determined from  $C$ - $V$  curves.

<sup>18</sup>The full depletion voltage (see Equation 3.6) depends on the effective concentration of impurities. The effective impurity concentration can be parametrized as a function of the fluence, and the initial donor concentration  $N_D$  in the form [75]:

$$N_{eff}(\Phi) = N_{eff}(0) - N_D \cdot (1 - e^{-c \cdot \Phi}) - (g_c + g_Y) \cdot \Phi \quad (3.21)$$

where  $\Phi$  is the fluence and the parameters  $g_Y = 5.8 \cdot 10^{-2} \text{ cm}^{-1}$ ,  $g_c = 1.15 \cdot 10^{-2} \text{ cm}^{-1}$ ,  $c = 0.96 \cdot 10^{-13} \text{ cm}^{-2}$  are taken from Reference [75].

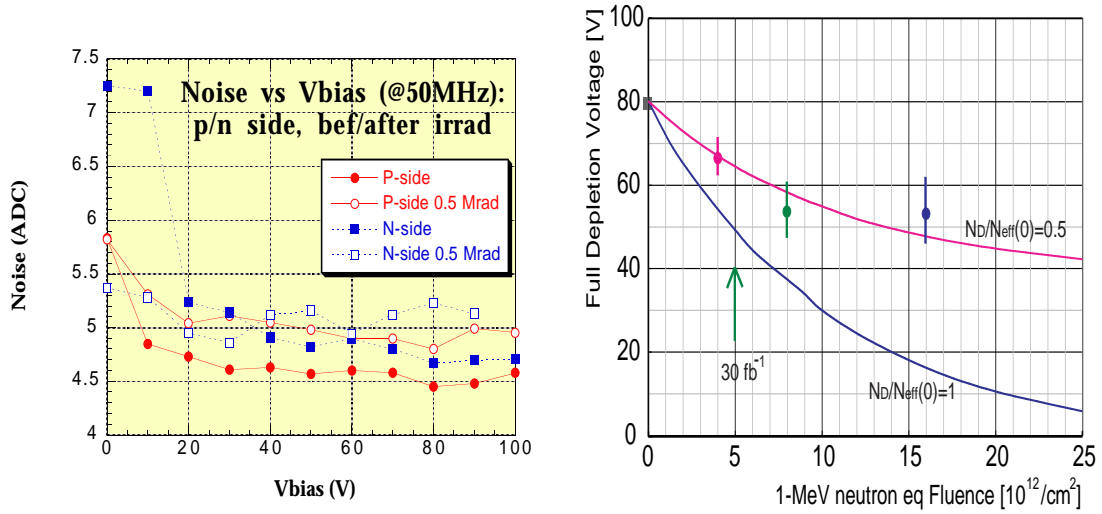


Figure 3.19: From Reference [64, 72]. Left figure: Micro sensors noise measured before and after 8 GeV proton irradiation. Right figure: Full depletion voltage of 63 MeV proton irradiated Hamamatsu sensors as a function of the equivalent (1 MeV) neutron fluence (dots) and the predicted assuming a complete removal of the initial concentration of donors (blue line), and assuming the removal of only half the initial concentration of donors (violet line).

### 3.2.8 ISL Radiation Length

The CDF's Run-II silicon system represents an average of more than 10% of a radiation length for normal incident particles [77]. For the ISL its contribution have

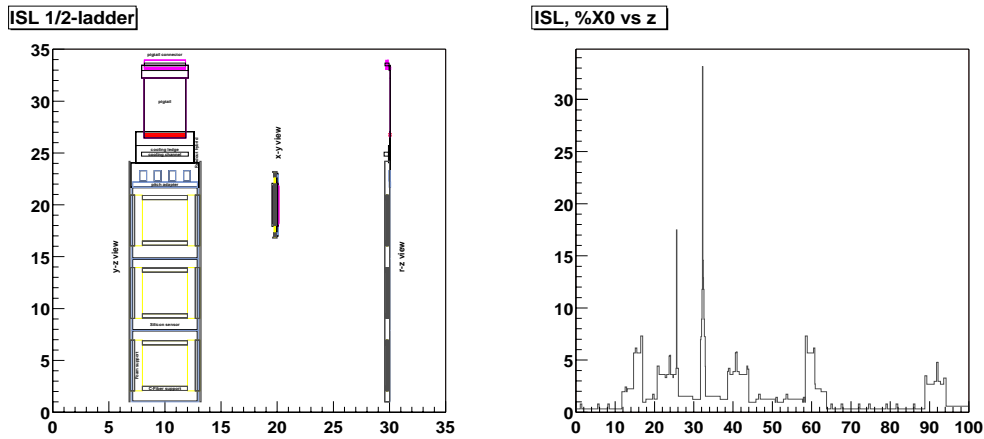


Figure 3.20: From Reference [77]. Left: views of an ISL half-ladder. Axis coordinates are in cm. Right: percentage of a radiation length traversed by a normally incident tracks in ISL plotted as a function of the z-coordinate.

been estimated [77] using artificially generated particle tracks at normal incidence angle. Figure 3.20 shows the percentage of a radiation length traversed as a function of the  $z$  coordinate. The regions where  $X_0 \approx 0.5\%$  are the silicon only regions in which a single layer is traversed. The regions where  $X_0 \approx 1\%$  are the silicon only regions in which two layers are traversed. The regions with  $X_0$  between 3 and 5% are the readout hybrids. The large spikes are due to the pins in the hybrid's connectors.

# Chapter 4

## ISL Ladder Electrical Characterization Tests

ISL modules are built in three stages: hybrid and silicon sensor manufacturing, ladder construction, and module assembly. To build a ladder, three double sided sensors together with the readout hybrid are glued on a carbon fiber support. By means of ultrasonic microbonds the three sensors are serially chained, and connected to the hybrid placed at one edge [78].

At the silicon detector facilities of the Istituto Nazionale di Fisica Nucleare (INFN) of Pisa (Italy), the sensors, hybrids and carbon fiber supports were received from the manufacturos. At the laboratory facilities half of the total number of ISL ladders were assembled, fully instrumented, and after a series of performance tests sent to the Fermilab National Accelerator Laboratory (FNAL) for its final insertion into the ISL detector.

Upon arrival all the components are tested (the sensors are visually inspected, and the hybrids tested for normal readout operation readout). Tests are also performed at each construction stage to ensure the delivery of the full ladder functionality. They basically consist in the detection of broken coupling capacitors (pin-holes) produced in the microbonding process, detection of anomalous electrical couplings, readout channel integrity tests with an infrared laser, which allows to verify the whole detector chain and, finally, a 72 hours burn-in test aimed to detect latent defects appearing shortly after the beginning of the device operational life.

After testing, each ladder is graded in terms of channel occupancy *versus* signal efficiency. For selected ladders, signal to noise ratio measurements with a  $\beta$ -source were also performed.

In this Chapter we describe the different electrical tests to characterize the ladder, as well as the experimental setup specially developed for these tests. A summary of the results is also given.

## 4.1 Components

The active elements of the ISL ladder are three doubled sided sensors and a hybrid, all of them glued on the carbon fiber support.

- *Sensors.* All the sensors used at the INFN are produced by Micron [79]. Sensors are tested by the manufacturer<sup>1</sup>. In particular, the sensors are visually inspected under microscope for damages. The leakage current and the microstrip capacitance is measured for biases voltages up to 100 V. Every sensor is delivered together with a list of defective channels and the measured value of the full depletion voltage. A microstrip is considered defective in the following cases:
  - Microstrips with broken coupling capacitors (*pin-holes*).
  - Shorts between adjacent microstrips.
  - Broken microstrips, where the Al contact or the implant is interrupted.
  - Microstrips with large leakage current. A microstrip is considered to draw unacceptable high leakage current if it drains more than 100 nA at  $V_{bias} = 80$  V.

Sensors are accepted only if the number of defective channels in one single side is less than 3% of the total, and if the total number of channels with defects does not exceed 2%.

- *Hybrids.* Hybrids are built and fully tested at the Berkeley Lawrence National Laboratory (California, USA). Upon receipt at Pisa, they are tested again to verify that no damage occurred during shipping. The tests must confirm that the hybrids reads out properly with acceptable pedestals, noise and differential noise (see Section 4.3). The hybrids are accompanied with a *traveler* with measurements of average and instantaneous pedestals, noise, and gain for all readout channels.
- *Ladder supports.* Upon receipt from the manufacturer, a thin film of kapton is glued in the zones with direct contact with the sensors, to avoid electrical connection.

The silicon sensors and readout electronics are very fragile components, both mechanically and electrically. Any mechanical stress such as vibration, improper bend, crash or strong air flow can break or unbond the microbonds. Hybrids and readout chips are devices very sensitive to extremely small amounts of charge. Ambient electrostatic phenomena can easily burn out the circuits. Air dust, deposited on the electrical components, can short the power lines with the consequent device

---

<sup>1</sup>See Appendix A for a detailed list of ISL sensor specifications.

malfunction. Ambient humidity must be kept also under control because some insulators can acquire non-negligible conductivity absorbing the ambient humidity, and thus cause distortions on the the circuitry behavior.

To reduce as much as possible all these potential sources of problems, assembly and handling procedures are carried out in the so called *clean rooms*. Basically, clean rooms are work areas under controlled environment. There are a great variety of *clean rooms*. For the ISL ladder assembly the typical measures adopted in silicon laboratories for high energy physics were applied: the room is kept in slightly overatmospheric pressure to keep out the dust, the air flowing into the room is filtered and dehumified, and the temperature is kept at a constant value. Specially dress are required to enter in the room. The human body can accumulate enough electrostatic charge to burn the detector circuitry during manipulation. Therefore, constant grounding is performed wearing a metallic bracelet, plugged into a ground source. Assembled ladders are stored in special containers with a constant flow of dry nitrogen.

## 4.2 DAQ During Production

The production tests were performed with a full custom DAQ system specifically developed by the author to read out the SVX II and ISL ladders. The setup is described in detail in Appendix B. This system was developed in order to cover the lack of final DAQ modules (Section 3.2.5) to perform all tests at each ladder's construction stage when ladder production started. On the other hand, due to the complexity of the final DAQ system, the fragility of some of their components and their high cost, the use of a more robust, simple and less expensive system, with the basic functionality of the final DAQ (operation of the SVX3 chip at the nominal working frequency of 50 MHz, and data acquisition rate of  $\sim 100$  Hz) was highly desirable.

The DAQ system developed for production tests basically consists in two printed circuit boards: a MUX/FIFO board, and a scrambler board (Figure 4.1). The DAQ system works in the following way. A logic bitstream pattern for SVX3 chip initialization and operational control is downloaded from a Personal Computer (PC) through an *Input/Output* ISA bus card, and stored in a *First In First Out* (FIFO) memory chip of the MUX/FIFO board. All signals sent and received by the FIFO chips are single ended TTL or CMOS compatible logic levels. Each MUX/FIFO board has 5 ports. In each port, an ISL or SVX II ladder with different chip multiplicity can be attached through a scrambler board. The scrambler board is used as the interface between the MUX/FIFO board and the readout devices. It provides the differential line drivers to generate the clock signals needed by the SVX3 chips, and the differential line receivers for the data bus coming from the readout chips. On the MUX/FIFO board, an oscillator clocks the data out of the FIFO chips to the SVX3 chips with constant timing and at a desired frequency (50 MHz).

A demultiplexing circuitry in the MUX/FIFO board takes the data and routes it to one or more than one of the several possible ladders according to an input binary address. The other addresses are hold in inactive states. After initialization, readout pattern cycles can be sent individually or separately to the readout devices. The data coming from the chips is read out through a multiplex circuitry from a single DAQ FIFO in the MUX/FIFO board, and uploaded to the DAQ PC through the same *Input/Output* ISA bus card.

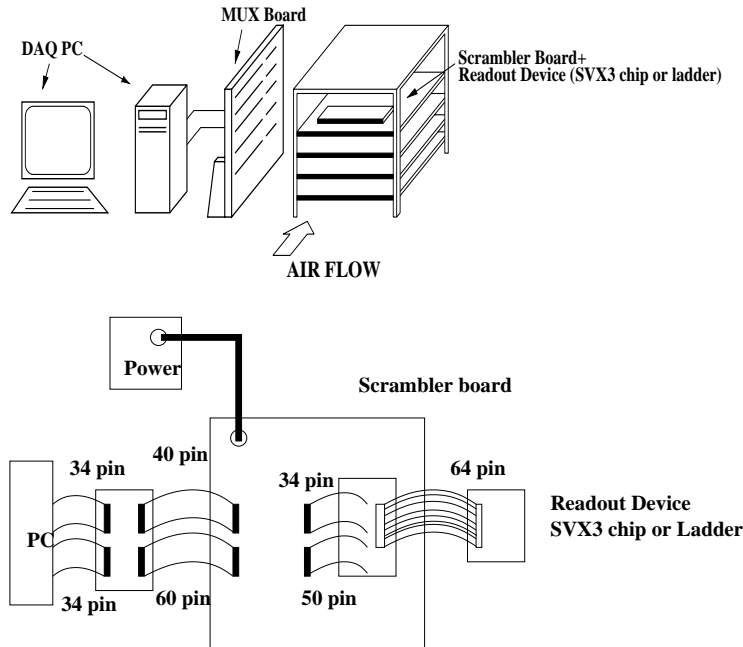


Figure 4.1: Schematic representation of DAQ system for production tests (upper Figure) and the electronic connections (bottom Figure). The MUX/FIFO board allows readout of up to 5 ladders. In the picture only one attached ladder is shown in a single port.

### 4.3 Preliminary Tests

Every component of the ladder is tested prior to its use for the ladder assembly. For testing procedures, chips are operated in *latch-all* mode, *i.e.*, all their channels are read out regardless of the amount of input charge. The data, obtained when no signal is expected, can be used to diagnose most of the features of ladder malfunctioning. The most used physical magnitudes are listed below:

- *Pedestals*. The pedestal for channel  $i$  is defined as the mean of the digitized charge in absence of a known signal:

$$ped_i = \overline{v_i} \quad (4.1)$$

- *Noise*. Assuming a Gaussian distribution of pedestals (see Figures 4.2 and 4.3), the noise of channel  $i$ ,  $\sigma_i$ , is defined as the standard deviation of the pedestal distribution:

$$\sigma_i = \sqrt{v_i^2 - \bar{v}_i^2} \quad (4.2)$$

- *Differential noise*: Common mode noise (also known as differential noise or *dnoise*) refers to a variation of the signal which affects groups of channels in a coherent way. It can be caused by a common electromagnetic pick-up, noise on the supply voltage, *etc.* The susceptibility to common mode noise depends both on the individual detector module and on the system environment. The common mode noise can be measured on an event-by-event basis as:

$$\sigma_i^d = \sqrt{\frac{(v_i - v_{i+1})^2 - \overline{(v_i - v_{i+1})}^2}{2}} \quad (4.3)$$

Generally the noise level in all channels is of the same order. In this case, if  $\sigma_i \approx \sigma_{i+1}$  then  $\sigma_i^d \approx \sigma_i \cdot (1 - \rho)$ , where  $\rho$  is the correlation coefficient between  $v_i$  and  $v_{i+1}$ . When chips are bonded to silicon microstrips sensors in a configuration where no coherent noise is present,  $\sigma_i^d$  is usually slightly larger than  $\sigma_i$ , indicating that  $v_i$  and  $v_{i+1}$  are anticorrelated. This is due to the interstrip capacitance of the sensors connected to the chips.

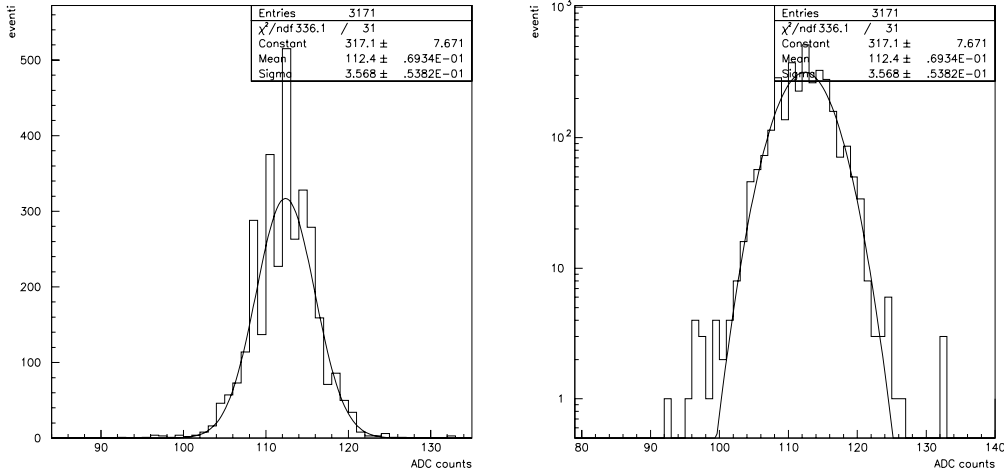


Figure 4.2: SVX3 pedestal distribution for one single channel in linear scale (left Figure) and logarithmic scale (right Figure). Both distributions are fit to a Gaussian function.

### 4.3.1 Sensor Tests

The sensors used for the ISL ladders at Pisa have depletion voltages ranging from 20 to 55 V (Figure 4.4). The three sensors on a ladder have a common voltage source

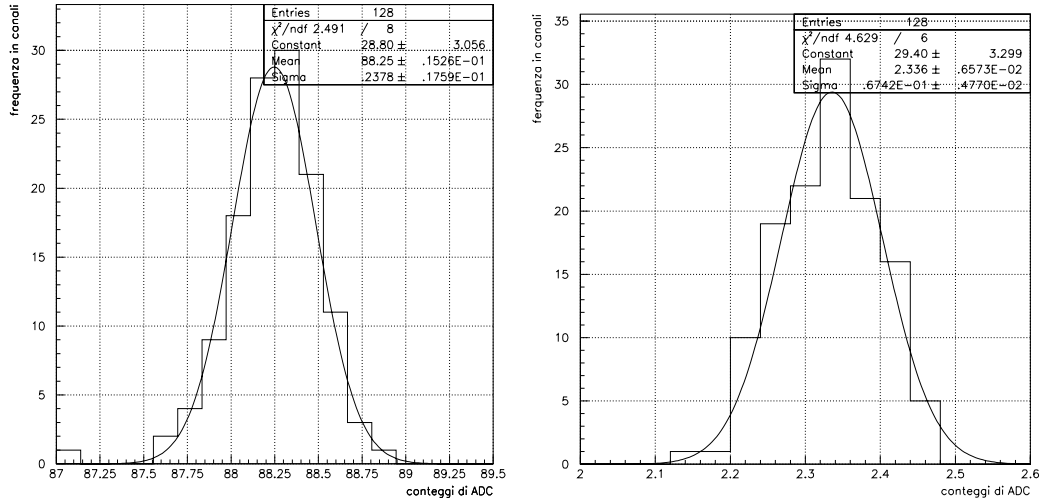


Figure 4.3: SVX3 pedestal distribution (left Figure) and noise distribution (right Figure) for all the 128 chip's channels. The distribution is fit to a Gaussian function.

for the bias voltage and therefore, to full deplete all three sensors and reach the maximum charge collection, sensors with similar depletion voltage must be bonded together.

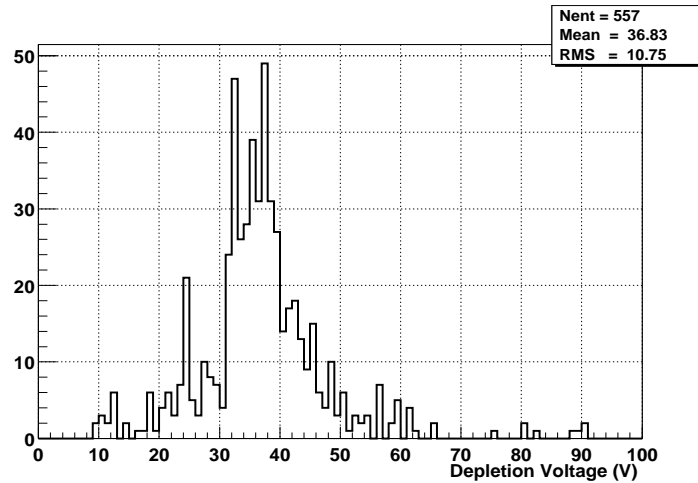


Figure 4.4: Nominal full depletion voltage distribution of ISL Micron sensors.

Before the gluing, sensors are again visually inspected under microscope to check for any damage during shipping. Since the three sensors are bonded serially, sensors with the highest number of microstrips defects are placed at the end of the readout strip (Figure 4.5). The best sensor is always bonded nearest to the hybrid, at the beginning of the readout strip. In this way the signal efficiency of the ladder is improved by attaching more active region of the ladder to the readout electronics.

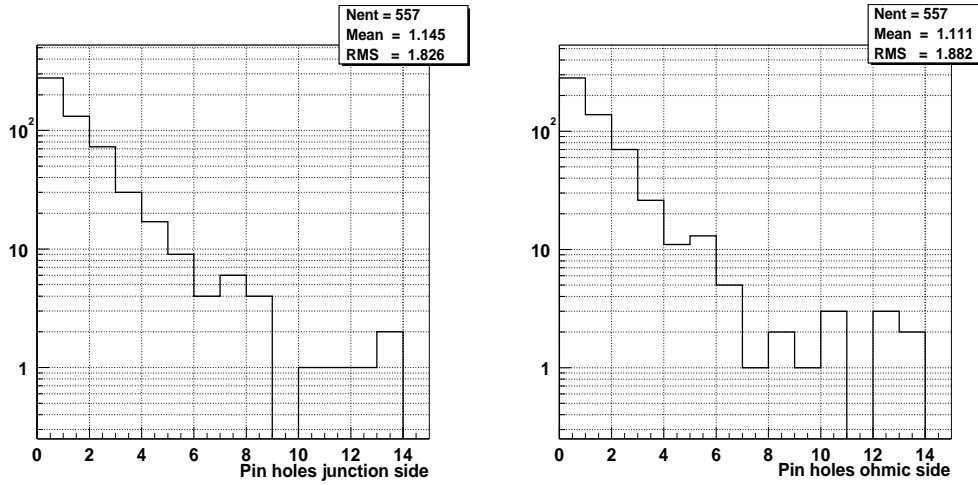


Figure 4.5: Number of broken coupling capacitors per sensor for the junction side (left Figure) and ohmic side (right Figure) for the Micron ISL sensors, as provided by the manufacturer.

### 4.3.2 Hybrid Tests

Hybrids arrive at the Pisa laboratory fully tested from LBL. However, a final testing is done before gluing on the ladder. Once the hybrid is glued and in case of malfunctioning, it is impossible to remove it without irreversible damage to the ladder support.

Tests are aimed to confirm the hybrid reads out properly with acceptable pedestals, noise and differential noise. Anomalous pedestals or high noise could indicate malfunctioning channels as shown in Figure 4.6. For the case shown in Figure 4.6, where channel 87 shows a suspicious pedestal and an extremely high noise. It will be recorded as a bad channel. Channels found defective are not bonded to the sensors.

Each channel is also tested by injecting charge at the input of the preamplifiers through a calibration capacitor built into the chip (49 pF) (see Section 3.2.3). The test input charges are generated by applying an external voltage on this capacitor. A comparison of the injected charge and the measured output from the chips gives a direct value of the gain in ADC counts per charge. For the SVX3 chip, the gain is determined by a combination of two different factors: the preamplifier gain, and the ADC converter gain, which is based upon a voltage ramp which is controlled by an external resistor used for setting the ramp current.

With this procedure the ADC gain is measured in all channels. The data shows the expected linear behavior (Figure 4.12), where typical values for channels with floating input is  $\approx 700 \text{ e}^-/\text{ADC counts}$ .

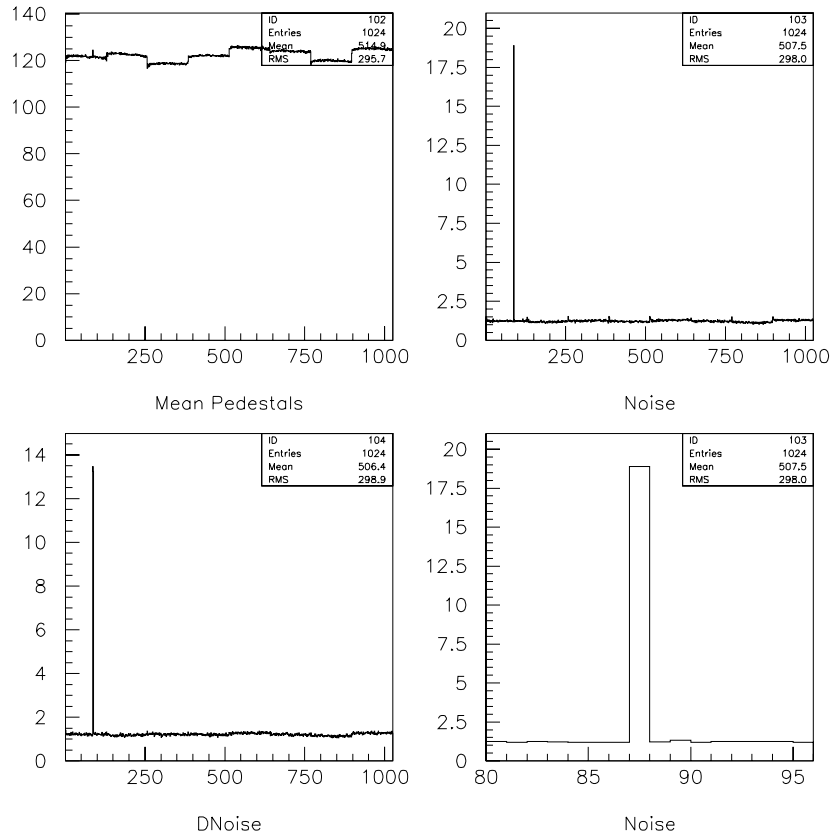


Figure 4.6: Typical failures from a hybrid readout test: pedestals (upper left), noise (upper right), differential noise (bottom left) and noise (bottom right) for a channel considered defective. Horizontal axis represents channel number. Channels are numbered from 0 to 1024. All the 8 chips on each hybrid are readout serially. With 128 channels per chip, the total number of channels is 1024. Vertical axis units are given in ADC counts.

## 4.4 ISL Ladder Assembly and Construction Procedures

The final alignment of the ISL detector will be done with isolated tracks reconstructed in both the SVX II and the COT. In this way, the position of the ISL with respect to the SVX II and the COT detectors can be determined with an accuracy of a few microns. However, this procedure converges only if the ISL sensors relative position with respect to the other sensors in the same ladder is known within of  $\sim 5\mu\text{m}$  precision, which imposes rather tight accuracy and precision constraints to the alignment during the ladder construction (Table 4.1).

Ladder construction and alignment is done with a Coordinate Measuring Machine (CMM) with the help of special mounting fixtures (see Figure 4.7). The jig

Alignment	Tolerance
Between sensors:	$\pm 5 \mu\text{m}$
Between sensors and hybrid:	$\pm 5 \mu\text{m}$
Between two modules:	$\pm 75 \mu\text{m}$
Between ISL and SVX II:	$\pm 200 \mu\text{m}$ , $\pm 2 \text{ mrad}$

Table 4.1: Maximum allowed mechanical tolerances between the ISL components.

is anchored in the granite table of the CMM machine. Four towers (shown in the figure) are used for the positioning of the hybrid and the three sensors. They can rotate and translate in the  $X$ - $Y$  plane with micrometric accuracy. A bridge can be moved in the  $z$  axis, parallel to the  $X$ - $Y$  plane also with micrometric precision.

#### 4.4.1 Assembly

The glue<sup>2</sup> is extended on top of the ladder carbon fiber support (CF). The CF support is fixed on the bridge, with the four towers passing through cavities specially made for this purpose (see Figure 4.7). Then the hybrid is placed in one of the towers and aligned respect to the machine axis. The origin of the reference system is taken to be a precision machined hole in the middle of the hybrid (see Figures 3.13 and 4.8). The  $x$  and  $y$  axis are oriented as shown in Figure 4.8 with the  $z$ -axis exiting from the page's surface.

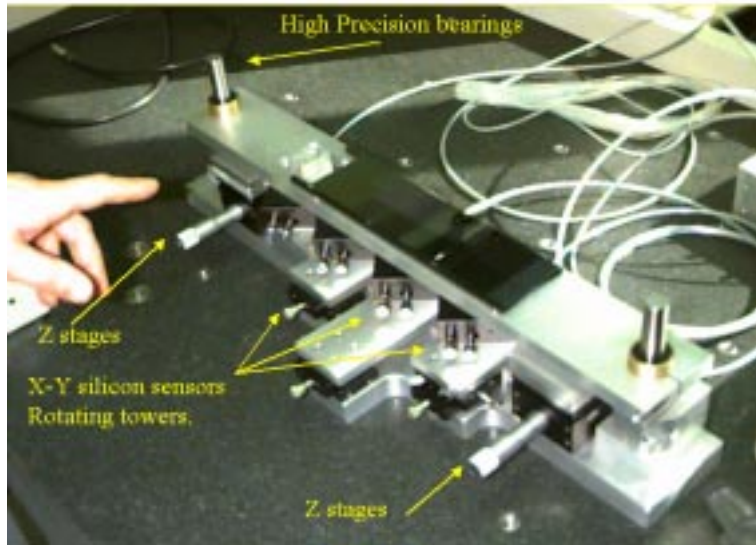


Figure 4.7: ISL ladder assembly fixture at the INFN (Pisa, Italy).

The first sensor is placed on the second tower. The surface of each tower is covered by Teflon with a planarity accuracy of  $5 \mu\text{m}$ , and channels buried on the

<sup>2</sup>Epoxy glue AW106/HW935 (kit name 2011) produced by Giba-Geigy.

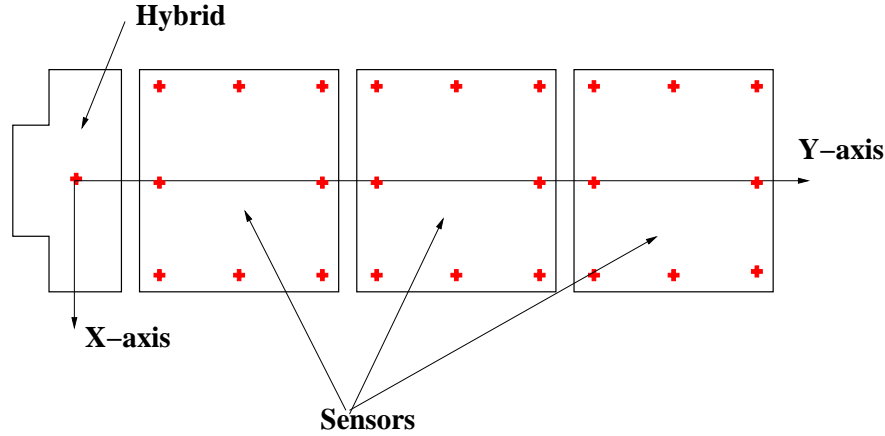


Figure 4.8: ISL ladder reference system for assembly. Crosses represent the precision machined hole in the hybrid, and the reference marks implanted on the sensors.

surface. Creating vacuum in these channels the sensor is fixed onto the tower. Once the sensor is placed on the tower, it is rotated and translated with the CMM to achieve the required alignment. The same procedure is done with the second and third sensors. Once all the sensors are aligned using the four reference marks implanted in each sensor by the manufacturer (see Figure 4.8), the bridge is slowly and very carefully elevated up to the full contact between the support, with glue already extended on it, and the sensors and the hybrid. In this assembly step, the most delicate, the bridge is elevated in such a way that the CF support makes contact with the sensors simultaneously on all of the glued surface to avoid the creation of asymmetric forces that could cause sensors' displacements or rotations. It is also important not to push the CF support against the sensors. This could cause permanent elastic stresses in the ladder structure compromising its long term stability. After 24 hours alignment is checked again with the CMM. The ladder is then ready for microbonding.

Figure 4.9 shows the residual distribution between the nominal and the measured sensor's position. For the  $x$ ,  $y$  coordinates the residuals have typically an spread of  $\sigma \approx 2 - 3 \mu\text{m}$ . For the  $z$  coordinate residuals are slightly larger  $\approx 15 \mu\text{m}$ .

## 4.5 Ladder Functionality Tests

After gluing, sensor's microbonding is performed in three steps. First, the bias lines for all three sensors are bonded, and a fast  $I - V$  scan is performed. Second, all the microstrips on one side are bonded to the readout electronics. After that, the channels marked as defective by the manufacturer are removed,<sup>3</sup> and damages

<sup>3</sup>Microbonding is performed in an automatic bonder machine. Thus, for practical reasons, is more convenient to bond all the 512 channels per side, and then by hand remove the few defective

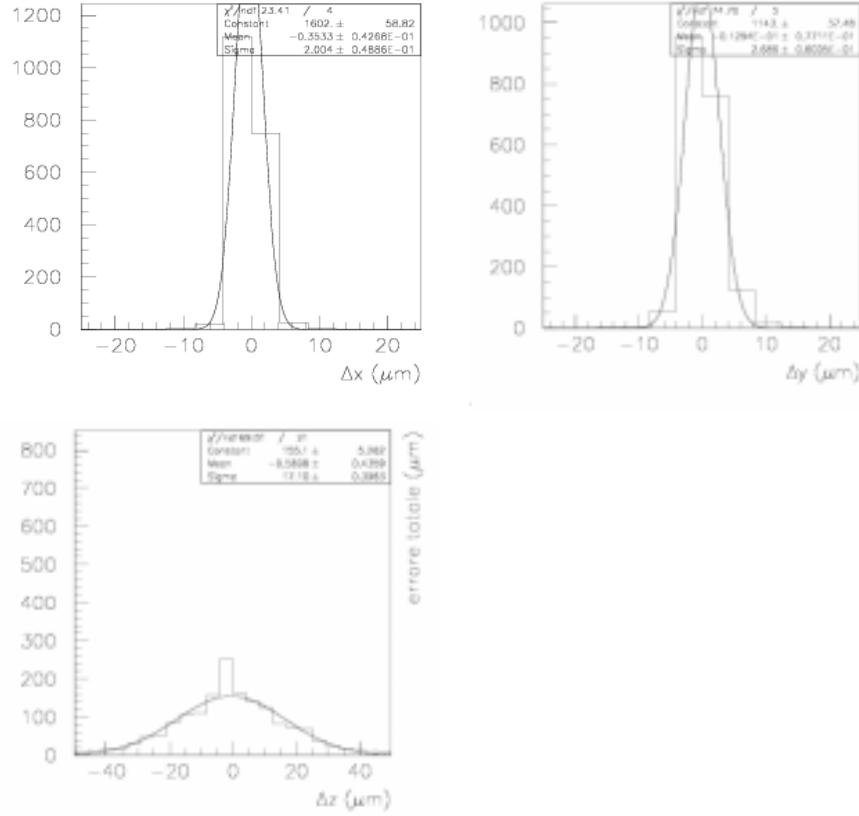


Figure 4.9: Residuals distribution between the nominal and measured sensor's position ( $x, y, z$ ) in the ladder reference frame.

produced in the bonding process identified. Finally, the opposite side is bonded and the defective channels also removed. At this point the operational depletion voltage is determined based on the known relation between the noise and the sensor capacitance at full depletion voltage (Section 4.5.2).

#### 4.5.1 Defective Channel Removal

The most common damages produced in the bonding process are pin-holes and accidental disconnection of readout channels.

##### Pin-holes

A pin-hole is created when the  $\text{SiO}_2$  substrate between the microstrip metallization and the  $\text{p}^+$  implant which forms the coupling capacitor is damaged, effectively resulting in a direct current (DC) path connection between the  $\text{p}^+$  implant and the readout electronics. The presence of a pin-hole on a particular side of the sensor channels.

can be detected by applying a bias voltage to the side under test (Figure 4.10). An anomalous high leakage current usually indicates the presence of a pin-hole. This is due to the fact that when a pin-hole appears, the bias voltage is applied directly to the input of the readout electronics through the broken coupling capacitor. To protect the SVX3 chip from the high voltage a diode inside the chip opens and connects the input channel to ground. This shorts the bias to ground through the readout electronics and creates a low impedance path that increases the leakage current.<sup>4</sup>

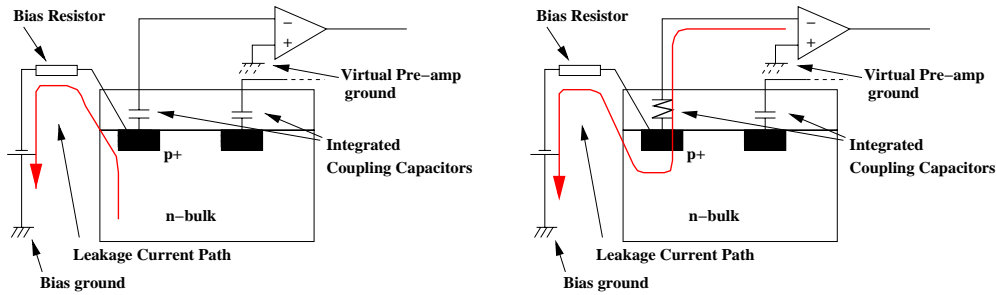


Figure 4.10: Schematic representation of a pin-hole. In normal operating conditions (left Figure) the readout electronics is isolated from the bias voltage through the integrated coupling capacitor. The leakage current flows then through the silicon bulk. If the coupling capacitor is broken (right Figure) a protection diode inside the SVX3 chip shorts the channel input to ground, and all the current flows through the readout electronics.

The exact pin-hole location can be identified by an anomalous pedestal and noise behavior. Channels with pin-holes have the bias voltage line shorted to the input of the front-end electronics. Therefore, any voltage difference between the bias voltage and the virtual ground of the preamplifier ( $\sim 1$  V) produces a current which will be integrated as if it were a signal. Pin-hole channels will show a positive/negative pedestal shift according to this voltage difference (Figure 4.11). For higher voltages, and thus higher current flow, the preamplifier saturates and the pin-hole channel shows a lower than the base line pedestal and noise. For even higher voltages, the current is also spread to the neighbor channels, and the pedestal level presents anomalies over a wider region.

Channels with pin-holes must be disconnected from the readout electronics. In this way, the high impedance path through the silicon bulk is restored, the leakage current returns to its normal value, and the readout electronics is again AC coupled to the bias line.

For the ISL, the typical number of pin-holes created during microbonding and testing was  $\sim 3$  per ladder.<sup>5</sup>

<sup>4</sup>Note that the presence of a polysilicon bias resistor (Section 3.1.8) with resistances of  $\sim 4$  M $\Omega$  provides additional protection for the chip by limiting the current flow.

<sup>5</sup>Each ladder has a total number of 1024 readout channels, 512 per side.

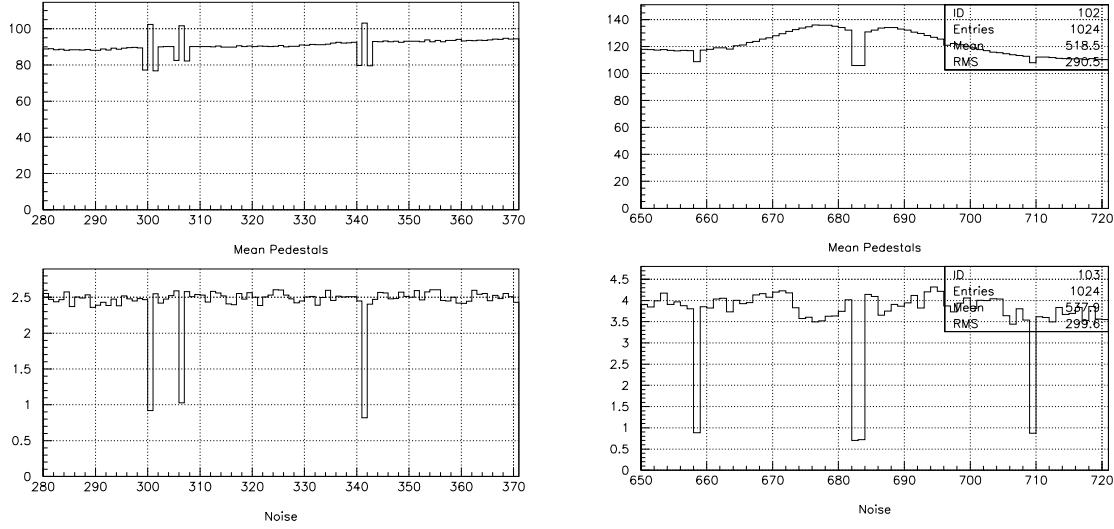


Figure 4.11: Typical pedestal (top) and noise profiles (bottom) in presence of pin-holes. Left Figure shows three pin-holes (channels No 300, 306 and 341). Right Figure shows two neighboring pin-holes (channels No 682 and 683). Channels No 658 and 669 are disconnected channels.

### Disconnected Channels

Channels disconnected from the readout electronics generally show a normal pedestal, but a lower than the base line noise (Figure 4.11). This is because disconnected channels have no input capacitive load, and thus, following Equation 3.18, they will present also lower noise levels.

### Gain Scans

As described in Section 4.3.2, each input channel of the SVX3 chip has a calibration capacitor (49 pF) where an external voltage level can be set and thus, different amounts of charge injected directly into the preamplifier (Figure 4.12). Channels with pinholes usually show saturation or near saturation at the preamplifier input. Therefore, the injection of additional charge has no effect and they show an almost  $\sim 0$  gain. This behavior helps to solve ambiguities, specially in the case when pin-holes draw very large current and neighbor microstrips present also heavily distorted pedestals.

Channels connected to the sensor show higher gains than disconnected channels (Figure 4.12). This is a complex effect that can be explained as an interaction between the attached input capacitance from the sensor microstrip and the SVX3 chip preamplifier gain.

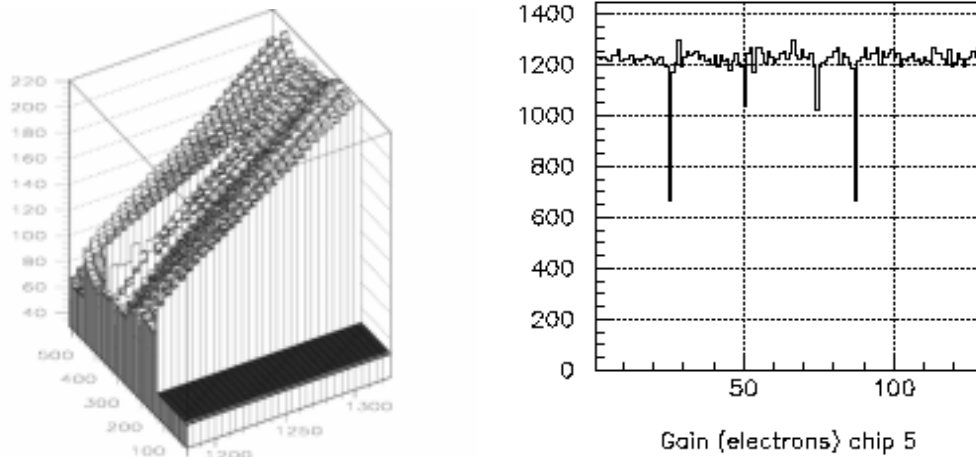


Figure 4.12: Left Figure: typical view of a charge injection scan through the calibration capacitor for one side of the ISL ladder.  $x$ -axis shows the channel number,  $y$  axis the voltage level set to the calibration capacitor (arbitrary units), and the  $z$ -axis the channel output in ADC counts. The first 128 channels have been cut away. Right Figure: typical single chip (128 channels,  $x$ -axis) gain profile in electrons per ADC count. Channels with low gain are disconnected channels.

## 4.5.2 Operational Bias Voltage

Although for every sensor the full depletion voltage has been measured by the manufacturer (see Section 4.3.1), a common operational voltage for the three sensors in the ladder must be defined<sup>6</sup>.

The determination of a common full depletion voltage is based in the relation between the noise and the microstrip capacitance (Equation 3.18). When bias voltage is applied, the width of the depletion zone progressively grows from the p-n junction side towards the ohmic side (Equation 3.6). For the p-n junction side, few volts are enough to isolate the different  $p^+$  strips, reducing the interstrip capacitance, with a rapidly decrease of the noise<sup>7</sup> (Figure 4.13). When the bias voltage is high enough to make the depletion zone reach the ohmic side (full depletion voltage), the p-stop strips became active and the n-strips result also isolated, with the corresponding noise decrease. Therefore, both curves, for the n and p-side, show a plateau of low noise, slowly growing for high enough voltages where breakdown phenomena becomes relevant (see Section 3.1.9). The operational voltage is thus chosen to be  $\sim 10$  V after the beginning of the plateau region, where full n-strip isolation has been reached but still far away from the breakdown phenomena region.

<sup>6</sup>Each of the three sensors has slightly different depletion voltages. Furthermore, they are serially biased. Thus, due to the  $IR$  losses full depletion voltage may vary.

<sup>7</sup>The noise here refers to the noise averaged over all channels in one side.

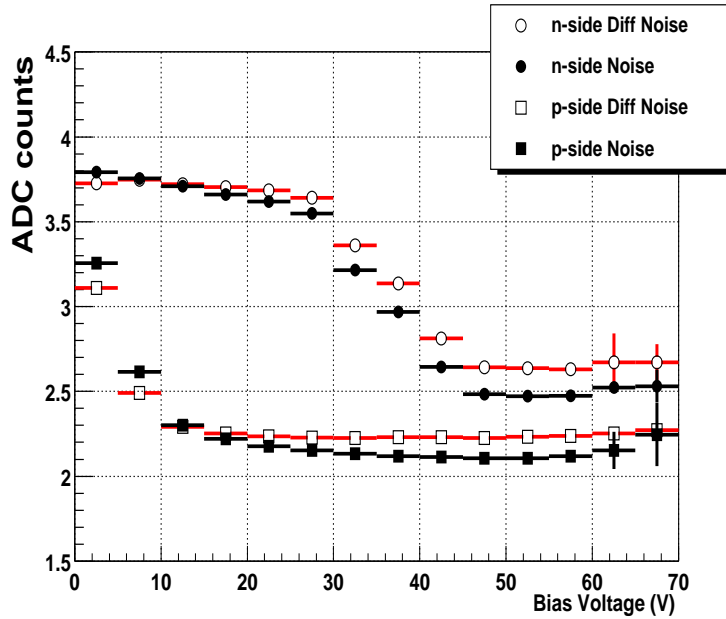


Figure 4.13: Noise (solid marks) and differential noise (open marks) scan for an ISL ladder. p-side refers to the junction side and n-side to the ohmic side.

## 4.6 Burn-in Tests

In the microelectronics industry the experience shows that for mass-produced microelectronics devices the failure rate depends on time [80]. This failure rate as a function of time has been found to follow the so called *bathtub* dependence (Figure 4.14). An electronic device will most like fail in the early part of its operating life (the “infant mortality” life stage). The failure rate then levels off through the device’s normal life and again increases when the device becomes old, at the end of the operational life. For the case of silicon devices the “infant” mortality is due mainly to the presence of micro-fissures, which in the first time of operation thermally expand because of the released heat producing the failure of the device.

In the microelectronics industry a burn-in test consists in the holding of the produced devices at an elevated temperature for a specified number of hours, generally with bias and an electrical load applied. This way all elements of the device are stressed at maximum rated operating conditions to reveal all the time dependent failure modes, thus eliminating the fraction of devices that will fail shortly after the beginning of the operational period. Experience [80] shows that devices which survive the burn-in test have low and predictable failure rates.

The conditions for a burn-in test may vary. Devices can be held at high temperatures or in an environment close to the real operating conditions, and for a period of time that depends on the degree of screening that must be achieved.<sup>8</sup>

<sup>8</sup>The industry usually follows the US army burn-in test standard MIL-STD-883, Method 115,

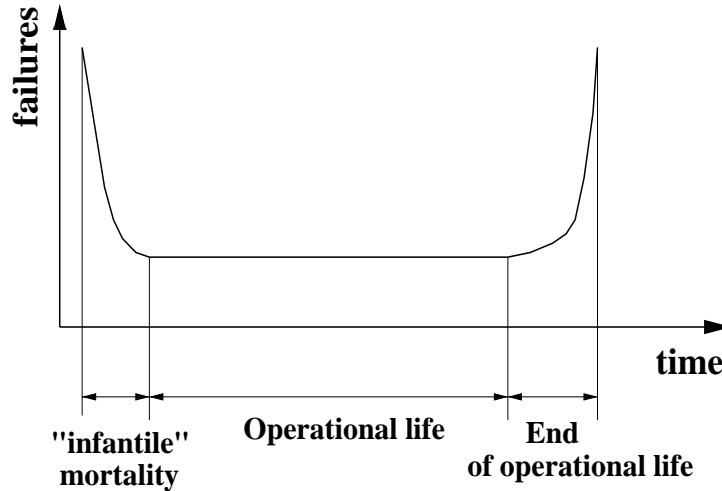


Figure 4.14: Failure rate as a function of time for microelectronics devices. Axis are expressed in arbitrary units.

For the fully instrumented ladders a burn-in test time of 72 hours was considered to yield a high reliability check based on the previous experience with the SVX'.

#### 4.6.1 ISL Ladder Burn-in

For the ISL burn-in test fully instrumented ladders were kept inside closed metallic boxes, with bias voltages 20 V above the fully depletion voltage. The readout electronics was continuously exercised during 72 hours, and the pedestals, noise, differential noise and leakage current monitored and recorded with a fully custom designed system (see Appendix B). The ladder temperature was kept at  $\sim 20^\circ\text{C}$  with constant air flow.

For the ISL no ladders were rejected due to failures produced during the burn-in tests. No drifts of the leakage current, nor the creation of pin-holes were observed. The read-out electronics performed also well, with the exception of regular failures due to the loss of the chip initialization parameters, strongly correlated with environmental electrical noise.

#### 4.6.2 SVX II Ladder Burn-in

The DAQ system described in Section 4.2 was also used for the burn-in test of SVX II ladders at FNAL [81].

SVX II ladders (Section 2.2.3) were kept in a cooled, dry and dark environment during the 72 hours of the burn-in test. The SVX3 chips were continuously exercised

---

where, *e.g.*, normal burn-in procedures require at least a temperature of  $125^\circ\text{C}$  with a burn-in time of 168 hours.

and pedestal data were periodically readout ( $\sim$  every 5 minutes) and recorded. To keep the needed environmental conditions, specially metallic boxes were built to place together up to 5 SVX II ladders (Figure 4.15). The boxes had cooling channels epoxied to the bottom of the box, with a chilled water ( $0^\circ$ ) flow designed to draw up to 70 Watts of total power<sup>9</sup>. A constant flow of dry nitrogen was injected into the boxes to avoid humidity condensation at low temperatures. SVX II ladders were kept under full bias voltage with the same system of CAEN voltage modules and controllers as those used in the final CDF detector operation [82]. Temperature and other operation parameters like sensor bias voltages and leakage currents were recorded during all the burn-in test period for later analysis. For the periods where the burn-in test was unattended, an interlock system (both hardware and software) was implemented. The interlock system was designed to protect the SVX II ladders against overheating and humidity condensation in the burn-in box (Appendix B).

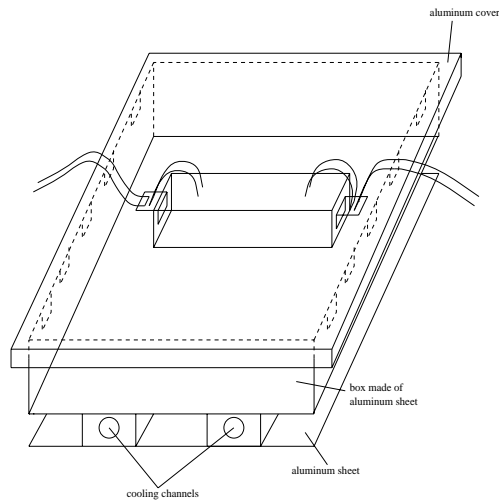


Figure 4.15: Metallic box designed to keep up to 5 SVX II ladders during the burn-in test at FNAL.

### Pin-hole Detection

During the burn-in test each one of the SVX II ladder types was biased at a different bias voltage. This voltage was chosen to reach full depletion after the irradiation damage caused by  $2 \text{ fb}^{-1}$  of integrated luminosity (Table 4.2). The burn-in test was aimed to monitor the apparition rate of pin-holes, as already discussed in Section 4.6.

Pin-holes were identified by looking at the data for jumps in the bias voltage current in coincidence with a drop in noise on any channel. A program was developed to scan the pedestals and sensor's leakage current and identify leakage current jumps larger than  $30 \mu\text{A}$ . For each jump in current, the noise was calculated before and

<sup>9</sup>The temperature of the SVX3 chips was kept at  $12^\circ$ .

	Bias Voltage	Manufacturer
<b>Layers 0,1</b>	180 V	Hamamatsu Photonics Co.
<b>Layers 2,4</b>	120 V	Micron Ltd.
<b>Layers 3</b>	140 V	Hamamatus Photonics Co.

Table 4.2: Maximum bias voltage of the SVX II ladders during the burn-in test at FNAL. The bias voltage was symmetrically split between the ohmic and junction sides.

Description	Default value
Minimum current jump	$30 \mu\text{A}$
Number of records to average noise over	8
Gap before averaging starts	2
Minimum drop in noise	$-0.35$ ADC counts
Minimum drop in noise	$-1.7$ standard deviations
Maximum noise after pinhole	$1.5$ ADC counts

Table 4.3: Pin-hole identification loose parameters.

after the jump for all channels. The noise was averaged over  $\sim 8$  records (each record taken with 5 minutes interval), starting at 2 records before and after the jump. The four records gap was used as in some cases the noise increased in the record prior to the pinhole apparition. Channels with significant drops in noise were flagged as pinhole candidates. The noise drop was considered significant if at least one of the following conditions was satisfied:

- The noise drops more than 0.35 ADC counts.
- The noise drop is higher than 1.7 standard deviations.
- The noise afterwards the presumed pin-hole creation is less than 1.5 ADC counts.

All these values were found empirically (Table 4.3), and served as a first identification of pin-holes with a loose criteria. Figure 4.16 illustrates a typical pin-hole creation during the burn-in test of a SVX II ladder. A substantial jump of the sensor leakage current is accompanied by a drop on the noise of the channel identified as a pin-hole. The neighbors to the pin-hole channels show a characteristic noise increase due to the charge spread from the pin-hole current (see Section 4.5.1).

### Pin-holes as a Function of Time

As discussed in Section 4.6, the burn-in test aims the detection of defects which appear in the early stages of the operational life of the devices under test. Afterwards, the rate at which defects appear is usually constant in time and can be predicted.

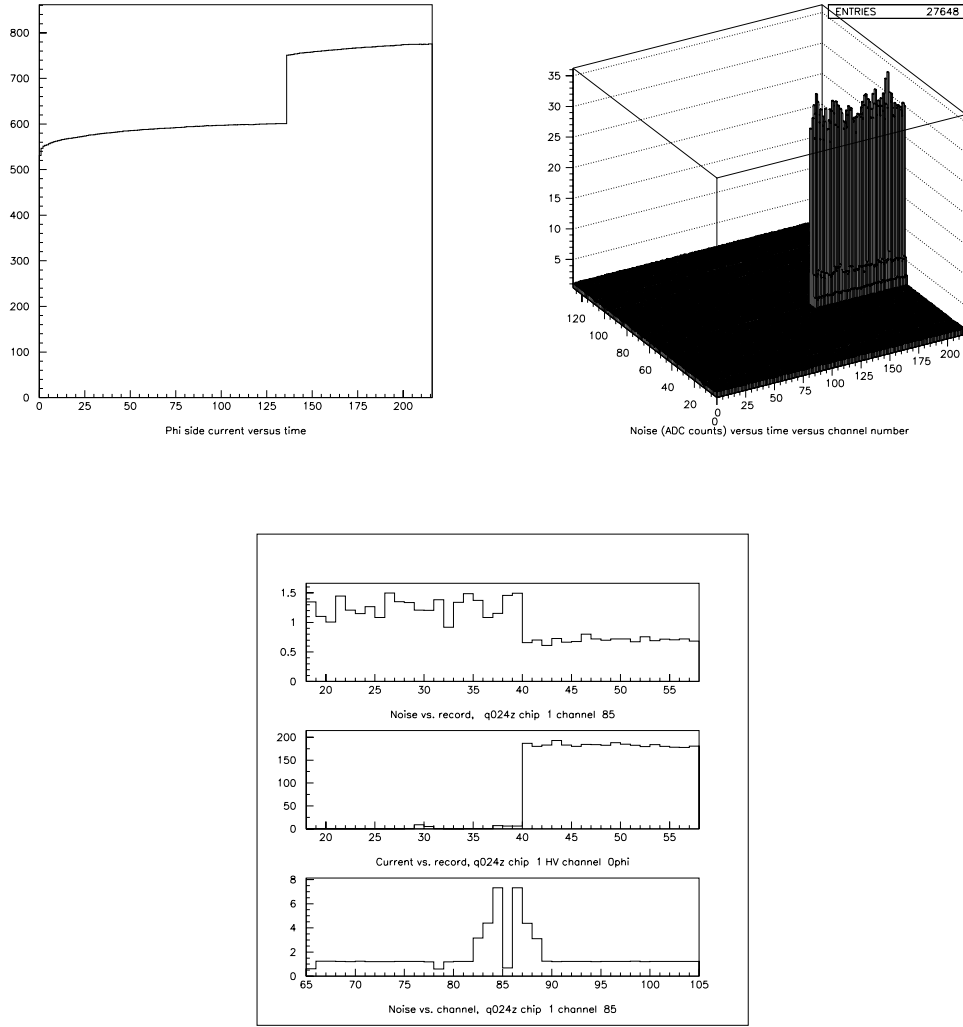


Figure 4.16: Pin-hole creation during the burn-in test of a SVX II ladder. A steep increase of the leakage current (upper left Figure) is correlated with a noise increase in the neighbors channels of a pin-hole (upper right Figure). The bottom Figure shows a drop in noise in the pinhole channel, correlated with the jump of the leakage current and the characteristic noise pattern.

For the case of the SVX II ladders, the defects are mainly pin-holes which must be disconnected from the channel input of the SVX3 chip. Figure 4.17 shows the number of detected pin-holes for each of the five SVX II ladder types during the burn-in test as a function of time. For layers 0 and 1 an *infant mortality* stage is clearly visible. A non negligible pin-hole production rate is also present for times longer than one day. The bias voltages used represent thus a limiting factor for the operational lifetime of the innermost ladders. For layers 2, 3 and 4, the *infant mortality* stage is also visible but the pin-hole production rate is smaller after one day. For layers

2 and 4 a large current increase and the presence of many noisy channels were also seen when operating the ladders with a split bias voltage scheme. These effects disappear when operating the ladders with a single side bias scheme. The lower radiation environment suffered by these ladders compared to the innermost layer 0 and 1 will allow their operation with a single side bias scheme through the full lifetime of the SVX II.

The different behavior observed between layers 0 and 1, and layers 2, 3 and 4 has been investigated [83] and explained as due to the different silicon sensor quality of layers 0 and 1. These layers show microdischarge phenomena (see Section 3.1.9) for bias voltages  $\sim 170$  V, which makes the appearance of pin-holes more probable. The maximum operational bias voltage of these sensors is thus limited to  $\sim 170$  V. This may reduce their operational life if, due to the bulk radiation damage, the bias voltage has to be increased above these values.

## 4.7 Laser Tests

After defective channel removal and ladder burn-in, a final readout channel functionality test was performed for each ladder in a fully automatic laser station [85] (Figure 4.18). Each microstrip on each sensor side was illuminated with an infra-red laser of 905 nm wavelength, which penetrates  $\sim 30 \mu\text{m}$  in the silicon [84]. The laser light was produced by a 10 ns pulsed laser diode<sup>10</sup>. Laser pulses were synchronized with the *Front-End* clock of the SVX3 chip. The laser light was transmitted via an optical fiber 6  $\mu\text{m}$  diameter. The focusing system consisted of a collimating lens and an adjustable post holder which allowed vertical positioning of the lens relative to the detector. The height of the lens and the laser beam ( $\sim 5$  cm) were adjusted to produce a narrow beam with a Gaussian width of 50  $\mu\text{m}$  (signal cluster of 3 strips). The DAQ system consisted on a slightly modified MUX/FIFO and scrambler boards, where one TTL signal specially left for trigger purposes (see Appendix B), was connect with a Lemmo cable to a delay unit and to the TTL trigger input of the laser driver<sup>11</sup>. The ladder was positioned under the laser spot with a table provided with stepping motors with angular encoders, which allowed an  $x$ -axis movement with a precision of  $\sim 2 \mu\text{m}$  and a  $y$  axis movement with a precision of  $\sim 1$  mm. Laser alignment was achieved by means of an online graphical display, which allowed to visualize the laser signal and memorize the coordinates of three different microstrips (two of them belonging to different sensors) successively placed under the laser spot.

Once the ladder was aligned, an automatic program positioned each microstrip of each sensor under the laser spot, and several hundreds of events per microstrip were acquired and stored on a DAQ PC. Figure 4.19 shows the the residual distribution between the  $x$ -axis nominal position of the illuminated microstrip, and the position

<sup>10</sup>Produced by EG&G, model C86092E13.

<sup>11</sup>The laser driver was a custom driver fabricated at the electronic laboratories of the INFN, Sezione di Padova, Italy.

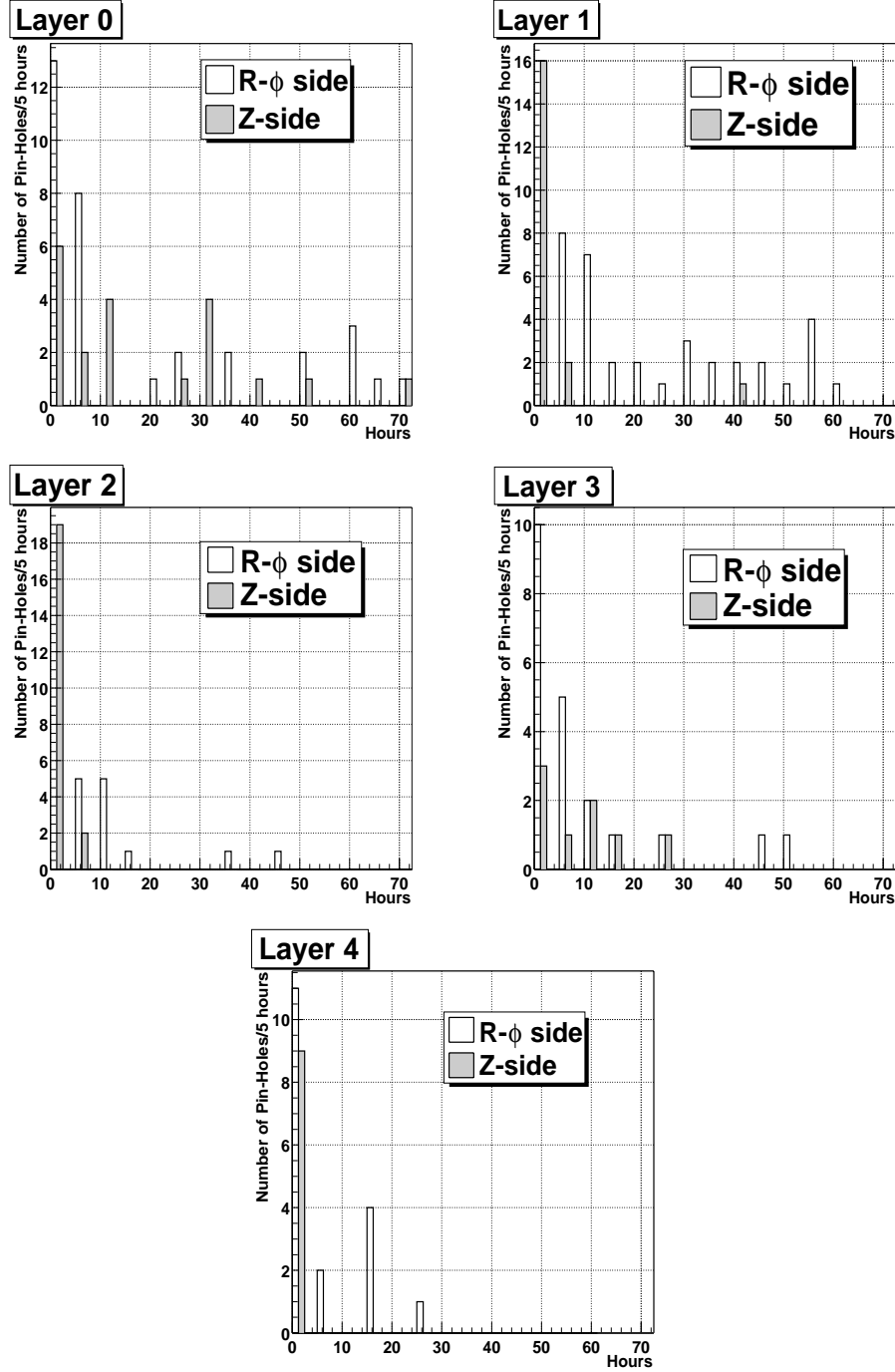


Figure 4.17: Number of pin-holes created during the burn-in test as a function of time (hours) for each SVX II ladder type.

obtained from the charge gravity center of the cluster formed by the illuminated strip and its left and right side neighbors. The achieved precision was of  $\sim 4 \mu\text{m}$ .

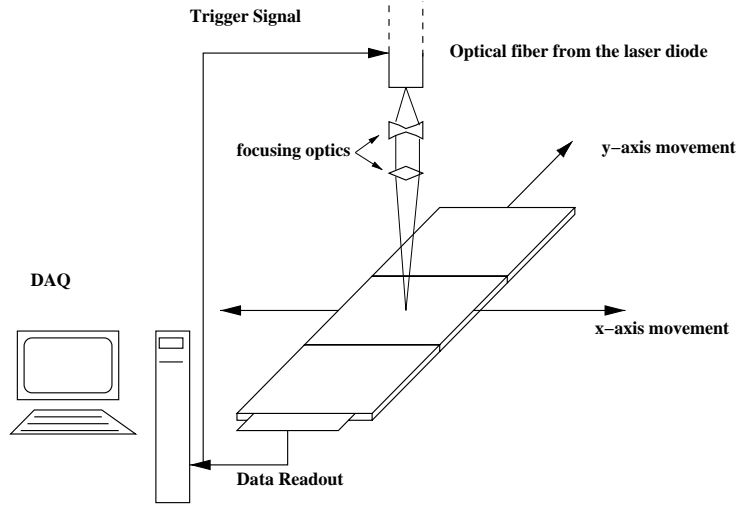


Figure 4.18: Laser test setup for the ISL ladders at the INFN laboratories.

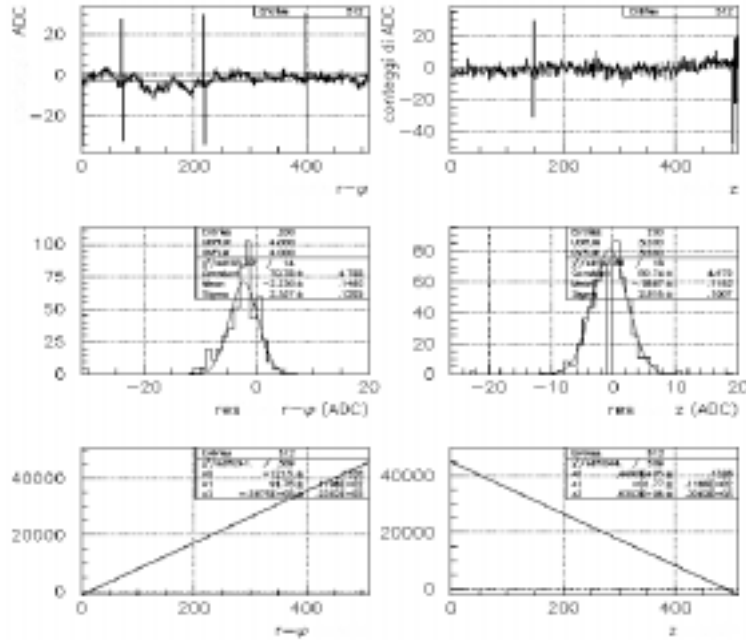


Figure 4.19: Upper Figure:  $x$ -axis channel position residuals in stepping motor encoder counts (1 encoder count  $\approx 2 \mu\text{m}$ ). Left Figure shows the  $r-\phi$  sensor coordinate side where the microstrips run parallel to the sensor longitudinal edges. Right Figure shows the  $z$  sensor coordinate side where the microstrips have a small stereo angle ( $1.2^\circ$ ). Channels with anomalous high residual values correspond to channels with disconnected neighbor microstrips. The middle row plots show the corresponding residual distributions and their Gaussian fit. Bottom plots show the encoder counts as a function of the channel number.

### 4.7.1 Laser Diagnostics

The automatic laser station was used to perform several final tests as channel-to-channel uniformity checks, a final list of disconnected channels and operational bias voltage characterization for some ladders.

#### Channel-to-Channel Uniformity

The laser scan of all channels on all three ISL sensors of every ladder produced a definitive list of disconnected channels, which allowed for a fast inventory of non functioning channels (Figure 4.20), and a check of the channel-to-channel uniformity.

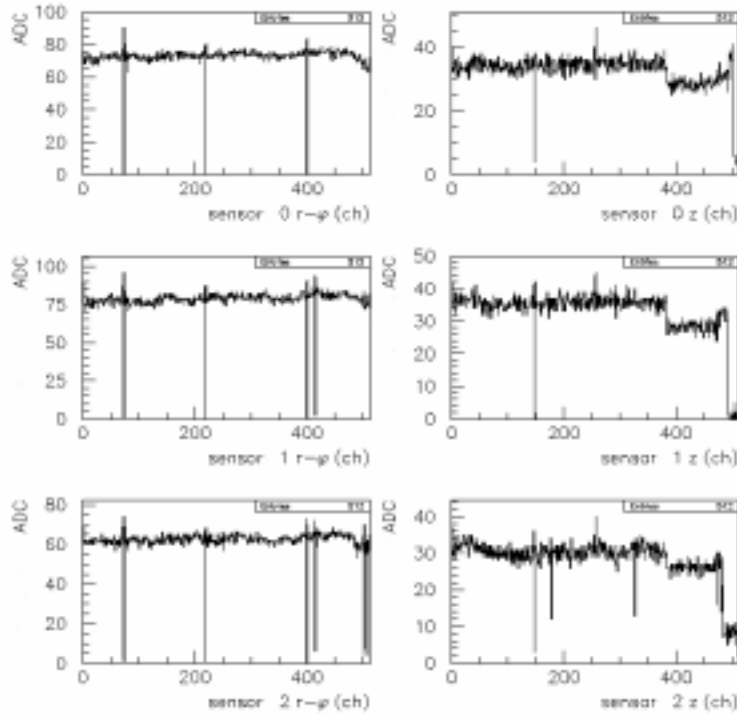


Figure 4.20: Laser scan of an ISL ladder: charge (in ADC counts) of the illuminated microstrip for each of the three sensors. Left column shows the junction side and right column the ohmic side.

#### Bias Voltage Characterization

For a few ladders, the operating voltage measured with the method described in Section 4.5.2 yielded values significantly lower than the sensor's full depletion voltage indicated by the manufacturer. On the other hand, for ladders showing a relatively high number of noisy channels it was desirable to set the lowest possible full depletion voltage to avoid the appearance of microdischarges, and thus reduce the noise to

the minimum. In these cases, the full depletion voltage was studied by measuring the charge collection efficiency with the laser setup as a function of the bias voltage. The laser light was focused on the junction side of the sensor, and the cluster charge on the ohmic side was measured as a function of the applied voltage. By increasing the bias voltage one expects an increase of the collected charge. When the sensor is fully depleted, the amount of collected charge reaches a plateau. The point where the plateau begins can be considered as the point where full depletion is achieved with the lowest bias voltage.

An example of this procedure is shown in Figure 4.21 for an ISL ladder. The nominal full depletion voltage provided by the manufacturer was  $\sim 33$  V, while the operational voltage measured with the method described in Section 4.5.2 was 40 V. Figure 4.21 shows a plateau for 35 V from a bias voltage scan with the laser setup. This value was taken as the minimal full depletion voltage.

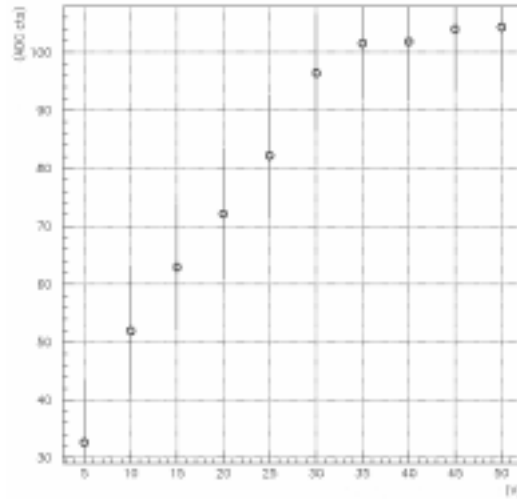


Figure 4.21: Cluster charge (3 strips, ADC counts) as a function of the bias voltage for a ISL ladder. An infrared laser (905 nm) was focused on the junction side while the cluster was measured on the ohmic side.

#### 4.7.2 Charge Collection Efficiency and Rise Time Measurements

The laser station was also used to study the charge collection efficiency and risetime optimization along the chip integration time.

When the bias voltage is applied to the silicon sensors, the p-n junction effectively forms a capacitance, with the depleted zone acting as the insulator and the n and p microstrips as the conductor (Section 3.1.5). The value of this capacitance is a function of the area of the junction, the resistivity of the material, and the voltage applied across the junction. The capacitance associated with a p-n junction

represents a limiting factor on the frequency response of semiconductor devices, and therefore on the charge collection efficiency [61]. To compensate the slow down response of the preamplifier due to this capacitance and therefore the reduction on charge collection efficiency, a set of discrete capacitors inside the SVX3 chips can be added in parallel to the feedback capacitor of the SVX3 preamplifier. The number of such capacitors (bandwidth) is digitally set at initialization time (Section 3.2.3). Seven different values for the bandwidth (BW1-BW7) can be set. The smaller the bandwidth, the more the number of these capacitors added to the preamplifier chain. The bandwidth settings allow to compensate for the difference in input capacitance of each SVX II layer (different geometry of the silicon sensors).

The bandwidth settings can be studied by measuring the preamplifier output risetime of a known signal. For different bandwidth values, the sensor input capacitance will be compensated in a different degree, yielding faster or slower signal risetimes.

A way to measure the risetime is by using a laser and vary the time delay between the laser pulse and the readout clock.<sup>12</sup> The collected signal as a function of this delay provides an estimation of the preamplifier risetime, defined as the elapsed time between the 1% and the 90-100% of the maximum collected signal. Figure 4.22 shows the collected charge as a function of time delay in ns for various bandwidth settings with a 140 ns integration time. The slope of the risetime is observed to be steeper at smaller bandwidths (at smaller bandwidths, more capacitors are added to the preamplifier feedback capacitor). The final bandwidth settings must be chosen as a compromise between the higher signal collection efficiency and the lower possible noise, thus optimizing the signal-to-noise ratio. This has been studied with signals from a  $\beta$  source and is discussed in Section 4.8.4.

## 4.8 ISL Ladder Signal to Noise Measurements

During the construction process some ladders were chosen to measure the expected signal to noise ratio ( $S/N$ ) with a  $\beta$  source. For this purpose, the experimental setup for the laser test station was modified to operate with an external trigger (Appendix B).

### 4.8.1 $\beta$ -source Test Setup

The ladders were exposed to a  $\beta^-$   $^{106}\text{Ru}$  source (9.25 MBq of activity) placed 1 cm above the ladder. The trigger was provided by a 1 cm thick scintillator coupled to a photomultiplier and placed under the ladder (Figure 4.23). The photomultiplier signal was directed to a preamplifier (gain  $\sim 10$ ) and to a NIM discriminator module.

---

<sup>12</sup>The SVX3 chip integrates the charge present at the input only when the *Front-End* clock signal is low. The *Front-End* clock is synchronized with the Tevatron clock, and is low at each bunch crossing (132 or 396 ns).

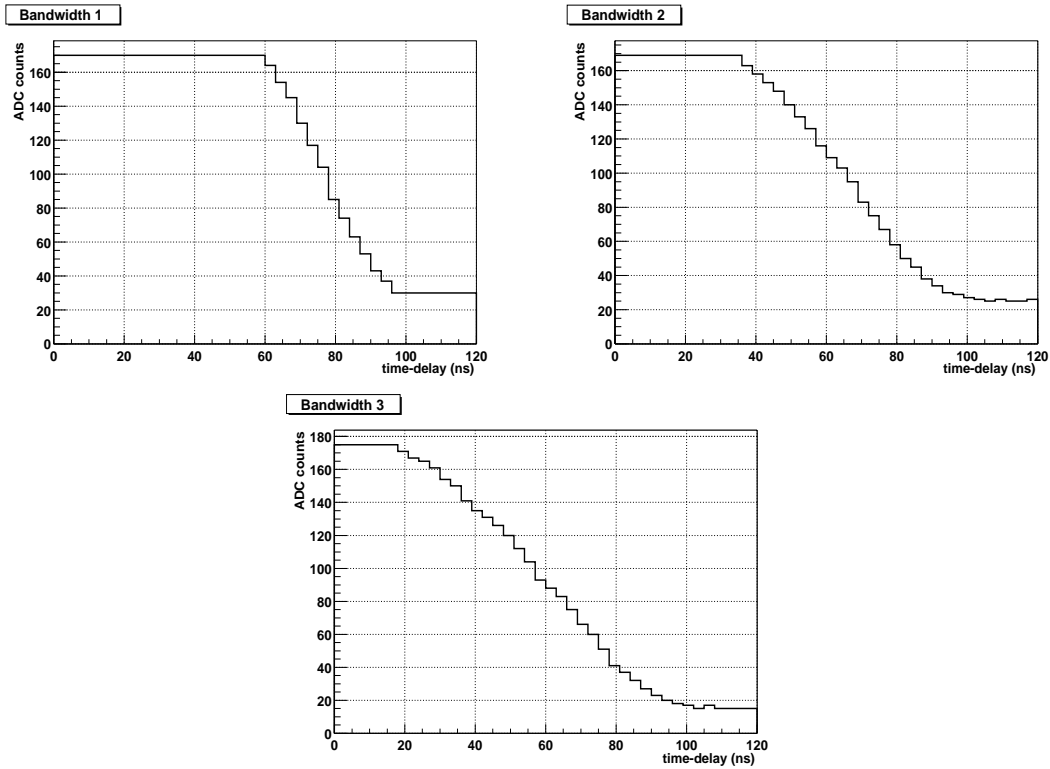
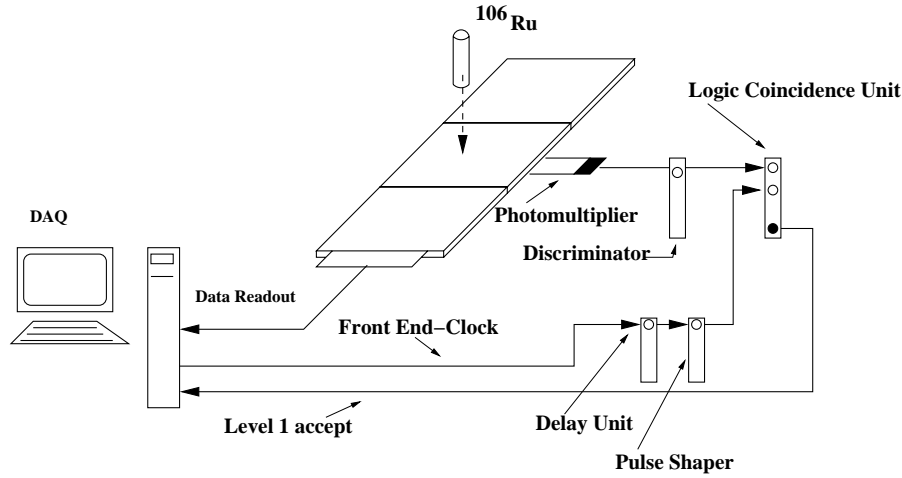
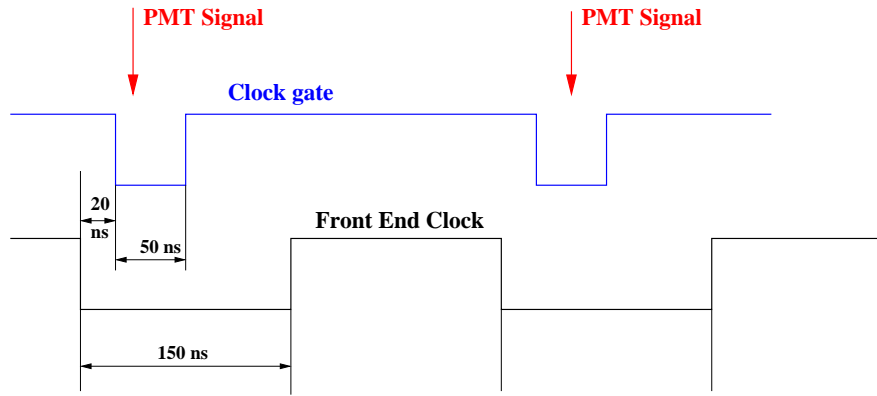


Figure 4.22: Collected charge from a laser pulse as a function of the time delay between the laser pulse and the readout clock for various bandwidth settings. All results correspond to a SVX II Layer 0 prototype ladder.

Then it was further sent to one of the inputs of a logical coincidence unit. A gate signal synchronized with the SVX3 chip *Front-End* clock<sup>13</sup> (Figure 4.24) was also sent to the other input of the coincidence unit. The gate signal was shorter than the *Front-End* clock window to ensure that all the released charge was integrated by the SVX3 chip preamplifier.

When the photomultiplier signal arrives in coincidence with the gate, the output signal is directed to a shaper and to a NIM-to-TTL converter, and finally conducted through the scrambler board to the Level 1 accept input of the SVX3 chip. The Level 1 accept signal is used by the SVX3 chip to mark the pipe-line capacitor where the integrated charge was stored. When a coincidence is issued, the decoded output data from the SVX3 chip contains the number of the corresponding pipe-line capacitor (see Section 3.2.3). In absence of coincidences, the Level 1 accept signal is not issued, and the cell number indicates an inexistent pipe-line capacitor. These events are software rejected prior to their storage in the DAQ PC.

<sup>13</sup>When the *Front-End* clock signal is low, all the charge present at the channel input of the SVX3 chip is integrated by the preamplifier. This gate is set to 132 or 396 ns, in coincidence with the Tevatron bunch crossing (see Section 3.2.3).

Figure 4.23:  $\beta$ -source test station for the ISL ladders.Figure 4.24: *Front-End* clock and gate signal synchronization for the  $\beta$ -source test setup.

## 4.8.2 Clustering Algorithm

Signal events were reconstructed with the following clustering algorithm. First, pedestal events were taken and the digitized input charge for every channel fit to a Gaussian distribution (Figure 4.2). The channel pedestal and noise are defined, respectively, as the mean and the standard deviation of the fit. For every event, the signal of each channel is then defined as the digitized charge minus the pedestal. The clustering algorithm looks for seed channels with a  $S/N$  ratio  $\geq 3$  for the junction side and  $\geq 2$  for the ohmic side.<sup>14</sup> The selected seeds are then ordered in decreasing  $S/N$ . Starting with the first seed, a cluster is defined by adding the right and left neighbor strips if their charge is higher than 1.5 times the channel noise for the junction side, and 1 times the channel noise for the ohmic side. The cluster charge

<sup>14</sup>The different thresholds are due to what seems lower charge collection efficiency of the ohmic side. Up to now this phenomena is not completely understood.

is defined as the sum of the charge of the channels which form the cluster. Once a cluster is defined, the channels which form the cluster are masked to avoid its use as seeds for other clusters. For the ohmic side, more channels with signal charge higher than 1 ADC count can be added to the cluster, up to a total maximum of 5 channels per cluster. The algorithm is iterated to exclude known noisy channels or channels always present as a seed. From the selected clusters, the cluster with the highest  $S/N$  is considered to be the signal cluster, where the noise is the seed channel noise. Only events with at least one cluster on both detector sides are considered.

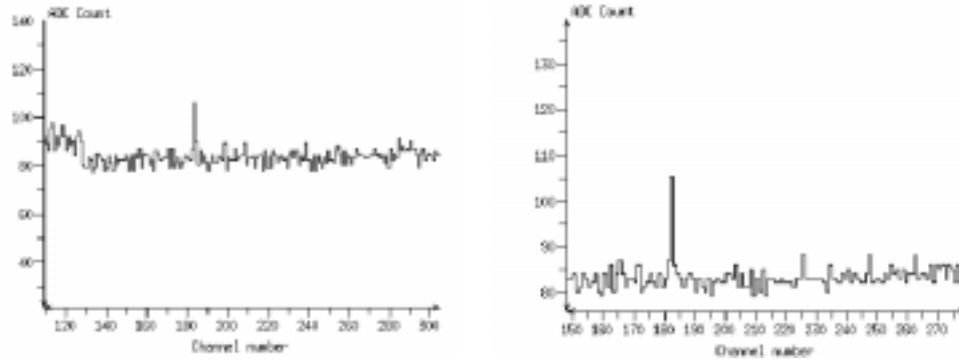


Figure 4.25:  $\beta$ -source events from the online event display for the junction side (left Figure) and the ohmic side (right Figure).

Figure 4.26 shows the cluster signal charge distribution for both ladder sides. The fit shown is a convolution of a core Gaussian distribution plus a Landau distribution for the tail (Section 3.1.1). The Gaussian core is enhanced due to systematic effects of the  $\beta$  source. The electrons emitted from the  $Ru^{106}$  source have a maximum energy of 3.5 MeV, with a most probable value of  $\sim 1.2$  MeV, very close to the minimum ionizing energies. However, the low energy fraction of the spectrum is still significant, which leads to enhanced ionization losses with respect to minimum ionizing particles, and to a wider distribution due to multiple scattering which is stronger for low energy particles.<sup>15</sup>

Figure 4.27 shows the correlation between the cluster charge on both ladder sides, which serves as a cross check of the correct behavior of the clustering algorithm.

The Micron ISL sensors are double sided, with microstrips running parallel to the sensor edges on the junction side, and with a small stereo angle ( $1.2^\circ$ ) for the ohmic side. Therefore, it is possible to reconstruct the signal hit position on the  $x$ - $y$  plane. Figure 4.28 shows the source image obtained by plotting the reconstructed  $x$  and  $y$  coordinates of the seed clusters.

<sup>15</sup>In a silicon layer of  $300\ \mu\text{m}$  thick the average multiple scattering angle is  $\sim 12^\circ$ .

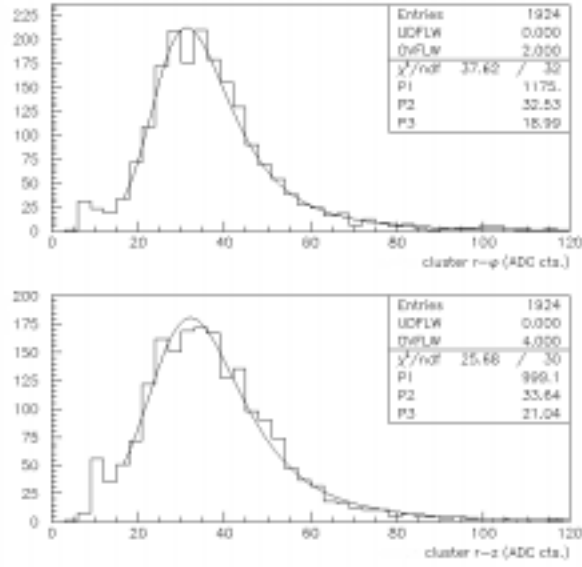


Figure 4.26: Cluster charge distribution for  $\beta$ -source signals for the junction side (upper Figure) and the ohmic side (bottom Figure). The fit is a convolution of a Gaussian and Landau distribution.

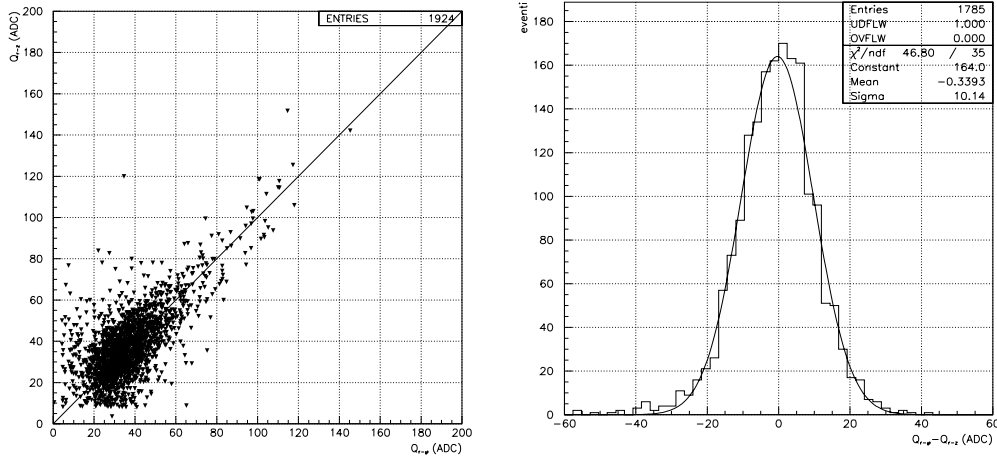


Figure 4.27: Left Figure shows the cluster charge correlation between clusters on the ohmic and the junction side. Right Figure shows the distribution of the difference between the cluster charge on the ohmic and junctions sides.

### 4.8.3 $S/N$ Measurement

Figure 4.29 shows the  $S/N$  distribution for both ladder sides. The fit yields a most probable value of  $S/N = 12.9 \pm 0.1$  for the junction side, and  $S/N = 9.2 \pm 0.1$  for the ohmic side. The discrepancy is related to the higher noise of the ohmic side. In double sided detectors the interstrip capacitance is usually higher for the ohmic side

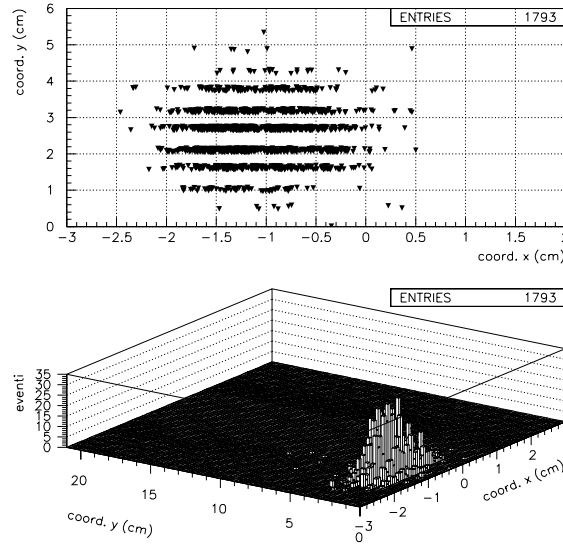


Figure 4.28:  $x$ - $y$  position of the cluster seeds for  $\beta$ -source hits of an ISL ladder.

than for the junction side. Taking into account the non optimized noise environment of the test setup, the results are satisfactory. The CDF Run-I experience shows that for tracking reconstruction, a  $S/N \sim 8$  is enough to assure the convergence of the algorithms [88].

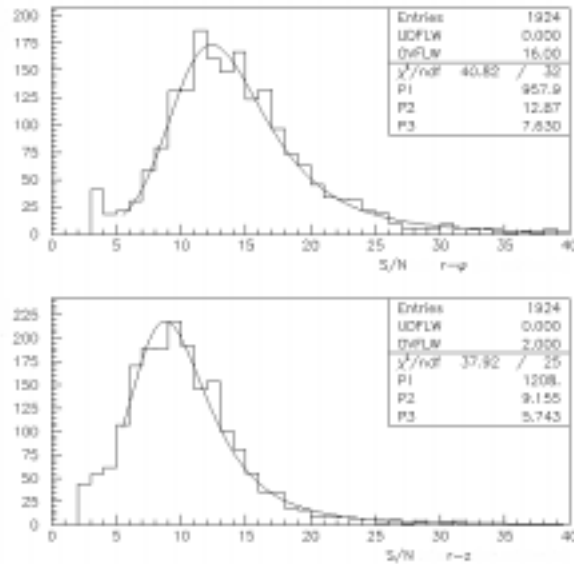


Figure 4.29:  $S/N$  ratio distribution for the junction side (upper Figure) and the ohmic side (bottom Figure).

### 4.8.4 Bandwidth Optimization

The SVX3 chip preamplifier bandwidth settings are used to maximize the signal-to-noise ratio for a particular detector configuration. Seven different bandwidth values can be set (BW1-BW7), where the lower bandwidth value corresponds to the faster risetime (Section 4.7.2). With a fast risetime the signal collection efficiency increases (Figure 4.22). However, signals with faster risetimes are more sensible to the so called *shot noise*, produced by the statistical fluctuations in the number of charge carriers (Section 3.1.6). With longer risetimes (higher bandwidths), the shot noise contribution decreases, but the reduction in signal collection efficiency might yield lower signal-to-noise ratios.

The dependence of the signal-to-noise ratio with respect to the bandwidth settings has been studied with the  $\beta$ -source setup described in Section 4.8. Figure 4.30 shows the  $S/N$  distribution for three different bandwidth settings (1, 4 and 7) for both the ohmic and junction sides. In our test setup, the best  $S/N$  ratios are achieved with the higher bandwidth, and therefore with longer risetimes for an integration time of 140 ns.

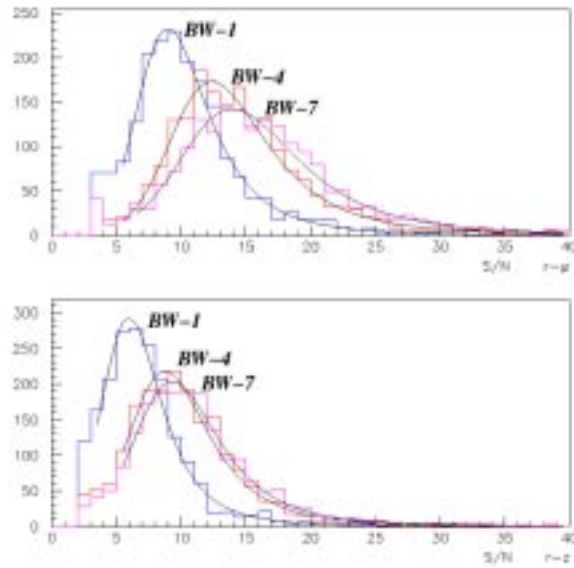


Figure 4.30:  $\beta$ -source  $S/N$  ratio distribution for different preamplifier bandwidth settings (1, 4 and 7) for the junction side (upper Figure) and ohmic side (bottom Figure). The integration time was 140 ns.

## 4.9 ISL Ladder Grading

The Level 2 readout time for the ISL detector is, on average,  $\sim 10 \mu\text{s}$  per event (Section 5.1). The SVX3 chip can be set to readout channels above a predefined

threshold (sparse mode). In this case, the ISL event size, and thus the time necessary to read out the event, strongly depends on the number of noisy channels with charge above threshold.<sup>16</sup> In principle, the event size from noisy channels could be reduced by increasing the sparsification threshold. However, an increase on the threshold reduces the hit detection efficiency. ISL ladders are graded based on the resulting noise occupancy for a given signal efficiency. A ladder is accepted if the occupancy due to noisy channels is  $\leq 2\%$  for signal efficiencies  $\geq 94\%$ .

For each ladder, the noise occupancy versus signal efficiency is calculated in the following way [87]. For each chip a threshold on the digitized charge can be set. This threshold is set equal to the average pedestal value ( $\overline{ped}$ ) plus an additional quantity ( $thres$ ), which may vary between 5 and 15 ADC counts. The pedestal and noise are measured for each channel. The fraction of time that a given channel is above  $\overline{ped} + thres$  is calculated using the channel's pedestal average value and noise, assuming a Gaussian distribution function (see Figure 4.2). Due to the neighbor logic, when a channel has a pedestal above threshold, the two neighbor channels are also readout. To include this effect, the fraction of time that a channel is readout is multiplied by 3. This overestimates the noise occupancy because two or more adjacent channels may be above threshold. The noise occupancy is calculated by averaging this number over all the channels in a chip.

Signal efficiency is calculated using a parameterization based on data taken with a radioactive source [87]. From the source data, the charge distribution on the strip with the maximum charge in the cluster is computed. From this distribution, the fraction of clusters where the value of the maximum charge strip is greater than  $\overline{ped} + thres$  minus the channels pedestal is calculated for each readout channel. This fraction is taken to be the signal efficiency. The result is scaled to 0, 0.33 or 0.66 depending whether the readout channel is completely disconnected, it has only one sensor disconnected, or has two disconnected sensors.

There is a threshold for which the noise occupancy is below the 2%. The signal efficiency is then calculated for such threshold. If the resulting efficiency is  $\geq 94\%$ , then the ladder is graded (Figure 4.31). From the 150 ladders built in Pisa, 144 met these requirements.

## 4.10 Final Assembly

Every two ladders with similar signal efficiency and noise occupancy are assembled together to form a module. The ladders are assembled gluing two thin carbon fiber strips along the edges of the ladder's carbon fiber support under the CMM machine.

After this procedure, another final test for pedestal and noise anomalies is performed, and finally the modules are shipped to Fermilab.

---

<sup>16</sup>For  $t\bar{t}$  events with a pile-up of 3 minimum bias and a noise occupancy of 1.6%, the readout time is  $\sim 8 \mu s$  [86].

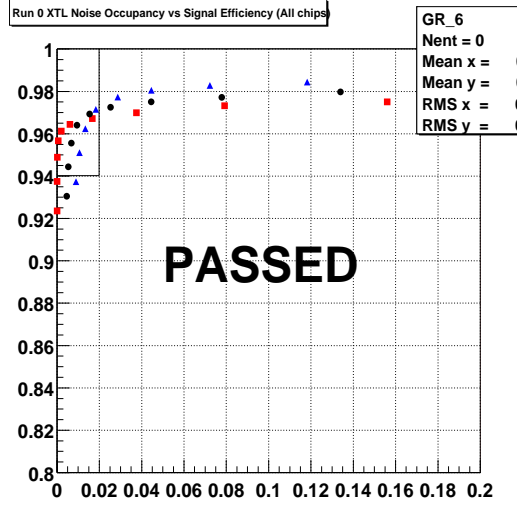


Figure 4.31: Signal efficiency *versus* noise occupancy for different threshold values for an ISL ladder. Red squares (blue triangles) show average values for the junction (ohmic) side. Black dots shows average values for both sides. The black box show the requirements for ladder grading ( $\geq 94\%$  of efficiency and  $\leq 2\%$  of occupancy). The ladder is accepted if at least one threshold passes the requirements.

## 4.11 Summary

As a result of the above described procedures, in the period between December 1999 and June 2000, 150 ISL ladders (over a total of 300) were assembled, fully instrumented, and tested at the INFN. They were shipped to the Fermi National Laboratory for its final insertion into the ISL detector as scheduled (Figure 4.32). Out of the 150 production ladders, 144 met the efficiency and noise occupancy requirements. The remaining 6 ladders were also accepted, but classified as lower quality ladders.

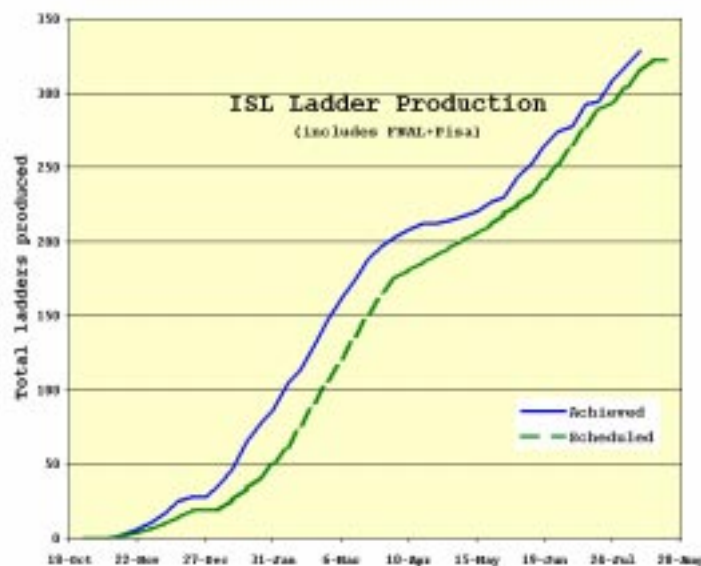


Figure 4.32: ISL ladder production schedule (green line) and achieved (blue line). About one half of the total number of ISL ladders were produced at the INFN, Pisa.

# Chapter 5

## The CDF Trigger System

In this chapter we describe the structure of the Run-II CDF trigger system and the hardware and software objects used for trigger decision at each trigger level. We also briefly describe the most relevant CDF offline event observables: primary vertices, jets, missing transverse energy, tracks and b-jet identification.

### 5.1 Introduction

In a  $p\bar{p}$  collider at  $\sqrt{s} = 1.98$  the elastic  $p\bar{p}$  cross section is approximately 50 mb [89]. At luminosities  $\sim 1 \cdot 10^{32}$  this cross section yields an event rate of 8 MHz. Typical interesting physics processes like  $W$  boson production,  $t\bar{t}$  production, or Higgs boson production (Figure 5.1) have cross sections ranging from  $10^{-8}$  to  $10^{-12}$  b, corresponding to production rates between 1 and  $10^{-4}$  Hz. Therefore, to study such processes only one event out of  $10^{12}$  is potentially interesting. Due to the limitations in data acquisition speed, available data storage, and analysis computing resources, an on-line data reduction system must be implemented. Data reduction is organized in a series of hierarchically decision levels, where discrimination between “interesting events” and other physical processes relies on their different event signatures and topologies, as well as on the amount of detector information and computing power available at each decision level.

The CDF trigger system is a buffered multilevel trigger system with 3 decision levels (Figure 5.2). The multilevel architecture allows higher data reduction than a single trigger level. At each trigger level more detailed detector data is available, and due to the rate reduction obtained from the previous level, more time is available to implement more powerful rejection algorithms (software or hardwired in dedicated processors), which leads to a net gain in “interesting” *versus* “background” events [94]. The buffering between the output and the input of the successive trigger levels allows to decouple the statistical fluctuations of the trigger decision latency inherent to each trigger level.

At CDF the Level 1 trigger uses custom designed hardware to find physics objects based on a subset of the detector information, and makes a decision based on a simple

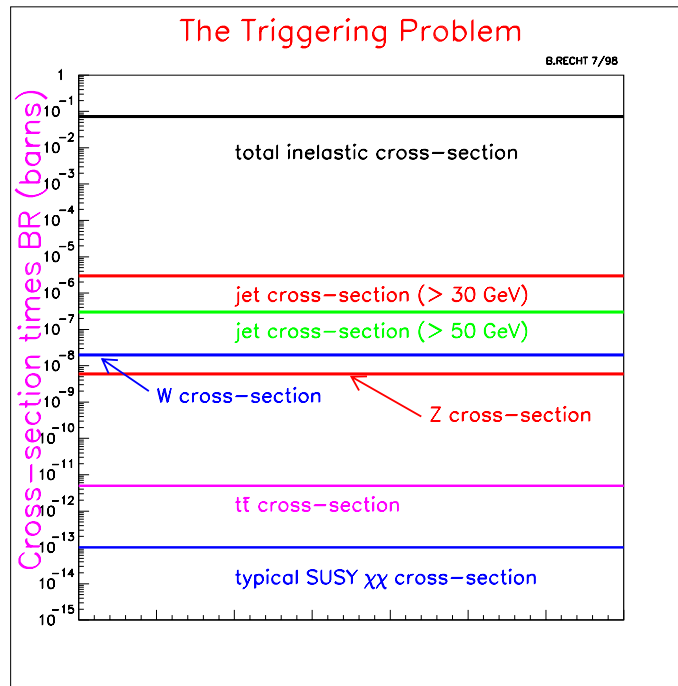


Figure 5.1: Production cross sections for typical processes in  $p\bar{p}$  collisions at  $\sqrt{s} = 1.8$  TeV.

counting of these objects. It consists of three parallel synchronous processing streams which feed the input of the single Global Level 1 decision unit. One stream processes calorimeter based objects, another finds muons, while the third finds tracks in the central tracking chamber. The latency is  $5.5\mu s$  and therefore, at each Tevatron bunch crossing, the incoming data is buffered in a pipeline waiting for the trigger decision. The maximum Level 1 output rate is 40 kHz.

The Level 2 trigger consists of several asynchronous subsystems which provide input data to programmable processors. When an event is accepted with the Level 1 trigger it is transferred to one of the four input Level 2 buffers. If the four buffers are full then the trigger system incurs in deadtime and eventually the Level 1 output rate must be reduced. To avoid this and minimize the deadtime [10], the Level 2 analysis is divided in two steps that can occur simultaneously: data collection of the trigger subsystems into the the Level 2 processors memory, and event analysis, also in the Level 2 processors. Each step takes  $\approx 10\mu s$ . Event analysis includes calorimeter clustering and track reconstruction with the silicon vertex data. The Level 3 trigger is based on a Personal Computer Farm. It processes the complete event record and partially reconstructs the event using the fully digitized information of the full detector. On average the event size is about 250 kbyte with an output rate to tape of  $\approx 75$  Hz. Table 5.1 summarizes the trigger rates at each level.

Data is collected through trigger paths. A trigger path is a unique combination of a Level 1, Level 2 and Level 3 trigger requirements which an event must satisfy to be

Scenario	Medium Luminosity	High Luminosity
$\mathcal{L} \text{ (cm}^{-2}\text{s}^{-1}\text{)}$	$1 \cdot 10^{32}$	$2 \cdot 10^{32}$
Number of bunches	36	108
Bunch-cross time ( $ns$ )	396	132
Mean interactions per crossing	2.3	1.5
Level 1 bandwidth	40 kHz ( $400 \mu b$ )	40 kHz ( $200 \mu b$ )
Level 2 bandwidth	300 Hz ( $3.0 \mu b$ )	300 Hz ( $1.5 \mu b$ )
Level 3 bandwidth	75 Hz ( $750 nb$ )	75 Hz ( $375 nb$ )

Table 5.1: Run-II nominal trigger bandwidth and conditions.

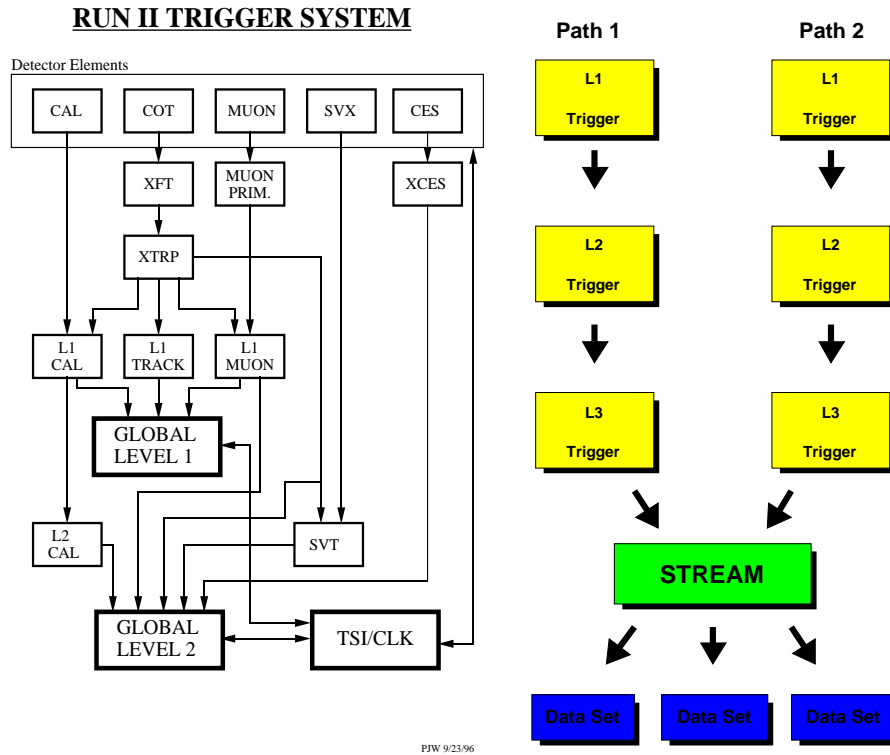


Figure 5.2: The Run-II CDF trigger functional block diagram (left figure), and the schematic representation of CDF trigger data paths and trigger data sets (right figure).

acquired with full detector information and be transferred to the permanent storage media. Trigger paths are grouped in datasets. A dataset is composed by events acquired only by a well defined group of trigger paths. Datasets are further grouped into “streams”. The DAQ system write each “stream” into a separate file. The event reconstruction farm then processes each “stream” independently and splits the output in several files each corresponding to the previously defined datasets. Events satisfying several trigger paths may enter in more than one “stream”. The definition

of the “streams” minimizes the amount of overlap. An schematic representation is shown in Figure 5.2.

## 5.2 Level 1 Trigger

The Level 1 trigger consists of three parallel synchronous processing streams (calorimeter, muon and tracking subsystem) and one global decision unit which can take decisions combining the hardware based objects found by each of the subsystems.

### 5.2.1 Calorimetric Objects

The goal of the Level 1 calorimeter trigger is to trigger on electrons, photons, jets, total event transverse energy ( $\sum E_T$ ) and missing transverse energy ( $\cancel{E}_T$ ). The calorimeter is organized into a bidimensional array of  $24 \times 24$  trigger towers. Each tower corresponds to a rectangle in  $\eta - \phi$  space of  $0.2 \times 15^\circ$ . For each tower the digitized electromagnetic and the electromagnetic plus hadronic energy is summed separately and weighted<sup>1</sup> by  $\sin \theta$  on the front-end cards to produce the transverse energy ( $E_T$ ) of the tower. The transverse energy is stored in 8 bit words with a least count of 250 MeV and a full scale of 63.75 GeV. The objects computed are:

1. Global  $\sum E_T$ : the sum of the hadronic and electromagnetic tower energy over the trigger towers. Two thresholds can be set on this quantity. A tower must have  $E_T$  over a pre-determined threshold to be included in the sum. This threshold can be 0., 0.5, 1.0 or 2 GeV. Currently it is set to 1.0 GeV.
2.  $\cancel{E}_T$ : the missing transverse energy is the magnitude of  $\vec{\cancel{E}}_T \equiv -\sum E_T^i \cdot \hat{n}_i$ , where  $\hat{n}_i$  is the unit vector in the transverse plane pointing from the detector geometrical center to the center of the calorimeter trigger tower.  $E_T^i$  is the total transverse energy ( $E^i \cdot \sin \theta$ ) deposited in the trigger tower. Only towers above a certain threshold are included in the sum. This threshold must be the same as the one set for the  $\sum E_T$ .
3. Single electromagnetic trigger tower over  $E_T$  threshold: a single trigger tower above a predefined threshold can generate a Level 1 trigger. The thresholds are set simultaneously in electromagnetic  $E_T$  and maximum hadronic  $E_T$ . The thresholds can be set separately tower-by-tower.
4. Single trigger tower with electromagnetic plus hadronic transverse energy over  $E_T$  threshold: the same as above but the threshold is set in the total transverse energy (electromagnetic plus hadronic).
5. Tower topology: conditions on the  $\eta$ ,  $\phi$  tower correlations can be set, *e.g.*, towers not adjacent in  $\phi$  or  $\eta$ , not back-to-back in  $\phi$ , *etc.*

---

<sup>1</sup>The angle  $\theta$  is computed respect to the detector geometrical center. See Section 2.2.1

### 5.2.2 Tracking Objects

At Level 1 tracking information is available for trigger decision. Tracks in the  $r - \phi$  plane of the Central Outer Tracker (COT) are found, and the  $p_T$ , sign and  $\phi_0$  (the track's azimuthal direction at the point of minimum approach with respect to the beam axis) are made available for matching with calorimeter or muon objects. Also certain selection criteria on the tracks can generate Level 1 triggers.

At each bunch crossing all the axial COT wires are read in parallel to the input of the eXtremely Fast Tracker (XFT). Within the Level 1 trigger latency of ( $5.5 \mu\text{s}$ ), the XFT finds the tracks in three steps (Figure 5.3): 1) the input hits from the axial sense wires are classified in *prompt* ( $\leq 44 \text{ ns}$ ) and *delayed* hits ( $> 44 \text{ ns}$ ).<sup>2</sup> Particles passing close to sense wires will produce prompt hits, and those passing far from sense wires will produce delayed hits. 2) In each superlayer hits are grouped into segments. The XFT boards hold dictionaries of masks of prompt and delayed hits that represent segments of valid hits (those originated from the beamline and have sufficient  $p_T$ ) passing through a given superlayer. The input hits must match the masks in the dictionaries. If they match, they form a *segment* and its average  $\phi$  position and slope is calculated. 3) Each of the four superlayer segments is compared to a mask that represents valid roads. The segments must match in  $\phi$  and slope. Once all tracks are found, for each road ( $\Delta\phi = 1.25^\circ$ ) the track with the highest  $p_T$  is selected and its  $p_T$  (6 bit resolution),  $\phi_0$  (3 bits) and sign is sent to the other Level 1 trigger subsystems for track matching and to the Trigger Level 1 global decision unit.

Starting from March 2001 Tevatron have been delivering  $p\bar{p}$  collisions at 1.980 TeV in the  $36 \times 36$  bunches mode with instantaneous luminosities of  $\sim 10^{30} - 10^{31} \text{ cm}^{-2}\text{s}^{-1}$ . As shown in Table 5.2, the XFT has been able to find tracks with better performance than the initial design goals [95].

	Projected	Achieved Aug 2001
Track finding efficiency:	96%	96%
Momentum resolution:	$\leq 2.0\% \cdot P_T^2 \text{ GeV}/c$	$\leq 1.8\% \cdot P_T^2 \text{ GeV}/c$
$\phi_0$ resolution:	$\leq 8 \text{ mR}$	$\leq 5.3 \text{ mR}$
Fake fraction ( $P_T = 10 \text{ GeV}/c$ ):	50%	50%

Table 5.2: Run-II XFT performance parameters.

A Level 1 trigger can be also generated based in the two track topology for events with at least two tracks<sup>3</sup>. A boolean function with all the two track combinations can be built such a way that, *e.g.*, it is possible to require minimum  $p_T$ , opposite sign and  $\phi_{min} < |\phi^i - \phi^j| < \phi_{max}$ .

<sup>2</sup>The COT TDC has a 1 ns resolution.

<sup>3</sup>For events with more than 7 tracks only an accept or reject decision can be issued.

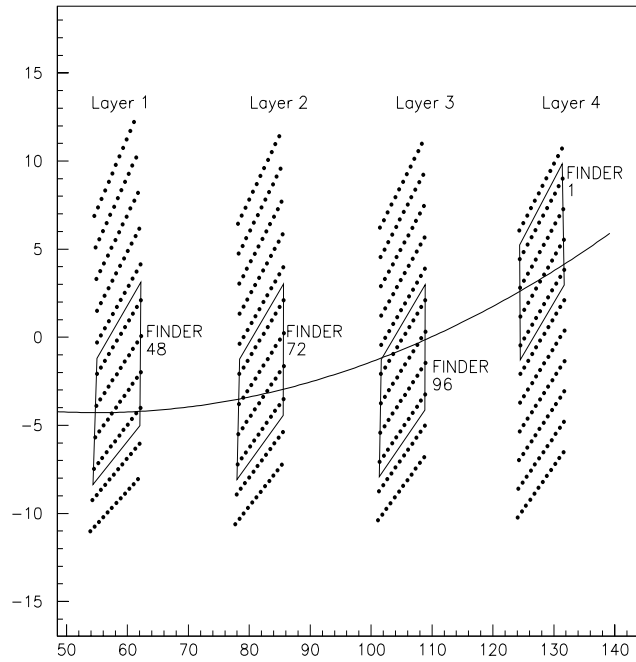


Figure 5.3: A view of a track in the COT. All cells in all four layers are shown. The relevant Finder segments in each layer is highlighted.

### 5.2.3 Muon Objects

The purpose of the Level 1 muon trigger is to provide single and dimuon objects for the Level-1 trigger decision. The muon system is composed of wire chambers and scintillators stacked radially from the interaction point. The definition of a muon object depends on the specific muon detector type (Figure 2.8): for scintillators (Central Scintillator Upgrade [CSP], Central Extension Scintillator [CSX]) is either single hits or two coincidence hits. For the wire chambers (Central Muon [CMU], Central Muon Upgrade [CMP], Central Muon Extension [CMX]) a set of aligned hits (*stub*) is searched for. Stubs can be matched with an XFT track if required [10].

### 5.2.4 Global Decision

The Level 1 trigger decision is issued by the Level 1 Decision card. Its output fills four event deep buffer where the triggered events are stored until the Level 2 Trigger system is free to receive them. This card is also able to *prescale* or limit the trigger rate in a programmable way. The level 1 triggers that can be issued are:

1. Calorimeter triggers: A total of 10 single object calorimeter triggers with different thresholds are allowed. Also 3 di-object triggers (triggers based on two tower topologies, as tower  $\eta$  and  $\phi$  correlations, towers not adjacent in  $\phi$  or  $\eta$ , not back-to-back, *etc.*) can be defined. In addition, is possible to cut on the

number of towers passing a particular list of thresholds. The maximum count is three.

2. Muon triggers They consist in the muon match to track trigger, and the multiple muons trigger, based in the presence of multiple muons with various thresholds, with or without tracks matched to them.
3. Electron triggers A single calorimeter trigger tower with electromagnetic or electromagnetic plus hadronic  $E_T$  above threshold can be match to tracks found by the XFT.
4. Two track topology. Combinations of different XFT tracks topologies.
5. Combinations of towers, muons and tracks: the Level 1 trigger decision board can require any combination of 8 trigger bits reported from the muon, calorimetry or tracking system.

## 5.3 Level 2 Trigger

The Level 2 trigger consists of three asynchronous subsystems aimed to the detection of jets and electrons, muons, and tracks with high impact parameter. The Level 2 trigger processing is divided in two steps that can run simultaneously: first all the data is collected from the Level 1 buffers, and all the three subsystems calculate their respective hardware objects simultaneously. This step takes  $\approx 10 \mu s$ . Next, the different Level 2 trigger cuts are implemented. In this step simple algorithms ranging from array ordering to simple linear equations solving can be implemented. The time latency for this part is also  $\approx 10 \mu s$ .

### 5.3.1 Calorimetric Clustering

Jets are not fully contained by a single trigger tower<sup>4</sup>. To be fully efficient, the thresholds on the towers must be lowered. However, lowering the trigger tower thresholds at Level 2 would yield unacceptably high rates to the input of Level 3. To avoid this rate increase, a clustering algorithm is performed to identify the jets using low single tower energy thresholds. The clustering algorithm uses the same Level 1 segmentation in trigger towers: a grid of  $24 \times 24$  trigger towers corresponding to a segmentation in  $\eta \times \phi$  of  $0.2 \times 15^\circ$ . In each event this grid is scanned beginning from tower (0,0) up to tower (24,24) in increasing  $\phi$ , and every 12 towers increasing in  $\eta$ . Every time a tower with transverse energy<sup>5</sup> above threshold

<sup>4</sup>Triggers based in single trigger towers are needed to find electrons.

<sup>5</sup>The transverse energy of the trigger tower at Level 2 is defined as  $E_T = E \times \sin \theta$  where  $\theta$  is measured from the geometrical center of the detector. This  $E_T$  is measured with 125 MeV precision and a maximum value of 127,875 MeV.

(*seed threshold*) is found, all the adjacent towers with transverse energy above another threshold (*shoulder threshold*) are added to the cluster. The addition finishes only when no more adjacent towers above the shoulder threshold are found. Towers once used are not used anymore. A list of found clusters together with their electromagnetic and hadronic transverse energy and the  $\phi$  and  $\eta$  index of the tower that initiated the cluster (the *seed* tower) are made available for trigger selection. Clustering is done four times with four different sets of thresholds for the seed and shoulder towers (Table 5.3), depending on which physical object must be identified (jets, high  $p_T$  leptons and photons, low  $p_T$  leptons, low  $p_T$  leptons for B-physics<sup>6</sup>). For the *seed* tower of the

cluster an isolation criteria is available for trigger decision. The triggers towers around the *seed* are summed in five different forms as shown in Figure 5.4. For each sum different thresholds can be set.

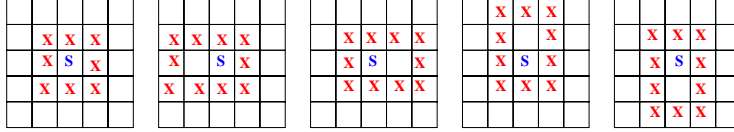


Figure 5.4: Tower sums for cluster isolation criteria. **S** denotes the seed tower, **X** the tower included in the sum.

	Seed		Shoulder		Physical Object
	$E_T^{em}$ (GeV)	$E_T^{had}$ (GeV)	$E_T^{em}$ (GeV)	$E_T^{had}$ (GeV)	
Pass 1:	3.0	1.0	—	—	low $p_T$ electron/photon
Pass 2:	8.0	7.5	—	—	high $p_T$ electron/photon
Pass 3:	3.0	1.0	3.0	1.0	jets
Pass 4:	2.0	—	—	—	low $p_T$ B-electron

Table 5.3: Level 2 clustering thresholds for seed and shoulder towers for the four passes.

### 5.3.2 $\sum E_T$ and $\cancel{E}_T$

Single tower information is not available at Level 2. Missing transverse energy ( $\cancel{E}_T$ ) and  $\sum E_T$  are not recalculated. However, both the  $\sum E_T$  and the  $x$  and  $y$  components of the  $\cancel{E}_T$  are available for trigger decisions.

### 5.3.3 Muons

A complete copy of muon objects is propagated from the Level 1 trigger and are available for the Level 2 trigger. However, association of the tracks to muon stubs is done with a  $1.25^\circ$  interval instead of  $2.5^\circ$  as done in Level 1.

<sup>6</sup>Low  $p_T$  leptons for B-physics requires also the rejection of clusters with hadronic energy. This requirement removes any other contribution to the energy of the reconstructed B-lepton.

### 5.3.4 Electrons

The information from the shower maximum detectors of the Electromagnetic Calorimeter (Section 2.2.6) is available at Level 2. It can be used to reduce the trigger rates in triggers aimed at the detection of electrons and photons, in particular those with low transverse energy thresholds.

Two thresholds on the pulse-heights of the wires can be set for high/low  $p_T$  electrons. When within a chamber a bit is set, an XFT track can be matched to the chamber (electron trigger) within a  $2^\circ$  resolution. When triggering with photons, the XFT matching is used as a veto. For the plug shower maximum the information available for triggering is basically the same, but there is not track matching since the detector is located outside of the  $\eta$  coverage of the Central Outer Tracker.

### 5.3.5 Silicon Vertex Trigger

At Level 2 track finding using the silicon detector data and track reconstruction with almost offline quality is possible with the Silicon Vertex Trigger (SVT) [12]. A list of reconstructed tracks in the plane transverse to the beam together with its  $p_T$ , track's charge,  $\phi_0$  (the track's azimuthal direction at the point of minimum approach respect to the beam axis) and track's impact parameter (respect to the beam-line) is available for trigger decision. The SVT performs tracking reconstruction in two separate steps: pattern recognition using associative memory (AM) algorithms with custom designed chips [96], and track fitting with dedicated boards.

To optimize the performance, the SVT data flow and data processing follows very closely the SVX II structure. The SVX II detector is divided in  $\phi$  in 12 wedges. The SVT processes each of the SVX II wedges in parallel, and each wedge is treated in an independent way. SVX II data is digitized and sparsified at the detector front end (Figure 5.5).

When an event is accepted by the Level 1 trigger, the digitized pulse heights in the SVX II is directed to the input of the Hit Finder boards [97]. The Hit Finder board performs pedestal subtraction and bad channel suppression. It scans the data stream for clusters of hit strips. When acceptable clusters are found, the Hit Finder computes and outputs the centroid of each cluster, defined as the most probable track intersection point at the SVX II layer. The output from the Hit Finder is sent to the Associative Memory (AM) [96], which also receives XFT tracks. With a look-up table, the cluster centroid position is translated into a coarser position resolution of  $250 \mu m$  (superstrip).<sup>7</sup> In the AM a set of custom designed CMOS chips at 30 MHz finds all the possible combinations of silicon hits in the four innermost layers of the SVX II plus extrapolated XFT tracks that corresponds to legitimate particle trajectory (roads) (see Figure 5.5). Road's configuration is programmable

---

<sup>7</sup>This translation is a compromise between a small size that would provide more precise pattern recognition and produce fewer fake-track candidates but require larger memory, and a large size which would output more fakes but require a small memory

to correct for any geometric misalignment. Once the AM is done, the road identifiers are sent to the Hit Buffer [98]. The Hit Buffer uses another look-up table to find the superstrips corresponding to each road. With the superstrip identifiers for each road the full SVX II hit information is retrieved and transmitted to the Track Fitter boards. The track fit is a linear approximation consisting of a set of scalar products. The resolution of the fit is nearly as good as offline reconstruction. Figure 5.6 shows the achieved resolution on impact parameter for data taken from March 2001 at  $\sqrt{s} = 1.980$  TeV at instantaneous luminosities of  $10^{30} \text{ cm}^{-2}\text{s}^{-1}$ . The design resolution is  $\sigma_d = 35 \mu\text{m}$  (at  $P_T = 2 \text{ GeV}/c$ ),  $\sigma_\phi = 1 \text{ mrad}$  and  $\sigma_{p_T} = 0.3\% p_T^2$  ( $p_T$  in  $\text{GeV}/c$ ). Note that to achieve this resolution detector misalignments must be kept under control. Misalignments in the  $z$ -direction between the beam-line and the SVX II ladders will produce incorrect impact parameter results (SVT has no available information about the  $z$ -coordinate). The SVX II barrels must be aligned with respect to the beam within  $100 \mu\text{rad}$ .

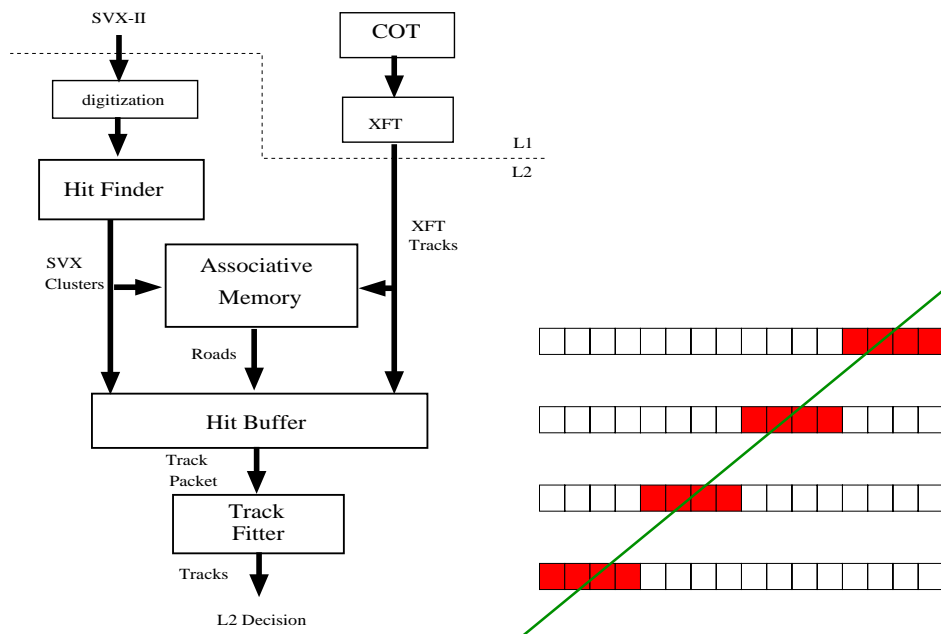


Figure 5.5: Architecture of the SVT trigger (left figure) and schematic representation of the pattern recognition algorithm (right figure).

## 5.4 Level 3 Trigger

At Level 3 trigger the full power of the offline reconstruction algorithms is in principle available, with the only limitation of the CPU time. Until now (August 2001), the

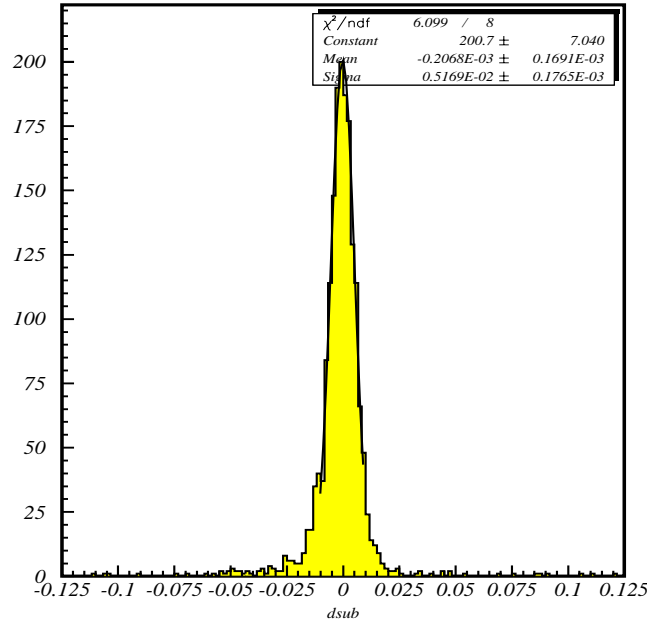


Figure 5.6: Impact parameter distribution of SVT reconstructed tracks with Run II early data ( $\mathcal{L} = 10^{30} \text{ cm}^{-2}\text{s}^{-1}$ ). Tracks have been reconstructed without any special detector alignment.

implemented algorithms that can be run every event<sup>8</sup> are:

1. Calorimeter *clean-up*: this algorithm is intended to discard calorimeter towers with energetic content due to photomultiplier spikes rather than energy released by particles originated in  $p\bar{p}$  collisions. The criteria is based in the charge asymmetry of the two photomultipliers that read the same calorimeter scintillating tile in the calorimeter tower (for true particles both photomultipliers yield the same pulse while for spikes only one yields a significant [usually huge] pulse). This procedure is only valid for the central calorimeter<sup>9</sup>.
2. Jet clustering: the offline jet reconstruction algorithms can be run for each event. See Section 5.5.
3. Central and Plug Electromagnetic shower clustering: reconstruction of electrons using the information of the Shower Maximum Detector can be done at Level 3 trigger.
4. Muon reconstruction.

<sup>8</sup>The maximum allowed input rate of the Level 3 Trigger is 300 Hz.

<sup>9</sup>The plug has only one photomultiplier per tile.

5. Central Outer Tracker reconstruction: reconstruction of tracks in the Central Outer Tracker can be done around seeds based on tracks found by the XFT that caused the Level 1 or Level 2 trigger. Reconstruction of all the tracks in the COT will be possible for tracks above certain threshold, or for single subsets of events to reduce the average execution time.

## 5.5 Event Reconstruction

Event reconstruction is aimed to the identification and measurement of physical entities such as electrons, muons, jets, b-jets and neutrinos using the fully digitized detector information. The event reconstruction software package consists of a number of independent modules, each of them performing a specific task. Modules communicates between them through a well defined interface and are executed sequentially (Figure 5.7), and, in some cases, in a well defined order (*e.g.* the tracking module must run before the electron finding module because electron identification requires tracks).

Event reconstruction can be run on the data stored in the permanent storage area or for some modules that are not very CPU consuming at Level 3 trigger, in the Level 3 trigger PC farm.

Below we give a very brief description of how CDF reconstructs the physical objects that are most relevant for this thesis: jets, missing transverse energy, track reconstruction, primary vertex finding and b-jet identification.

### 5.5.1 Jet Reconstruction

The fragmentation of quarks and gluons yields collimated showers of hadrons. A jet is a cluster of particles, such that its kinematic properties (*e.g.*, momenta) can be related to the corresponding properties of the energetic partons produced in the hard scattering process. In practice, jets appear in the detector as clusters of energy deposited in the calorimeter. There are two logical steps in the definition of a jet: the *jet algorithm* and the *recombination scheme*. The jet algorithm selects a set of particles (at the experimental level calorimeter towers), which are typically emitted close to each other in angle. The recombination scheme defines the procedure to combine their momenta to obtain the momenta of the jet. The standard CDF jet reconstruction algorithm uses a cone of fixed radius  $\Delta R \equiv \sqrt{(\Delta\eta)^2 + (\Delta\phi)^2}$  in  $\eta - \phi$  space. Other algorithms such the  $K_T$  algorithms are part of the standard CDF event reconstruction but they will be not discussed here. For the jet-cone algorithm, as a first step the calorimeter towers in the plug region are combined to match the  $\eta - \phi$  segmentation of the central region of the detector:  $\Delta\phi \times \Delta\eta = 15^\circ \times 0.1$ . Then the electromagnetic ( $E_T^{em}$ ) and hadronic ( $E_T^{had}$ ) transverse energies in all the towers are summed to form the total transverse energy ( $E_T$ ). The electromagnetic transverse energy,  $E_T^{em} \equiv E^{em} \sin \theta^{em}$ , is calculated

using the electromagnetic transverse energy in the tower,  $E^{em}$ , and the polar angle between the true event vertex and the center of the tower  $\theta^{em}$ .  $E_T^{had}$  is defined in the same way. For jet clustering all towers with  $E_T \geq 1$  GeV are taken as seed towers.

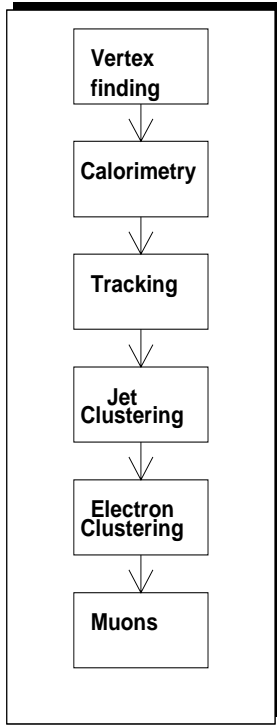


Figure 5.7: The logical flow of CDF event reconstruction in Run I.

ties:

$$E = \sum_i (E_i^{em} + E_i^{had}) \quad (5.1)$$

$$p_x = \sum_i (E_i^{em} \sin \theta_i^{em} + E_i^{had} \sin \theta_i^{had}) \cos \phi_i \quad (5.2)$$

$$p_y = \sum_i (E_i^{em} \cos \theta_i^{em} + E_i^{had} \cos \theta_i^{had}) \sin \phi_i \quad (5.3)$$

$$p_z = \sum_i (E_i^{em} \cos \theta_i^{em} + E_i^{had} \cos \theta_i^{had}) \quad (5.4)$$

The jet transverse momentum  $p_T \equiv \sqrt{p_x^2 + p_y^2}$ , its momentum  $p \equiv \sqrt{p_z^2 + p_T^2}$ , the pseudo-rapidity  $\eta \equiv \frac{1}{2} \ln \left( \frac{p+p_z}{p-p_z} \right)$ , and the transverse energy  $E_T \equiv E \cdot p_t/p$  are then defined. The detector pseudo-rapidity,  $\eta_d$ , is defined using the nominal interaction point ( $x = 0, y = 0, z = 0$ ) as the primary event vertex instead of the true event vertex used to define  $\eta$ .

Seed towers that are adjacent to one another, on a corner or side, are then grouped to form pre-clusters. The  $E_T$  weighted center of the pre-cluster is computed in  $\eta - \phi$  space. Pre-clusters are expanded to form clusters using a fixed cone algorithm; that is a cluster is defined as the set of all towers with  $E_T \geq 100$  MeV and within a distance  $\Delta R$  from the centroid of the pre-cluster. The cluster centroid is recomputed and its set of towers redefined accordingly. This procedure is repeated until the set of towers in the cluster does not change. In order to prevent the final cluster center from drifting too far away from the initial pre-cluster center, initial pre-clusters are always kept in a cluster irrespective of their distance from the final cluster center. If a cluster belongs to a larger cluster, only the larger cluster is retained. If two cluster share towers, they are merged into a single cluster if the total  $E_T$  in common towers is greater than one half of the  $E_T$  of the smaller cluster. Otherwise overlapping towers are divided according to their distance to the respective cluster centers.

Using the energy deposited in the calorimeters and the event vertex, the jet “four-momenta” ( $E, p$ ) is computed by summing over the towers in the clusters. In the following we give the definitions of the jet quantities:

On average, about 70% of the jet energy is contained in a cone of radius  $\Delta R = 0.4$ . At CDF, the typical cone sizes used are 0.4, 0.7 and 1.0.

### Jet Energy Corrections

The transverse energies and momenta as defined above refer only to the energy deposition observed in the calorimeter. These values differ from the true partonic values. There are five different corrections that are applied to jet energies: the *Absolute Energy Scale*, the *Relative Energy Scale*, the *Underlying Event*, the *Out of Cone* corrections, and the *Multiple Interactions* correction. Typically the jet energy corrections increase the jet energy by  $\approx 30\%$ , but they do not affect the jet energy resolution. The jet energy resolution is typically about  $120\%/\sqrt{E}$ .

1. The *Absolute Energy Scale* corrections compensate for the non-linear response of the calorimeters for hadronic and electromagnetic showers. They also compensate for the bending of low momentum particles in the magnetic field such that either they not reach the calorimeters or fall outside the jet clustering cone.
2. The *Relative Energy Scale* corrections compensate for the non uniform response of the calorimeters as a function of  $\eta_d$  and  $\phi$ .
3. The *Underlying Event* Corrections subtract the contribution of the underlying event to the jet energies. The correction accounts for additional energy deposited within the jet cone from sources other than the high energy parton originating the jet. For instance, from the uniformly distributed energy released during the rearrangement and deexcitation of the spectator partons.
4. The *Out of Cone* corrections compensate for the energy falling outside a particular jet clustering cone size. These corrections are derived using Monte Carlo simulation models.
5. The *Multiple Interactions Correction* take into account the effect of multiple interactions in the same event, when energy deposition from different interactions is overlayed.

The corrected  $p_T$  of a jet, clustered with a cone-size  $R$  is calculated in terms of its uncorrected  $p_T$ ,  $p_T^{raw}$ , via:

$$E_T(R) = E_T^{raw}(R) \cdot c_{rel}(R, \phi) \cdot c_{npv}(R) \cdot c_{abs}(R) - U(R) + O(R) \quad (5.5)$$

Where  $c_{rel}(R, \phi)$ ,  $c_{npv}(R)$  and  $c_{abs}(R)$  account for the relative  $\eta$  response of the detector, the effect of multiple interactions and for the absolute energy scale, respectively.  $U(R)$  takes into account the underlying event and  $O(R)$  corrects for the energy loss of particles such that due to the bending of the magnetic field either do not reach the calorimeter or fall outside the jet clustering cone.

### 5.5.2 Missing $E_T$ Measurement

The missing transverse energy is the magnitude of  $\vec{\cancel{E}}_T \equiv -\sum E_T^i \cdot \hat{n}_i$ , where  $\hat{n}_i$  is the unit vector in the transverse plane pointing from the detector geometrical center (for the uncorrected  $\cancel{E}_T$ ) or the primary vertex (corrected  $\cancel{E}_T$ ) to the center of the calorimeter tower.  $E_T^i$  is the total transverse energy ( $E^i \cdot \sin \theta$ ) deposited in the  $i$  tower. Only towers above a certain threshold are included in the sum.

$\cancel{E}_T$  must be corrected when muons are present in the event. High  $p_T$  muons are minimum ionizing particles leaving on average about 2–3 GeV in the calorimeters, regardless of their momentum. Therefore, the muon jet energy in the calorimeter is heavily underestimated, what significantly contributes to the  $\cancel{E}_T$  of the event. The correction is performed subtracting to the measured  $\cancel{E}_T$  the transverse momentum of the muon and adding its transverse energy.

### 5.5.3 Track Reconstruction

The CDF solenoid provides an almost uniform axial magnetic field of 1.5 Tesla over a volume of 2.8 diameter and 3.5 meters length. Within such magnetic field  $\vec{B}$ , particles of charge  $qe$  are subject to the Lorenz force:

$$\vec{F} = qe\vec{v} \times \vec{B} \quad (5.6)$$

and move along helices of radius

$$r = \left| \frac{p_T}{qeB} \right| \quad (5.7)$$

At CDF such helix is parametrized using the following 5 parameters [99]:

$\cot \theta$ : cotangent of the polar angle.

$C$ : semicurvature of the helix. The sign is the same as the particle charge.

$z_0$ :  $z$  coordinate of the helix's point closest to the  $z$  axis.

$D = Q \cdot |S - \rho|$ : signed impact parameter, where  $Q$  is the particle charge sign,  $S$  the distance from the center of the helix to the origin and  $\rho$  the helix radius (Figure 5.8).

$\phi_0$ : azimuthal direction of the track at the helix's point closest to the  $z$ -axis.

With such parametrization the helix equations are:

$$\phi(R) = \phi_0 + \sin^{-1} \left( \frac{CR + (1 + CD)D/R}{1 + 2CD} \right) \quad (5.8)$$

$$z(R) = z_0 + \frac{\cot \theta}{C} \sin^{-1} \left( C \sqrt{\frac{R^2 - D^2}{1 + 2CD}} \right) \quad (5.9)$$



a road in  $R - \phi$  and  $R - z$  projections are calculated. At each consecutive silicon layer the algorithm scans for hits inside the road and new hits are added fitting them to a helix via a progressive (Kalman) filter [100].

For the  $1. \leq |\eta| \leq 2$  region where there is not COT coverage tracking reconstruction is performed using silicon information only.

For reconstructed tracks the impact parameter resolution can be parametrized in the form:

$$\sigma_d = \sqrt{a^2 + \frac{b^2}{p_T^2}} \quad (5.10)$$

where  $\theta$  is the polar angle of the track, the constant term  $a$  depends on the intrinsic detector resolution and other systematic effects as primary vertex position and wedge to wedge misalignments, and the constant  $b$  reflects the impact parameter degradation at low  $p_T$  due to multiple Coulomb scattering, that ultimately depends in the amount and characteristics of the material crossing. Table 5.4 shows the values for the expected Run-IIa impact parameter resolution in the  $R - \phi$  and  $R - z$  planes.

$\sigma_d = \sqrt{A^2 + B^2/P_T^2}$	$R - \phi$		$R - z$	
	$A(\mu m)$	$B(\text{ GeV }/(c \cdot \mu m))$	$A(\mu m)$	$B(\text{ GeV }/(c \cdot \mu m))$
<b>Run-Ib</b>	19	33	–	–
<b>Run-IIa</b>	6	27	16	60

Table 5.4: Impact parameter resolution at normal incidence angle.

### 5.5.4 Primary Vertex Identification

The primary vertex is determined on an event by event basis. The algorithm fits all SVX tracks to a common vertex using the average beam position as a constraint. Tracks with large impact parameter are removed, and the fit repeated. This procedure is repeated until there is no large impact parameter track used in the fit. The uncertainty in the fitted primary vertex coordinates perpendicular to the direction of the beam lies in the range  $6 - 36 \mu m$  depending on the topology and the number of tracks in the event. When multiple interactions occur in the same event, multiple separated primary vertices can be identified. The event vertex with the highest total transverse momentum of attached tracks is chosen as default. All tracks used in the vertex fit and subsequent analysis are required to extrapolate within 5 cm of this vertex along the beam direction. In Run-I, for CTC tracks with  $P_T \geq 2 \text{ GeV}/c$ , the resolution on the extrapolation to the  $z$  position along the beam axis has been  $\approx 6 \text{ mm}$ .

### 5.5.5 b-Jet Identification

Jets from the hadronization of b-quarks can be identified by the presence of secondary vertices inside the jet. For high  $p_T$  b-hadrons (compared with the scale set by the b-quark mass), the long b-lifetime ( $\tau = 1.549 \pm 0.20$  ps [91]) results in a long average decay length ( $ct = 400 \mu\text{m} \cdot \gamma$ ), with the presence of detectable secondary vertices from the b-hadron decay.

CDF has developed three b-identification algorithms based on the long average decay length of B-hadrons: the SECVTX or *jet-vertexing* algorithm, *jet-probability* and the  $d - \phi$  algorithm.<sup>10</sup> All the three algorithms require the size of the track's impact parameter,  $d$ , to be large compared to its estimated uncertainty, and all of them are applied to sets of silicon tracks associated with jets [103].

The SECVTX or *jet-vertexing* algorithm,<sup>11</sup> selects tracks inside a jet (the opening angle between the track direction and the jet direction is required to be  $< 35^\circ$ ) with at least two silicon hits, an impact parameter significance  $|d|/\sigma_d \geq 2.5$  and  $P_T \geq 0.5$  GeV/ $c$ . For tracks with only two silicon hits, the hits are required to be in consecutive silicon layers and have a  $P_T \geq 1.5$  GeV. Tracks consistent with coming from the decay  $K_s \rightarrow \pi^+\pi^-$  or  $\Lambda \rightarrow \pi^-p$  are not used. Pairs of tracks, one of them with  $P_T \geq 1.5$  GeV/ $c$  are constrained to pass through the same space point to form a seed vertex. If at least one additional track is found to be consistent with intersecting this seed vertex, the seed vertex is used as a secondary vertex. If no additional tracks are found, additional requirements are imposed on the seed vertex tracks: one of the tracks must have  $p_T \geq 1.5$  GeV/ $c$  and the other  $p_T \geq 1.0$  GeV/ $c$ , both must have at least three silicon hits and  $|d|/\sigma_d \geq 3.0$ . The reconstructed vertex has an associated  $\chi^2$ . If one of the tracks contributes to the  $\chi^2$  by more than 50, then they are removed and a new seed vertex is formed. Next, the decay length of the secondary vertex  $L_{xy}$  (Figure 5.9), is computed by projecting in the plane transverse to the beam line the vector pointing from the primary vertex to the secondary. The jet axis is also projected in the plane transverse to the beam axis. If the cosine of the angle between these two projections is positive (negative), then  $L_{xy}$  is positive (negative). Most of the secondary vertices from the b or c-hadrons are expected to have positive  $L_{xy}$ , while secondary vertices constructed from a random combination of missmeasured tracks have a symmetric distribution around  $L_{xy} = 0$ . To reduce the background, a jet is considered tagged by SECVTX if it contains a secondary vertex with  $\frac{L_{xy}}{\sigma_{L_{xy}}} > 3$ , where  $\sigma_{L_{xy}}$  is the estimated uncertainty on  $L_{xy}$ , which is of the order of  $100 \mu\text{m}$ .

The *jet-vertexing* algorithm is the most consistent with our trigger strategy, and thus it is the only one used to evaluate the b-tag rates. The b-tag efficiency and

<sup>10</sup>We will not consider the alternative way of b-identification searching leptons produced in the decays of the b-quark through  $b \rightarrow l\nu_l X$  ( $l = e \text{ or } \mu$ ), or  $b \rightarrow c \rightarrow l\nu_l X$ . It is described in detail in [103].

<sup>11</sup>The SECVTX algorithm is the most used algorithm in CDF and is the only one that will be discussed here. The other two algorithms are described in detail in [103].

fakes tags rate per taggeable jet<sup>12</sup> inside the SVX' fiducial region measured with the CDF Run-I data is shown in Figure 5.10.

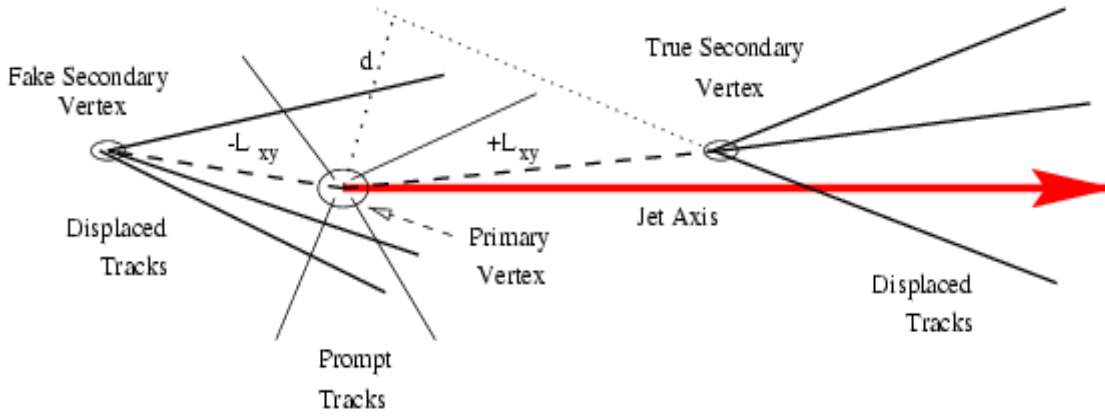


Figure 5.9: Schematic representation of the *jet vertexing* algorithm.

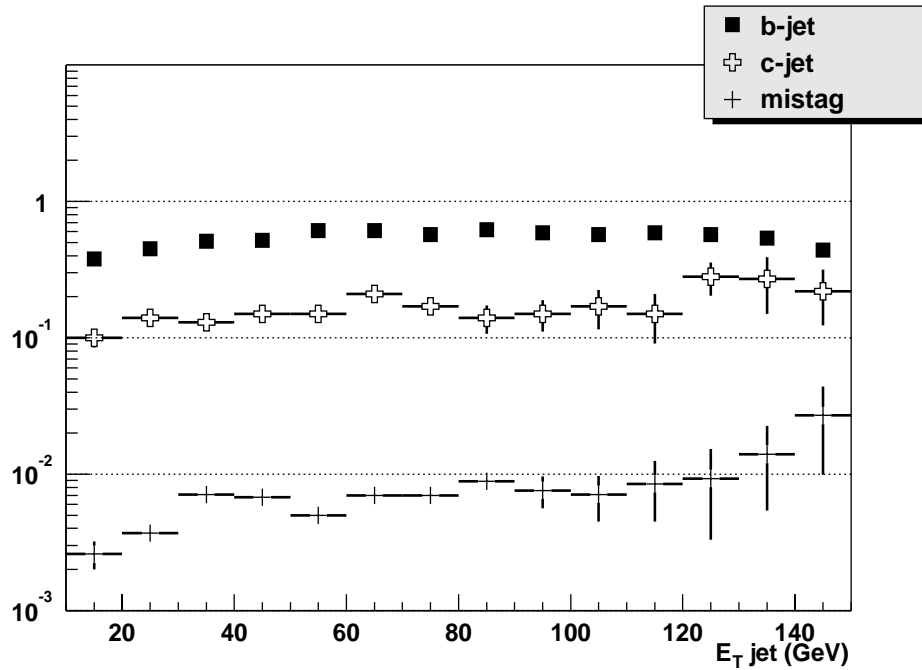


Figure 5.10: The SVX' b/c/fakes tagging efficiency per jet inside the SVX' fiducial region with the SECVTX tagger [104].

<sup>12</sup>A taggeable jet is defined as a jet with at least two or more good silicon tracks inside the jet cone. Good silicon tracks must have at least two silicon hits, not coming from channels with low gain or high noise, and must have a charge profile consistent with that of a single particle. They must exactly match a COT track. A condition on the  $\chi^2$  of the track fit is also required [103].



# Chapter 6

## Trigger Rate and Efficiency Calculation

In this chapter we discuss the general procedures used in next chapters to estimate the rate and signal efficiency of an arbitrary trigger. The formula relating the rate, trigger efficiency and instantaneous luminosity is presented, and the correction for the case of multiple interactions is deduced. Detector and accelerator effects, with a high impact in trigger rates (like the beam halo) are very difficult to reproduce with Monte Carlo simulations. Therefore, a reliable trigger rate estimation can only be done using real data. In absence of quality Run-II data at the time of this work, we use Run-I data for this purpose. Therefore, signal efficiency and trigger rates are evaluated using the CDF detector with the Run-I configuration. From a functional point of view, the Run-I and Run-II calorimeter triggers are the same, thus the functionality of the Run-II CDF trigger can be successfully evaluated using the Run-I CDF offline reconstruction code. The Run-II Silicon Vertex Trigger (SVT) uses the SVX II information in a configuration very similar to the Run-I SVX' detector, with the only exception of the larger geometrical acceptance. However, corrections to account for it can be easily calculated. Finally, a cross check with preliminary Run-II data taken at low instantaneous luminosities is presented.

### 6.1 Rate Calculation

In a particle collision experiment the number of observed events related to a particular process can be described as the product of two independent factors:

$$\text{Rate (events/s)} = \mathcal{L} (cm^{-2}s^{-1}) \cdot \sigma (cm^2) \quad (6.1)$$

where  $\sigma$  (the *cross section*) depends on the dynamics of the process itself (collision energy, spin polarization and others), and the constant coefficient  $\mathcal{L}$  (*luminosity*) depends on the properties of the colliding particle beams. For a collider accelerator like Tevatron, where one bunch of  $N_p$  protons and one bunch of  $N_{\bar{p}}$  antiprotons

collide every  $1/f_c$  seconds (where  $f_c$  is the crossing frequency), the luminosity can be expressed as [38]:

$$\mathcal{L} = \frac{N_p \cdot N_{\bar{p}}}{A} \cdot f_c \quad (6.2)$$

where  $A$  is the effective overlap area of the two colliding bunches.

For a given trigger scheme with efficiency  $\epsilon_T$ <sup>1</sup>, assuming at most one interaction per bunch crossing, the trigger rate can be expressed in the form:

$$R_T = \epsilon_T \cdot \mathcal{L} \cdot \sigma \quad (6.3)$$

where  $\sigma$  is the inclusive cross section of the total inelastic cross section and  $\mathcal{L}$  the instantaneous luminosity. In practice the corrections for the multiple interactions are sizeable. We will describe then in the following Section.

## 6.2 Correction for Multiple Interactions

The number of  $p\bar{p}$  interactions at each bunch crossing follows a Poisson distribution function with mean:

$$\mu = \sigma \cdot \frac{\mathcal{L}}{f_c} \quad (6.4)$$

where  $f_c$  is the bunch crossing frequency. Therefore, the trigger rate can be written as:<sup>2</sup>

$$R_T = (1 - e^{-\mu}) \cdot f_c \cdot \epsilon_T \quad (6.5)$$

where  $\epsilon_T$  is the trigger efficiency. From Equations 6.4 and 6.5, the trigger rate can be written as:

$$R_T = \epsilon_T \cdot \frac{1 - e^{-\mu}}{\mu} \cdot \mathcal{L} \cdot \sigma \quad (6.6)$$

The trigger cross section  $\sigma_T$  is obtained dividing by the luminosity, therefore:

$$\sigma_T = \epsilon_T \cdot \frac{1 - e^{-\mu}}{\mu} \cdot \sigma \quad (6.7)$$

and (assuming that the multiple interactions do not affect the  $\epsilon_T$ ) the trigger rate can be written as:

$$R_T = \sigma_T \cdot \mathcal{L} \quad (6.8)$$

Note that in the limit of small  $\mu$  equations 6.8 and 6.7 yield the formula 6.3.

---

<sup>1</sup>The trigger efficiency is calculated as the number of events which satisfy the trigger requirements divided by the total number of inelastic events.

<sup>2</sup>In a Poisson distribution with mean  $\mu$  the probability of no events at all is  $e^{-\mu}$ . Therefore, the probability of at least one event is  $1 - e^{-\mu}$ .

## 6.3 Data Samples for Rate Estimation

We use Run I data samples to calculate rates for an arbitrary trigger in the following way. First, we select a Run-I data sample with trigger requirements less restrictive than the requirements under study. In this way, any possible event which satisfies our trigger requirements will be contained in the data sample. The use of data samples taken with the loosest requirements gives us more space to apply different trigger strategies. We must ensure also that the data sample contains enough statistics in events which satisfy our trigger requirements. Next, the efficiency,  $\epsilon_T$ , of our trigger applied to the data sample is calculated. If the cross section of the data sample,  $\sigma_T$ , is known, Equation 6.8 gives the rate for a given luminosity. With this procedure we neglect the possible dependence of  $\epsilon_T$  on the number of primary interactions. How to deal with this is explained in Section 6.5.

The *minimum bias* data sample is used to evaluate the Level 1 trigger rate. In particular, we use a minimum bias data sample which consists of about 1.383.000 events recorded at all instantaneous luminosity conditions across the entire Run-IB with the *minimum bias trigger*.<sup>3</sup> This trigger is the most inclusive trigger in the CDF detector and thus the most suitable to study the trigger at Level 1. Its cross section [105] has been measured to be  $\sigma_{BBC} = 51 \pm 2$  mb.<sup>4</sup> The corresponding trigger cross section can be calculated using Equation 6.7.

At Level 2 the minimum bias data sample is not appropriate. For our studies at Level 2 at least one calorimeter cluster with high transverse energy ( $E_T \geq 20$  GeV) will be required. From the 1.383.000 events of the minimum bias sample only  $\approx 1500$  events remain after requiring at least a cluster with  $E_T > 20$  GeV. These are too few to make statistically reliable estimations. Instead, we can use a data sample acquired with the loosest possible requirements at Level 2 and with a well known trigger cross section. With such data sample, trigger rates can be calculated following the above described procedure. The most appropriate is the *JET-20* data sample which consists of  $\approx 400.000$  events recorded at all luminosity conditions across the Run-IB. The Level 2 trigger on this sample requires at least one cluster with  $E_T > 20$  GeV. From the QCD triggers the *JET-20* is the one with the lesser restrictive requirements. Since all trigger strategies studied in this thesis required jets at Level 2 trigger, this dataset is perfectly adequate. The cross section of this trigger has been measured

---

<sup>3</sup>The minimum bias trigger requires one event in the Beam-Beam Counter (BBC) detectors [105]. The Beam-Beam counters were two sets of scintillator counters, each of them located at  $\pm 5.82$  m from the nominal interaction point. The counters were placed at a low angle with respect to the beam direction, covering the angular region (measured along either the horizontal or vertical axes) from  $0.32^\circ$  to  $4.47^\circ$  ( $179.68^\circ$  to  $175.53^\circ$ ). A BBC interaction was defined as the coincidence of an *in time* hit in any of the 16 counters on one side and an *in time* hit in any of the 16 counters in the opposite side, where an *in time* hit was a hit in a 30 ns gate centered on the expected arrival time.

<sup>4</sup>The CDF measured value of the total  $p\bar{p}$  cross section at  $\sqrt{s} = 1.8$  TeV using the luminosity independent method is  $\sigma_{total} = 80 \pm 3$  mb [89] with a value for the inelastic cross section very close to  $\sigma_{BBC}$ .

and its value found to be  $\sigma_{JET20} = 7.50 \pm 0.30 \mu\text{b}^5$  [107].

The *minimum bias* and the *JET-20* samples are correlated. The CDF measured inclusive jet production at  $\sqrt{s} = 1.8 \text{ TeV}$  ( $E_T^{jet} \geq 20 \text{ GeV}$ ) has a cross section of the order of several microbarns [108], three orders of magnitude less than the total  $p\bar{p}$  cross section. Therefore, in the minimum bias data sample one could expect the same proportion of events satisfying the *JET-20* requirements. Indeed, as stated above, from the 1.383.000 events of the minimum bias sample only  $\approx 1500$  events remain after requiring at least a cluster with  $E_T > 20 \text{ GeV}$ .

Several cleanup cuts are made on the raw *JET-20* samples to remove effects specific to the performance of the Run-I operational conditions. In addition, only events with a well determined primary vertex are used for studies depending on the track's impact parameters cuts.

In Run-II the center of mass collision energy will increase from the Run-I  $\sqrt{s} = 1.8 \text{ TeV}$  to  $\sqrt{s} = 1.98 \text{ TeV}$ . The increase in the cross section for the generic QCD data samples is estimated to be of the order of 20% [109]. This increase is included as an uncertainty in the trigger rate estimations.

Trigger rate estimates can be affected by a series of other systematic errors leading to higher trigger rates. For each trigger proposal, a complementary trigger requirement has been identified, such that increasing its threshold the rates can be controlled without abrupt reductions of signal efficiency.

## 6.4 Signal Trigger Efficiency

In this thesis all signal processes are simulated at generator level with the PYTHIA Monte Carlo program<sup>6</sup> [90] at  $\sqrt{s} = 1.98 \text{ TeV}$ . Subsequent decay of B-hadrons are corrected with the program CLEOMC [110]. Detector response is simulated with the standard Run-I CDF program QFL'. The program QFL' can accept as input the list of the final state particles generated by PYTHIA and simulate the detector response in each of the subsystems. The simulation is a parameterization of the detector response tuned to  $p\bar{p}$  collisions data or based on testbeam measurements. The calorimeter trigger simulation consists simply in the rearrangement of the digitized energy according to the trigger tower segmentation. The simulation of the SVT is evaluated using offline reconstructed tracks and is discussed in detail in Section 7.5.2.

## 6.5 Run-II Luminosity Extrapolation

In Run-II the average instantaneous luminosity will be increased by a factor of  $\sim 20$  (from  $1 \cdot 10^{30}$  to  $1\text{-}2 \cdot 10^{32} \text{ cm}^{-2}\text{s}^{-1}$ ). For a given bunch spacing, an increase in

<sup>5</sup>The total prescale factor was 1000: 40 at Level 1 and 25 at Level 2.

<sup>6</sup>Version 6.115.

the instantaneous luminosity translates into an increase in the number of multiple interactions, as shown in Figure 6.1 and Table 6.1

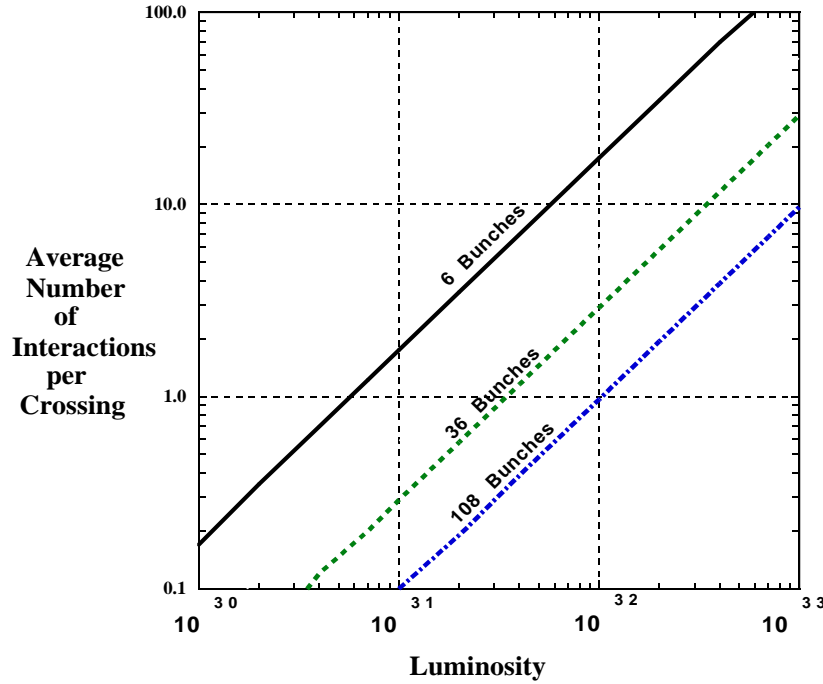


Figure 6.1: Average number of interactions per bunch crossing as a function of the average instantaneous luminosity, from Reference [10]). The plot shows the Run-I configuration (6 bunches,  $\Delta t = 3.5 \mu s$ ) and the Run-II configuration (36 bunches,  $\Delta t = 396 \text{ ns}$ , and 108 bunches  $\Delta t = 132 \text{ ns}$ ).

	Average Luminosity ( $\times 10^{30} \text{ cm}^{-2} \text{ s}^{-1}$ ).			
	3.77	7.32	11.98	16.92
Data vertices	$1.7 \pm 0.2$	$2.0 \pm 0.3$	$2.5 \pm 0.3$	$3.0 \pm 0.2$
Estimated $\mu$	$1.4 \pm 0.2$	$1.8 \pm 0.2$	$2.4 \pm 0.2$	$3.2 \pm 0.1$

Table 6.1: Measured average number of vertices found by the CDF Run-I vertex time-projection chamber VTX [111] as a function of the instantaneous luminosity [112] for the minimum bias data sample. The average number of interactions  $\mu$  is estimated from Equation 6.4 for the Run-I bunch crossing interval of  $\Delta t = 3.5 \mu s$ , a cross section given by  $\sigma_{BBC} = 51.15 \pm 1.60 \text{ mb}$ , and corrected by  $1/(1 - e^{-\mu})$  to take into account that the data sample was taken with the condition of at least one interaction.  $\mathcal{L}$  is taken equal to the average value per luminosity bin ( $\Delta \mathcal{L}_{bin} = 5 \text{ cm}^{-2} \text{ s}^{-1}$ ).

The increase of multiple interactions greatly deteriorates the detector performance and potentially can vary the trigger efficiency.<sup>7</sup> The ideal condition is to

<sup>7</sup>Event overlaps produce a greater number of hits and thus tracking reconstruction becomes

have one interaction per bunch crossing. In Run-I, with an average instantaneous luminosity of  $8.3 \cdot 10^{30} \text{ cm}^{-2}\text{s}^{-1}$  and a bunch interval of  $3.5 \mu\text{s}$ , the average number of interactions was  $\sim 2.3$ . In Run-II, to avoid the increase of multiple interactions at higher luminosities the bunch crossing interval will be reduced (Equation 6.4). In Run-II two operational scenarios are considered:

- $\mathcal{L} = 1 \times 10^{32} \text{ cm}^{-2}\text{s}^{-1}$ ,  $\Delta t = 396 \text{ ns}$ ,  $\bar{\mu} \sim 3$
- $\mathcal{L} = 2 \times 10^{32} \text{ cm}^{-2}\text{s}^{-1}$ ,  $\Delta t = 132 \text{ ns}$ ,  $\bar{\mu} \sim 2$

Therefore, a reliable trigger efficiency estimation for Run-II conditions using Run-I data must be done with data acquired with the same number of multiple interactions. As a first approximation, to have enough statistics when applying trigger cuts, all the events in the data sample will be used to calculate the trigger efficiency. As a second approximation the Run-I data will be binned according to the number of interactions per bunch crossing, and trigger efficiencies will be calculated for each bin. If no dependence from the 2 to the 3–4 interactions bins is observed the obtained value for the trigger efficiency will be considered as a reliable estimation.

---

more difficult due to the increase of the combinatorial background. In the calorimeter, energy deposits from multiple events will be overlayed.

# Chapter 7

## Design of a Dedicated Trigger for $H + W/Z \rightarrow b\bar{b}jj$ Searches

Run-I CDF searches for the Higgs boson in the  $H + W/Z \rightarrow b\bar{b}jj$  channel were done with data collected with the multijet trigger, specifically designed for the top quark search. For Higgs boson searches this trigger needs significant improvements since it rejects almost 75 % of the events for Higgs boson masses below  $135 \text{ GeV}/c^2$ . In this Chapter we study the design of a new improved multijet trigger exploiting the CDF capability to trigger on large impact parameter tracks at Level 2. It intends to be efficient for Higgs boson masses up to  $135 \text{ GeV}/c^2$ . We show that the trigger efficiency can be improved by a factor of 2 with respect to the Run-I multijet trigger with background rates well under control. In addition, with this trigger the specific selection of the Run-I analysis is enhanced by a factor of 2.

### 7.1 Motivation

In the mass region covered by the Tevatron c.o.m energies ( $100 \text{ GeV}/c^2 \lesssim m_{\text{hSM}} \lesssim 200 \text{ GeV}/c^2$ ) the two most copious production mechanisms for the SM Higgs boson are the gluon-gluon fusion process  $gg \rightarrow H$  ( $\sigma = 1 - 0.1 \text{ pb}$ ) and the associated production with a vector boson  $H+W/Z$  ( $\sigma = 0.38 - 0.16 \text{ pb}$ ). For masses below  $135 \text{ GeV}/c^2$ , the low mass region, the predominant decay is  $H \rightarrow b\bar{b}$  with branching ratios ranging from 0.76 to 0.44. For higher masses the predominant decay channel is  $H \rightarrow WW^*$ .

For the low mass region the gluon-gluon fusion production mechanism with the subsequent decay  $H \rightarrow b\bar{b}$  is very hard to resolve from the overwhelming background of QCD heavy flavor production [113]. In the associated production channel the signature of the vector boson ( $W \rightarrow q\bar{q}', l\bar{\nu}$ ;  $Z \rightarrow q\bar{q}, l\bar{l}, \nu\bar{\nu}$ ) provides a simple criteria for signal discrimination, while the identification of the b-jets from the  $H \rightarrow b\bar{b}$  decay allows to reconstruct its mass without ambiguities. Earlier studies [13] have identified the leptonic decay channels of the associated boson as the most likely modes for

$M_H$ (GeV/ $c^2$ )	$\sigma_{HW}$ (pb)	$\sigma_{HZ}$ (pb)	BR( $H \rightarrow b\bar{b}$ )	Events (2 fb $^{-1}$ )	Events (15 fb $^{-1}$ )
110	0.25	0.13	0.76	397	2976
115	0.20	0.12	0.73	321	2409
120	0.17	0.10	0.68	253	1893
125	0.13	0.09	0.61	187	1385
130	0.12	0.08	0.53	146	1094
135	0.10	0.06	0.44	97	726

Table 7.1: Predicted total number of events for the associated production channel  $H + W/Z \rightarrow b\bar{b}jj$  ( $\text{BR}(W \rightarrow q\bar{q}') = 0.68$ ,  $\text{BR}(Z \rightarrow q\bar{q}) = 0.70$ ) with 2 fb $^{-1}$  and 15 fb $^{-1}$  of integrated luminosity [8, 90].

discovering the Higgs boson at the Tevatron. However, most of the events (70 %) come from the fully hadronic decay of the associated boson (Table 7.1) with a final state signature of four jets: two from the vector boson decay and two b-quark jets from the Higgs boson decay. Indeed, despite the very high QCD background rates, the limits set by Run-I analysis of this mode have proven to be competitive to those from the leptonic channels [114]. From the trigger point of view the leptonic channels are not a concern since the high  $p_T$  lepton provides a straight-forward trigger with low rates and high efficiency. For the fully hadronic final state the analysis of the Run-I data showed that the CDF standard multijet trigger, specifically designed for the top quark search [115], needs significant improvements since it rejects almost 70 – 80 % of the events (Table 7.2).

$M_H$ (GeV/ $c^2$ )	$\epsilon_{\text{trigger}}(\%)$
110	$21.2 \pm 0.3$
120	$24.6 \pm 0.4$
130	$27.8 \pm 0.3$
140	$31.5 \pm 0.4$

Table 7.2: CDF Run-I multijet trigger efficiencies as a function of the Higgs mass [115]. Level 1 requirement:  $\sum E_T \geq 120$  GeV; Level 2 requirements:  $N_{clus} \geq 4$  ( $E_T^{clus} \geq 15$  GeV) and  $\sum E_T^{clus} \geq 125$  GeV. Quoted uncertainties include statistical errors only.

## 7.2 Trigger Strategy

In the signal topology under study we expect at least four rather central high  $E_T$  jets ( $E_T \approx 50$  GeV/ $c$ , see Figure 7.1): two from the fully hadronic decay of the vector boson, and two b-jets from the Higgs boson decay  $H \rightarrow b\bar{b}$ .

In a signature with four high  $E_T$  jets the aim of the Level 1 trigger is to discard events with low transverse momentum.

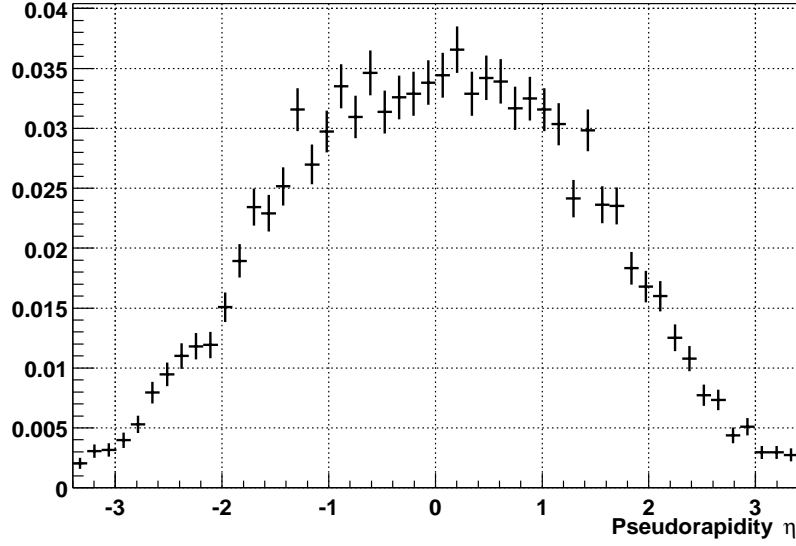


Figure 7.1: Higgs boson pseudorapidity distribution for the channel  $H + W/Z \rightarrow b\bar{b}jj$  at  $\sqrt{s} = 2.0 \text{ TeV}$  ( $M_H = 120 \text{ GeV}/c^2$ ) [90]. The distribution is normalized to unit area.

The most convenient discrimination variable is the transverse energy deposited in the calorimeter. The calorimeter segmentation in trigger towers has been optimized to contain most of the energy released by a jet hitting the center of the tower [116]; therefore, the requirement of a single calorimeter tower with high enough thresholds is fully efficient for jets and discards almost all the  $p\bar{p}$  interactions with low transverse energy.

At Level 2 coarse calorimeter clustering and track reconstruction in the  $r - \phi$  plane with offline quality are available. At this level the main background is QCD jet production. For QCD jet production the leading order processes are  $2 \rightarrow 2$  scattering with  $N$  jet processes suppressed by a factor  $\sim \alpha_s^{(N-2)}$ . Since the signal topology contains at least four jets, the requirement of a minimum number of clusters will be very efficient for the signal while rejecting a substantial fraction of QCD events.

Signal jets are produced from the decay of massive objects releasing in the calorimeter a total transverse energy of the order of  $\sim M_T^H + M_T^{W/Z} \approx 200 \text{ GeV}/c^2$ . In the other hand, the QCD multijet cross section exponentially decreases with the  $\sum E_T^{\text{jets}}$ . Therefore, a threshold in  $\sum E_T^{\text{clus}}$  near 200 GeV should also reject a significant fraction of QCD events, while keeping a high efficiency for the signal.

At Level 2 a further rejection factor can be obtained exploiting the information provided by the SVT and the Higgs boson decay  $H \rightarrow b\bar{b}$ . Large impact parameter (IP) tracks are strongly correlated with the presence of high  $p_T$  b-jets (Figure 7.2) due to the long lifetime of the b-hadrons. Thus, the requirement of tracks with large IP will enhance the content of b-jets while discarding jets due to gluon irradiation or hadronization of light quarks.

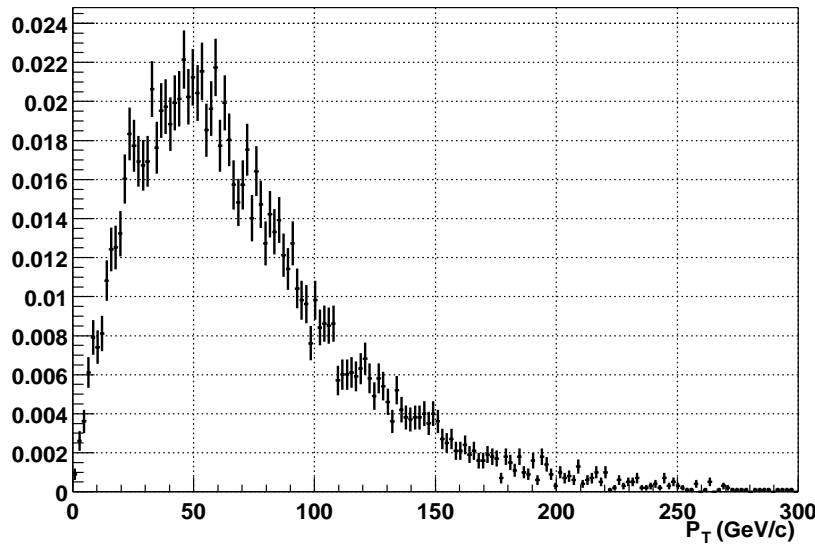


Figure 7.2: b-quark  $p_T$  distribution for the decay  $H \rightarrow b\bar{b}$  ( $M_H = 120 \text{ GeV}/c^2$ ) [90]. The distribution is normalized to unit area.

At Level 3 trigger offline jet reconstruction will be available. Therefore the confirmation of four jets in the event can be required. As a result a multijet sample with enriched heavy flavor content can be obtained with an acceptable occupancy of the total trigger bandwidth ( $< 5\%$ ), while keeping a high efficiency for the signal.

### 7.3 Trigger Rate and Efficiency Calculation

The trigger rate and the signal efficiency are estimated following the procedure described in Chapter 6. The process  $H + W/Z \rightarrow b\bar{b}jj$  is simulated at  $\sqrt{s} = 2 \text{ TeV}$  with the PYTHIA Monte Carlo program [90]. The decay of B-hadrons are corrected with the CLEOMC program [110]. Detector response is simulated with the standard Run-I CDF program QFL'. Level 1 trigger rates are estimated using the Run-I *minimum bias* data sample. At Level 2 we use the *JET-20* data sample. See Section 6.3 for a detailed description of these samples.

### 7.4 Level 1 Trigger Rates and Efficiencies

The Level 1 input rate<sup>1</sup> is 1.7 MHz while the maximum output rate must be 50 kHz to not incur in deadtime at Level 2. Therefore, a rejection factor of 50 is necessary.

<sup>1</sup>The Level 1 trigger and the Tevatron bunch crossing are synchronous. In the 396 ns of inter-bunch spacing regim with 36 bunches every  $21 \mu\text{s}$  (revolution period) the average input rate is 1.7 MHz. In the 132 ns of interbunch spacing with 108 bunches the average input rate is 5.3 MHz.

The process  $H + W/Z \rightarrow b\bar{b}jj$  leads to a final signature of four rather central jets, which originate a high multiplicity of both low and high  $p_T$  charge particles releasing almost all their energy in the calorimeter. Hence, from the three parallel synchronous processing streams available at Level 1 (calorimeter objects, muons objects and track objects<sup>2</sup>) the most straight forward choice is the calorimeter objects. At Level 1 a variety of inclusive unprescaled<sup>3</sup> triggers are available for generic studies. Overlap of the proposed trigger with one of the generic triggers is highly desirable. For multijet triggers there are two options at Level 1, either the requirement of at least one calorimeter trigger tower with total transverse energy above 10 GeV ( $E_T^{low} \geq 10 \text{ GeV}$ ) or a global  $\sum E_T$  trigger. Both are used to select QCD jet events [107].

### 7.4.1 Single Trigger Tower

Figure 7.3 shows the distribution of the trigger tower with the highest  $E_T$  (leading tower) for the minimum bias data sample and for the signal ( $M_H = 120 \text{ GeV}/c^2$ ). Minimum bias events are mostly found in the region with  $E_T < 10 \text{ GeV}$ , abruptly decreasing by three orders of magnitude starting from  $E_T \approx 1.5 \text{ GeV}$ . On the other hand the signal distribution becomes significant for  $E_T \approx 5 \text{ GeV}$ , reaches a plateau for  $E_T \approx 10 \text{ GeV}$  and has a long decreasing tail for  $E_T \geq 40$ . This is a consequence of the low transverse momentum events present in the minimum bias trigger sample, while for

signal events the situation is completely different. Signal jets are produced by the decay of massive particles, the Higgs boson and the W boson. The typical transverse energy scale of these jets is of the order of half the mass of the decaying particle. Furthermore, fairly central partonic collisions are needed to create these large masses, which leads to a reduced longitudinal boost of the  $W^*$  system and therefore to more central jets. Since the size of the trigger tower has been optimized to contain most of the energy released by a jet hitting the center of the tower [116], the leading  $E_T$  trigger tower has a high  $E_T$  and tends to be rather central. We conclude that the single trigger tower primitive can be used as a discrimination variable between signal and minimum bias events.

Figure 7.4 shows the trigger rate ( $\mathcal{L} = 1 \cdot 10^{32} \text{ cm}^{-2}\text{s}^{-1}$ ) and the signal efficiency as a function of the leading tower  $E_T$  threshold. For  $E_T \geq 10 \text{ GeV}$  the efficiency is very high (98.5%) [ $M_H = 120 \text{ GeV}/c^2$ ] and flat. Even increasing the threshold up to  $E_T \geq 14 \text{ GeV}$  the efficiency is over 90%. At  $E_T \geq 10 \text{ GeV}$  the rate is reduced by three orders of magnitude, from 1.7 MHz to 1.6 kHz, which represents less than 5% of the total Level 1 output bandwidth. For an inclusive QCD trigger this is a completely acceptable value.

---

<sup>2</sup>All of them are hardware implemented objects.

<sup>3</sup>A trigger is prescaled when only a fraction of the generated triggers is accepted by the data acquisition system.

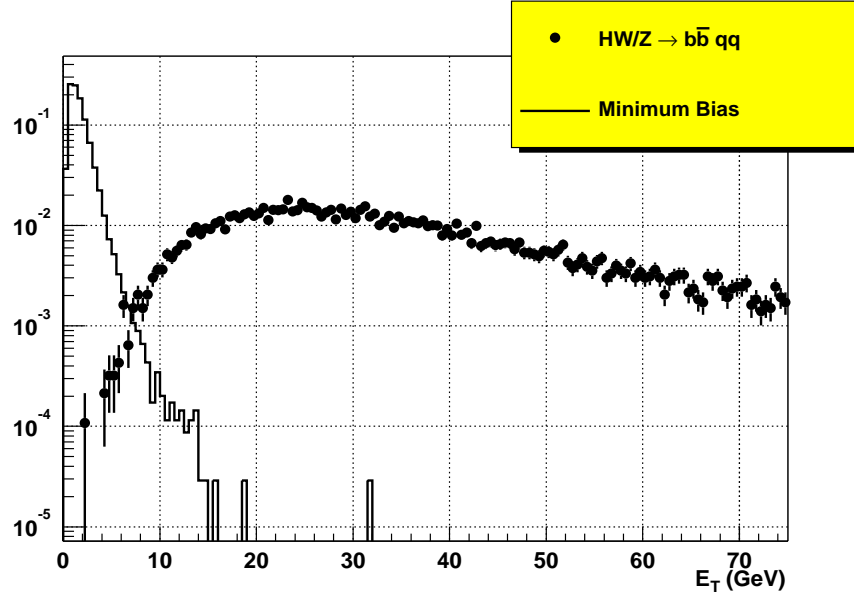


Figure 7.3: Highest  $E_T$  trigger tower distribution for minimum bias events (histogram) and signal events (dots) [ $M_H = 120 \text{ GeV}/c^2$ ]. Both distributions are normalized to unit area.

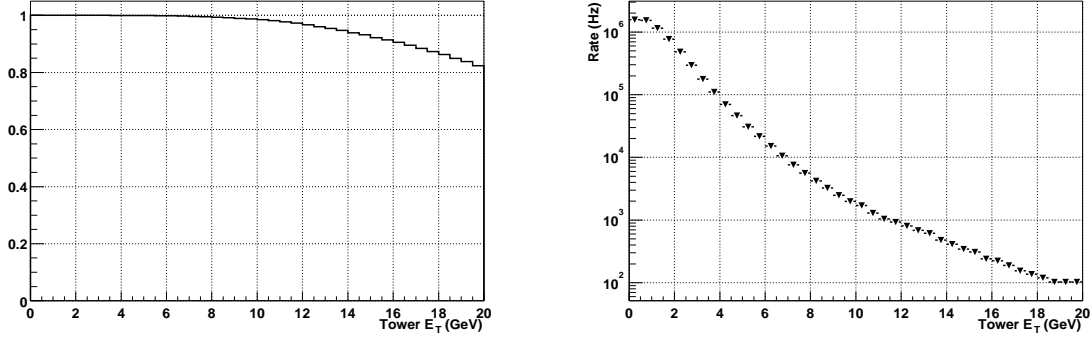


Figure 7.4: Level 1 signal efficiency (left figure) [ $M_H = 120 \text{ GeV}/c^2$ ] and trigger rates for  $\mathcal{L} = 1 \cdot 10^{32} \text{ cm}^{-2}\text{s}^{-1}$  (right figure) as a function of the threshold on the highest  $E_T$  tower.

### 7.4.2 Global $\sum E_T$ Trigger

We have also studied the global  $\sum E_T$  primitive (see Section 5) defined as the sum of the  $E_T$  of all the towers in the calorimeter. Only towers with  $E_T$  above a certain threshold can be added to the sum. This threshold is hardwired and can be set to 0.5, 1.0 and 2.0 GeV, and it also has to be the same as for the missing transverse energy trigger primitive. CDF has initially fixed this threshold to 1.0 GeV [117]. Figure 7.5 shows the trigger rates and signal efficiencies for each of these thresholds.

Only two thresholds can be set for the  $\sum E_T$ , either 60 or 80 GeV. For 60 GeV the rates are high (Table 7.4). For 80 GeV we obtain a rate reduction of a factor 2 with respect to the single trigger tower, with similar signal efficiencies (Table 7.3). However, the large variation of the rates with the individual tower threshold suggests an instantaneous luminosity dependence that must be checked with early Run-II data, and favors the single trigger tower ( $E_T \geq 10$  GeV) as a more reliable trigger.

Tables 7.3 and 7.4 summarizes the rates and trigger efficiencies.

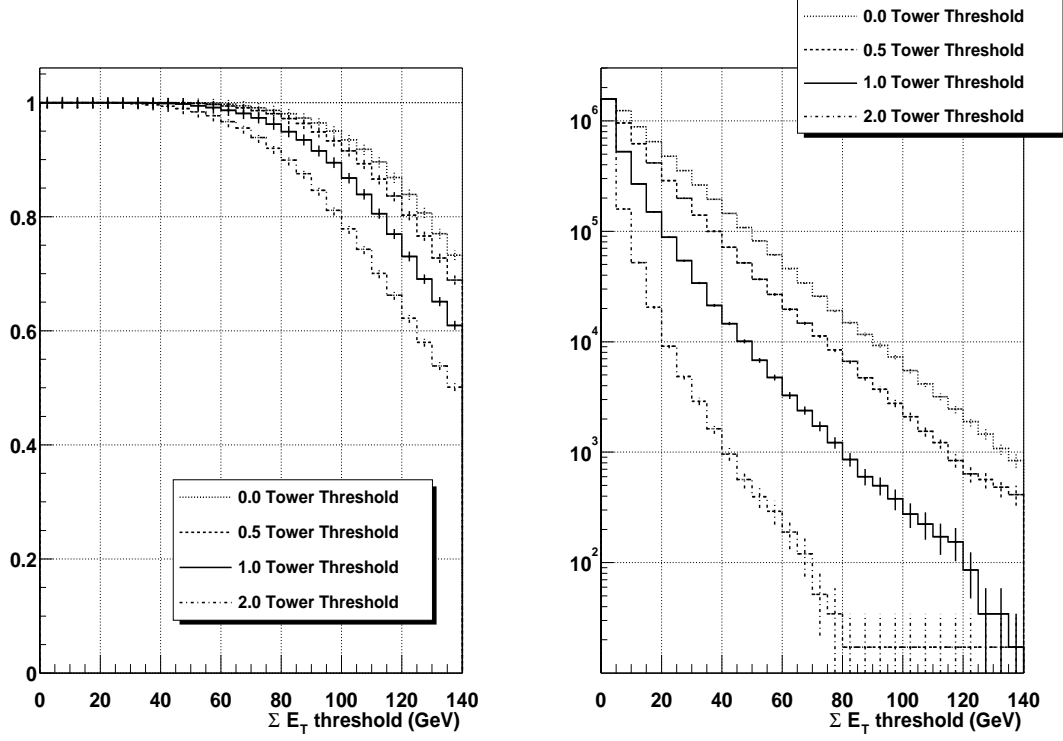


Figure 7.5: Level 1 trigger rate (Hz) for  $\mathcal{L} = 1 \cdot 10^{32} \text{ cm}^{-2}\text{s}^{-1}$  (right figure) and signal efficiency (left figure) as a function of the  $\sum E_T$ . The  $\sum E_T$  is calculated summing all the trigger towers with  $E_T$  above 0.0, 0.5, 1.0 or 2.0 GeV.

Trigger	Higgs Mass ( GeV/ $c^2$ )				
	110	115	120	125	130
$E_T^{tow} \geq 10 \text{ GeV}$	$97.4 \pm 0.2\%$	$98.1 \pm 0.1\%$	$98.5 \pm 0.1\%$	$98.5 \pm 0.1\%$	$98.5 \pm 0.2\%$
$\sum E_T \geq 60 \text{ GeV}$	$98.4 \pm 0.1\%$	$98.5 \pm 0.2\%$	$98.6 \pm 0.1\%$	$99.0 \pm 0.1\%$	$98.6 \pm 0.1\%$
$\sum E_T \geq 80 \text{ GeV}$	$92.9 \pm 0.2\%$	$94.1 \pm 0.2\%$	$94.7 \pm 0.1\%$	$95.4 \pm 0.2\%$	$94.9 \pm 0.2\%$

Table 7.3: Level 1 signal efficiencies for the single trigger tower ( $E_T^{tow}$ ) and the  $\sum E_T$  trigger primitives. The  $\sum E_T$  is computed summing all the trigger towers with  $E_T \geq 1.0 \text{ GeV}$ .

Trigger	$\sigma_T$ ( $\mu\text{b}$ )	Rate (kHz)	Rejection Factor
$E_T^{tow} \geq 10 \text{ GeV}$	$15.8 \pm 0.6$	$1.58 \pm 0.06$	$930 \pm 90$
$\sum E_T \geq 60 \text{ GeV}$	$32 \pm 1$	$3.2 \pm 0.1$	$480 \pm 50$
$\sum E_T \geq 80 \text{ GeV}$	$8.5 \pm 0.3$	$0.85 \pm 0.03$	$1800 \pm 200$

Table 7.4: Level 1 trigger rates ( $\mathcal{L} = 1 \cdot 10^{32} \text{ cm}^{-2}\text{s}^{-1}$ ), trigger cross section ( $\sigma_T$ ) and rejection factor for the single trigger tower ( $E_T^{tow}$ ) and the  $\sum E_T$  trigger primitives. The  $\sum E_T$  is computed summing all the trigger towers with  $E_T \geq 1.0 \text{ GeV}$ .

## 7.5 Level 2 Trigger Rates and Efficiencies

At Level 2 a dedicated trigger can occupy only a few percent of the total bandwidth. Therefore, with an input rate of 50 kHz and a maximum output rate of 300 Hz a rejection factor of two orders of magnitude is necessary. The data from five detector subsystems are available: muon trigger data, tracks reconstructed in the COT by the *eXtremely Fast Tracker* (XFT) and extrapolated for calorimeter tower matching, trigger data from the central strip chambers, calorimeter energy clustering, and tracks reconstructed by the *Silicon Vertex Trigger* (SVT). For the Higgs channel under study only information from the calorimeter and from the SVT will be considered<sup>4</sup>.

SVT data arrives later than the data from the other four systems.<sup>5</sup> It has been established [10] that for all triggers which require SVT impact parameter cuts, if they are rejected by other cuts, then the impact parameter cut will not be tested. Therefore, the trigger strategy will be based on a first selection using only calorimetric information. A second selection relying on the SVT data will then be applied.

### 7.5.1 Calorimetric Selection

The Level 2 clustering simulation of the signal yields a signature where mostly four or more energetic clusters ( $E_T^{clus} \approx 10 - 100 \text{ GeV}$ ) are found (Figure 7.6).

To estimate the rates for triggers requiring calorimetric clustering the *JET-20* data sample is the most appropriate. It has the loosest trigger requirement (at

<sup>4</sup>Tracks from the XFT, extrapolated to match a calorimeter trigger tower, are not used. Due to the high track multiplicity of the signal the matching does not provide any additional discrimination.

<sup>5</sup>The SVT latency is  $\approx 20 \mu\text{s}$ .

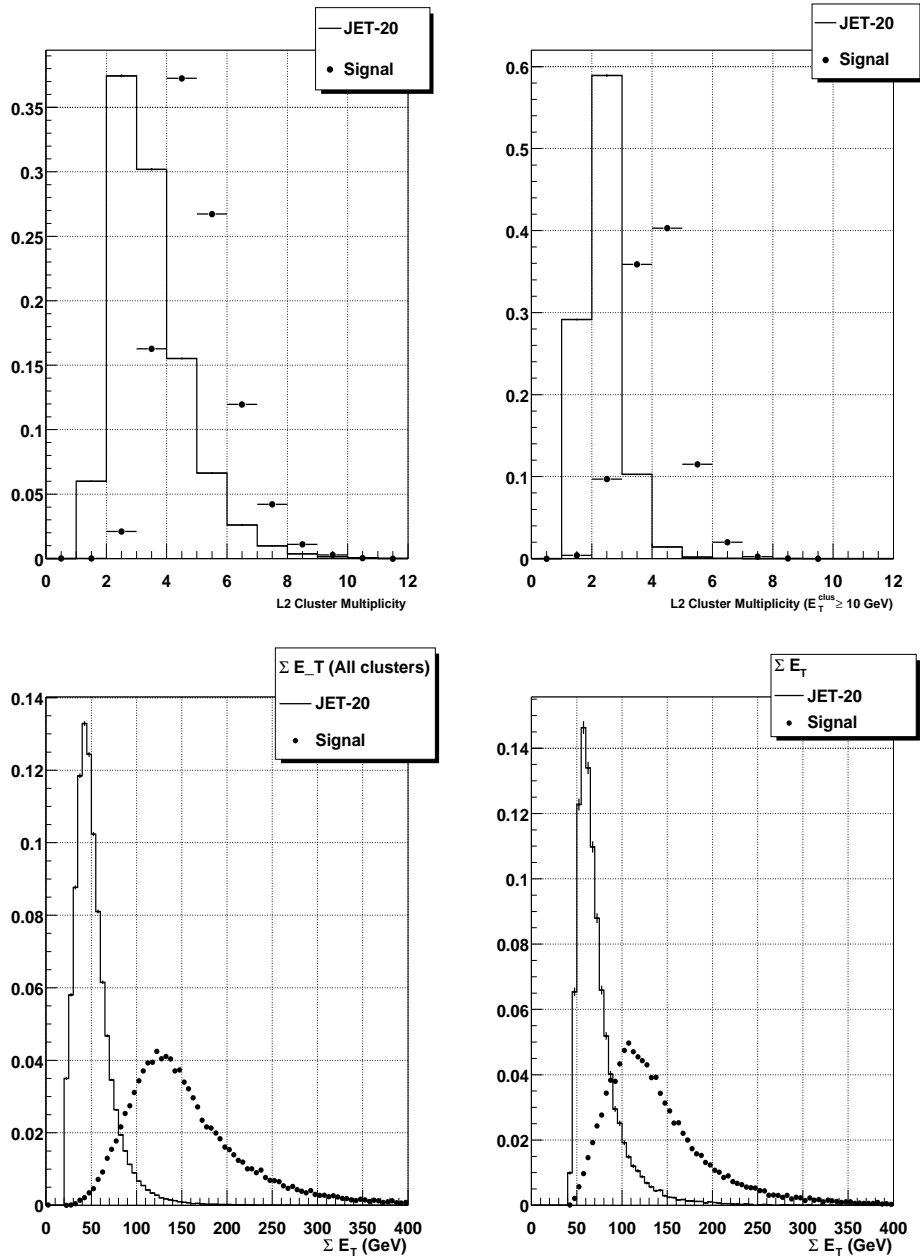


Figure 7.6: Signal (dots) [ $M_H \geq 120$  GeV] and *JET-20* (histograms) Level 2 calorimeter trigger primitives. The plots show the distributions for the cluster multiplicity (top left), cluster multiplicity of clusters with  $E_T^{clus} \geq 10$  GeV (top right),  $\Sigma E_T^{clus}$  computed over all clusters (bottom left), and  $\Sigma E_T^{clus}$  over clusters with  $E_T^{clus} \geq 10$  GeV (bottom right). All distributions are normalized to unit area.

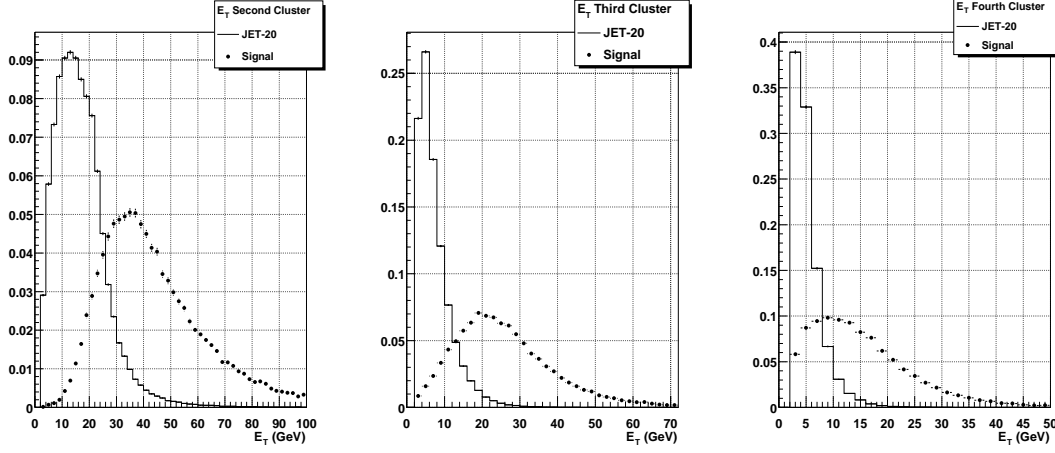


Figure 7.7: Signal (dots) [ $M_H \geq 120$  GeV] and *JET-20* (histograms) Level 2 calorimeter trigger primitives. The plots show the  $E_T^{clus}$  distribution of second highest  $E_T^{clus}$  cluster (left), the third highest  $E_T^{clus}$  cluster (center), and fourth highest  $E_T^{clus}$  cluster (right). All distributions are normalized to unit area.

least one cluster with  $E_T \geq 20$  GeV), the trigger cross section is well known ( $\sigma_T = 7.5 \mu b$ ), and has enough statistics (see Section 6).

The Level 2 calorimeter selection is based on a list of found clusters. For the definition of the trigger requirements we will consider only three magnitudes: the threshold on the transverse energy of the cluster ( $E_T^{clus}$ ), the number of clusters ( $N_{clus}$ ) over the threshold, and the the sum of the cluster  $E_T$  over all clusters ( $\sum E_T^{clus}$ )<sup>6</sup> (see Figures 7.6 and 7.7).

We search for a set of thresholds on these three variables that maximizes the signal efficiency while keeping the rates under control. For the cases where significant rate reduction can be achieved with small loss in signal efficiency, the corresponding trigger requirements will be applied, improving in this way the signal to background ratio. Note that similar cuts will in any case applied in the analysis when searching for the optimization of the signal statistical significance.

We begin by ordering the clusters in decreasing values of  $E_T^{clus}$ . Different numbers of clusters are required, and a threshold on the lowest  $E_T^{clus}$  is applied. For each one of these combinations both efficiency and rates are calculated for different  $\sum E_T^{clus}$  values. The minimum value for a cluster  $E_T^{clus}$  to be included in the  $\sum E_T^{clus}$  will be studied later, and initially we calculate  $\sum E_T^{clus}$  over all the clusters in the event.

Figures 7.8 and 7.9 show, respectively, the signal efficiency and trigger rates for the different cases. For a fixed value of  $\sum E_T^{clus}$  the efficiency does not change significantly when  $N_{clus} \geq 2$  or  $N_{clus} \geq 3$ ; but it does for  $N_{clus} \geq 4$ , where it

<sup>6</sup>Cluster topology in  $\phi$  and  $\eta$  is not used. Due to the coarse segmentation in  $\phi$  and  $\eta$  and the high cluster multiplicity of the signal, no significant spatial correlations between clusters have been observed.

drops by about 10% no matter the value of  $\sum E_T^{clus}$ . Rates continuously decrease as we require more clusters. For  $N_{clus} \geq 3$ , increasing the  $\sum E_T^{clus}$  threshold from 70 GeV to 90 GeV reduces the efficiency only by a 6% (from 92% to 86%), while the rate is reduced by a factor of 2.6 (from 95 to 37 Hz). Therefore, the requirement of  $N_{clus} \geq 3$  and  $\sum E_T^{clus} \geq 90$  GeV provides a good background discrimination

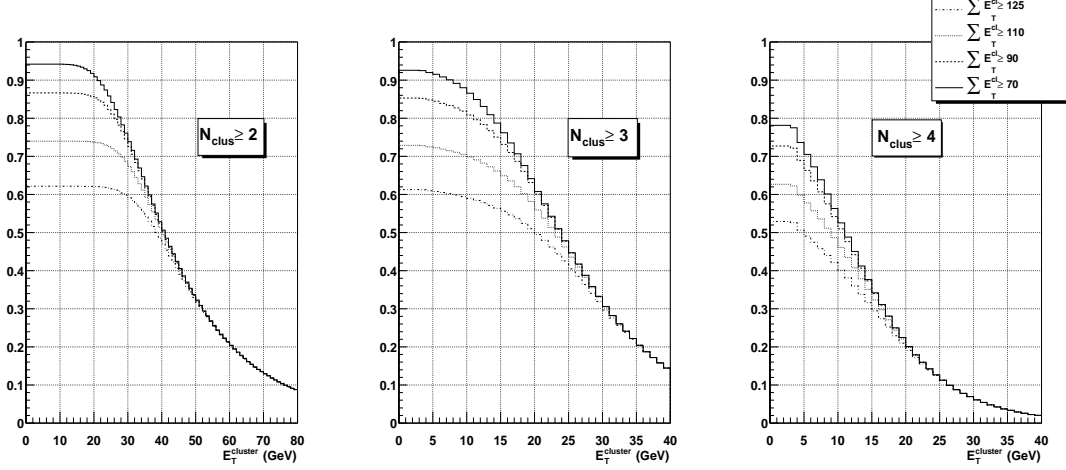


Figure 7.8: Signal efficiency ( $M_H = 120$  GeV/ $c^2$ ) for different selections of the minimum number of required clusters (2, 3 or 4) versus the  $E_T^{clus}$  of the second cluster (left figure), third cluster (center), and the fourth cluster (right figure). Clusters are ordered in decreasing  $E_T^{clus}$ . The different curves shown refer to different choices of the  $\sum E_T^{clus}$ , calculated over all the clusters in the event. Level 1 trigger requirement of at least one trigger tower with  $E_T \geq 10$  GeV is applied.

(Figures 7.6 and 7.7) with moderate rates (37 Hz). A  $E_T^{clus}$  threshold of 10 GeV can be required on the third cluster with no significant efficiency loss, while the rates are additionally reduced by a factor of 1.6.

This selection ( $N_{clus} \geq 3$  with  $E_T^{clus} \geq 10$  and  $\sum E_T^{clus} \geq 90$  GeV) yields a rate of 23 Hz with a signal efficiency of  $\sim 82\%$  ( $M_H = 120$  GeV). To keep high signal efficiencies, individual thresholds for the two most energetic clusters are not set.<sup>7</sup>

Further trigger rate reduction with little signal efficiency loss can be done. So far the  $\sum E_T^{clus}$  has been calculated over all the clusters in the event. This is not the optimal selection since for generic QCD events one can expect a greater population of clusters with low  $E_T^{clus}$ . A more signal-like  $\sum E_T^{clus}$  distribution is obtained by summing over the required clusters, *i.e.* clusters with  $E_T^{clus} \geq 10$  GeV (see Figure 7.6). Figures 7.10 and 7.11 show respectively the efficiencies and rates when  $N_{clus} \geq 3$  ( $E_T^{clus} \geq 10$  GeV) and  $\sum E_T^{clus} \geq 90$  GeV in two cases: the sum is performed over

<sup>7</sup>The JET-20 data sample was recorded with the trigger requirement of at least one cluster with  $E_T^{clus} \geq 20$  GeV. To be consistent with the trigger rate estimation, the same condition should be applied to the signal. For both signal and JET-20 data sample the requirement of 3 clusters and  $\sum E_T^{clus} \geq 90$  GeV necessarily implies that, for the most energetic cluster,  $E_T \geq 20$  GeV.

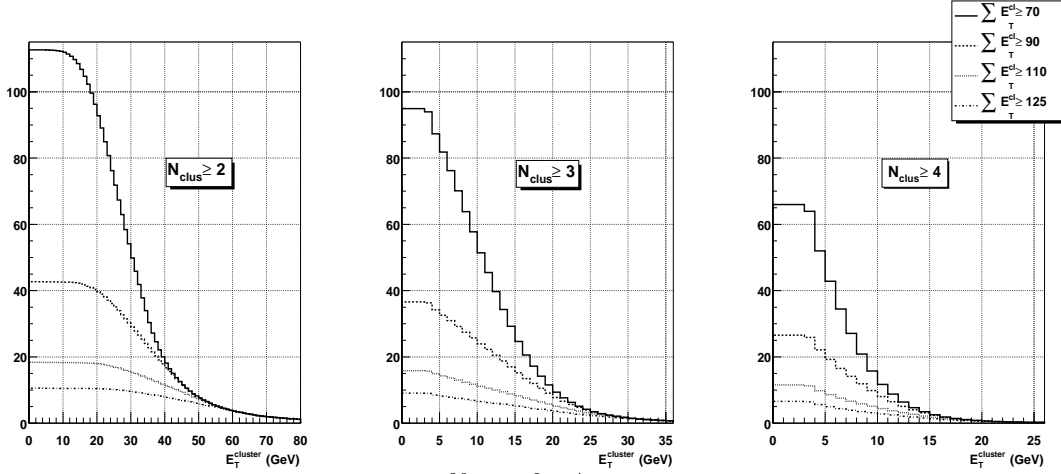


Figure 7.9: Rates (Hz) ( $\mathcal{L} = 1 \cdot 10^{32} \text{ cm}^{-2} \text{ s}^{-1}$ ) for different selections of the minimum number of required clusters (2, 3 or 4) *versus* the  $E_T^{clus}$  of the second cluster (left figure), third cluster (center), and the fourth cluster (right figure). Clusters are ordered in decreasing  $E_T^{clus}$ . The different curves shown refer to different choices of the  $\sum E_T^{clus}$ , calculated over all the clusters in the event. The Level 1 trigger requirement of at least one trigger tower with  $E_T \geq 10 \text{ GeV}$  is applied.

all clusters<sup>8</sup> and only over clusters with  $E_T^{clus} \geq 10 \text{ GeV}$ . Setting  $E_T^{clus} \geq 10 \text{ GeV}$  the efficiency is reduced only by a few percent (from 82% to 78%), while the rates are reduced by 26%, from 23 Hz to 17 Hz. Higher cluster  $E_T^{clus}$  thresholds and other combinations, like thresholds in the sum of the two most energetic clusters, do not yield equal efficiency with lower rates.

Tables 7.5 and 7.6 summarize, respectively, the trigger efficiencies for different Higgs boson masses and the trigger rate, the trigger cross section, and the rejection factor for the final trigger cuts.

	Higgs Mass ( GeV/ $c^2$ )				
	110	115	120	125	130
Eff. (%)	$73.4 \pm 0.4$	$76.4 \pm 0.4$	$78.1 \pm 0.2$	$80.8 \pm 0.4$	$82.4 \pm 0.6$

Table 7.5: Level 2 calorimetric trigger efficiency as a function of the Higgs boson mass. The trigger conditions are:  $N_{clus} \geq 3$  ( $E_T^{clus} \geq 10 \text{ GeV}$ ) and  $\sum E_T^{clus} \geq 90 \text{ GeV}$ .  $\sum E_T^{clus}$  is calculated over all clusters with  $E_T^{clus} \geq 10 \text{ GeV}$ . The Level 1 trigger ( $E_T^{tower} \geq 10 \text{ GeV}$ ) is applied.

<sup>8</sup>Effectively  $E_T^{clus} \geq 3 \text{ GeV}$ , since 3 GeV is the minimum energy of the trigger tower to begin to form a cluster.

$\sigma_T$ (nb)	Rate (Hz)	Rejection Factor
$171 \pm 6$	$17.1 \pm 0.6$	$43.8 \pm 0.5$

Table 7.6: Level 2 calorimetric trigger rate ( $\mathcal{L} = 1 \cdot 10^{32} \text{ cm}^{-2}\text{s}^{-1}$ ), trigger cross section ( $\sigma_T$ ) and rejection factor. The trigger conditions are:  $N_{clus} \geq 3$  ( $E_T^{clus} \geq 10 \text{ GeV}$ ) and  $\sum E_T^{clus} \geq 90 \text{ GeV}$ .  $\sum E_T^{clus}$  is calculated over all clusters with  $E_T^{clus} \geq 10 \text{ GeV}$ .

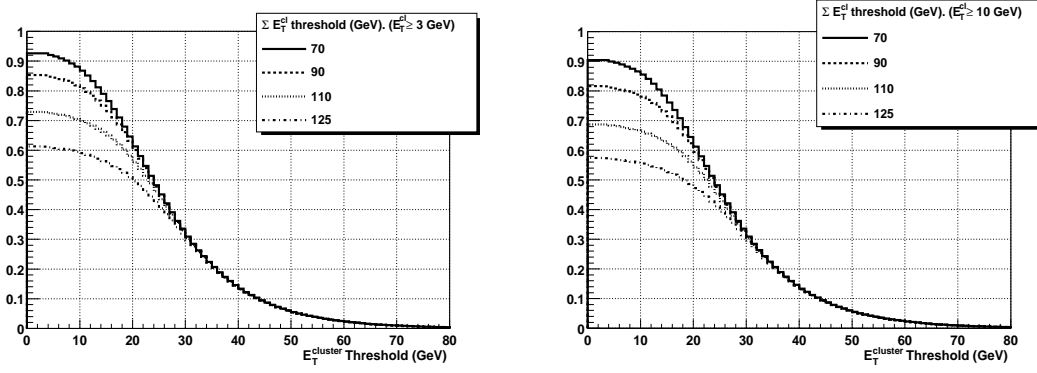


Figure 7.10: Signal efficiencies ( $M_H = 120 \text{ GeV}/c^2$ ) for a Level 2 trigger with  $N_{clus} \geq 3$  and different choices of  $\sum E_T^{clus}$  as a function of the  $E_T^{clus}$  of the third cluster. The  $\sum E_T^{clus}$  is computed over all clusters (left figure) and over all clusters with  $E_T \geq 10 \text{ GeV}$  (right figure).

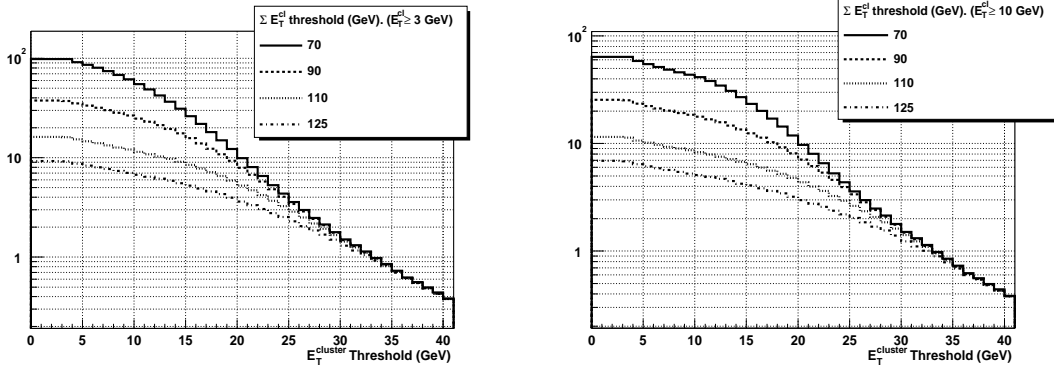


Figure 7.11: Trigger rates [Hz] ( $\mathcal{L} = 1 \cdot 10^{32} \text{ cm}^{-2}\text{s}^{-1}$ ) for a Level 2 trigger with  $N_{clus} \geq 3$  and different choices of  $\sum E_T^{clus}$  as a function of the  $E_T$  of the third cluster. The  $\sum E_T^{clus}$  is computed over all clusters (left figure) and over all clusters with  $E_T \geq 10 \text{ GeV}$  (right figure).

### 7.5.2 SVT Selection

After the calorimetric cuts we obtain a rate of 17 Hz ( $\mathcal{L} = 1 \cdot 10^{32} \text{ cm}^{-2} \text{ s}^{-1}$ ) with an efficiency of 78% ( $M_H = 120 \text{ GeV}/c^2$ ). This rate is acceptable for the Level 3 trigger input but still too high for the output rate to tape (50 Hz). Taking into account that we want to occupy only a few percent of the total bandwidth, an additional rejection factor of 5 is needed. At Level 3 trigger offline calorimeter reconstruction algorithms are guaranteed to run for every event but, as we will see in the next Section, they do not provide such a high rejection factor. Taking advantage of the Higgs boson decay to two b-quarks the best rejection factor is provided by the offline b-jet identification algorithms. However, they need full tracking reconstruction with silicon data for an efficient reconstruction of secondary vertices. The tracking algorithms are very CPU consuming (mainly due to the unpacking of the silicon data) and can not be run at the required frequency at Level 3.<sup>9</sup> Further rejection factor at Level 2 can be obtained using the information provided by the SVT reconstructed tracks.<sup>10</sup>

#### SVT Efficiency

The SVT performance for *JET-20* events can not be evaluated using the full SVT simulation. The constants of the SVT pattern recognition and track fitting algorithms must be recalculated every time the beam position is changed. This process is very CPU time consuming (several hours).<sup>11</sup> The events of the *JET-20* data sample are spread over a great number of runs, each run with only a few events and different beam position conditions. Therefore, the SVT constants must be recalculated almost for every run, what makes practically impossible to apply the full SVT simulation to the *JET-20* data sample. Another approach is to evaluate the SVT performance using Run-I offline reconstructed tracks.

The SVT is able to reconstruct tracks with the following characteristics:

- $p_T \geq 2.0 \text{ GeV}/c$
- $|\eta| \leq 1.0$
- The track must be linked to a track reconstructed in the Central Tracking Chamber (COT) by the XFT at Level 1.<sup>12</sup>

---

<sup>9</sup>Up to date, full tracking reconstruction of a  $t\bar{t}$  event requires more than one second [117].

<sup>10</sup>In principle, one could think about to use the offline b-tag algorithms at Level 3 using the SVT tracks instead of using the tracks reconstructed with the offline algorithms. However, SVT reconstructs only tracks with  $p_T \geq 2.0 \text{ GeV}/c$  and four silicon hits. With only this kind of tracks the efficiency of the offline b-jets identification algorithms is very poor.

<sup>11</sup>In Run-II SVT pattern and fitting constants recalculation are avoided placing the beam in the needed position at the beginning of each injection. Beam adjustment will take only few seconds. [119]

<sup>12</sup>The  $p_T \geq 2.0 \text{ GeV}/c$  and  $|\eta| \leq 1.0$  conditions are imposed by the XFT. The XFT will be able to find tracks only with these requirements. SVT needs the linking with the XFT tracks to reduce the combinatorial background for the tracks reconstructed using only silicon hits.

- The track must have one hit in each of the 4 innermost layers of the SVX II, and all the hits must be in the same wedge.

Therefore, we will use offline reconstructed tracks with the same characteristics (SVT-like tracks). XFT tracks will be simulated using tracks reconstructed in the Run-I CTC drift chamber [47] with a transverse momentum smearing. The SVT track finding efficiency with respect to this kind of selected tracks has been calculated in [113] using the CDF Run-I  $J/\Psi \rightarrow \mu\mu$  data sample and the full SVT simulation. The efficiency to find an offline reconstructed 4-hit track is  $91.0 \pm 0.3\%$  [113], with a fake rate of  $\approx 5\%$ . The loss in efficiency is due to the SVT reduction of the pattern recognition space, when the strips are merged into superstrips (see Section 5.3.5). The SVT reconstruction accuracy is very similar to the offline reconstruction, and the expected precision is:  $\sigma_d = 35\mu m$  (at  $p_T = 2.0 \text{ GeV}/c$ ),  $\sigma_\phi = 1 \text{ mrad}$  and  $\sigma_{p_T} = 0.3\% \cdot p_T^2 (\text{GeV}/c)$  [12].

Therefore, trigger rates and efficiencies using the SVT information were estimated as follows: from the offline reconstructed tracks, tracks with one hit in each of the 4 innermost silicon layers of the same SVX wedge,  $|\eta| \leq 1$ , and with a smeared CTC  $p_T \geq 2 \text{ GeV}/c$  were selected. The track parameters have been computed with respect to the center of the beam position<sup>13</sup>. To each track a 90% probability to be found was applied.

### SVT Cuts

The selection using the SVT information is based on the ordering of the SVT-like reconstructed tracks in decreasing value of impact parameter (IP). Figure 7.12 shows the number of SVT-like tracks per event. The large number of events with no tracks is due to the limited Run-I SVX geometrical acceptance. In Run-II with a large SVX II detector the geometrical acceptance will be larger, and thus the number of events with no SVT tracks will be reduced. The necessary correction is calculated in Section 7.7.

After the calorimeter requirements, thresholds on the largest and second largest IP are applied. Figures 7.13 and 7.14 show the signal efficiencies and rates for three sets of thresholds:

- A threshold is set in the largest IP.
- A threshold is set in the second largest IP
- A threshold is set in the second largest IP while the largest is required to be  $\geq 100 \mu m$ .

For thresholds on the largest IP up to  $100 \mu m$  the rate decreases faster than the efficiency, therefore the purity of the sample increases. Applying a threshold also on

---

<sup>13</sup>SVT calculates the track IP respect to the beam position. Beam spot has an spread of  $\sigma_{xy} = 30\mu m$ . The effect of this spread has been already added to the nominal SVT resolution.

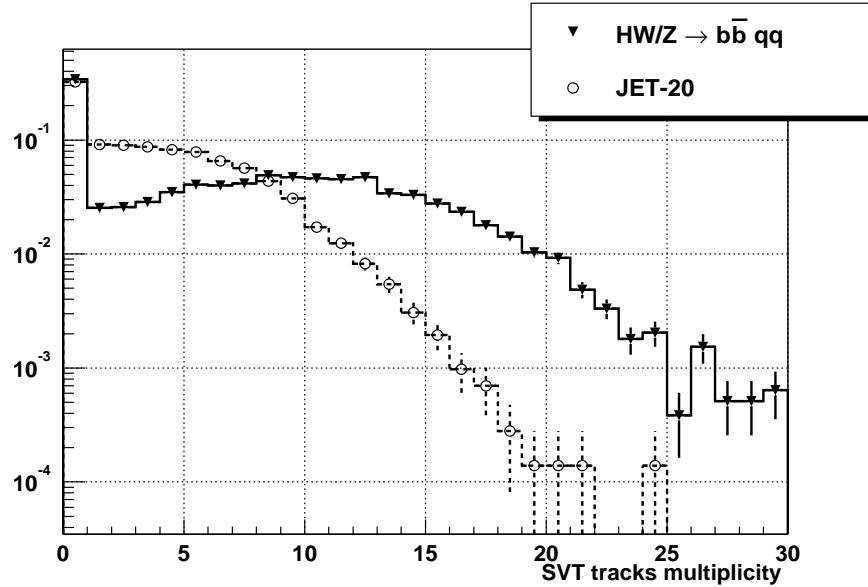


Figure 7.12: Offline tracks multiplicity for  $H + W/Z \rightarrow b\bar{b}jj$  events (triangles) and JET-20 events (open circles). Tracks are required to be equivalent to SVT reconstructed tracks: one hit in each of the 4 innermost silicon layers,  $|\eta| \leq 1$  and a smeared  $p_T \geq 2$  GeV/ $c$ . Both distributions are normalized to unit area

the second largest IP, for values up to  $80 \mu\text{m}$  we observe the same tendency. We have found that the selection of two SVT tracks, one with  $\text{IP} \geq 100 \mu\text{m}$  and the other with  $\text{IP} \geq 80 \mu\text{m}$ , provides a good background discrimination (Figures 7.15 and 7.16) with moderate rates. For this selection the efficiency is 30% ( $M_H = 120 \text{ GeV}/c^2$ ) with a rate of 1 Hz, below the 5% of the Level 3 output rate.

Thresholds on the  $p_T$  of the tracks (Figures 7.17 and 7.18) reduces in the same amount both rate and efficiency, and therefore they are not used. Other combinations like the sum of the first and second largest IP, or a single threshold on the second largest IP have been studied, but they do not yield an improved rejection with the same signal efficiency.

Tables 7.7 and 7.8 summarize, respectively, the trigger rates and efficiencies after the SVT requirements.

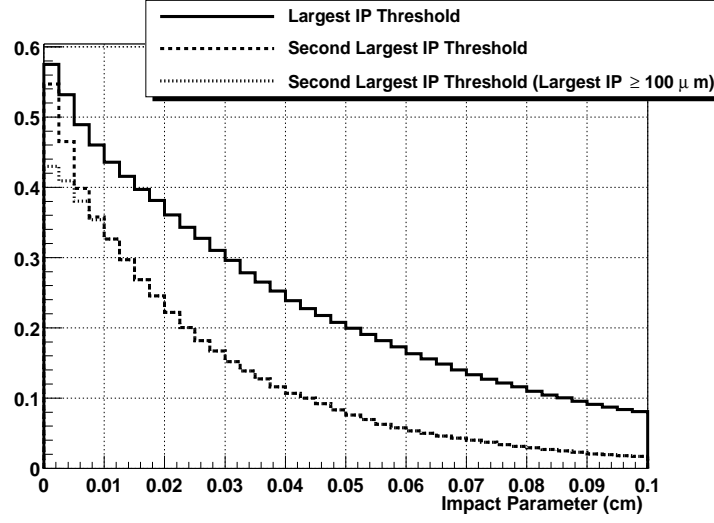


Figure 7.13: Signal trigger efficiencies ( $M_H = 120 \text{ GeV}/c^2$ ) as a function of the threshold on the largest impact parameter, the threshold on the second largest impact parameter, and the threshold on the second largest impact parameter when the largest is required to be  $\geq 100 \mu\text{m}$ . The Level 2 calorimetric requirements  $N_{clus}(E_T^{clus} \geq 10) \geq 3$ ,  $\sum E_T^{clus} \geq 90 \text{ GeV}$  and Level 1 trigger are applied.

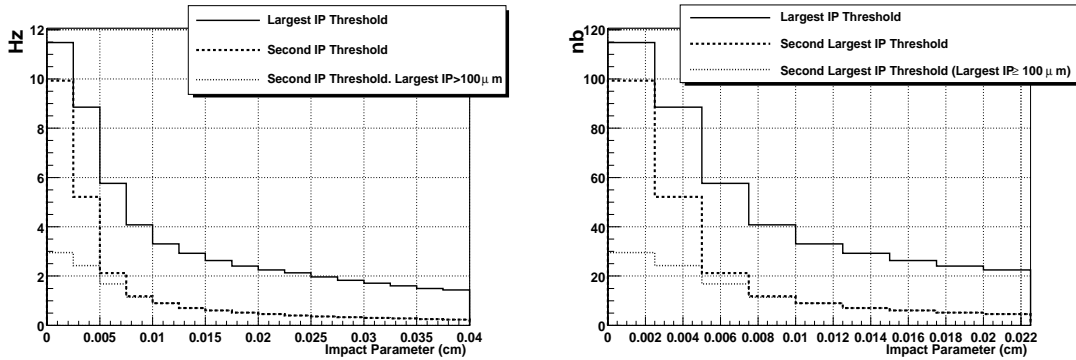


Figure 7.14: Trigger rates ( $\mathcal{L} = 1 \cdot 10^{32} \text{ cm}^{-2}\text{s}^{-1}$ ) and trigger cross sections as a function of the threshold on the largest impact parameter, the threshold on the second largest impact parameter, and the threshold on the second largest impact parameter when the largest is required to be  $\geq 100 \mu\text{m}$ . The Level 2 calorimetric requirements  $N_{clus}(E_T^{clus} \geq 10) \geq 3$ ,  $\sum E_T^{clus} \geq 90 \text{ GeV}$ , and Level 1 trigger are applied.

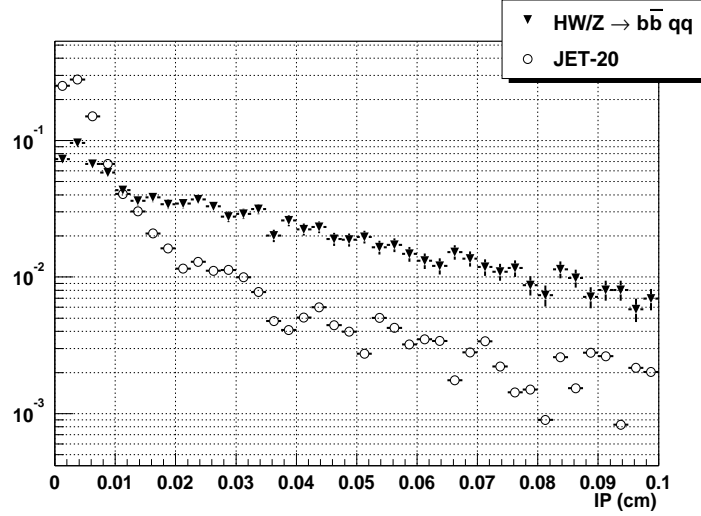


Figure 7.15: Largest impact parameter distribution of SVT tracks for signal (triangles) [ $M_H = 120 \text{ GeV}/c^2$ ] and  $\text{JET-20}$  events (open circles). The Level 2 calorimetric requirements  $N_{clus} \geq 3$ ,  $\sum E_T^{clus} \geq 90 \text{ GeV}$  and  $E_T^{clus} \geq 10 \text{ GeV}$  are applied. Both distributions are normalized to unit area.

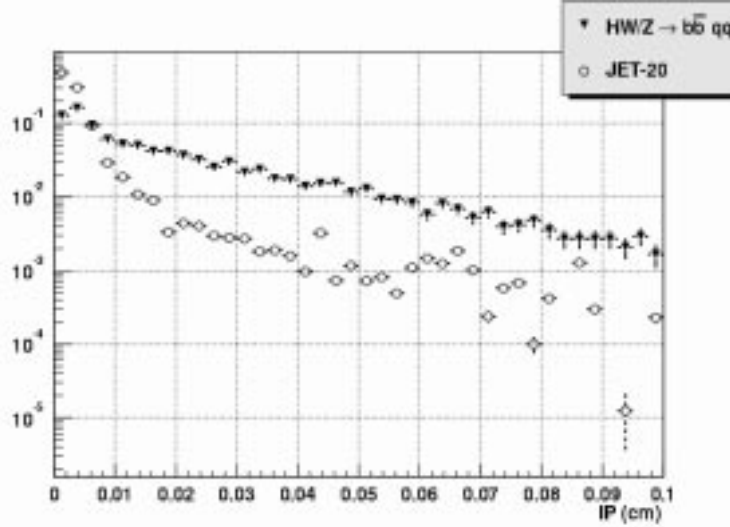


Figure 7.16: Second largest impact parameter distribution of SVT tracks for signal (triangles) [ $M_H = 120 \text{ GeV}/c^2$ ] and  $\text{JET-20}$  events (open circles). The Level 2 calorimetric requirements  $N_{clus} \geq 3$ ,  $\sum E_T^{clus} \geq 90 \text{ GeV}$  and  $E_T^{clus} \geq 10 \text{ GeV}$  are applied. Both distributions are normalized to unit area.

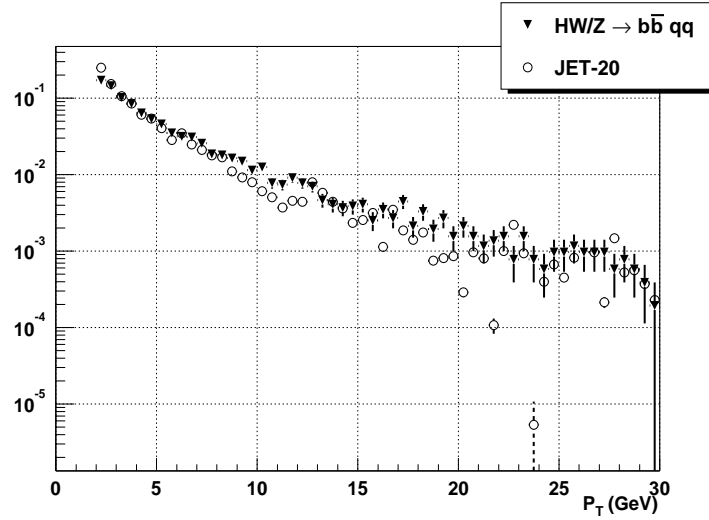


Figure 7.17:  $p_T$  distribution of SVT tracks with the largest impact parameter for signal [ $M_H = 120 \text{ GeV}/c^2$ ] and *JET-20* events. Level 2 trigger calorimetric requirements  $N_{clus} \geq 3$ ,  $\sum E_T^{clus} \geq 90 \text{ GeV}$  and  $E_T^{clus} \geq 10 \text{ GeV}$  are applied. Both distributions are normalized to unit area.

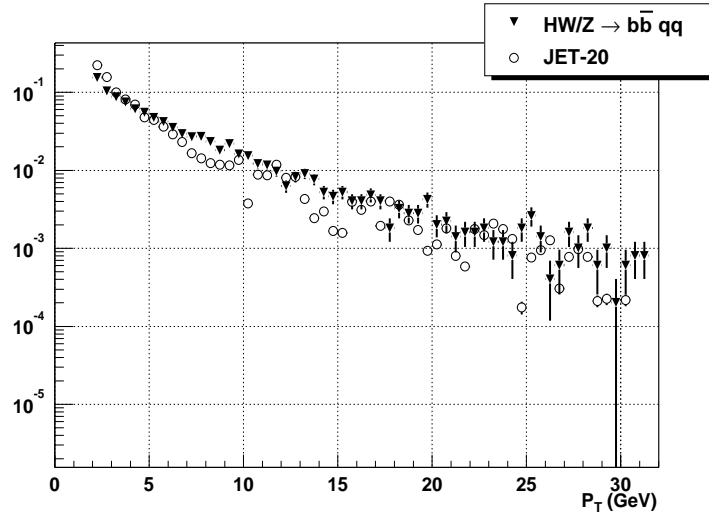


Figure 7.18:  $p_T$  distribution of SVT tracks with the second largest impact parameter for signal [ $M_H = 120 \text{ GeV}/c^2$ ] and *JET-20* events. Level 2 trigger calorimetric requirements  $N_{clus} \geq 3$ ,  $\sum E_T^{clus} \geq 90 \text{ GeV}$  and  $E_T^{clus} \geq 10 \text{ GeV}$  are applied. Both distributions are normalized to unit area.

Selection Cut (JET20)	Rate (Hz)	$\sigma_T$ (nb)	Rejection factor
Calorimetry only $N_{clus}(E_T^{clus} \geq 10) \geq 3$ $\sum E_T^{clus} \geq 90$ GeV	$17.1 \pm 0.6$	$171 \pm 6$	1
Calorimetry + $\geq 1$ SVT track $ d_0  \geq 100 \mu\text{m}$	$3.3 \pm 0.1$	$33 \pm 1$	$5.2 \pm 0.2$
Calorimetry + $\geq 2$ SVT track $ d_0  \geq 100 \mu\text{m},  d_1  \geq 80 \mu\text{m}$	$1.08 \pm 0.04$	$10.8 \pm 0.4$	$16 \pm 1$

Table 7.7: Level 2 trigger rates, cross sections ( $\sigma_T$ ) and rejection factors. The rejection factors are calculated with respect to the events already selected with the calorimetric conditions.

Selection Cut	$M_H$ (GeV/ $c^2$ )				
	110	115	120	125	130
Calorimetry only $N_{clus}(E_T^{clus} \geq 10) \geq 3$ $\sum E_T^{clus} \geq 90$ GeV	$73.4 \pm 0.4\%$	$76.4 \pm 0.4\%$	$78.1 \pm 0.2\%$	$80.8 \pm 0.4\%$	$82.4 \pm 0.6\%$
Calorimetry + $\geq 1$ SVT track $ d_0  \geq 100 \mu\text{m}$	$36.9 \pm 0.4\%$	$37.7 \pm 0.4\%$	$39.7 \pm 0.4\%$	$41.3 \pm 0.4\%$	$42.3 \pm 0.7\%$
Calorimetry + $\geq 2$ SVT track: $ d_0  \geq 100 \mu\text{m}$ $ d_1  \geq 80 \mu\text{m}$	$28.7 \pm 0.4\%$	$29.2 \pm 0.5\%$	$30.6 \pm 0.2\%$	$32.3 \pm 0.5\%$	$33.2 \pm 0.7\%$

Table 7.8: Level 2 signal trigger efficiencies for different Higgs boson masses. The Level 1 requirement  $E_T^{low} \geq 10$  GeV is applied.

### 7.5.3 Level 2 Trigger Rate Control

In running conditions  $\sum E_T^{clus}$  can be used to control the Level 2 trigger rates if they are higher than expected. Figure 7.19 shows the trigger rate and efficiency as a function of the  $\sum E_T^{clus}$  threshold when calorimetric and SVT trigger requirements are applied. The shape of the rate curve is much sharper than the efficiency (*e.g.* an increase of 10 GeV in the sum reduces the rate by  $\sim 33\%$  while the efficiency decreases only by  $\sim 10\%$ ). Thus, this variable can be used for rate adjustment at Level 2.

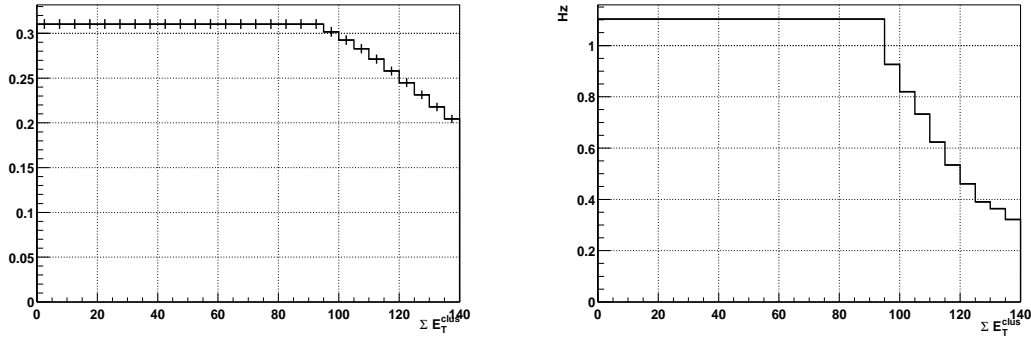


Figure 7.19: Level 2 trigger efficiency ( $M_H = 120 \text{ GeV}/c^2$ ) and rates ( $\mathcal{L} = 1 \cdot 10^{32} \text{ cm}^{-2}\text{s}^{-1}$ ) after Level 2 requirements as a function of the  $\sum E_T^{clus}$  threshold.

### 7.5.4 Multiple Interactions Dependence

So far all the events in the *JET-20* data sample have been used independently of the number of multiple interactions in the event. To consider this as a reliable estimation we must check that trigger efficiencies do not vary significantly with the number of multiple interactions per bunch crossing. The data is binned according to the number of primary vertices found in the event<sup>14</sup> and the trigger efficiencies are calculated for each bin, following the procedure described in Section 6. As described in Section 7.5, the Level 2 the trigger decision is organized in two steps. A first selection is made based in the calorimetric requirements. For events satisfying the trigger a second selection is done with the SVT information. Therefore, trigger efficiencies have been calculated for the calorimetric requirements and for the calorimetric plus the SVT requirements separately. Table 7.9 summarizes the trigger efficiencies as a function of the number of primary vertices in the event. A small trend of increasing trigger efficiency, and therefore a deterioration of the background rejection, is observed. However, for the 2 and 3 vertices bins the trigger efficiencies are constant within the statistical errors and do not change when compared to those obtained with the complete data sample.

### 7.5.5 Run-II Extrapolation

In Run-I the two colliding bunches at Tevatron have a spread in  $z$  of  $\approx 1 \text{ m}$ . The convolution of both yields an interaction region spread of  $\sigma_z \approx 30 \text{ cm}$  around the detector center. The Run-I SVX' detector, with a total length of 51 cm, covered  $\approx 60\%$  of the  $p\bar{p}$  interactions. The new Run-II SVX II detector, with a total length of 87 cm, will cover  $\approx 85\%$  of the interactions. This increase in acceptance means that both the trigger rates and efficiencies will be higher than the estimates based

<sup>14</sup>We assume that each reconstructed primary vertex is originated by a  $p\bar{p}$  collision. See Section 5.5.4 and Table 6.1.

Level 2	Trigger Efficiency (%)				
	$\bar{\mu} = 2$	$\bar{\mu} = 3$	$\bar{\mu} = 4$	$\bar{\mu} = 5$	$\bar{\mu} = 2.2$
<b>Calorimetry:</b> $N_{clus}(E_T \geq 10) \geq 3$ , $\sum E_T(\geq 10) \geq 90 \text{ GeV}$	$2.18 \pm 0.05$	$2.42 \pm 0.07$	$2.32 \pm 0.1$	$3.12 \pm 0.01$	$2.32 \pm 0.03$
<b>Calorimetry +</b> $\geq 2 \text{ SVT tracks:}$ $ d_0  \geq 100 \mu\text{m},  d_1  \geq 80 \mu\text{m}$	$0.15 \pm 0.01$	$0.18 \pm 0.02$	$0.17 \pm 0.03$	$0.27 \pm 0.06$	$0.158 \pm 0.007$

Table 7.9: Level 2 trigger efficiencies for the *JET-20* data sample as a function of the number of primary vertices found in the event ( $\bar{\mu}$ ). Last column shows the trigger efficiencies when the trigger requirements are applied to the complete data sample. Uncertainties include statistical errors only.

on the Run-I detector configuration. In the following we will describe how to correct for this.

As stated before, SVT-like tracks must have one hit in each of the four innermost layers of the SVX' detector, all the layers must belong to the same wedge, and it must be possible to link the track with a CTC track. This introduces two inefficiencies:

- Many tracks within the SVX' acceptance do not have hits in all four layers.
- The SVX' has a lower geometrical acceptance than the CTC drift chamber. Thus, for collisions that occur outside the SVX' acceptance ( $|z| \geq 50 \text{ cm}$ ) only CTC tracks can be reconstructed.

In Run-II, with a larger SVX II detector, the inefficiency due to the geometrical acceptance will decrease.<sup>15</sup> A scale factor to account for this increase in acceptance can be estimated as the ratio:

$$f = \frac{A^{\text{Run-II}}}{A^{\text{Run-I}}} \quad (7.1)$$

where  $A$  represents the fraction of events that satisfy the Level 2 calorimeter requirements and have at least two SVT tracks.  $A$  can be written as:

$$A = \sum_n P_n \cdot \int g(z) \cdot \epsilon_{cal}(z) \cdot p_{\geq 2 \text{ SVT}}(z, n) \cdot dz \quad (7.2)$$

where:

- The sum is performed over the total number of tracks,  $n$ , reconstructed in the CTC ( $|\eta| \leq 1$ ,  $p_T \geq 2.0 \text{ GeV}/c$ ) and multiplied by their probability distribution  $P_n$ . On average,  $n = 13 \pm 5$  (rms) for the signal, while for the background (*JET-20*)  $n = 4 \pm 3$  (rms) (Figure 7.20).  $n$  has been found to be independent of  $z$ .

<sup>15</sup>The CTC has been also replaced by a new Central Outer Tracker (COT) but its acceptance remains the same.

- $g(z)$  is the distribution of the  $p\bar{p}$  interactions as a function of the  $z$  coordinate measured along the beam axis.
- $\epsilon_{cal}(z)$  is the probability for an event to satisfy the Level 2 calorimetric requirements as a function of the  $z$  coordinate. Its value has been found to be independent of  $z$  and equal to  $0.78 \pm 0.10$  for the signal ( $M_H = 120 \text{ GeV}/c^2$ ), and  $2.28 \pm 0.03$  for the background (*JET-20*).
- $p_{\geq 2SVT}(z, n)$  is the probability to have at least two SVT-like tracks for an event with  $n$  tracks reconstructed in the CTC. It can be written as:

$$p_{\geq 2SVT}(z, n) = 1 - (1 - \epsilon_{tr}(z))^n - n \cdot \epsilon_{tr}(z) \cdot (1 - \epsilon_{tr}(z))^{(n-1)} \quad (7.3)$$

where  $\epsilon_{tr}(z)$  is the probability for a CTC track to have four hits in the silicon.  $\epsilon_{tr}(z)$  is calculated for both signal and background as the ratio between the two distributions shown in Figure 7.21. These curves represent the distribution of the track's  $z_0$  coordinate along the beam axis for all tracks found in the CTC, and for those with additional four hits in the SVX'. All events satisfy the calorimetric trigger requirements, and only tracks with  $p_T \geq 2 \text{ GeV}/c$  and  $|\eta| \leq 1$  are considered. Figure 7.22 shows  $\epsilon_{tr}(z)$  for the signal ( $M_H = 120 \text{ GeV}/c^2$ ) and background for the Run-I detector configuration. For Run-II, with the new SVX II detector, the estimated value of  $\epsilon_{tr}(z)$  has been taken from reference [120]. It assumes the same Run-I intrinsic efficiency for a track to have at least four silicon hits, but takes into account the extended coverage in  $z$ .

Table 7.10 summarizes the values obtained for the acceptances  $A^{Run-I}$ ,  $A^{Run-II}$ , and for the scale factor  $f$ . Results are shown for the signal ( $M_H = 120 \text{ GeV}/c^2$ ) and the background (*JET-20*). To extrapolate to Run-II conditions where the trigger requires at least two SVT tracks signal efficiencies must be multiplied by a factor  $f_S = 1.30 \pm 0.02$ , while the rates are increased by a factor  $f_R = 1.295 \pm 0.007$ .

	$A^{Run-I}$	$A^{Run-II}$	$f$
<i>JET-20</i>	$0.01220 \pm 0.00005$	$0.01581 \pm 0.00002$	$1.295 \pm 0.007$
Signal	$0.539 \pm 0.005$	$0.701 \pm 0.005$	$1.30 \pm 0.02$

Table 7.10: Run-I ( $A^{Run-I}$ ) and Run-II ( $A^{Run-II}$ ) acceptances for events with at least two SVT-like tracks for  $H + W/Z \rightarrow b\bar{b}jj$  ( $M_H = 120 \text{ GeV}/c^2$ ) and *JET-20* events. Last column shows the corresponding scale factor  $f = A^{Run-II}/A^{Run-I}$ . Level 2 calorimetric requirements are also applied.

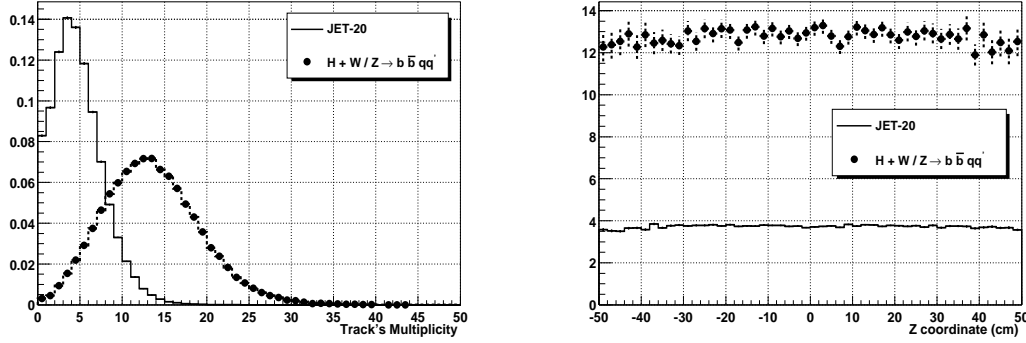


Figure 7.20: Left Figure: CTC track multiplicity ( $p_T \geq 2 \text{ GeV}/c$ ,  $|\eta| \leq 1$ ) for *JET-20* events (histogram) and for  $H + W/Z \rightarrow b\bar{b}jj$  events (dots) [ $M_H = 120 \text{ GeV}/c^2$ ]. Both distributions are normalized to unit area. Right Figure: average CTC track multiplicity ( $p_T \geq 2 \text{ GeV}/c$ ,  $|\eta| \leq 1$ ) versus the  $z$  coordinate of the primary vertex for *JET-20* events (histogram) and for  $H + W/Z \rightarrow b\bar{b}jj$  events (dots) [ $M_H = 120 \text{ GeV}/c^2$ ], simulated with an interaction point spread of  $\sigma_z = 30 \text{ cm}$ . In both figures all events satisfy the Level 2 trigger calorimeter requirements.

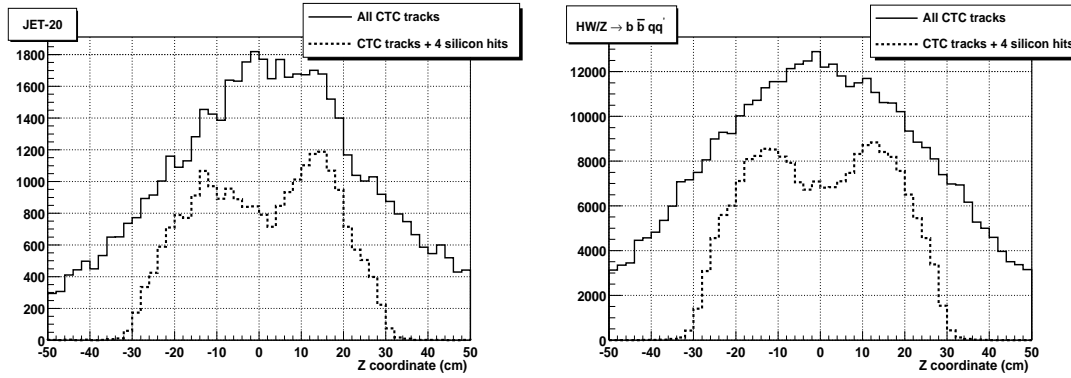


Figure 7.21: Distribution of track's  $z_0$  origin coordinate along the beam axis for all CTC tracks (solid histogram) and for CTC tracks with one hit in each of the four innermost layers of the SVX' (dashed histogram). Distributions are shown for the *JET-20* data sample (left figure) and for  $H + W/Z \rightarrow b\bar{b}jj$  events [ $M_H = 120 \text{ GeV}/c^2$ ] (right figure) simulated with an interaction point spread of  $\sigma_z = 30 \text{ cm}$ . All events satisfy the Level 2 trigger calorimeter requirements.

## 7.6 Level 3 Trigger

The Level 3 trigger has a maximum input rate of 300 Hz, while the maximum output rate to tape is 75 Hz. As studied in the previous section, using the SVT at Level 2 the output rate is  $1.08 \times 1.3 = 1.40 \pm 0.05 \text{ Hz}$  (Table 7.7), well below the 5% of the total output rate to tape, and thus the data stream can be log to the permanent storage media. However, at Level 3 calorimeter data and jet reconstruction algorithms

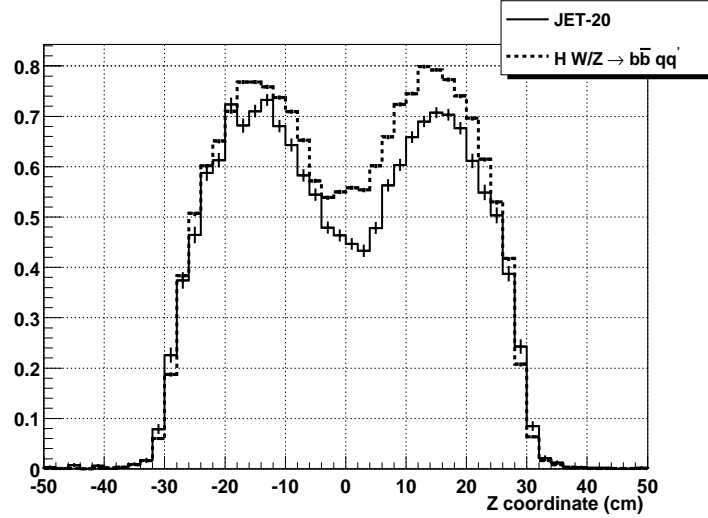


Figure 7.22: Probability for a CTC track to have one hit in each of the four innermost layers of the SVX' as a function of the track origin coordinate along the beam axis. Distributions are shown for the *JET-20* data sample (solid histogram) and for the  $H + W/Z \rightarrow b\bar{b}jj$  signal [ $M_H = 120 \text{ GeV}/c^2$ ] (dashed histogram), simulated with an interaction point spread of  $\sigma_z = 30 \text{ cm}$  along the beam axis. All events satisfy the Level 2 trigger calorimetric requirements.

with offline precision are available for every event. Therefore, further filtering can be performed by requiring the confirmation of the Level 2 calorimetric conditions with “offline” jet reconstruction algorithms. A conservative approach<sup>16</sup> at Level 3 is to confirm the Level 2 trigger requirements, with at least three jets with  $E_T^{jet} \geq 10 \text{ GeV}$ , and  $\sum E_T^{jet} \geq 90 \text{ GeV}$  (Figure 7.23). Tables 7.11 and 7.12 summarize the Level 3 trigger requirements and the expected rates.

Figure 7.24 shows the signal efficiency ( $M_H = 120 \text{ GeV}/c^2$ ) and trigger rate ( $\mathcal{L} = 1 \cdot 10^{32} \text{ cm}^{-2}\text{s}^{-1}$ ) as a function of the  $\sum E_T^{jet}$ . The rate curves fall down more rapidly than the efficiency curves, and thus the  $\sum E_T^{jet}$  at Level 3 can be used for rate control (see Section 7.5.3).

## 7.7 b-Tag Rates

The most straight-forward search strategy for the Higgs boson in the  $H + W/Z \rightarrow b\bar{b}jj$  channel is the requirement of events with four jets, where two of them are identified as b-quark jets [114].

Therefore, with the proposed trigger requirements we must ensure that we are not rejecting a significant number of events where the b-jets could be successfully identified by the offline algorithms. For this purpose we evaluate the b-tag rates

<sup>16</sup>Once the trigger rates are under control, the general approach is to have the loosest trigger conditions to accept as much signatures as possible.

Level 3 (signal)	Eff. $M_H$ (GeV/ $c^2$ )				
	110	115	120	125	130
$N_{\text{jet}}(E_T^{\text{jet}} \geq 10 \text{ GeV}) \geq 3$ $\Sigma E_T^{\text{jet}} \geq 90 \text{ GeV}$	$37.3 \pm 0.5\%$	$38.0 \pm 0.7\%$	$39.3 \pm 0.3\%$	$42.0 \pm 0.7\%$	$43.2 \pm 0.9\%$

Table 7.11: Level 3 signal trigger efficiencies for different Higgs boson masses. Level 1 and Level 2 trigger requirements are also applied. The scale factor for the increased SVX II acceptance is included.

Level 3 <i>JET-20</i>	Rate (Hz)	$\sigma_T$ (nb)
$N_{\text{jet}}(E_T^{\text{jet}} \geq 10 \text{ GeV}) \geq 3$ $\Sigma E_T^{\text{jet}} \geq 90 \text{ GeV}$	$1.39 \pm 0.05$	$13.9 \pm 0.5$

Table 7.12: Level 3 trigger rates. Level 1 and Level 2 trigger requirements are also applied. The scale factor for the increased SVX II acceptance is included.

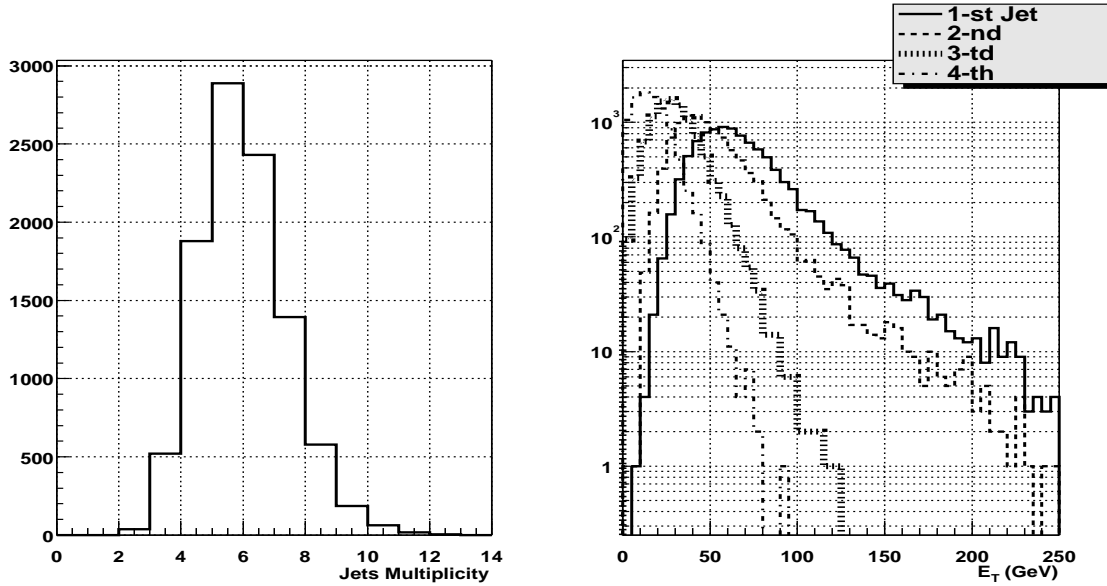


Figure 7.23: Signal jet multiplicity (left figure) [ $M_H = 120 \text{ GeV}/c^2$ ] and  $E_T^{\text{jet}}$  spectrum (right figure) of the four highest  $E_T^{\text{jet}}$  jets in the event.

in a signal sample that satisfies the trigger requirements using the CDF SECVTX [103] algorithm with the Run I detector configuration (see Section 5.5.5). Note that with the new SVX II vertex detector, the b-tag efficiencies will improve due to the increased number of silicon layers available for track reconstruction (7 instead of 4), the additional stereo information (that will allow three dimensional reconstruction

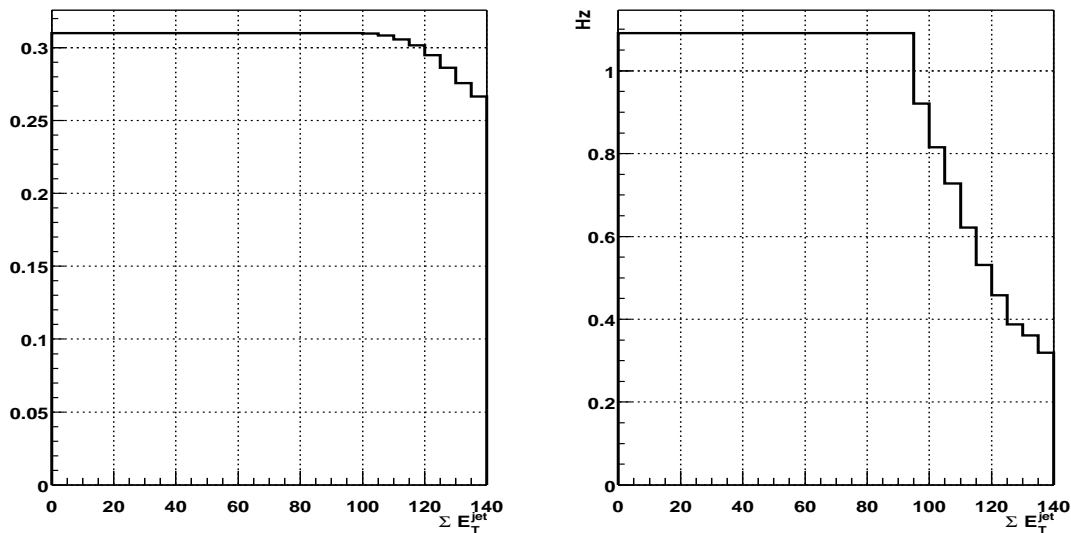


Figure 7.24: Level 3 trigger efficiency ( $M_H = 120 \text{ GeV}/c^2$ ) and rates ( $\mathcal{L} = 1 \cdot 10^{32} \text{ cm}^{-2}\text{s}^{-1}$ ) after Level 2 plus Level 3 requirements as a function of the  $\sum E_T^{jet}$  threshold.

and better rejection of fake b-tags), and the extended coverage in pseudorapidity with the ISL detector (that will allow to perform standalone silicon tracking up to pseudorapidities of  $|\eta| \leq 2$ ). However, no attempt to evaluate such improvements is done in this thesis. Without a detailed simulation of the geometry of the new detector and the corresponding tuning to real data is practically impossible to make reliable estimations. On the other hand, the SVX II with a larger acceptance in  $z$  (Section 7.5.5) will allow track reconstruction with silicon data for  $\sim 80\%$  of the events, instead of  $\sim 60\%$  in Run-I.

Table 7.13 shows the single and double b-tag rates for a signal sample which satisfies the different Level 2 trigger requirements.<sup>17</sup> For comparison, the b-tag rates for a sample selected with the Run-I multijet trigger is also shown. Single and double b-tag rates are defined as the fraction of events with at least one or two b-tags after the trigger requirements, respectively.

With only the calorimetric requirements the single b-tag rate is  $44.7 \pm 0.1\%$ , while the double b-tag rate is  $12.8 \pm 0.1\%$ . With the SVT requirements the single and double b-tag efficiencies are, respectively,  $80.7 \pm 0.1\%$  and  $27.7 \pm 0.1\%$ , which represents, a gain by a factor of  $\sim 2$ . This result is consistent with the expected correlation between the performance of the SECVTX algorithm and the presence of high impact parameter tracks, since the SECVTX algorithm identifies b-quark jets by searching for secondary vertices using tracks with high impact parameter significance (Section 5.5.5).

<sup>17</sup>The Level 1 requirement of one single trigger tower with  $E_T^{low} \geq 10 \text{ GeV}$  is satisfied by almost  $\sim 100\%$  of the events.

Trigger Cuts	$M_H = 120 \text{ GeV}/c^2$			Rate (Hz)
	b-tag rates (%)		$\epsilon_{\text{trigger}}$ (%)	
	Single tag	Double tag		
<b>Run-I</b> $N_{\text{cl}}(E_{\text{T}}^{\text{cl}} \geq 15 \text{ GeV}) \geq 4$ $\Sigma E_T^{\text{cl}} \geq 125 \text{ GeV}$	$40.3 \pm 0.1$	$12.6 \pm 0.4$	$24.6 \pm 0.4$	–
<b>Run-II</b> Level 2 Calorimetry: $N_{\text{clus}}(E_T^{\text{cl}} \geq 10 \text{ GeV}) \geq 3$ , $\Sigma E_T^{\text{cl}} \geq 90 \text{ GeV}$	$44.7 \pm 0.1$	$12.8 \pm 0.2$	$78.1 \pm 0.2$	$17.1 \pm 0.6$
Level 2 Calorimetry + $\geq 2$ SVT tracks $ d_0  \geq 100,  d_1  \geq 80 \mu\text{m}$	$80.7 \pm 0.1$	$27.7 \pm 0.1$	$39.9 \pm 0.3$	$1.40 \pm 0.05$
Level 2 + Level 3: $N_{\text{jet}}(E_T^{\text{jet}} \geq 10 \text{ GeV}) \geq 3$ , $\Sigma E_T^{\text{jet}} \geq 90 \text{ GeV}$	$80.7 \pm 0.1$	$27.0 \pm 0.1$	$39.3 \pm 0.3$	$1.39 \pm 0.05$

Table 7.13: Signal single and double b-tag rates, trigger efficiency ( $\epsilon_{\text{trigger}}$ ) and trigger rate ( $\mathcal{L} = 1 \cdot 10^{32} \text{ cm}^{-2} \text{ s}^{-1}$ ) for the Run-I multijet trigger and for the each of the Run-II trigger requirements, computed with the SECVTX b-tag algorithm in Run-I configuration. Quoted uncertainties include statistical errors only. The scale factors calculated in Section 7.5.5 have been applied.

With the Run-I multijets trigger the total efficiency for double b-tag events after the trigger requirements is  $3.1 \pm 0.1\%$ , while for the trigger under study is  $10.7 \pm 0.1\%$ . This represents a net gain by a factor of  $\sim 3.4$ .

## 7.8 Run-II *versus* Run-I Improvement and Trigger Cuts Summary

In Run-I the search for a SM Higgs boson in the  $H + W/Z \rightarrow b\bar{b}jj$  channel was done with the Run-I multijet data sample [115], collected with the following trigger requirements:

- **Level 1 trigger:**  $\Sigma E_T \geq 120 \text{ GeV}$
- **Level 2 trigger:**  $N_{\text{clus}} \geq 4$  ( $E_T^{\text{clus}} \geq 15$ ), and  $\Sigma E_T^{\text{clus}} \geq 125 \text{ GeV}$

This trigger was optimized for the top quark search in the fully hadronic mode, where  $p\bar{p} \rightarrow t\bar{t} \rightarrow bW^- \bar{b}W^+$ ,  $W^\pm \rightarrow q\bar{q}'$  [118], with a high jet multiplicity ( $\approx 5$  jets) and a high total transverse energy ( $\Sigma E_T \approx 350 \text{ GeV}$ ) final signature. The trigger was very efficient, with signal efficiencies  $\sim 80\%$ .

However, for the  $H + W/Z \rightarrow b\bar{b}jj$  channel the Run-I multijet trigger is quite inadequate because it rejects  $\sim 75\%$  of the events for Higgs boson masses up to  $140 \text{ GeV}$ . This is due to the lower jet multiplicity ( $\approx 4$  jets) and lower total transverse energy  $\Sigma E_T \approx 200 \text{ GeV}$  of the  $H + W/Z \rightarrow b\bar{b}jj$  process.

In this thesis we have studied and proposed a trigger specially designed for the  $H + W/Z \rightarrow b\bar{b}jj$  channel, more efficient and able to keep the rates under control for instantaneous luminosities up to  $2 \cdot 10^{32} \text{ cm}^{-2} \text{ s}^{-1}$ , which represents a 20 fold increase with respect to Run-I luminosities.

The basic idea is to lower the Level 2 calorimetric requirements to obtain a higher efficiency. The increased rate due to the lower calorimetric requirements can be suppressed with the use of the new Run-II SVT, which allows to trigger on large impact parameter tracks.

A summary of the proposed trigger cuts is:

- **TRIGGER LEVEL 1:**

- **Calorimetric Primitives:**

- \* Single Calorimeter Trigger-Tower  $E_T^{tow} \geq 10 \text{ GeV}$

- **TRIGGER LEVEL 2:**

- **Calorimeter Clustering:**

- \*  $N_{clus} \geq 3$  ( $E_T^{clus} \geq 10 \text{ GeV}$ )

- \*  $\sum E_T^{clus} \geq 90 \text{ GeV}$

- **SVT:**

- \* At least two SVT tracks with impact parameter

- $|d_0| \geq 100 \mu\text{m}, |d_1| \geq 80 \mu\text{m}$

- **TRIGGER LEVEL 3:**

- **Calorimeter Reconstruction:**

- \*  $N^{jets} \geq 3, E_T^{jet} \geq 10 \text{ GeV}$

- \*  $\sum E_T^{jets} \geq 90 \text{ GeV}$

By relaxing the Level 2 calorimetric requirements the trigger efficiency is improved up to  $\sim 78\%$ , with Level 2 rates well under control ( $\sim 17 \text{ Hz}$ ) and with a net gain by a factor of  $\sim 3$  respect to the Run-I efficiencies. However, at Level 3 these rates are still excessive and further rejection is needed. We find that exploiting the novel CDF capability to trigger on large impact parameter tracks with the SVT [12] acceptable rates can be reached ( $\sim 1.4 \text{ Hz}$ ) with still high signal efficiencies ( $\sim 40\%$ ).

Trigger on high impact parameter tracks is specially efficient for heavy flavor jets. High impact parameter tracks are correlated with the presence of secondary vertices due to the long lifetime of B-hadrons, which are produced in the hadronization of b-quarks.<sup>18</sup> As a reference, we have evaluated the single and double b-tag rates for

---

<sup>18</sup>We do not consider the identification of b-jets searching for leptons inside a jet produced in the leptonic decays of the b-quark through  $b \rightarrow l\nu X$  ( $l = e \text{ or } \mu$ ).

a sample satisfying the new trigger requirements and for a sample selected with the Run-I multijet trigger. For the new trigger the double b-tag rate is  $\sim 28\%$ , while with the Run-I multijet trigger is  $\sim 13\%$ , which represents a net gain in double b-tag events by a factor of  $\sim 3$ .



# Chapter 8

## Design of a Dedicated Trigger for $H + Z \rightarrow b\bar{b}\nu\bar{\nu}$ Searches

In this Chapter we discuss the design of a trigger optimized for Higgs boson searches in the  $H + Z \rightarrow b\bar{b}\nu\bar{\nu}$  channel. Although this channel yields less events than the  $H + W/Z \rightarrow b\bar{b}jj$  process due to the lower branching ratio of  $Z \rightarrow \nu\bar{\nu}$  decays, it is very promising because it has a cleaner signature that allows to keep the backgrounds under control. Indeed, the best exclusion limits in the CDF Run-I searches were set in this channel, where an inclusive missing transverse energy trigger was used.

In Run-II, with the increase of the instantaneous luminosity, the inclusive missing transverse energy trigger will require higher thresholds to avoid the saturation of the data acquisition bandwidth, with the subsequent loss of signal efficiency. We show that the use of the Silicon Vertex Trigger at Level 2 will allow to keep low thresholds on the missing transverse energy, while reducing the rates with a high signal efficiency. In addition, with this trigger the efficiency for the specific selection of the Run-I analysis is also enhanced.

This Chapter is organized as follows. First we discuss the trigger strategy and calculate the efficiencies and rates at each level. Next we study the impact of the proposed trigger on the performance of the offline reconstruction algorithms, like the b-jet identification and the missing transverse energy turn-on behavior. Finally, all results are summarized.

### 8.1 Motivation

In the  $H + Z \rightarrow b\bar{b}\nu\bar{\nu}$  channel the branching ratio for the  $Z \rightarrow \nu\bar{\nu}$  decay represents roughly a third of the fully hadronic modes, as is the case for the  $H + W/Z \rightarrow b\bar{b}jj$  channel, where  $\text{BR}(W/Z \rightarrow q\bar{q}') = 0.70$ . However, the number of events is still significant (Table 8.1), and its clean signature allows to keep the backgrounds under control. With a final state signature of two energetic b-jets and large missing transverse energy ( $\cancel{E}_T$ ) (Figure 8.1), the main backgrounds are QCD heavy flavor jet production where the  $\cancel{E}_T$  comes from mismeasured jet energy, and  $W + \text{jets}$

production. The QCD heavy flavor background can be reduced by requiring large  $\cancel{E}_T$  and taking into account the existing correlations between  $\cancel{E}_T$  from missmeasured jets and the jet topology. The  $W + \text{jets}$  background can be excluded by rejecting leptons. In all cases, the presence of two b-jets allows to reconstruct the Higgs boson invariant mass without ambiguities.

$M_H$ ( GeV/ $c^2$ )	$\sigma_{HZ}$ (pb)	B.R. $H \rightarrow b\bar{b}$	# Ev. in 2 fb $^{-1}$	#Ev. in 15 fb $^{-1}$
110	0.13	0.76	40	296
115	0.12	0.73	35	263
120	0.10	0.68	27	204
125	0.09	0.61	22	165
130	0.08	0.53	17	127
135	0.06	0.44	11	79

Table 8.1: Expected total number of events for the  $H + Z \rightarrow b\bar{b}\nu\bar{\nu}$  channel ( $\text{BR}(Z \rightarrow \nu\bar{\nu}) = 0.20$ ) at  $\sqrt{s} = 2.0$  TeV with 2 and 15 fb $^{-1}$  of integrated luminosity [8, 90].

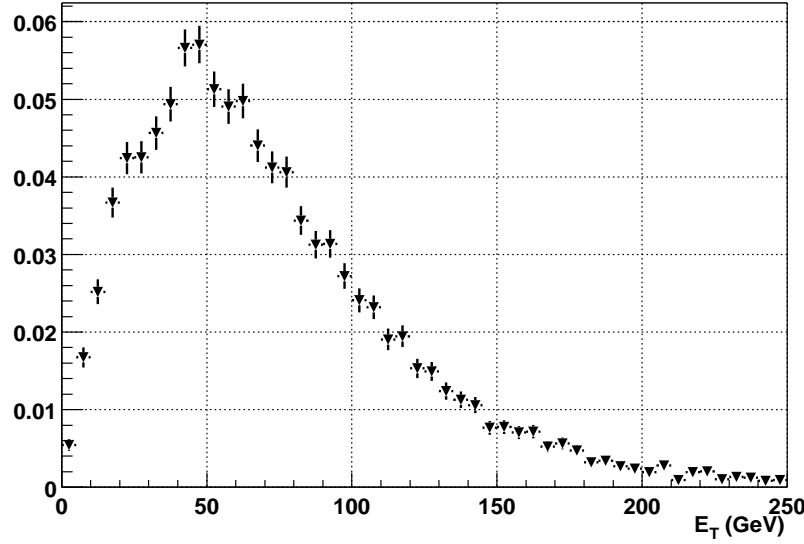


Figure 8.1: Transverse energy distribution for the  $\nu\bar{\nu}$  system of  $H + Z \rightarrow b\bar{b}\nu\bar{\nu}$  events ( $M_H = 120$  GeV) at  $\sqrt{s} = 2.0$  TeV [90]. The distribution is normalized to unit area.

The Run-I trigger for this channel required  $\cancel{E}_T$  above 35 GeV at Level 2. In Run-II, with a 20 fold increase of instantaneous luminosity, the threshold must be raised up to 45 GeV to keep acceptable rates [117]. To reduce the rates without increasing the  $\cancel{E}_T$  threshold, additional information provided by the signature of the two b-jets can be used by requiring the presence of calorimeter clusters. With this selection the main background is QCD di-jet production, where the missing energy

comes from missmeasured clusters. Further background rejection at Level 2 can be achieved with tracks reconstructed with the Silicon Vertex Trigger (SVT) by selecting only jets with large impact parameter tracks.

At Level 1 trigger the aim is to reject events with low transferred momentum. The energy deposition in the calorimeter can be effectively used as a discrimination variable. We found that the requirement of a single calorimeter trigger tower with high  $E_T^{tow}$  provides enough background reduction with high signal efficiency. As stated above, at Level 2 the selection requires a combination of  $\cancel{E}_T$ , calorimeter clusters, and tracks with high impact parameter. At Level 3 offline jet-clustering and  $\cancel{E}_T$  calculation with offline resolution are available. Therefore, the confirmation of at least two jets and the presence of  $\cancel{E}_T$  reconstructed with the offline algorithms is required.

## 8.2 Trigger Rate and Efficiency Calculation

Trigger rate and signal efficiencies are estimated following the procedure described in Chapter 6. The process  $H + Z \rightarrow b\bar{b}\nu\bar{\nu}$  is simulated with the PYTHIA Monte Carlo program [90] at  $\sqrt{s} = 2$  TeV. B-hadron decays are corrected with the program CLEOMC [110]. The detector response is simulated with the standard Run-I CDF program QFL'. The Level 1 trigger rate is estimated with the Run-I *minimum bias* data sample. For Level 2 we use the *JET-20* data sample, acquired requiring at least one calorimeter cluster with  $E_T^{clus} \geq 20$  GeV, and no requirements on  $\cancel{E}_T$ .

## 8.3 Level 1 Trigger Rates and Efficiencies

The signature under study contains at least two energetic jets ( $E_T \approx 50$  GeV) in the final state. The aim of the Level 1 trigger is to reject events with low transverse momentum. As discussed in Section 7, for a jets based signature the Level 1 single calorimeter tower trigger is the most adequate. The segmentation of the calorimeter in trigger towers has been optimized to contain the most part of the energy released by a jet hitting the center of the tower [116]. Therefore, the presence of at least one trigger tower with transverse energy above a certain threshold will be efficient for the signal, while discarding most of the events with low transverse momentum (Figure 8.2). In Chapter 7 we have found that a trigger based on a 10 GeV threshold on the highest  $E_T^{tow}$  trigger tower provides an acceptable rate of  $1.58 \pm 0.06$  kHz ( $\mathcal{L} = 1 \cdot 10^{32} \text{ cm}^{-2}\text{s}^{-1}$ ). Figure 8.3 shows the signal efficiency as a function of the threshold on the highest  $E_T^{tow}$  trigger tower. The efficiency is almost  $\approx 100\%$  up to thresholds of 4 GeV, and remains above 90% for thresholds up to 12 GeV. For  $E_T^{tow} = 10$  GeV the efficiency is  $92.6 \pm 0.2\%$ . Therefore, an inclusive Level 1 trigger which requires one single trigger tower with  $E_T^{tow} \geq 10$  GeV is completely adequate

for the channel under study. Table 8.2 summarizes the trigger efficiencies for different Higgs boson masses. The quoted uncertainties include statistical errors only.

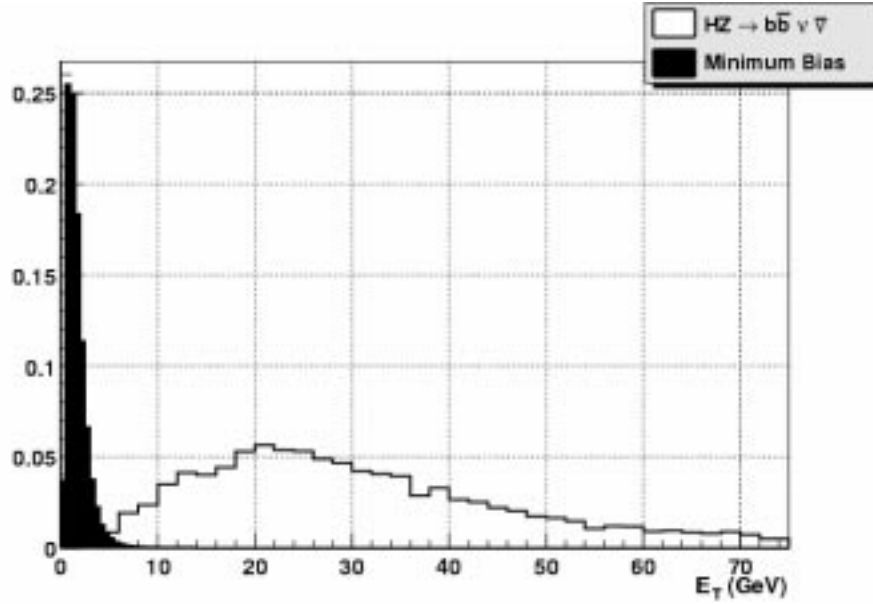


Figure 8.2: Highest  $E_T$  calorimeter trigger tower distribution for the minimum bias data sample (solid histogram) and for signal events (open histogram) [ $M_H = 120 \text{ GeV}/c^2$ ]. Both distributions are normalized to unit area.

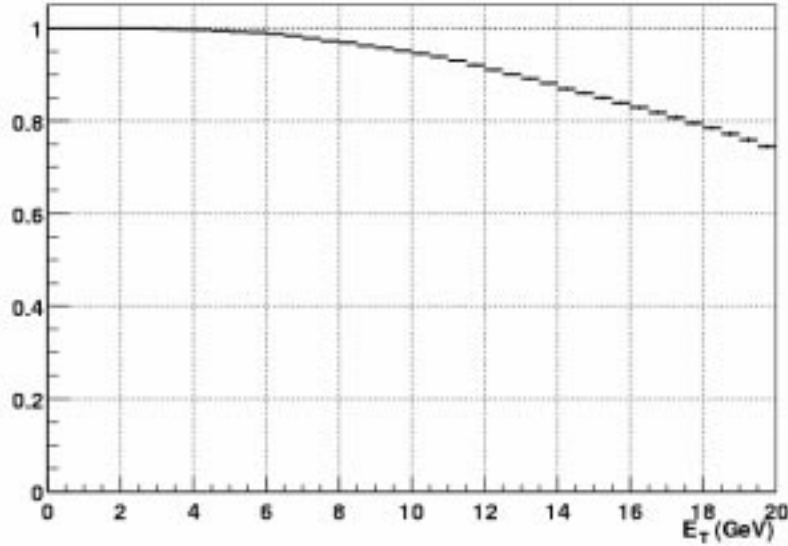


Figure 8.3: Level 1 trigger efficiency for the process  $H + Z \rightarrow b\bar{b}\nu\bar{\nu}$  as a function of the threshold on the highest  $E_T^{low}$  trigger tower ( $M_H = 120 \text{ GeV}/c^2$ ).

	Higgs Mass ( GeV/ $c^2$ )				
	110	115	120	125	130
Eff.(%)	$91.1 \pm 0.3$	$92.0 \pm 0.3$	$92.6 \pm 0.2$	$93.2 \pm 0.2$	$94.5 \pm 0.2$

Table 8.2: Level 1  $H + Z \rightarrow b\bar{b}\nu\bar{\nu}$  efficiencies as a function of the Higgs mass. The trigger requires at least one trigger tower with  $E_T^{tow} \geq 10$  GeV. Uncertainties include only statistical errors.

## 8.4 Level 2 Trigger Rates and Efficiencies

At Level 2 the maximum input rate is 50 kHz, while the maximum output rate is 300 Hz. Therefore, at this level a rejection factor of two orders of magnitude is necessary.

At Level 2 the  $\cancel{E}_T$ , already computed at Level 1, together with calorimeter clustering and the SVT information is available.<sup>1</sup> For all the trigger paths using SVT information it has been established [117] that if they are rejected by other requirements, then the SVT cut won't be tested.<sup>2</sup> Therefore, a first selection is performed based only in calorimetric information. A second selection based in SVT cuts is then applied.

### 8.4.1 Trigger Requirements

The first Level 2 requirement is a calorimeter cluster with  $E_T^{clus} \geq 20$  GeV. This confirms the presence of jet activity in the calorimeter. Figure 8.4 shows the signal cluster multiplicity and the transverse energy spectrum for the three highest  $E_T^{clus}$  clusters. All events have at least one cluster, and for  $\sim 96\%$  of them this cluster has  $E_T^{clus} \geq 20$  GeV. The next requirement is a threshold on  $\cancel{E}_T$ . Figure 8.5 shows the trigger  $\cancel{E}_T$  distribution for the signal and for the *JET-20* data sample. The signal has a substantially larger  $\cancel{E}_T$  distribution, and a good discrimination from background is reached for  $\cancel{E}_T \geq 20$  GeV.

The *JET-20* data sample contains practically only QCD events. The presence of  $\cancel{E}_T$  in QCD events is mainly due to detector effects such as cluster  $E_T^{clus}$  mismeasurement. Therefore, we must ensure that the  $E_T^{clus}$  of the required cluster is not strongly correlated with the amount of  $\cancel{E}_T$  in the event. Figure 8.6 shows the corre-

<sup>1</sup>At Level 1 we do not use the Level 1  $\cancel{E}_T$  trigger. The Level 1  $\cancel{E}_T$  trigger is an inclusive trigger that feeds also other trigger paths. Actually its threshold is fixed to 25 GeV [117]. If eventually at Level 2 we want to use lower thresholds on the  $\cancel{E}_T$ , we must lower also the threshold at Level 1. This threshold is very difficult to reduce, as for other trigger paths which also use the Level 1  $\cancel{E}_T$  trigger the input rate would unnecessary increase (and thus would occupy a higher percentage of the total bandwidth) since they have more tight requirements on the  $\cancel{E}_T$  at higher levels.

<sup>2</sup>The data from the SVT needs more time to be processed and arrives later than the other four trigger systems at Level 2. This procedure helps to reduce possible dead-time at Level 2 due to the SVT latency.

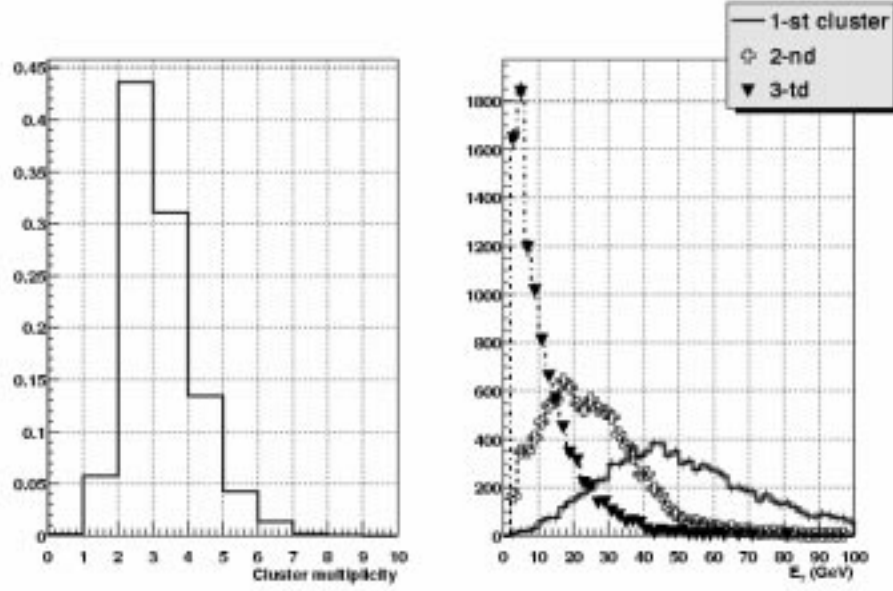


Figure 8.4: Level 2 cluster multiplicity (left figure) and  $E_T^{clus}$  spectrum (right figure) of the three highest  $E_T^{clus}$  clusters for  $H + Z \rightarrow b\bar{b}\nu\bar{\nu}$  events ( $M_H = 120 \text{ GeV}/c^2$ ).

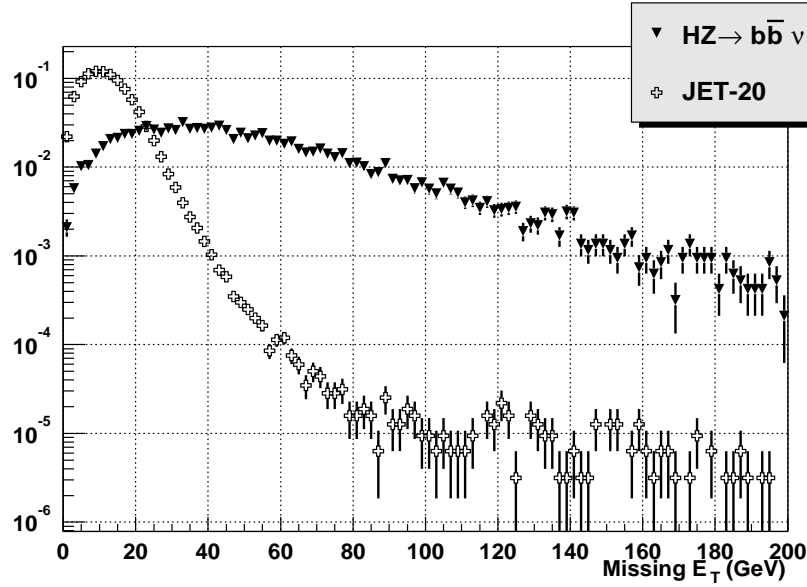


Figure 8.5: Trigger Level 2  $E_T$  distribution for  $H + Z \rightarrow b\bar{b}\nu\bar{\nu}$  (solid triangles) [ $M_H = 120 \text{ GeV}/c^2$ ] and *JET-20* (open crosses) events.

lation between the highest  $E_T^{clus}$  cluster and the trigger  $E_T$  for signal events, *JET-20* events, and for a simulated sample of QCD  $2 \rightarrow 2$  hard scattered events. As we could expect, the signal shows a clear linear correlation due to the energy conservation between the  $\nu\bar{\nu}$  system from the Z decay and the  $b\bar{b}$  system from the Higgs decay. For the QCD Monte Carlo or the *JET-20* data sample this correlation is

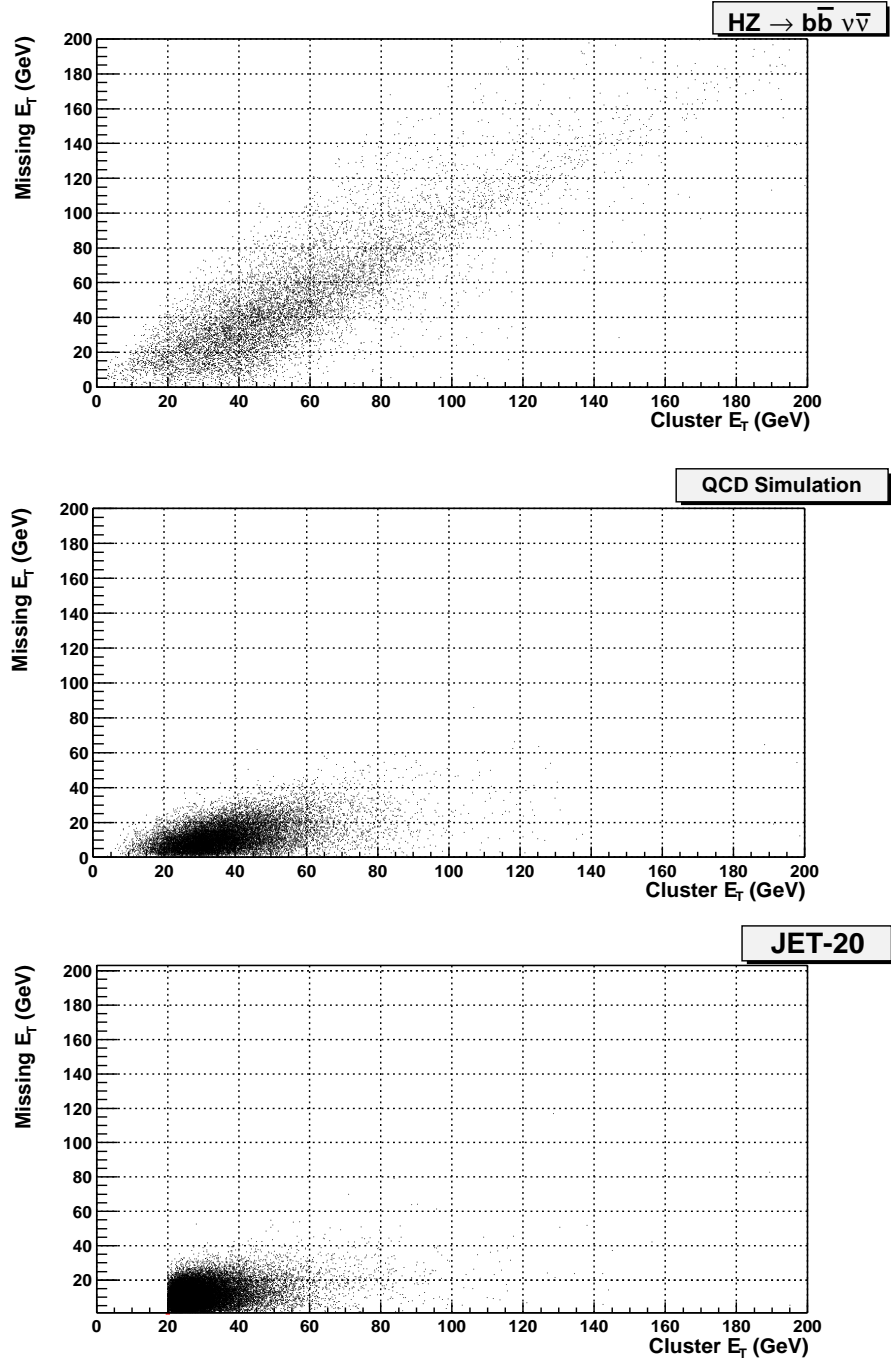


Figure 8.6: Level 2  $\cancel{E}_T$  versus the  $E_T$  of highest  $E_T^{clus}$  cluster for  $H + Z \rightarrow b\bar{b}\nu\bar{\nu}$  events (upper plot) [ $M_H = 120 \text{ GeV}/c^2$ ], for a QCD simulated sample of  $2 \rightarrow 2$  events ( $p_T^{min} \geq 40 \text{ GeV}/c$ ) [123], and *JET-20* events (bottom plot).

very weak and originates from events with cluster energy mismeasurements leading

to  $\cancel{E}_T$ <sup>3</sup>. Thus, the requirement of one cluster with at least  $E_T \geq 20$  GeV with a simultaneous threshold on the  $\cancel{E}_T$  should be efficient for the signal while rejecting a significant part of the background. As a starting point, at least one cluster with  $E_T^{clus} \geq 20$  GeV and  $\cancel{E}_T \geq 25$  GeV will be required. With the addition of the SVT requirements we will try to relax the requirements in  $\cancel{E}_T$  while keeping the rates under control.

Figure 8.7 shows the total Level 2 signal efficiency as a function of the Level 2  $\cancel{E}_T$  threshold for three sets of requirements:

- At least one cluster with  $E_T^{clus} \geq 20$  GeV.
- At least one cluster with  $E_T^{clus} \geq 20$  GeV, and at least one SVT track with impact parameter  $|d_0| \geq 100 \mu\text{m}$ .
- At least one cluster with  $E_T^{clus} \geq 20$  GeV, and at least two SVT tracks, one with impact parameter  $|d_0| \geq 100 \mu\text{m}$  and the other with  $|d_1| \geq 80 \mu\text{m}$ .

The first case represents the selection when only calorimetric information is used.

For any threshold in  $\cancel{E}_T$  the requirement of at least one SVT track with impact parameter  $\geq 100 \mu\text{m}$  reduces the background by a factor of  $\sim 7.5$ , while the efficiency is reduced by  $\sim 50\%$ . The trigger efficiency requiring SVT tracks already includes the enhancement factor due to the increased geometrical acceptance of the SVX II detector, and it can be estimated in a similar way as it was done in Section 7.5.5. The calculation for the  $H + Z \rightarrow b\bar{b}\nu\bar{\nu}$  channel yields a gain of  $\sim 1.3$  for both signal and background efficiencies. A further requirement of a second SVT track with impact parameter  $\geq 80 \mu\text{m}$  reduces the background by an additional factor of  $\sim 5$ , while the signal efficiency decreases only by  $\sim 30\%$ . As for the case of the  $H + W/Z \rightarrow b\bar{b}jj$  channel (see Section 7.5.2) this requirement provides a good background discrimination<sup>4</sup> (Figure 8.8).

The allowed bandwidth for a dedicated trigger is  $\approx 9$  Hz ( $\mathcal{L} = 1 \cdot 10^{32} \text{ cm}^{-2}\text{s}^{-1}$ ). Therefore, the  $\cancel{E}_T$  threshold can be safely set to 15 GeV, which yields a rate of  $\sim 6$  Hz (Figure 8.9). With these requirements the signal efficiency is  $\sim 40\%$ . The results in terms of signal efficiencies and rates are summarized in Tables 8.3 and 8.4 respectively.

In Run-II an inclusive  $\cancel{E}_T$  trigger exists [117]. The requirements for this trigger are  $\cancel{E}_T \geq 35$  GeV at Level 2 and  $\cancel{E}_T^{off} \geq 45$  GeV at Level 3. This trigger yields a Level 2 trigger rate of  $\sim 8$  Hz, while the trigger efficiency for  $H + Z \rightarrow b\bar{b}\nu\bar{\nu}$  is  $\sim 60\%$  (Table 8.3). Therefore, at Level 2 the addition of SVT requirements seems to be rather inefficient. The rates are similar ( $\sim 5$  Hz), but the signal efficiency for the inclusive  $\cancel{E}_T$  trigger is twice the obtained with the SVT requirements. However, the advantages of a lower threshold on the  $\cancel{E}_T$  will be clear in Section 8.6, where the

<sup>3</sup>For such events the  $\cancel{E}_T$  is pointing roughly in the direction of the cluster.

<sup>4</sup>Other combinations, as the requirement of a third track or combinations of the two impact parameters do not yield significant enhancements.

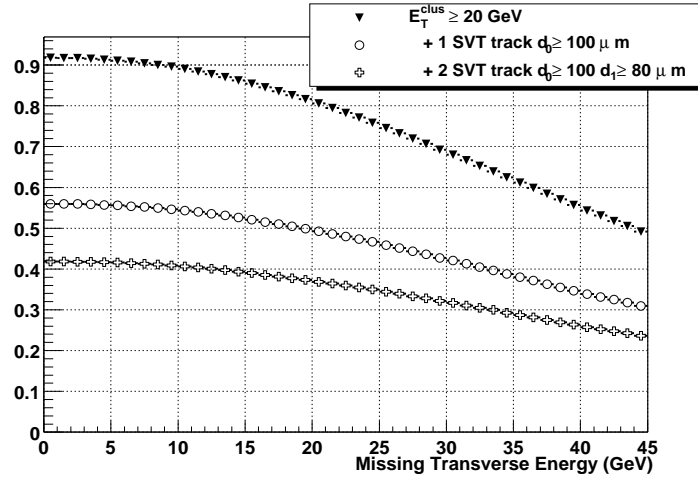


Figure 8.7: Level 2 trigger signal efficiency ( $M_H = 120 \text{ GeV}/c^2$ ) as a function of the  $\cancel{E}_T$  threshold for different calorimetric and SVT requirements: at least one cluster with  $E_T^{clus} \geq 20 \text{ GeV}$  (solid triangles); one cluster with  $E_T^{clus} \geq 20 \text{ GeV}$ , and at least one SVT track with  $|d_0| \geq 100 \mu\text{m}$  (open circles); a cluster with  $E_T^{clus} \geq 20 \text{ GeV}$ , and two SVT tracks, one with  $|d_0| \geq 100 \mu\text{m}$  and other with  $|d_1| \geq 80 \mu\text{m}$  (open crosses).

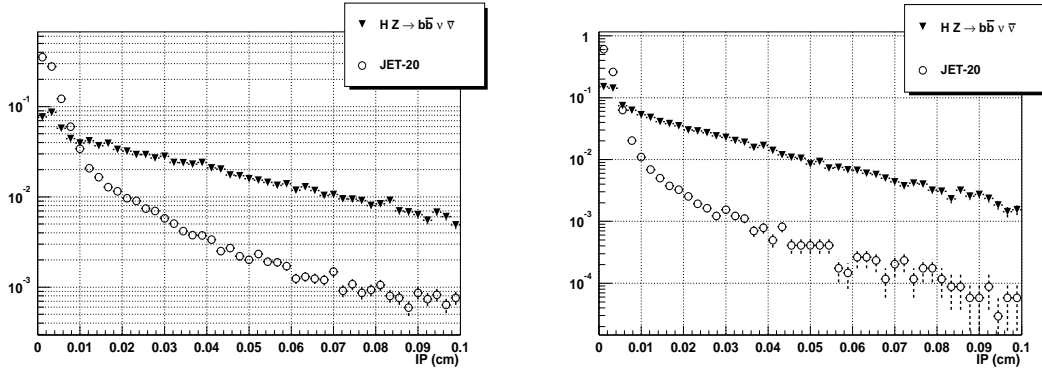


Figure 8.8: Distribution of the largest impact parameter (left) and second largest impact parameter (right) of SVT tracks for signal (triangles) [ $M_H = 120 \text{ GeV}/c^2$ ] and *JET-20* events (open circles). The Level 2 calorimetric requirements  $N_{clus} \geq 1$  ( $E_T^{clus} \geq 20 \text{ GeV}$ ) and  $\cancel{E}_T \geq 15 \text{ GeV}$  are applied. Both distributions are normalized to unit area.

$\cancel{E}_T$  trigger turn-on behavior will be studied. On the other hand, the SVT trigger requirements are very correlated with the performance of the offline b-tagging algorithms. In Section 8.7 we will show how the b-tagging algorithms are much more efficient in samples acquired with the SVT, yielding a higher total efficiency when double b-tagging is required.

The stability of the studied cuts have been checked against the number of multiple interactions as described in Section 6.5. No variations beyond the statistical uncertainties have been observed.

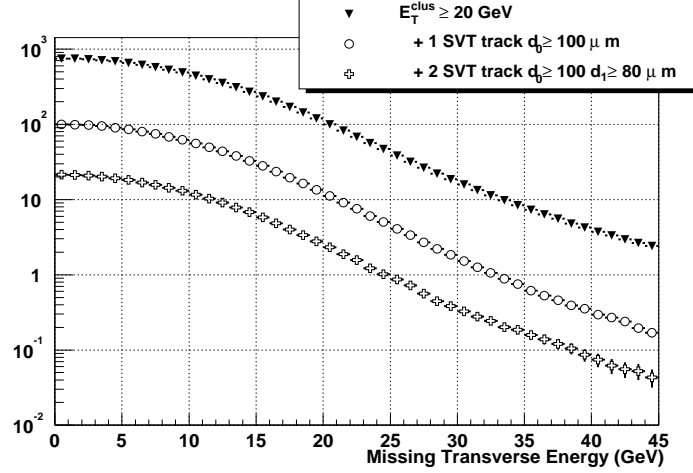


Figure 8.9: Level 2 trigger rates ( $\mathcal{L} = 1 \cdot 10^{32} \text{ cm}^{-2} \text{ s}^{-1}$ ) as a function of the  $\cancel{E}_T$  threshold for different calorimetric and SVT requirements: at least one cluster with  $E_T^{\text{clus}} \geq 20 \text{ GeV}$  (solid triangles); one cluster with  $E_T^{\text{clus}} \geq 20 \text{ GeV}$ , and at least one SVT track with  $|d_0| \geq 100 \mu\text{m}$  (open circles); one cluster with  $E_T^{\text{clus}} \geq 20 \text{ GeV}$ , and two SVT tracks, one with  $|d_0| \geq 100 \mu\text{m}$  and other with  $|d_1| \geq 80 \mu\text{m}$  (open crosses).

Selection Cut	Higgs Mass ( $\text{GeV}/c^2$ )				
	110	115	120	125	130
Inclusive $\cancel{E}_T \geq 35 \text{ GeV}$	$60.4 \pm 0.9$	$61.6 \pm 0.9$	$62.9 \pm 0.9$	$63.7 \pm 0.9$	$64.7 \pm 0.9$
$\cancel{E}_T \geq 15 \text{ GeV}$ $E_T^{\text{clus}} \geq 20 \text{ GeV}$	$85.4 \pm 0.9$	$86.6 \pm 0.9$	$86.9 \pm 0.3$	$88.7 \pm 0.9$	$84.7 \pm 0.9$
$\cancel{E}_T \geq 15 \text{ GeV} +$ $E_T^{\text{clus}} \geq 20 \text{ GeV}$ 1 SVT, $ d_0  \geq 100 \mu\text{m}$	$51.3 \pm 0.6$	$52.0 \pm 0.6$	$52.6 \pm 0.6$	$55.1 \pm 0.6$	$51.4 \pm 0.6$
$\cancel{E}_T \geq 15 \text{ GeV} +$ $E_T^{\text{clus}} \geq 20 \text{ GeV} +$ 1 SVT, $ d_0  \geq 100 \mu\text{m}$ 1 SVT, $ d_1  \geq 80 \mu\text{m}$	$38.2 \pm 0.5$	$38.6 \pm 0.5$	$39.2 \pm 0.7$	$40.9 \pm 0.5$	$38.2 \pm 0.5$

Table 8.3: Level 2 trigger efficiencies (%) for different selection of trigger requirements. The scale factors for the SVT requirements calculated in Section 7.5.5 have been applied.

## 8.5 Level 3 Trigger

At Level 3 the maximum input rate is 300 Hz with a maximum output rate to tape of 50 Hz. Our Level 2 trigger output rate is  $\sim 6 \text{ Hz}$ . Thus, to stay within the 5% of the total output bandwidth, a rejection factor of 3 is needed. The  $\cancel{E}_T$  calculation and jet reconstruction are available at Level 3 trigger with offline precision. Therefore,

	$\sigma_T$ (nb)	Rate (Hz)	Rejection Factor
<b>Inclusive <math>\cancel{E}_T \geq 35</math> GeV</b>	$77 \pm 1$	$7.7 \pm 0.7$	$97 \pm 2$
$\cancel{E}_T \geq 15$ GeV $E_T^{clus} \geq 20$ GeV	$2344 \pm 7$	$234.4 \pm 0.7$	$3.2 \pm 0.1$
$\cancel{E}_T \geq 15$ GeV + $E_T^{clus} \geq 20$ GeV 1 SVT, $ d_0  \geq 100 \mu\text{m}$	$280 \pm 3$	$28.0 \pm 0.3$	$26.8 \pm 0.3$
$\cancel{E}_T \geq 15$ GeV + $E_T^{clus} \geq 20$ GeV 1 SVT, $ d_0  \geq 100 \mu\text{m}$ 1 SVT, $ d_1  \geq 80 \mu\text{m}$	$58 \pm 6$	$5.8 \pm 0.6$	$129 \pm 3$

Table 8.4: Level 2 trigger rates ( $\mathcal{L} = 1 \cdot 10^{32} \text{ cm}^{-2} \text{ s}^{-1}$ ), trigger cross sections ( $\sigma_T$ ), and rejection factors for different selection of trigger requirements. The scale factors for the SVT requirements calculated in Section 7.5.5 have been applied.

further filtering can be performed by requiring the confirmation of the Level 2 trigger conditions. The filter requires at least two jets with uncorrected  $E_T \geq 15$  GeV, and  $\cancel{E}_T \geq 15$  GeV. 87% of signal events that satisfy the Level 2 trigger cuts have two jets with  $E_T \geq 15$  GeV and offline  $\cancel{E}_T \geq 15$  GeV. For background events this requirement produces an additional rejection factor of  $\sim 2.7$  (with a final output rate of  $1.7 \pm 0.1$  Hz). The results are summarized in Tables 8.5 and 8.6.

	Higgs Mass ( GeV/ $c^2$ )				
	110	115	120	125	130
Level 2:	$38.2 \pm 0.5$	$38.6 \pm 0.5$	$39.2 \pm 0.7$	$41.0 \pm 0.5$	$38.2 \pm 0.5$
Level 3: $\geq 2$ Jets, $E_T \geq 15$ GeV $\cancel{E}_T \geq 15$ GeV	$33.5 \pm 0.5$	$33.8 \pm 0.5$	$34.3 \pm 0.7$	$35.8 \pm 0.6$	$33.5 \pm 0.6$

Table 8.5: Level 3 trigger efficiencies (%). Level 1 and Level 2 trigger requirements are also applied.

## 8.6 $\cancel{E}_T$ Trigger Turn-On

As exposed in Section 8.4.1, the use of the SVT allows to set lower thresholds on the  $\cancel{E}_T$  trigger while keeping acceptable rates. Lower thresholds not only enhances

Selection Cut	$\sigma_T$ (nb)	Rate (Hz)	Rejection Factor
Level 2:	$58 \pm 6$	$5.8 \pm 0.6$	1.0
Level 3: $\geq 2$ Jets, $E_T \geq 15$ GeV $\cancel{E}_T \geq 15$ GeV	$17 \pm 1$	$1.7 \pm 0.1$	$2.7 \pm 0.2$

Table 8.6: Level 3 trigger rates ( $\mathcal{L} = 1 \cdot 10^{32} \text{ cm}^{-2}\text{s}^{-1}$ ), trigger cross sections ( $\sigma_T$ ) and rejection factors.

the trigger efficiency, but also significantly improves the trigger *turn-on* behaviour as we will show in this Section.

The  $\cancel{E}_T$  measurement at trigger level is less precise than the obtained with offline algorithms.<sup>5</sup> At trigger level, a coarser calorimeter tower segmentation is needed to reduce the trigger occupancies.<sup>6</sup> Therefore, each term of the sum  $\vec{\cancel{E}}_T \equiv -\sum E_T^i \cdot \hat{n}_i$  (see Section 5.3.2) is averaged over a wider region of the calorimeter, which results in a poorer  $\cancel{E}_T$  resolution. Other factor that substantially degrades the  $\cancel{E}_T$  at trigger level is the threshold set in each tower to be included in the  $\cancel{E}_T$  calculation. At trigger level this threshold is  $E_T^{\text{tow}} \geq 1$  GeV, while at offline the thresholds depend on the pseudorapidity region, ranging from 100 MeV in the central region to 500 MeV in the plug calorimeters [122].

These factors lead to inefficiencies when the aim is to select events with a certain amount of offline  $\cancel{E}_T$  using the  $\cancel{E}_T$  trigger. The efficiency depends on both the required offline  $\cancel{E}_T$ , as well as on the threshold of the  $\cancel{E}_T$  trigger. For each trigger threshold this efficiency is characterized with the so called *trigger turn-on curve*. The turn-on is calculated as follows. In a data sample acquired with an independent trigger the  $\cancel{E}_T$  is calculated with both the offline and the trigger algorithms. For each offline  $\cancel{E}_T$  bin, the ratio between the number of events which satisfy the  $\cancel{E}_T$  trigger and the total number of events is calculated. For an ideal trigger behavior this curve should have the aspect of a step function, with efficiencies equal to 1 for offline  $\cancel{E}_T$  values over the trigger threshold, and 0 for offline  $\cancel{E}_T$  values below the threshold. In reality, due to the detector effects described above, the turn-on curve is not a perfect step function. The trigger is efficient for offline  $\cancel{E}_T$  values below the threshold (overefficiency), while at the same time it is inefficient for some values above the threshold. The point at which the fully efficient plateau is reached characterizes the quality of the trigger.

<sup>5</sup>We do not consider here the different corrections applied to the  $\cancel{E}_T$  like, *e.g.*, the correction due to the presence of minimum ionizing muons, or the presence of multiple interactions.

<sup>6</sup>In the central calorimeter the energy of four calorimeter towers is summed to form a single trigger tower [10].

We have calculated the turn-on behavior for our trigger requirements using the *JET-20* data sample. Figure 8.10 shows the trigger turn-on behavior for four different  $\cancel{E}_T$  trigger thresholds: 15, 20, 25 and 35 GeV. The 35 GeV threshold corresponds to the inclusive  $\cancel{E}_T$  trigger. At lower thresholds the turn-on behavior significantly improves. With the proposed threshold of 15 GeV full efficiency is reached for  $\cancel{E}_T^{off} \geq 26$  GeV, while for the inclusive  $\cancel{E}_T$  trigger full efficiency is reached for  $\cancel{E}_T^{off} \geq 50$  GeV.

The turn-on behavior has been checked with early Run-II data (August 2001) taken at low luminosities ( $\sim 10^{30} \text{ cm}^{-2} \text{ s}^{-1}$ ). The data sample was acquired with the same *JET-20* trigger requirements. Figure 8.11 shows the  $\cancel{E}_T$  trigger turn-on for three  $\cancel{E}_T$  thresholds: 15, 20 and 25 GeV. Note that the calorimeter readout electronics is completely new, since it has been replaced to cope with the new Tevatron bunch crossing interval (Section 2.1).

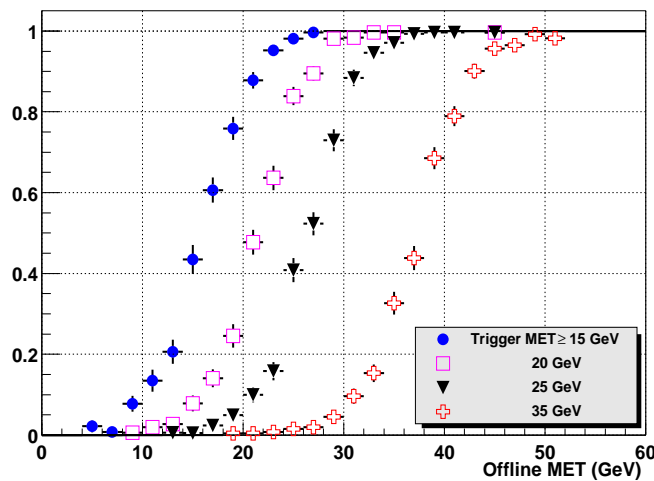


Figure 8.10: Run-I  $\cancel{E}_T$  trigger turn-on curves for four trigger thresholds:  $\cancel{E}_T \geq 15$  GeV (solid circles),  $\cancel{E}_T \geq 20$  GeV (open squares),  $\cancel{E}_T \geq 25$  GeV (solid triangles), and  $\cancel{E}_T \geq 35$  GeV (open crosses).

## 8.7 b-Tag Rates

Search strategies for the Higgs boson in this channel require the presence of two jets identified as b-jets [121]. This allows to reconstruct the Higgs boson mass without ambiguities using the  $H \rightarrow b\bar{b}$  decay. To evaluate the b-tagging rate in the sample after the trigger cuts the *jet-vertexing* (SECVTX) algorithm is used. Single and double b-tag rates are defined as the fraction of events with at least one or two b-jets, respectively, after the trigger requirements.

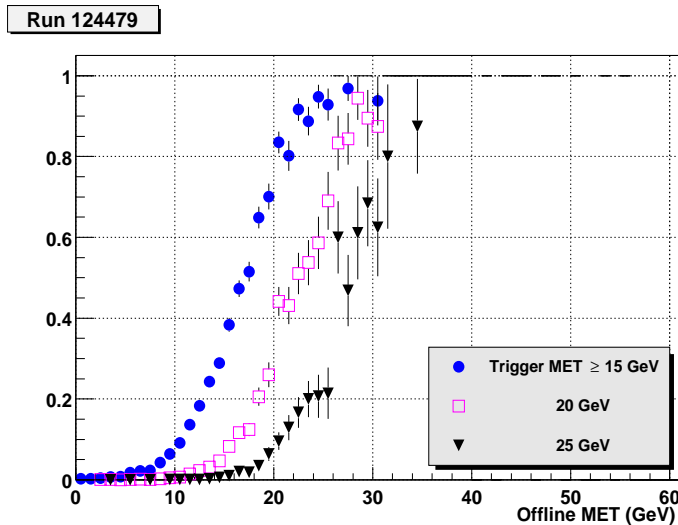


Figure 8.11: Run-II  $E_T$  trigger turn-on curve for three trigger thresholds:  $E_T \geq 15$  GeV (solid circles),  $E_T \geq 20$  GeV (open squares), and  $E_T \geq 25$  GeV (solid triangles).

Table 8.7 summarizes the single and double b-tag rates as a function of the  $E_T$  trigger threshold for three different requirements: (1) only  $E_T$  above threshold, (2)  $E_T$  above threshold, at least one cluster with  $E_T^{clus} \geq 20$  GeV and SVT cuts on impact parameter, and (3) all the trigger requirements, including the Level 3 are required<sup>7</sup>. Also the trigger efficiencies, single and double b-tag rate for the inclusive  $E_T$  trigger are shown.

As for the case of the  $H + W/Z \rightarrow b\bar{b}jj$  channel (Section 7.7), with the SVT selection a gain by a factor of  $\sim 2$  is achieved with respect to the selection with only calorimetric requirements, which is consistent with the expected correlation between the performance of the SECVTX algorithm and the presence of high impact parameter tracks (see Section 5.5.5).

With the inclusive  $E_T$  trigger the total efficiency for double b-tag events is  $4.5 \pm 0.2\%$ , while for the trigger under study the total efficiency is  $6.7 \pm 0.2\%$ , *i.e.*, a net gain by a factor of  $1.5 \pm 0.1$ .

## 8.8 Conclusions and Trigger Cuts Summary

Run-I searches for the Higgs boson in the channel  $H + Z \rightarrow b\bar{b}\nu\bar{\nu}$  were done with a data sample collected with a trigger requirement of  $E_T$  above 35 GeV at Level 2 trigger. In Run-II, with a 20-fold increase in instantaneous luminosity ( $\mathcal{L} = 1 \cdot 10^{32}$ ), the  $E_T$  threshold has to be raised up to 45 GeV to stay in the allowed percentage

<sup>7</sup>In all cases the Level 1 trigger requirement (at least one trigger tower with  $E_T \geq 10$  GeV) is required.

Trigger Cuts	b-tag rates (%)		$\epsilon_{\text{trigger}}$ (%)	Rate (Hz)
	Single tag	Double tag		
<b>Inclusive <math>\cancel{E}_T</math> sample</b> $\cancel{E}_T^{\text{trg}} \geq 35 \text{ GeV}$ $\cancel{E}_T^{\text{off}} \geq 45 \text{ GeV}$	$40.4 \pm 0.1$	$8.9 \pm 0.4$	$50.7 \pm 0.5$	–
<b>Run-II</b> Level 2 Calorimetry: $\cancel{E}_T^{\text{trg}} > 15 \text{ GeV}$	$40.0 \pm 0.7$	$8.9 \pm 0.3$	$86.9 \pm 0.3$	$234 \pm 1.0$
Level 2 Calorimetry + $\geq 2$ SVT tracks $ d_0  \geq 100 \mu\text{m},  d_1  \geq 80 \mu\text{m}$	$67.9 \pm 0.1$	$18.1 \pm 0.1$	$39.2 \pm 0.7$	$5.8 \pm 0.6$
Level 2 + Level 3: $N_{\text{jet}}(E_T^{\text{jet}} \geq 15 \text{ GeV}) \geq 2$ $\cancel{E}_T^{\text{off}} \geq 15 \text{ GeV}$	$69.1 \pm 0.1$	$19.8 \pm 0.1$	$34.3 \pm 0.7$	$1.7 \pm 0.1$

Table 8.7: Signal ( $M_H = 120 \text{ GeV}/c^2$ ) single and double b-tag rates, trigger efficiency ( $\epsilon_{\text{trigger}}$ ) and rates ( $\mathcal{L} = 1 \cdot 10^{32} \text{ cm}^{-2}\text{s}^{-1}$ ) for the inclusive  $\cancel{E}_T$  sample and for different calorimetric and SVT requirements. Uncertainties include statistical errors only. The scale factors calculated in Section 7.5.5 have been applied.

of the total output bandwidth. However, in Run-II at Level 2 will be possible to trigger on high impact parameter tracks. Therefore, we can exploit the presence of secondary vertices due to the Higgs boson decay and their correlation with high impact parameter tracks to lower the threshold on the  $\cancel{E}_T$ , while keeping the trigger rates well under control. At Level 3 jets and  $\cancel{E}_T$  computed with the offline algorithms are available. The requirement of 2 jets and  $\cancel{E}_T^{\text{off}} \geq 15 \text{ GeV}$  at Level 3 serves as a confirmation of the Level 2 trigger cuts, and further reduces the background rates. A summary of the trigger cuts follows:

- **TRIGGER LEVEL 1:**
  - **Calorimetric Primitives:**
    - \* Single Calorimeter Trigger-Tower  $E_T^{\text{tow}} \geq 10 \text{ GeV}$
- **TRIGGER LEVEL 2:**
  - **Calorimeter Clustering:**
    - \*  $N_{\text{clus}} \geq 1$  ( $E_T^{\text{clus}} \geq 20 \text{ GeV}$ )
    - \*  $\cancel{E}_T \geq 15 \text{ GeV}$
  - **SVT:**
    - \* At least two SVT tracks with impact parameter  
 $|d_0| \geq 100 \mu\text{m}, |d_1| \geq 80 \mu\text{m}$
- **TRIGGER LEVEL 3:**

– **Calorimeter Reconstruction:**

- \*  $N^{jets} \geq 2, E_T^{jet} \geq 15 \text{ GeV}.$
- \*  $\cancel{E}_T^{off} \geq 15 \text{ GeV}$

The final Level 3 trigger output rate is  $1.7 \pm 0.1 \text{ Hz}$  ( $\mathcal{L} = 1 \cdot 10^{32} \text{ cm}^{-2}\text{s}^{-1}$ ). For  $M_H = 120 \text{ GeV}/c^2$  the total trigger efficiency is  $34.3 \pm 0.7\%$ . As for the case of the  $H + W/Z \rightarrow b\bar{b}jj$  channel (Section 7.7) the obtained sample is enriched in heavy flavor content due to the SVT requirements. As a reference, the double b-tag rate evaluated with the SECVTX algorithm in Run-I configuration is, in a sample selected with the trigger under study, higher by a factor 1.5 compared with the rate in a sample selected with the inclusive  $\cancel{E}_T$  trigger.

## Chapter 9

# RUN-II Discovery Reach for the SM Higgs Boson in the $H + W/Z \rightarrow b\bar{b}jj$ and $H + Z \rightarrow b\bar{b}\nu\bar{\nu}$ Channels

The Tevatron Higgs Working Group has evaluated the CDF detector discovery reach potential for the Higgs boson up to masses of 180 GeV [13] in different channels. Limits and discovery significances for the Higgs boson in this mass range have been calculated individually for each channel and by combining all channels.

In the Tevatron Higgs Working Group analysis signal and background events are simulated mainly using a simple Monte Carlo parameterization of the CDF and D0 Run-II detectors, assuming 100% trigger efficiencies. However, Run-I CDF analysis had shown that a non optimal trigger design can greatly reduce the sensitivity. As discussed in Section 7, for the  $H + W/Z \rightarrow b\bar{b}jj$  channel the CDF Run-I multijet trigger rejected almost the 75% of the signal events ( $M_H = 120 \text{ GeV}/c^2$ ). The trigger proposed in this thesis (Chapter 7) yields a two-fold increase in trigger efficiency with respect to the one used in Run-I. This new trigger is also more efficient selecting events with heavy flavor content, with single and double b-tagging rates enhanced by a factor of  $\sim 3$  (see Section 7.7). In this Chapter we study the Run-II discovery potential for the Higgs boson in the  $H + W/Z \rightarrow b\bar{b}jj$  channel as estimated by the Tevatron Higgs Working group, taking into account the proposed trigger and using a more detailed and realistic CDF detector simulation.

For this channel we also perform a more detailed analysis template in order to fully exploit the increased efficiency of the new trigger. As a result, the CDF Run-I limits are extrapolated to the Run-II conditions.

As discussed in Section 8, for the  $H + Z \rightarrow b\bar{b}\nu\bar{\nu}$  channel a new trigger has been studied. In Run-II the increased instantaneous luminosity will require for the Run-I inclusive missing transverse energy trigger higher  $\cancel{E}_T$  thresholds to avoid the saturation of the data acquisition bandwidth. However, the trigger proposed in this thesis (Chapter 8) allows to keep low trigger thresholds in the  $\cancel{E}_T$ , while reducing the rates with a high signal efficiency. With this trigger we study the Run-

II discovery potential for this channel using the same offline optimization performed by the Tevatron Higgs Working group.

## 9.1 $H + W/Z \rightarrow b\bar{b}jj$ Channel

For the  $H + W/Z \rightarrow b\bar{b}jj$  channel, the selection criteria of the Tevatron Higgs working group is:

- $N_{jet} \geq 4$  jets with a jet cone algorithm of  $\Delta R = 0.5$ .
- More than two jets identified as b-jets with a displaced vertex algorithm or by identifying soft lepton tags. The b-tagged jets must satisfy  $E_T^{jet} \geq 15$  GeV and  $|\eta| \leq 2$ .
- The difference in pseudo-rapidity between the two b-tagged jets must be  $|\Delta_{b\bar{b}}| \leq 1$ . For the untagged jets  $|\Delta_{q\bar{q}'}| \leq 1$ .
- $M_{b\bar{b}} \geq m_H - \sigma(M_{b\bar{b}})$ , where  $\sigma(M_{b\bar{b}})$  is the  $M_{b\bar{b}}$  RMS value. The untagged jets must satisfy  $M_{jj} \geq m_W - \sigma(M_{jj})$ .

Table 9.1 shows the  $S/\sqrt{B}$  results for different Higgs boson masses. Note that the only background contribution considered is the QCD heavy flavor production (which is two orders of magnitude above the rest of the backgrounds, see Section 9.3), normalized with a multijet QCD data sample acquired with the D0 [133] detector at  $\sqrt{s} = 1.8$  TeV. Table 9.1 shows also the expected number of signal and QCD background events with the trigger studied in Section 7, applying the same offline cuts. In this case, the Higgs boson signal, the trigger and the detector response are modeled as described in Chapter 6, and the b-tagging rates are evaluated using the standard SECVTX algorithm. The QCD background is estimated using the CDF *JET-20* data sample, and is described in detail in Section 9.3.2.

$m_H$ (GeV)	Tevatron Higgs Working Group			Run-II multijets trigger		
	S	B	$S/\sqrt{B}$	S	B	$S/\sqrt{B}$
110	3.5	2800	0.07	3.7	$3900 \pm 1300$	$0.06 \pm 0.01$
120	2.5	2300	0.05	2.9	$3700 \pm 1200$	$0.047 \pm 0.007$
130	1.3	2000	0.03	2.4	$3000 \pm 1000$	$0.043 \pm 0.007$
140	0.45	1700	0.01	1.9	$2800 \pm 960$	$0.035 \pm 0.006$

Table 9.1: Statistical significance,  $H + W/Z \rightarrow b\bar{b}jj$  signal and QCD multijet expected events for  $1\text{ fb}^{-1}$  as reported by the Tevatron Higgs Working group [13] and taking into account the new multijets trigger.

The results are consistent with the results reported by the Tevatron Higgs Working Group. The new trigger will not reduce the sensitivity for the  $H + W/Z \rightarrow b\bar{b}jj$  channel.

## 9.2 $H + Z \rightarrow b\bar{b}\nu\bar{\nu}$ Channel

For the  $H + Z \rightarrow b\bar{b}\nu\bar{\nu}$  channel the Tevatron Higgs Working group reports three different analysis. The first is based on the CDF Run-I result [33] using a detailed CDF detector simulation. The second is based in a simple Monte-Carlo simulation of the CDF and D0 detector as for the case of the  $H + W/Z \rightarrow b\bar{b}jj$  channel (Section 9.1). The third is an extension of the second, where neural network techniques are applied to optimize the event selection. All of them assume a 100% trigger efficiency. In the following we will only consider the analysis based on the CDF Run-I results, since it is the one for which more reliable comparison can be made.

For the analysis based on the CDF Run-I results, the selection criteria is:

- $\cancel{E}_T \geq 35$  GeV .
- Two b-tagged jets with  $E_T \geq 15$  GeV ,  $|\eta| \leq 2$ .
- No extra jets with  $E_T \geq 8$  GeV ,  $|\eta| \geq 2.4$ .
- No isolated track above 10 GeV , where the isolation requirement is  $\sum P_T < 2.0$  GeV/ $c$  over the additional tracks inside a cone of radius  $\Delta R = 0.4$ .

Table 9.2 shows the expected number of signal events as reported by the Tevatron Higgs working group, and the expected number of signal events when the trigger requirements discussed in Chapter 8 are also applied. The trigger requirements reduce the expected number of events by a  $\sim 50\%$ .

$m_H$ ( GeV )	Tevatron Working Group	Run-II trigger
110	3.5	$1.29 \pm 0.05$
120	2.5	$0.95 \pm 0.02$
130	1.3	$0.83 \pm 0.03$
140	0.45	$0.65 \pm 0.02$

Table 9.2: Expected number of signal events in  $1\text{ fb}^{-1}$  as reported by the Tevatron Higgs Working group (left column) and when the trigger requirements are also applied (right column).

The offline requirement of  $\cancel{E}_T \geq 35$  GeV was motivated by the Run-I trigger requirement of  $\cancel{E}_T \geq 35$  GeV . With the new trigger, this threshold can be lowered down to  $\cancel{E}_T \geq 15$  GeV . The main background with low  $\cancel{E}_T$  is the QCD heavy flavor production, where the  $\cancel{E}_T$  comes from missmeasured jet energy. This background is extremely difficult and unreliable to simulate due to the large cross section, very small acceptance and the great dependence on detector effects. Figure 9.1 shows the  $\cancel{E}_T$  distribution for the signal and QCD heavy flavor events where the trigger requirements are  $\cancel{E}_T^{\text{trigger}} \geq 15$  GeV and  $\cancel{E}_T \geq 35$  GeV , respectively. It can be seen that once the detector effects will be understood, a requirement of  $\cancel{E}_T^{\text{trigger}} \geq 15$  GeV with  $\cancel{E}_T \geq 25$  GeV could yield more powerful statistical discrimination.

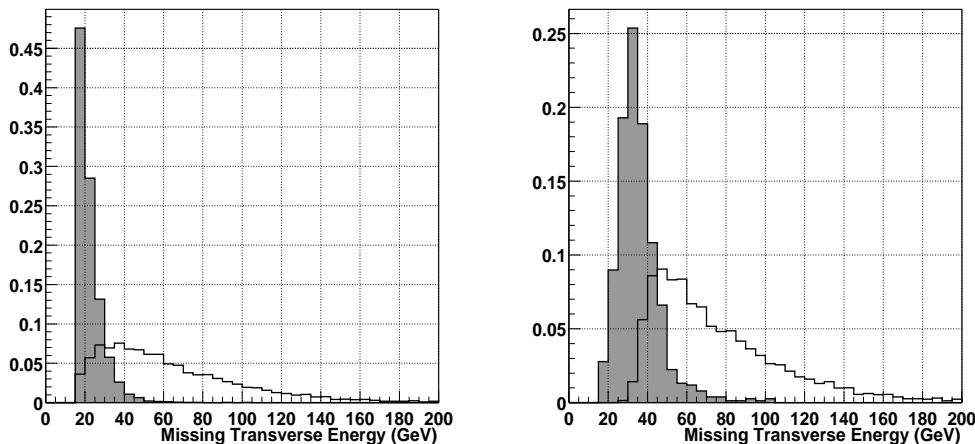


Figure 9.1: Offline  $E_T$  distribution for  $H + Z \rightarrow b\bar{b}\nu\bar{\nu}$  (open histogram) and QCD heavy flavor events (shaded histogram) with  $E_T^{\text{trigger}} \geq 15$  GeV (left) and  $E_T^{\text{trigger}} \geq 35$  GeV (right).

### 9.3 Run-II Analysis for the $H + W/Z \rightarrow b\bar{b}jj$ Channel

In this Section we study an alternative optimization of the offline selection cuts. The goal is to take profit from the increased trigger efficiency obtained with the new multijets trigger. The results are compared with those from the Tevatron Higgs Working. With this analysis, an extrapolation of the CDF Run-I exclusion limits to the Run-II scenario is studied in the next Section.

#### 9.3.1 Signal Monte Carlo Simulation

To simulate the Higgs boson signal, the trigger and the detector response are modeled as described in Chapter 6. For the  $H + W/Z \rightarrow b\bar{b}jj$  process we expect a final signature with four high  $E_T$  jets ( $E_T^{\text{jet}} \approx 10 - 50$  GeV, see Figure 7.23) where two of them are the result of b-quark hadronization. To identify the b-jets we use the SECVTX algorithm, developed for the top-quark discovery [103] and described in Section 5.5.3. Our starting selection is based on events satisfying the trigger proposed in Chapter 7 and where at least two jets among the four highest- $E_T$  jets of the event are identified as b-quark candidates by the SECVTX algorithm.

#### 9.3.2 Backgrounds

After the trigger requirements the expected number of background events is approximately four orders of magnitude higher than the signal.<sup>1</sup> In this Section we study

<sup>1</sup>With the new trigger the Level 3 trigger cross section is  $\sim 14$  nb (Table 7.12), while for the signal it is  $1.3 \cdot 10^{-3}$  nb ( $M_H = 120$  GeV/ $c^2$ , Table 7.11).

Standard Model background processes which have a signature similar to the signal and a relevant production cross section: QCD multijets,  $t\bar{t}$  pairs, W or Z boson plus  $b\bar{b}/c\bar{c}$  pairs, single top production, and production of W or Z pairs.

### QCD Multijets + Heavy Flavor

QCD processes are the dominant source of heavy flavor production in multijet events. The primary  $2 \rightarrow 2$  processes that yield a heavy flavor quark pair ( $Q\bar{Q}$ ,  $Q = b$  or  $c$ ) are classified as *Direct Production* ( $q\bar{q}, gg \rightarrow Q\bar{Q}$ ), *Flavor Excitation* ( $Qg \rightarrow Qg$ ) and *Gluon Splitting* ( $g \rightarrow Q\bar{Q}$ ) in the initial or final state. Some of the Feynman diagrams for these processes are shown in Figure 9.2. Higher jet multiplicities are due to gluon radiation and/or gluon splitting to quarks and gluons in the initial or final state.

QCD b-jets are characterized by an exponentially decreasing  $p_T$  distribution, while for the signal ( $M_H = 120 \text{ GeV}/c^2$ ) the average b-jet  $p_T$  is of the order of  $50 \text{ GeV}/c$  (Figure 9.5). Therefore, the trigger together with the b-tag requirements already exclude most of the QCD low  $p_T$  events while keeping a high efficiency for the signal.

Due to the large uncertainties in the Monte Carlo theoretical predictions for the QCD production cross sections, we estimate the expected rates from Run-I data. The total number of QCD events is normalized to the number of Run-I *JET-20* events which satisfy the trigger requirements and have at least two b-tagged jets.<sup>2</sup> Due to the poor heavy flavor content of the *JET-20* data sample we can not estimate from it the contribution of fake double tag events. Fake double tag events are defined as events where at least one of the two b tagged jets comes from a light quark or gluon hadronization. In Run-I searches with the multijets trigger data sample [115] the contribution from mistags was estimated on the basis of the positive and negative<sup>3</sup> b-tags found in the data [115]. It contributed to about 18% of the total number of double tagged events and here we will consider this quantity as a systematic uncertainty in our predictions. After this selection we find an estimated QCD heavy flavor cross section of  $\sigma = 0.4 \pm 0.1 \text{ nb}$ , including the trigger requirements and the presence of at least two b-tagged jets. Table 9.3 summarizes the expected cross section and number of events in  $1 \text{ fb}^{-1}$ .

$t\bar{t}$

In  $p\bar{p}$  collisions at  $\sqrt{s} = 2.0 \text{ TeV}$  top quarks are pair produced through  $q\bar{q}$  annihilation ( $\approx 90\%$ ) or gluon fusion ( $\approx 10\%$ ) (Figure 9.3). In the Standard Model the top quark decays into a W boson and a b quark with  $BR(t \rightarrow Wb) \sim 100\%$ . With the fully hadronic W boson decay the final state signature is similar to the

<sup>2</sup>We neglect here the increase in the production cross section due to the increase of the center of mass energy, from  $\sqrt{s} = 1.8 \text{ TeV}$  to  $2.0 \text{ TeV}$ .

<sup>3</sup>See Section 5.5.5 for a definition of positive and negative b-tags.

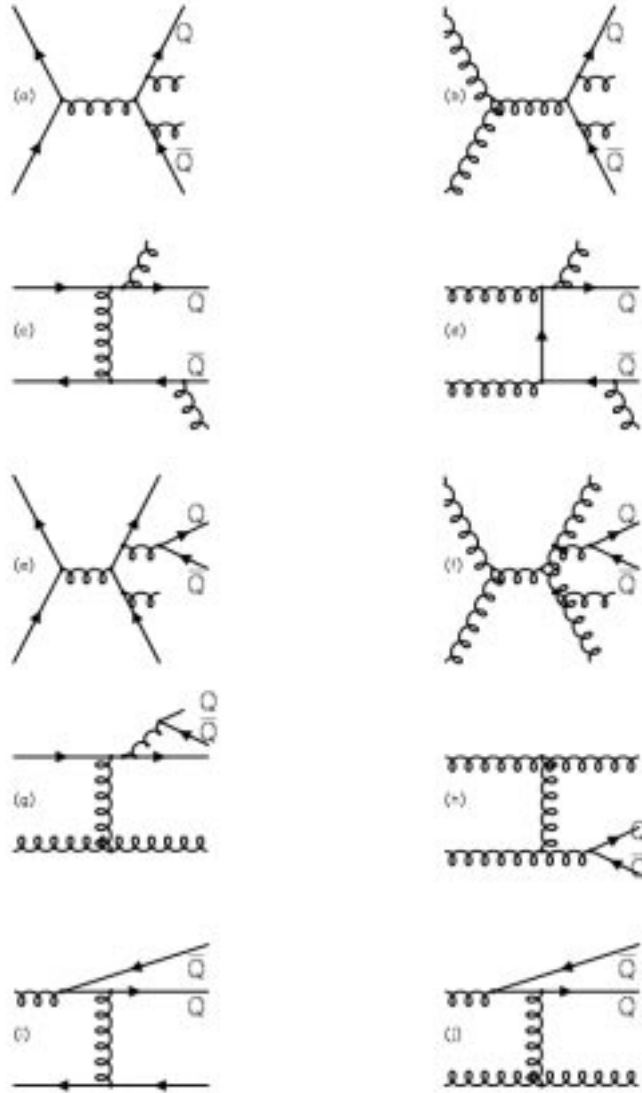


Figure 9.2: Some of the Feynman diagrams for QCD multijet heavy flavor production. Diagrams (a)-(d) are examples of *Direct Production*, (e)-(h) are examples of final state *Gluon Splitting* and (i)-(j) are examples of *Flavor Excitation*.

$H + W/Z \rightarrow b\bar{b}jj$  process, with more than four jets and with two high- $E_T$  b-jets among them (Figure 9.5). With the measured production cross section by CDF at  $\sqrt{s} = 1.8$  TeV  $\sigma_{t\bar{t}} = 6.5 \pm 1.7$  pb [124], increased by a 40% due to the higher Run-II center of mass energy ( $\sqrt{s} = 2.0$  TeV) [10], Table 9.3 summarizes the expected number of events in  $1 \text{ fb}^{-1}$ .

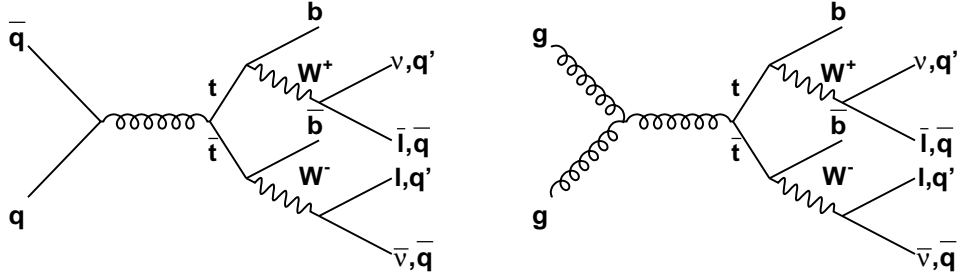


Figure 9.3: Feynman diagrams for  $t\bar{t}$  production through  $q\bar{q}$  annihilation (left Figure) and gluon fusion (right Figure) with the subsequent top quark  $t \rightarrow Wb$  and  $W$  boson decays.

$Wb\bar{b}$ ,  $Wc\bar{c}$ ,  $Zb\bar{b}$ ,  $Zc\bar{c}$

Figure 9.4 shows the leading order Feynman diagram for electroweak  $W/Z + b\bar{b}/c\bar{c}$  production. The predominant source of heavy flavor pair production is  $Z + \geq n$  jets with  $Z \rightarrow b\bar{b}/c\bar{c}$ , as well as some contribution from final and initial state gluon splitting and higher order diagrams. The CDF measured cross section for  $W$ +jets,  $W \rightarrow e\nu$  [125]<sup>4</sup> and  $Z$  + jets,  $Z \rightarrow ee$  [126]<sup>5</sup> is used to normalize the Monte Carlo production cross section for  $W/Z + \geq n$  jet events. Since the contribution from Drell-Yan production ( $q\bar{q} \rightarrow W/Z$ ) in  $W/Z + \geq 2$ -jet events is negligible with respect to the radiative QCD production ( $q\bar{q} \rightarrow Z + g$  and  $qg \rightarrow Z + q$  [127]), we consider here only the later QCD production mechanism.

Table 9.3 summarizes the cross section and the expected number of events in  $1 \text{ fb}^{-1}$ .

### Single Top Production

Although there is still no experimental evidence for single top quark production [128], in the Standard Model this process can be produced along with a  $b$ -quark through electro-weak interactions. In  $p\bar{p}$  collisions two different diagrams are expected to contribute: the  $W$ -gluon fusion ( $\sigma = 1.7 \pm 0.3 \text{ pb}$  [129]) and the  $W^*$  channel ( $\sigma = 0.73 \pm 0.10 \text{ pb}$  [130]). These two processes (Figure 9.6) have different signatures and their contribution have been evaluated separately. For the  $W$ -gluon fusion the  $b$ -quark jet from the  $t \rightarrow Wb$  decay is expected to be energetic ( $E_T^{jet} \sim 50 \text{ GeV}$ ) while the  $b$ -jet at the  $g b\bar{b}$  vertex softer ( $E_T^{jet} \approx 10 \text{ GeV}$ , Figure 9.5). Therefore, the requirement of at least two  $b$ -tags eliminates most of these events. For the  $W^*$

<sup>4</sup>The measured cross-section at  $\sqrt{s} = 1.8 \text{ TeV}$  for  $W \rightarrow e\nu + 3 \text{ jets}$  is  $9.19 \pm 0.81 \text{ pb}$ , where jets are reconstructed with a cone size of  $R = 0.4$  and are required to have corrected  $E_T^{jet} \geq 15 \text{ GeV}$ ,  $|\eta| \leq 2.4$  and  $\Delta R > 1.3 \times R$  with respect to the  $e/q$  from the  $W$ . Furthermore, if two jets are closer than  $1.3 \times R$ , they are collapsed into a single one [125].

<sup>5</sup>The measured cross-section at  $\sqrt{s} = 1.8 \text{ TeV}$  for  $Z \rightarrow ee + 4 \text{ jets}$  is  $9.19 \pm 0.81 \text{ pb}$ , where jets are defined in the same way as for  $W$ +jets.

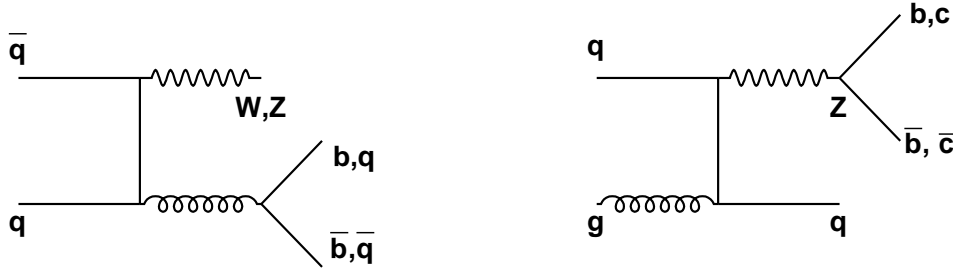


Figure 9.4: Leading order Feynman diagram for  $W/Z + b\bar{b}/c\bar{c}$  (left) and  $Z + jets$  with  $Z \rightarrow b\bar{b}/c\bar{c}$  production.

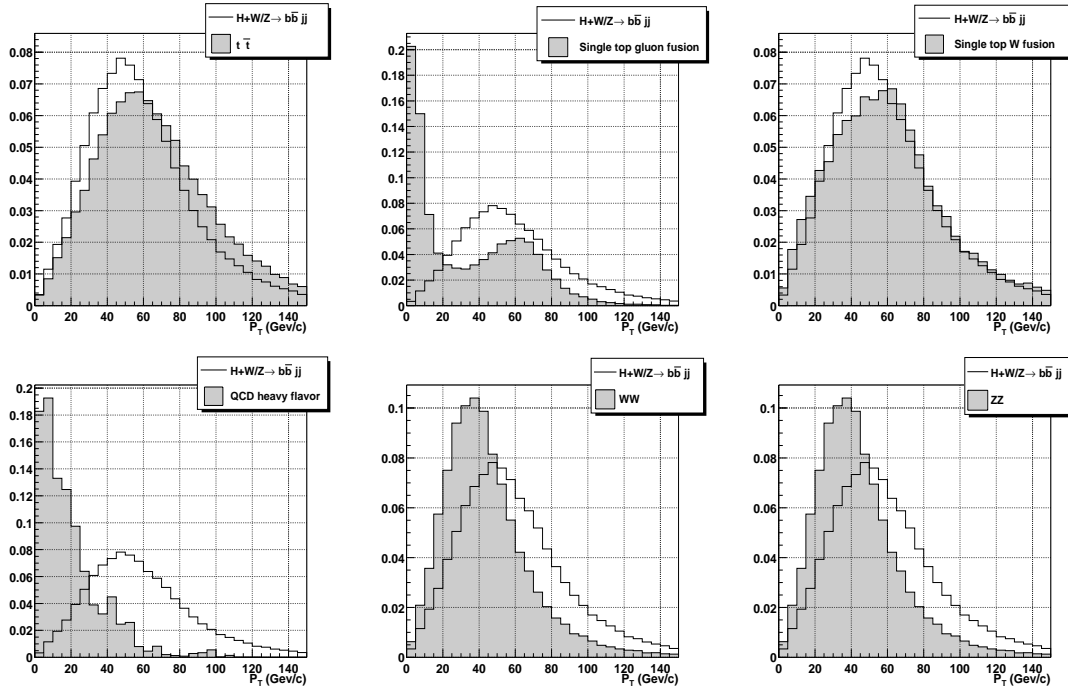


Figure 9.5:  $b$ -quark  $p_T$  distributions at generation level for the signal ( $H + W/Z \rightarrow b\bar{b}jj$  [ $M_H = 120 \text{ GeV}/c^2$ ]), the hadronic  $t\bar{t}$  production, single top through gluon fusion, single top through  $W$ -fusion, QCD heavy flavor,  $WW$  diboson, and  $ZZ$  diboson production.

channel the  $b$ -jet is also energetic ( $E_T^{jet} \approx 50 \text{ GeV}$ , Figure 9.5), and a final state with two  $b$ -jets is more likely to be selected. Table 9.3 summarizes the cross section and expected number of events in  $1 \text{ fb}^{-1}$ . Note that to observe single top events in the fully hadronic channel a data sample selected with this trigger is the most suitable one.

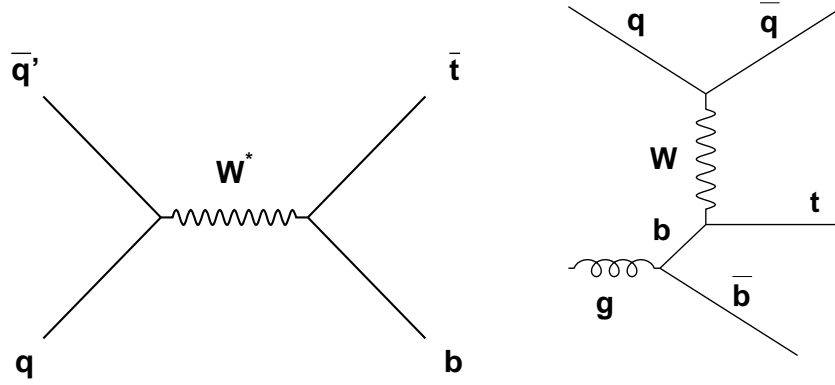


Figure 9.6: Leading order Feynman diagrams for single top quark production in the  $W$ -gluon fusion channel (right diagram) and the  $W^*$  channel (left diagram).

### Diboson Production

The production of heavy boson ( $W$  or  $Z$ ) pairs and their fully hadronic decay into quarks results also in events with a high jet multiplicity and heavy flavor jets ( $Z \rightarrow b\bar{b}$ ,  $W \rightarrow c\bar{s}$ ) with  $E_T^{jet} \sim 50$  GeV (Figure 9.5). We have simulated diboson production separately for  $WW$ ,  $WZ$  and  $ZZ$  pairs using the PYTHIA Monte Carlo program [90]. The production cross sections at  $\sqrt{s} = 2.0$  TeV at next-to-leading order, which are known accurately, are taken from [131]<sup>6</sup>. In  $WW$  events the  $b$ -tag efficiency for  $c$  quarks is low (Section 5.5.5) and therefore, the requirement of at least two  $b$ -tagged jets rejects almost all the events. Table 9.3 summarizes the cross sections and expected number of events in  $1 \text{ fb}^{-1}$ .

### 9.3.3 Kinematical Selection

Table 9.3 shows the QCD heavy flavor multijet production as the main background, with a contribution about two orders of magnitudes above the rest. In the following we will thus consider only QCD heavy flavor events as the main background contribution to optimize the signal significance.

To further reduce the background we have studied distributions like the jet multiplicity ( $N_{jet}$ ), the event  $\sum E_T^{jet}$ , and selection cuts on the reconstructed invariant mass of the two highest- $E_T$   $b$ -tagged jets and the two remaining jets of the event.

### Jet Multiplicity Selection

At least four reconstructed jets are expected in signal events (two from the  $H \rightarrow b\bar{b}$  decay, and another two from the  $W \rightarrow q\bar{q}'$  and  $Z \rightarrow q\bar{q}$  decays) with higher jet mul-

<sup>6</sup>Cross-sections for dibosons at  $\sqrt{s} = 2.0$  TeV are  $\sigma(WW) = 10.0$  pb,  $\sigma(WZ) = 2.5$  pb, and  $\sigma(ZZ) = 1.0$  pb.

	$\sigma$ (pb)	$\sigma \times \text{BR}(\text{had})$ (pb)	$\epsilon_T$ (%)	$\epsilon_{b\bar{b}}$ (%)	Events in $1 \text{ fb}^{-1}$
$M_H = 120 \text{ GeV}/c^2$	0.28	0.13	$39.3 \pm 0.3$	$27.0 \pm 0.1$	$13.8 \pm 0.1$
$JET-20$	$7.5 \cdot 10^6$	–	$0.143 \pm 0.007$	$2.3 \pm 0.7$	$250000 \pm 80000$
$t\bar{t}$	$9.1 \pm 2.5$	$4.5 \pm 1.2$	$54.5 \pm 0.7$	$24.6 \pm 0.7$	$600 \pm 150$
$Z + \text{jets} (Z \rightarrow b\bar{b}/c\bar{c})$	$57 \pm 5$	$40 \pm 5$	$0.77 \pm 0.06$	$27 \pm 4$	$80 \pm 10$
$Wb\bar{b}/c\bar{c}$	$114 \pm 7$	$80 \pm 5$	$0.30 \pm 0.01$	$1.1 \pm 0.5$	$0.26 \pm 0.02$
$t(W^*)$	0.73	0.51	$45.0 \pm 0.5$	$27.2 \pm 0.7$	$63 \pm 2$
$t(W - g)$	1.7	1.2	$18.5 \pm 0.4$	$7.1 \pm 0.6$	$16 \pm 1$
$WW$	10.0	4.9	$5.9 \pm 0.2$	$3.7 \pm 0.7$	$11 \pm 2$
$WZ$	2.5	1.23	$13.0 \pm 0.3$	$20 \pm 1$	$32 \pm 2$
$ZZ$	1.0	0.49	$22.3 \pm 0.5$	$34 \pm 1$	$37 \pm 1$

Table 9.3: Signal ( $H + W/Z \rightarrow b\bar{b}jj$ ) and background cross sections ( $\sigma$ ), cross section times branching ratios for the fully hadronic channel ( $\sigma \times \text{BR}(\text{had})$ ), trigger efficiencies ( $\epsilon_T$ ) and double b-tag efficiencies ( $\epsilon_{b\bar{b}}$ ). All errors include statistical and systematic uncertainties added in quadrature.

	$\epsilon_{N_{jet}}$ (%)	Events ( $1 \text{ fb}^{-1}$ )	$S/\sqrt{B}$ ( $1 \text{ fb}^{-1}$ )
$H + W/Z \rightarrow b\bar{b}jj$			
$M_H = 115 \text{ GeV}/c^2$	$76.4 \pm 0.4$	$13.4 \pm 1.8$	$0.047 \pm 0.007$
$M_H = 120 \text{ GeV}/c^2$	$76.3 \pm 0.4$	$10.5 \pm 1.5$	$0.037 \pm 0.006$
$M_H = 125 \text{ GeV}/c^2$	$75.8 \pm 0.5$	$7.3 \pm 1.3$	$0.025 \pm 0.004$
$M_H = 130 \text{ GeV}/c^2$	$76.9 \pm 0.6$	$7.2 \pm 1.3$	$0.025 \pm 0.004$
QCD	$32.5 \pm 0.4$	$81000 \pm 26000$	–

Table 9.4: Jet multiplicity selection efficiency, expected number of signal and QCD multijet events, and signal statistical significance for  $1 \text{ fb}^{-1}$ . The trigger and double b-tag requirements are applied.

tiplicities mainly coming from initial or final state irradiation. The QCD background is, on the other hand, characterized by dijet events with higher N-jet processes suppressed by a factor  $\alpha_s^{(N-2)}$ . Figure 9.7 shows the jet multiplicity distribution of the signal and QCD heavy flavor background. Also shown is the statistical significance of the signal ( $M_H = 120 \text{ GeV}/c^2$ ). The total number of signal and background events are normalized to  $1 \text{ fb}^{-1}$  after the trigger and the b-tag requirements. Only jets with uncorrected  $E_T^{jet} \geq 15 \text{ GeV}$  and reconstructed with a 0.4 cone radius are considered. The requirement of at least four jets maximizes the statistical significance of the signal. Table 9.4 summarizes the signal significance and the expected number of signal and background events in  $1 \text{ fb}^{-1}$  for different Higgs boson masses.

### $\sum E_T^{jets}$ Selection

Signal events produce massive objects with transverse energies  $M_T^H + M_T^{W/Z} \sim 200 \text{ GeV}/c^2$ . On the other hand, the QCD multijet cross section decreases expo-

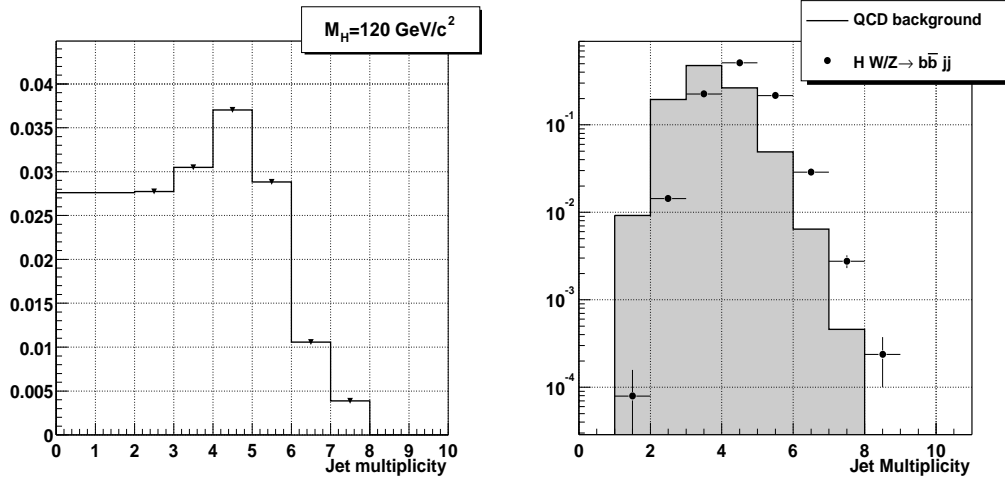


Figure 9.7: Left Figure: statistical significance of the jet multiplicity requirement for the signal with respect to the QCD heavy flavor background, normalized to the expected number of events in  $1 \text{ fb}^{-1}$ . Jets are reconstructed with a cone radius of 0.4 and are required to have uncorrected  $E_T^{jet} \geq 15 \text{ GeV}$  and  $|\eta| \leq 2$ . Right Figure: jet multiplicity for the signal (dots) [ $M_H = 120 \text{ GeV}/c^2$ ] and the QCD background (shaded histogram). Both histograms are normalized to unit area.

nentially with  $\sum E_T^{jets}$ . Therefore, for the same jet multiplicity, the requirement of a  $\sum E_T^{jets}$  threshold is very efficient for the signal while rejecting a significant background contribution. Figure 9.8 shows the  $\sum E_T^{jet}$  distribution for the signal and QCD heavy flavor background. Also shown is the statistical significance of the signal as a function of the  $\sum E_T^{jets}$  threshold for a signal mass of  $120 \text{ GeV}/c^2$ . The total number of signal and background events are normalized to  $1 \text{ fb}^{-1}$  and include the trigger, double b-tag, and jet multiplicity requirements. For a  $\sum E_T^{jets} \sim 140 \text{ GeV}$  the signal significance is maximized. This value coincides also with the  $\sum E_T^{clus}$  trigger turn-on plateau (Figure 9.9), which allows to avoid trigger effects. Table 9.5 summarizes the signal significance and expected number of signal and background events for different Higgs boson masses.

### Invariant Mass Selection

Due to the high mass of the Higgs boson, one could expect the two highest- $E_T$  b-tagged jets of  $H + W/Z \rightarrow b\bar{b}jj$  events to correspond to the b-jets from the Higgs decay, while the two remaining jets to the decay of the associated vector boson. Figure 9.10 shows the reconstructed signal invariant mass distribution of the two highest- $E_T$  b-tagged jets and the two remaining jets of the event ( $M_H = 120 \text{ GeV}/c^2$ ). The tails in the distributions are due to the cases where one of the b-tagged or remaining jets do not come from the Higgs boson or the vector boson decay, respectively. Only for  $\sim 57\%$  of the events the two highest- $E_T$  b-tagged jets come from the Higgs decay and the two other jets from the vector boson decay.

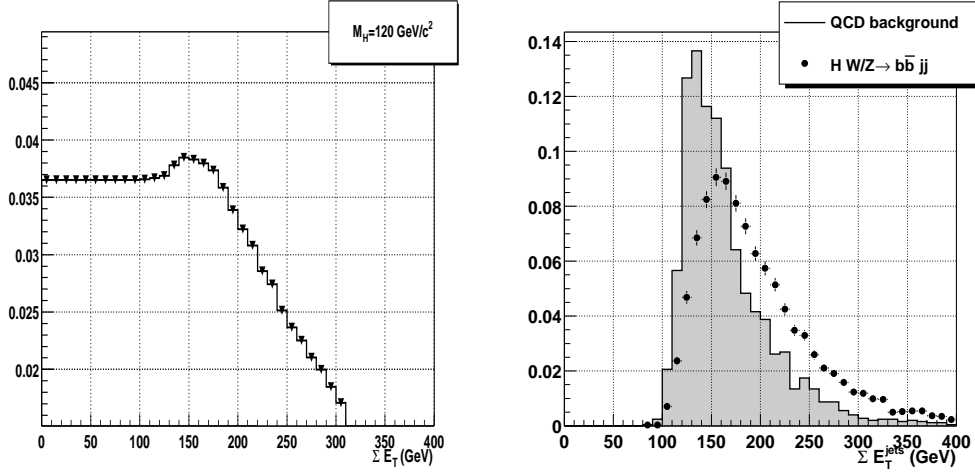


Figure 9.8: Left: statistical signal significance of the  $\sum E_T^{jets}$  requirement for  $1 \text{ fb}^{-1}$ . The trigger, double b-tag, and jet multiplicity requirements are applied. Right:  $\sum E_T^{jets}$  distribution for the signal (dots) [ $M_H = 120 \text{ GeV}/c^2$ ] and QCD background (shaded histogram). Both histograms are normalized to unit area.

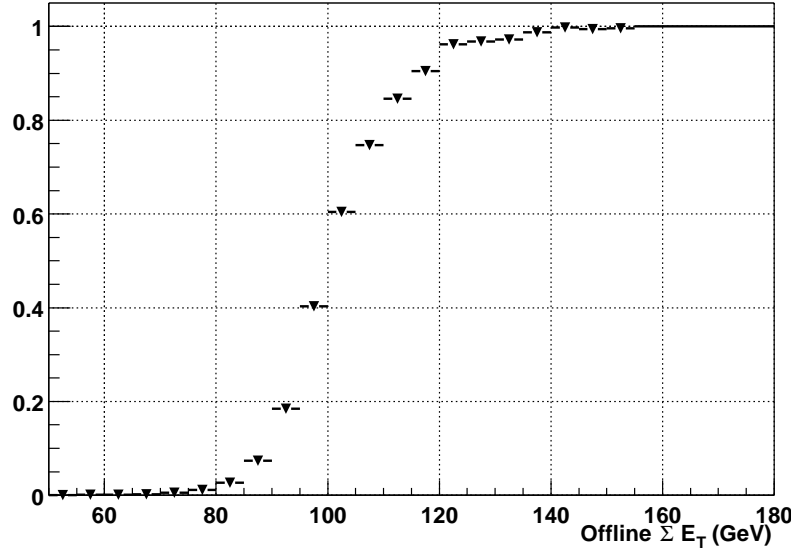


Figure 9.9: Level 2 trigger  $\sum E_T$  efficiency ( $\sum E_T^{trigger} \geq 90 \text{ GeV}$ ) as a function of the offline  $\sum E_T^{jets}$  calculated for the four highest- $E_T$  jets of the event ( $E_T^{jet} \geq 15 \text{ GeV}$ ,  $|\eta| < 2$ ) and evaluated with the *JET-20* data sample.

Figures 9.11 and 9.12 show, respectively, the invariant mass and  $p_T$  distributions of two highest- $E_T$  b-tagged jets and the two remaining jets of the event.<sup>7</sup> The distributions are shown for the signal ( $M_H = 120 \text{ GeV}/c^2$ ) and the QCD background.

<sup>7</sup>The invariant mass is calculated with the corrected jet energy as described in Section 5.5.1.

	$\sum E_T^{jets}$	$\epsilon_{\sum E_T^{jet}} (\%)$	Events ( $1 \text{ fb}^{-1}$ )	$S/\sqrt{B}$ ( $1 \text{ fb}^{-1}$ )
$H + W/Z \rightarrow b\bar{b}jj$				
$M_H = 115 \text{ GeV}/c^2$	140	$82.9 \pm 0.4$	$11.0 \pm 1.4$	$0.048 \pm 0.008$
$M_H = 120 \text{ GeV}/c^2$	150	$76.2 \pm 0.5$	$7.9 \pm 1.4$	$0.038 \pm 0.007$
$M_H = 125 \text{ GeV}/c^2$	150	$78.0 \pm 0.6$	$5.6 \pm 1.1$	$0.027 \pm 0.004$
$M_H = 130 \text{ GeV}/c^2$	160	$72.5 \pm 0.7$	$5.2 \pm 1.1$	$0.028 \pm 0.005$
QCD	140	$65.2 \pm 0.7$	$52000 \pm 17000$	—
	150	$52.5 \pm 0.8$	$42000 \pm 14000$	—
	160	$41.9 \pm 0.7$	$33000 \pm 11000$	—

Table 9.5:  $\sum E_T^{jet}$  selection efficiency, expected number of signal and QCD events, and signal statistical significances for  $1 \text{ fb}^{-1}$ . The trigger, double b-tag, and jet multiplicity requirements are applied.

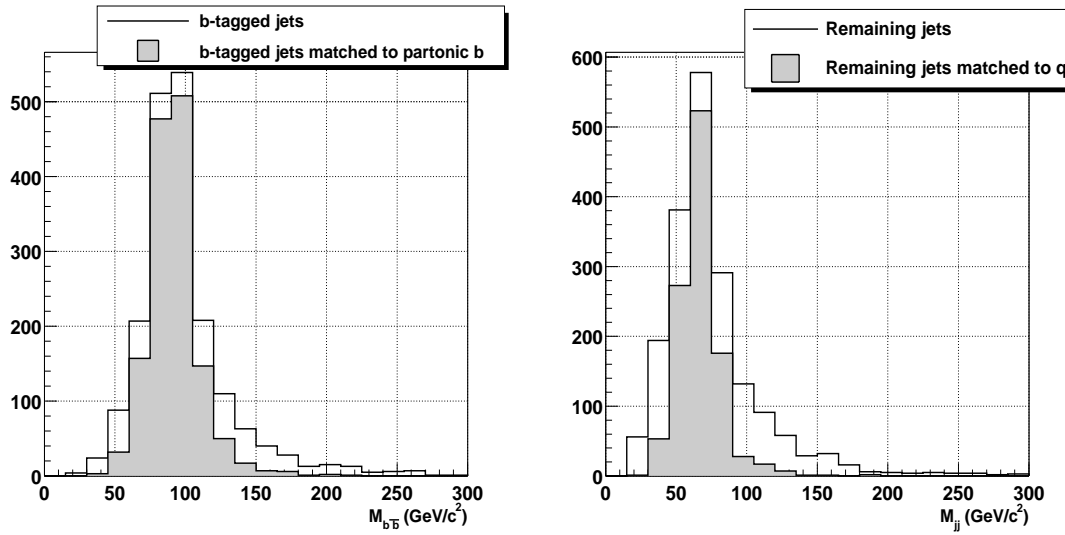


Figure 9.10: Left: signal ( $M_H = 120 \text{ GeV}/c^2$ ) invariant mass distribution of the two highest- $E_T$  b-tagged jets of the event (open histogram) and invariant mass of the b-tagged jets associated to the b-quark from the Higgs decay (shaded histogram). Right: invariant mass distribution of the two remaining jets of the event (open histogram) and invariant mass of the two remaining jets associated to the W/Z decays (shaded histogram). The trigger, double b-tag,  $N_{jets}$  and  $\sum E_T^{jets}$  requirements are applied. The matching is performed with the coincidence of the jet centroid and the quark direction inside of a 0.7 cone radius.

The trigger,  $N_{jets}$  and the  $\sum E_T^{jets}$  requirements are applied.

Figure 9.13 shows the signal statistical significance as a function of the upper threshold cut on the reconstructed invariant mass of the two remaining jets of the event ( $M_H = 120 \text{ GeV}/c^2$ ). For  $M_{jj} \leq 115 \text{ GeV}$  the statistical signal significance is maximized. It has been found that a cut on the  $p_T(jj)$  does not improve the signal statistical significance. Table 9.6 summarizes the expected number of signal

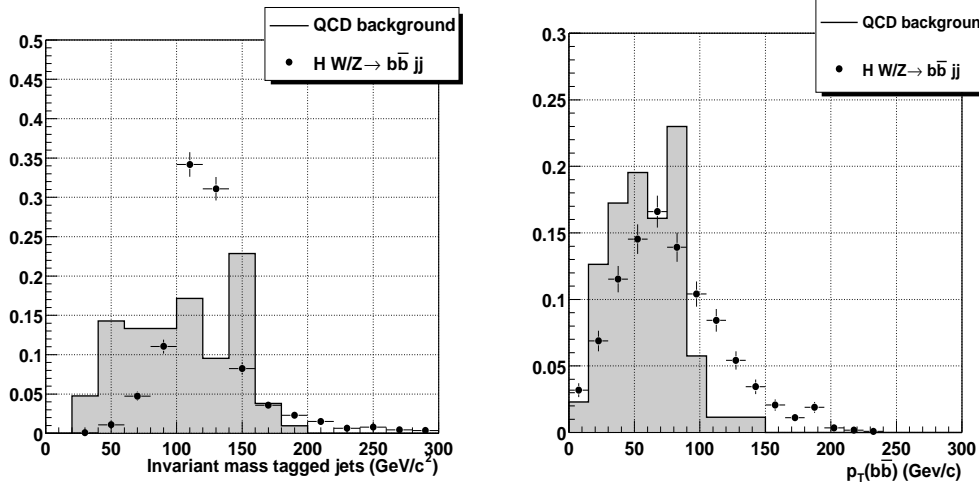


Figure 9.11: Invariant mass (left) and  $p_T$  distribution (right) of the two highest- $E_T$  b-tagged jets for the signal [ $M_H = 120 \text{ GeV}/c^2$ ] (dots) and QCD background (shaded histogram). The trigger and the requirement of at least four jets with  $E_T^{jet} \geq 15 \text{ GeV}$ ,  $|\eta| \leq 2$  and  $\sum E_T^{jets} \geq 140 \text{ GeV}$  are also applied. All distributions are normalized to unit area.

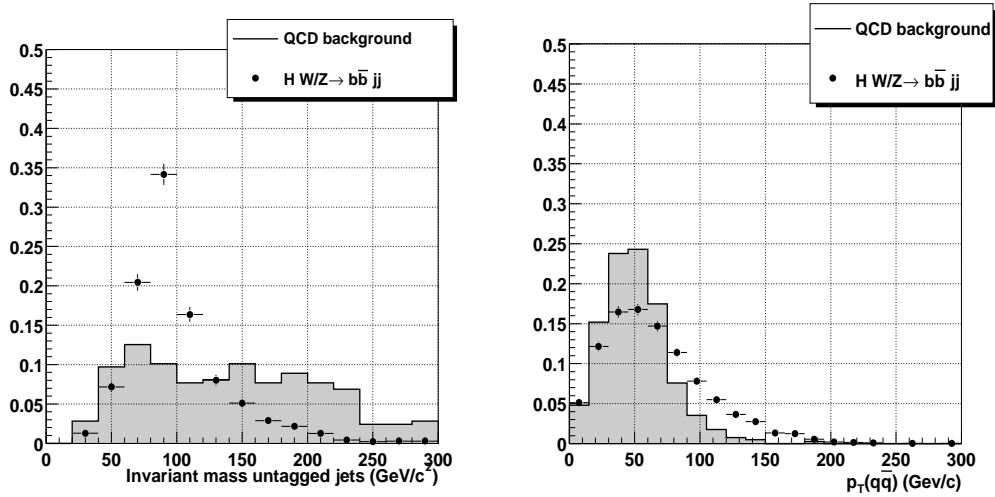


Figure 9.12: Invariant mass (left) and  $p_T$  distribution (right) of the two remaining jets for the signal [ $M_H = 120 \text{ GeV}/c^2$ ] (dots) and QCD background (shaded histogram). The trigger conditions and the requirement of at least four jets with  $E_T^{jet} \geq 15 \text{ GeV}$ ,  $|\eta| \leq 2$  and  $\sum E_T^{jets} \geq 140 \text{ GeV}$  are also applied. All distributions are normalized to unit area.

and background events in  $1 \text{ fb}^{-1}$  after the requirements on  $M_{jj}$ .

Further signal discrimination can be achieved with a cut on the invariant mass of two highest- $E_T$  b-tagged jets. Figure 9.13 shows the significance of the signal

with respect to the QCD background as a function of the threshold on the invariant mass of the two b-tagged jets. For  $M_H = 120 \text{ GeV}/c^2$  the requirement of  $M_{b\bar{b}} \geq 100 \text{ GeV}/c^2$  maximizes the statistical significance. Table 9.7 summarizes the expected number of signal and background events in  $1 \text{ fb}^{-1}$  after the requirements on  $M_{b\bar{b}}$ .

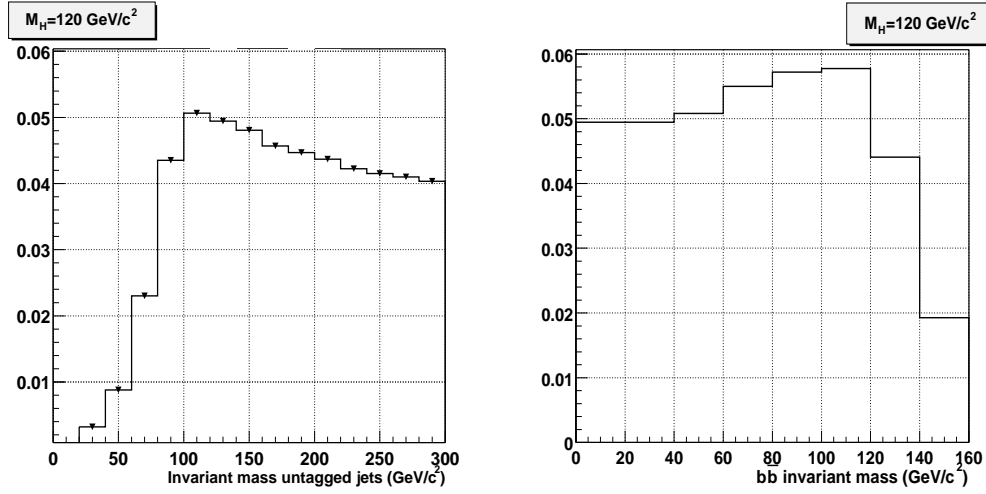


Figure 9.13: Left: statistical significance of the upper threshold on  $M_{jj}$  for the signal ( $M_H = 120 \text{ GeV}/c^2$ ) with respect to the QCD background. Right: statistical significance of the low threshold on  $M_{b\bar{b}}$  for the signal ( $M_H = 120 \text{ GeV}/c^2$ ) with respect to the QCD background. Both distributions are normalized to  $1 \text{ fb}^{-1}$ . The trigger, double b-tag, jet multiplicity, and  $\sum E_T^{jets}$  requirements are applied.

	$M_{jj}$ ( $\text{GeV}/c^2$ )	$\epsilon_{M_{jj}}$ (%)	Events ( $1 \text{ fb}^{-1}$ )	$S/\sqrt{B}$ ( $1 \text{ fb}^{-1}$ )
$H + W/Z \rightarrow b\bar{b}jj$				
$M_H = 115 \text{ GeV}/c^2$	115	$81.3 \pm 0.8$	$8.8 \pm 1.3$	$0.070 \pm 0.009$
$M_H = 120 \text{ GeV}/c^2$	115	$79.4 \pm 0.9$	$6.1 \pm 1.1$	$0.05 \pm 0.01$
$M_H = 125 \text{ GeV}/c^2$	115	$82 \pm 1$	$4.5 \pm 0.9$	$0.037 \pm 0.008$
$M_H = 130 \text{ GeV}/c^2$	115	$81 \pm 1$	$4.0 \pm 0.9$	$0.035 \pm 0.006$
QCD	115	$38 \pm 1$	$15000 \pm 6000$	—

Table 9.6:  $M_{jj}$  selection efficiencies, expected number of signal and QCD background events, and signal significances in  $1 \text{ fb}^{-1}$  after the  $M_{jj} \leq 115 \text{ GeV}/c^2$  selection for different Higgs boson masses. The trigger, double b-tag, jet multiplicity and  $\sum E_T^{jet}$  requirements are also applied. Efficiencies and expected number of QCD events are referred to the  $M_H = 120 \text{ GeV}/c^2$  selection.

	$M_{b\bar{b}}$ (GeV/ $c^2$ )	$\epsilon_{M_{b\bar{b}}}$ (%)	Events (1 fb $^{-1}$ )	$S/\sqrt{B}$ (1 fb $^{-1}$ )
H + W/Z $\rightarrow$ $b\bar{b}jj$				
$M_H = 115$ GeV/ $c^2$	90	$94 \pm 1$	$8.4 \pm 0.6$	$0.07 \pm 0.01$
$M_H = 120$ GeV/ $c^2$	100	$95 \pm 1$	$5.8 \pm 0.6$	$0.06 \pm 0.01$
$M_H = 125$ GeV/ $c^2$	100	$95 \pm 1$	$4.3 \pm 0.5$	$0.04 \pm 0.01$
$M_H = 130$ GeV/ $c^2$	110	$98.5 \pm 0.5$	$3.9 \pm 0.5$	$0.04 \pm 0.01$
QCD	100	$70 \pm 1$	$10000 \pm 4500$	–

Table 9.7:  $M_{b\bar{b}}$  selection efficiencies, expected number of signal and QCD background events and signal significances in 1 fb $^{-1}$  for different Higgs boson masses. The trigger, double b-tag, jet multiplicity,  $\sum E_T^{jet}$  and  $M_{jj} \leq 100$  GeV/ $c^2$  requirements are applied. Efficiencies and expected number of QCD events are referred to the  $M_H = 120$  GeV/ $c^2$  selection.

As mentioned in Section 9.3.2, the heavy flavor contribution to the QCD background comes from the *Direct Production*, *Flavor Excitation* and *Gluon Splitting* processes. b-jets from *Flavor Excitation* and *Direct Production* are characterized by high invariant masses ( $M_{b\bar{b}}$ ) and low transverse momentum ( $p_T(b\bar{b})$ ). For *Gluon Splitting* the  $b\bar{b}$  system tends to have larger  $p_T(b\bar{b})$  and lower invariant masses (Figure 9.14) [115]. From all these three process the *Gluon Splitting* is the dominant one before and after the selection cuts, with a contribution that increases with the jet multiplicity [118].

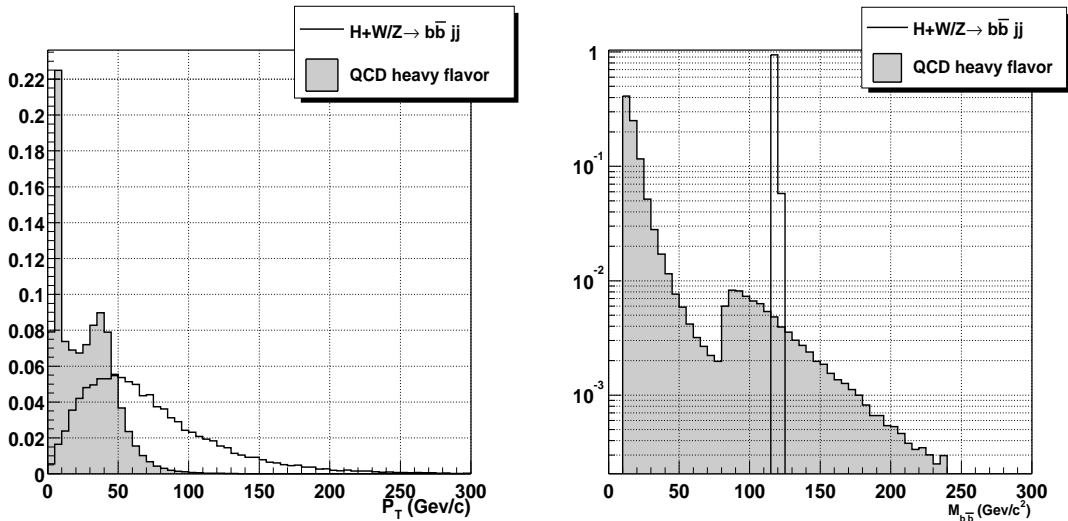


Figure 9.14:  $p_T$  (left Figure) and invariant mass distributions (right Figure) of the  $b\bar{b}$  system for QCD heavy flavor production (shaded histogram) and H + W/Z  $\rightarrow$   $b\bar{b}jj$  signal events ( $M_H = 120$  GeV/ $c^2$ , open histogram) at generation level. No cuts are applied.

Correlations between the  $p_T$  and invariant mass of the  $b$ -tagged and remaining jets have been studied (Figures 9.15 and 9.16) but they do not yield any improvement in signal discrimination. For the signal, the invariant mass of the  $b$ -tagged jets are distributed around the Higgs boson mass. For QCD we can distinguish two regions. A first region with low invariant masses and high  $p_T$  values (*Gluon Splitting*), and a second region with higher invariant mass values and slightly lower  $p_T$  values, corresponding to the *Direct Production* and *Flavor Excitation* processes. For the two remaining jets, the invariant mass of the signal is predominantly clustered between  $60 \text{ GeV}/c^2$  and  $140 \text{ GeV}/c^2$  and spread over a wide  $p_T(b\bar{b})$  range. On the other hand, the QCD background is characterized by an invariant mass for the untagged jets with an almost uniform distribution which does not allow to set a clear discriminant region in the  $p_T$ - $M_{jj}$  space.

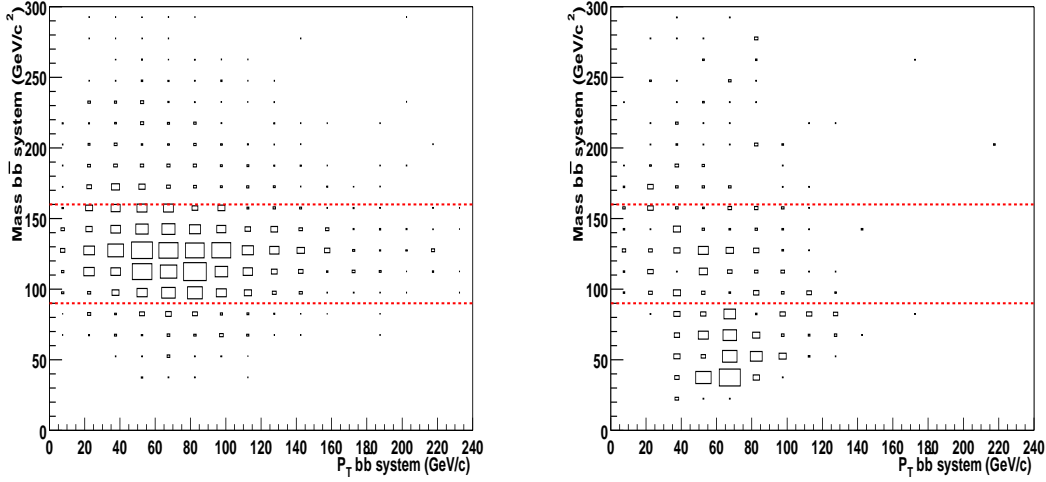


Figure 9.15: Reconstructed invariant mass of the two highest- $E_T$   $b$ -tag jets *versus* their transverse momentum for the signal ( $M_H = 120 \text{ GeV}$ ) (left) and the QCD background (right). The trigger and the requirement of at least four jets with  $E_T^{jet} \geq 15 \text{ GeV}$ ,  $|\eta| \leq 2$  and  $\sum E_T^{jets} \geq 140 \text{ GeV}$  are also applied.

### Selection Efficiencies for the Non-QCD Backgrounds

QCD heavy flavor multijet production is the main background with a contribution two orders of magnitude above the rest (Table 9.3). For the optimization of the kinematical cuts only this background has thus been considered. Table 9.8 shows the efficiencies of the kinematical selection and the expected number of events in  $1 \text{ fb}^{-1}$  for the rest of the physical backgrounds.

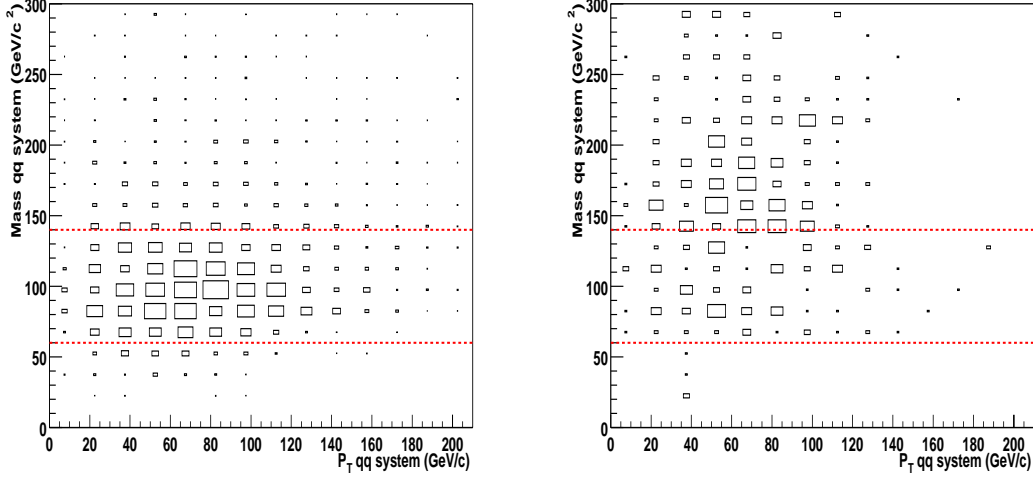


Figure 9.16: Reconstructed invariant mass of the two remaining untagged jets *versus* their transverse momentum for the signal ( $M_H = 120$  GeV) (left) and the QCD background (right). The trigger and the requirement of at least four jets with  $E_T^{jet} \geq 15$  GeV,  $|\eta| \leq 2$  and  $\sum E_T^{jets} \geq 140$  GeV are also applied.

### 9.3.4 Counting Experiment

Table 9.9 summarizes the estimated signal significance  $(S/\sqrt{B})_{1fb^{-1}}$ <sup>8</sup> for the channel studied in this work, where the offline selection criteria is:

- $N_{jets}(E_T^{jet} \geq 15 \text{ GeV}, |\eta| \leq 2) \geq 4$ , reconstructed with a 0.4 cone radius and with two b-tagged jets among the four highest- $E_T$  jets of the event.
- $\sum E_T^{jets} \geq 140 - 160$  GeV for Higgs boson masses of  $115 - 130$  GeV/ $c^2$ , where the sum is performed over the four highest- $E_T$  jets.
- The invariant mass of the two untagged jets must be  $M_{jj} \leq 115$  GeV/ $c^2$ .
- The invariant mass of the two highest- $E_T$  b-tagged jets must be  $M_{b\bar{b}} \geq 110 - 130$  GeV/ $c^2$ , depending on the Higgs boson mass.

Table 9.9 also shows the  $S/\sqrt{B}$  Tevatron Higgs Working group results for different Higgs boson masses. Note that the only background contribution considered is QCD heavy flavor, normalized with a multijet QCD data sample acquired with the D0 [133] detector at  $\sqrt{s} = 1.8$  TeV.

Both results agree within the uncertainties despite the fact that we do not consider any improvement jet energy resolution. Since we use a more realistic detector

<sup>8</sup>In our case the number of signal events  $S$  can be neglected with respect to the number of QCD multijet background events, and therefore  $\frac{S}{\sqrt{S+B}} \approx \frac{S}{\sqrt{B}}$ .

	$\epsilon_{N_{jets}}$ (%)	$\epsilon_{\sum E_T^{jets}}$ (%)	$\epsilon_{M_{jj}}$ (%)	$\epsilon_{M_{bb}}$ (%)	Events in $1 \text{ fb}^{-1}$
$H + W/Z \rightarrow b\bar{b}jj$ ( $M_H = 120 \text{ GeV}/c^2$ )	$76.0 \pm 0.4$	$85.3 \pm 0.3$	$79.8 \pm 0.8$	$98 \pm 1$	$6.7 \pm 0.4$
QCD	$32.1 \pm 0.5$	$65.5 \pm 0.5$	$47 \pm 2$	$76 \pm 3$	$18000 \pm 6000$
$t\bar{t}$	$96.3 \pm 0.3$	$92.6 \pm 0.5$	$75 \pm 1$	$92 \pm 1$	$372 \pm 105$
$Z + \text{jets}$ ( $Z \rightarrow b\bar{b}/c\bar{c}$ )	$57.0 \pm 0.4$	$27.0 \pm 0.5$	$64.1 \pm 0.7$	$66 \pm 1$	$5.2 \pm 0.8$
$Wb\bar{b}/c\bar{c}$	$48.3 \pm 0.2$	$33.2 \pm 0.3$	100	0	0
$t(W^*)$	$75.5 \pm 0.7$	$65.9 \pm 0.9$	$93.5 \pm 0.9$	$85 \pm 1$	$24 \pm 2$
$t(W - g)$	$62.1 \pm 0.9$	$47.3 \pm 0.9$	$76 \pm 1$	$89 \pm 1$	$3.2 \pm 0.5$
WW	$67.9 \pm 0.5$	$45.2 \pm 0.7$	100	$85 \pm 1$	$2.8 \pm 0.6$
WZ	$71.6 \pm 0.5$	$35.5 \pm 0.6$	$90 \pm 1$	$87 \pm 1$	$6.4 \pm 0.7$
ZZ	$73.2 \pm 0.6$	$39 \pm 1$	$90 \pm 1$	$87 \pm 1$	$8.3 \pm 0.6$

Table 9.8: Signal ( $H + W/Z \rightarrow b\bar{b}jj$ ) and background efficiencies for the kinematical selection: jet multiplicity selection ( $\epsilon_{N_{jets}}$ ),  $\sum E_T^{jets}$  selection ( $\epsilon_{\sum E_T^{jets}}$ ), invariant mass of the untagged jets ( $\epsilon_{M_{jj}}$ ), and invariant mass of the tagged jets ( $\epsilon_{M_{bb}}$ ). Last column shows the expected events for  $1 \text{ fb}^{-1}$ .

$m_H$ (GeV)	Run-II multijets analysis			Tevatron Working Group		
	S	B	$S/\sqrt{B}$	S	B	$S/\sqrt{B}$
115	$8.4 \pm 0.6$	$12000 \pm 5000$	$0.07 \pm 0.01$	3.5	2800	0.07
120	$5.8 \pm 0.6$	$10000 \pm 4500$	$0.06 \pm 0.01$	2.5	2300	0.05
125	$4.3 \pm 0.5$	$10000 \pm 4500$	$0.04 \pm 0.01$	1.3	2000	0.03
130	$3.9 \pm 0.5$	$7500 \pm 3500$	$0.04 \pm 0.01$	0.45	1700	0.01

Table 9.9: Number of events for the  $H + W/Z \rightarrow b\bar{b}jj$  signal and QCD heavy flavor background and statistical significance after all selection requirements for  $1 \text{ fb}^{-1}$ .

simulation in our study, with an implementation of such enhancements the results obtained should significantly improve.

## 9.4 Extrapolation of Run-I Searches

CDF has searched for the Higgs boson associated production in the fully hadronic mode  $H + W/Z \rightarrow b\bar{b}jj$  with  $91 \pm 7 \text{ pb}^{-1}$  of Run-I data [114]. The trigger requirements were four calorimeter clusters at Level 2 with  $E_T^{jet} \geq 15 \text{ GeV}$ , and a total transverse energy  $\sum E_T^{jets} \geq 125 \text{ GeV}$  (See Table 7.2). Further steps in the data reduction were: 1) four or more reconstructed jets with uncorrected  $E_T \geq 15 \text{ GeV}$  and  $|\eta| \leq 2.1$ ; 2) at least two among the four highest- $E_T$  jets in the event identified as b-quark jets candidates, and 3) a cut on the transverse momentum of the  $b\bar{b}$  system,  $p_T(b\bar{b}) \geq 50 \text{ GeV}/c$ . The backgrounds considered were the QCD multijet heavy flavor production,  $t\bar{t}$  production,  $Wb\bar{b}$ ,  $Zb\bar{b}$  and fake double-tags. Finding no evidence of signal excess in the invariant mass distribution of the  $b\bar{b}$  system, a

limit at the 95% C.L. on the Higgs boson production cross section was set by fitting the double tag invariant mass distribution with a binned maximum likelihood function. The results of the fit are shown in Figure 9.17. The limit is expressed in terms of  $\sigma \cdot \beta$  as a function of the Higgs mass, where  $\beta$  is the product of the branching ratios  $\text{BR}(H \rightarrow b\bar{b})$  and  $\text{BR}(W/Z \rightarrow jj)$ . Also shown in Figure 9.17 are the Standard Model predictions. For  $M_H = 120 \text{ GeV}/c^2$  the upper limit at the 95% C.L. is 17.6 pb, two orders of magnitude above the theoretical predictions.

The Run-I results can be extrapolated to the Run-II conditions by assuming the absence of signal observation. The upper limit in the cross section at the 95% C.L. can then be expressed in the form:

$$\sigma_{95\% \text{ C.L.}}^I = \frac{N_{95\% \text{ C.L.}}^I}{\epsilon_I^{\text{sig}} \cdot \mathcal{L}^I} \quad (\text{Run - I}) \quad (9.1)$$

$$\sigma_{95\% \text{ C.L.}}^{II} = \frac{N_{95\% \text{ C.L.}}^{II}}{\epsilon_{II}^{\text{sig}} \cdot \mathcal{L}^{II}} \quad (\text{Run - II}) \quad (9.2)$$

Assuming  $N_{95\% \text{ C.L.}}$  proportional to the fluctuations of the background  $\sqrt{\epsilon^{bkg} \cdot \mathcal{L} \cdot \sigma^{bkg}}$ , then:

$$\sigma_{95\% \text{ C.L.}}^{II} \sim \sigma_{95\% \text{ C.L.}}^I \cdot \sqrt{\frac{\epsilon_{II}^{\text{back}}}{\epsilon_I^{\text{back}}}} \cdot \frac{\epsilon_I^{\text{sig}}}{\epsilon_{II}^{\text{sig}}} \cdot \sqrt{\frac{\mathcal{L}^I}{\mathcal{L}^{II}}} \quad (9.3)$$

Here we neglect the background cross section variation due to the center of mass energy increase.

In Run-II the expected integrated luminosity will increase by a factor of  $\sim 140$  (from  $90 \text{ pb}^{-1}$  to  $\sim 15 \text{ fb}^{-1}$ ) which enhances the sensitivity by a factor of  $\sim 13$ . The new trigger, together with the selection criteria studied in previous Sections, yields a total signal and background efficiency of  $\sim 6.5\%$  ( $M_H = 120 \text{ GeV}/c^2$ ) and  $\sim 3 \cdot 10^{-5}\%$ , respectively. In Run-I the signal and background efficiencies were  $\sim 2.4\%$  and  $\sim 2.5 \cdot 10^{-4}\%$ , respectively [115]. Therefore, the signal efficiency is increased by a factor of  $\sim 2.7$  while for the background it increases only by a factor of  $\sim 2$ . Taking into account these efficiencies the sensitivity is further enhanced by a factor of  $\sim 2$ . Table 9.10 summarizes the different sensitivity enhancements for Higgs boson masses ranging from 115 to  $135 \text{ GeV}/c^2$ .

Figure 9.17 shows the extrapolation of the Run-I 95% C.L. exclusion limits to the Run-II conditions. It shows that with  $15 \text{ fb}^{-1}$  of integrated luminosity it is not possible to exclude any Higgs boson mass using only the information provided by this channel.

$M_H$ (GeV/ $c^2$ )	$\epsilon_I^{sig}$ (%)	$\epsilon_{II}^{sig}$ (%)	$\epsilon_I^{bkg}$ (% · 10 <sup>-4</sup> )	$\epsilon_{II}^{bkg}$ (% · 10 <sup>-4</sup> )	$\sigma \beta_{95\% \text{ C.L.}}^I$ (pb <sup>-1</sup> )	$\sigma \beta_{95\% \text{ C.L.}}^{II}$ (pb <sup>-1</sup> )	$\sigma \beta^{th}$ (pb <sup>-1</sup> )
115	2.3 ± 0.4	6.2 ± 0.4	2.5 ± 0.4	3 ± 2	18.1	0.75	0.25
120	2.4 ± 0.7	6.6 ± 0.5	2.5 ± 0.4	3 ± 2	17.8	0.73	0.20
125	2.5 ± 0.8	6.7 ± 0.8	2.5 ± 0.4	2 ± 1	17.2	0.67	0.15
130	2.6 ± 0.9	6.8 ± 0.8	2.5 ± 0.4	2 ± 1	16.9	0.64	0.12

Table 9.10: Signal and background efficiencies and cross section upper limits at the 95% C.L. for Run-I (90 pb<sup>-1</sup>) and Run-II expectations for 15 fb<sup>-1</sup>. Last column shows the SM theoretical predictions for the Higgs boson production cross section times the branching ratio [8].

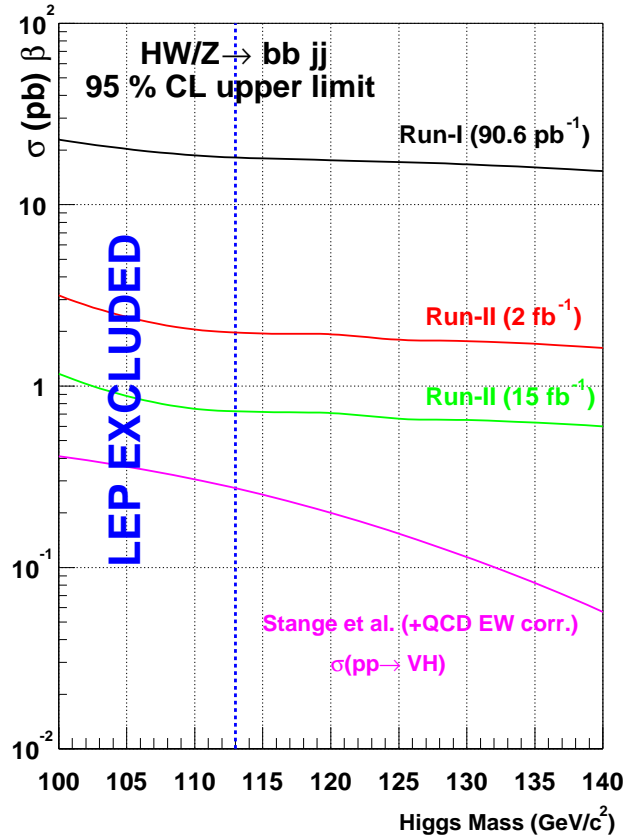


Figure 9.17: Run-II extrapolation for the CDF 95% C.L. upper limits on  $\sigma(p\bar{p} \rightarrow HW/Z) \cdot \beta$ , where  $\beta = BR(H \rightarrow b\bar{b})$ .



# Conclusions

In this thesis we describe work done to develop and utilize a test system for the production of ISL silicon microstrip ladders, and a study of how to improve the trigger on some Higgs production and decay channels making use of the new secondary vertex trigger of CDF. A complete DAQ system for electrical characterization of SVX II and ISL ladders has been developed together with the CDF Rutgers University group (New Jersey, USA). The system included all the necessary experimental setup for single ISL and SVX II ladder characterization at each construction stage during production, as well as the necessary infrastructure for a massive burn-in test. The system was modified at the INFN-Pisa laboratory to allow for laser scans and measurements with a  $\beta$ -source. Tests were aimed to detect defects present in the sensors and read-out electronics, as well as damages created during ladder assembly or created in the early stages of device operation. The final objective was to deliver complete functional ladders (in total more than 150,000 ISL readout channels) prior to their insertion into the ISL space frame at Fermilab (USA). The objective was accomplished with the on-schedule delivery of  $\sim 150$  fully tested and instrumented ladders (50% of the total ISL ladders) by the end of July 2001. This fulfilled the ladder construction responsibilities of the INFN-Pisa ISL group. During all the construction period, the system and characterization methods described in this thesis allowed the assembly of two ISL ladders per day.

For Higgs boson searches in Run-II two new dedicated triggers have been designed in this work and proposed to the CDF collaboration.

A first trigger has been designed to optimize the detection efficiency of Higgs bosons produced in association with vector bosons in all-hadronic decay modes. The optimized trigger requirements at each level are:

- Level 1 Trigger:** Single trigger tower  $E_T^{low} \geq 10$  GeV
- Level 2 Trigger:**  $N_{clus}(E_T^{clus} \geq 10 \text{ GeV}) \geq 3$ , and  $\sum E_T^{clus} \geq 90$  GeV  
(calorimeter)
- Level 2 Trigger:** At least 2 SVT tracks with impact parameter  $d_0 \geq 100 \mu m$  and  
(tracking)  $d_1 \geq 80 \mu m$

The Level 2 signal trigger efficiency of the calorimeter only requirements is  $\sim 74\%$  ( $M_H = 120 \text{ GeV}/c^2$ ) with rates below  $\sim 15$  Hz. However, at Level 3 a further rejection factor of  $\sim 15$  is necessary to stay in the allowed trigger output bandwidth

( $\sim 1 - 2$  Hz at  $\mathcal{L} = 1 \cdot 10^{32} \text{ cm}^{-2}\text{s}^{-1}$ ). This can be achieved by the use of the Silicon Vertex Trigger (SVT) to trigger on large impact parameter tracks at Level 2. We have shown that the additional requirement of at least two SVT reconstructed tracks ( $p_T^{\text{track}} \geq 2.0 \text{ GeV}/c$ ) with impact parameters  $d_0 \geq 100 \mu\text{m}$  and  $d_1 \geq 80 \mu\text{m}$  reduces the rates by a factor of  $\sim 15$ , which results in a final rate of  $\sim 1$  Hz with signal trigger efficiencies of  $\sim 40\%$  ( $M_H = 120 \text{ GeV}/c^2$ ). With this new trigger, the total efficiency for  $H + W/Z \rightarrow b\bar{b}jj$  events where at least two b-jets can be identified with the standard CDF offline algorithms is  $\sim 10\%$ , an improvement by a factor of 3.5 with respect to the Run-I multijet trigger. The impact of this new trigger design in the CDF Run-II discovery potential for the Higgs boson in this channel has also been studied. The offline search analysis for the Higgs boson performed by the Tevatron Higgs Working Group, whose studies assumed 100% trigger efficiencies, has been evaluated taking into account the new trigger and a more detailed simulation of the CDF detector. We find that our results are consistent with the results reported by the Tevatron Higgs Working Group, and that the new trigger will not change the sensitivity for the  $H + W/Z \rightarrow b\bar{b}jj$  channel. To fully exploit the enhanced efficiency provided by this new trigger, we have studied an alternative optimization of the offline search strategy with looser requirements. We obtain slightly improved results, consistent within uncertainties. Finally, the CDF Run-I sensitivity is extrapolated to the Run-II conditions. We found that due to the new trigger design, the CDF sensitivity is increased by a factor of  $\sim 2$  respect to the previous Run-I searches.

In Run-II, one of the most promising channels to detect the SM Higgs boson is through the associated production  $H + Z \rightarrow b\bar{b}\nu\bar{\nu}$ . Run-I searches in this channel were based on the inclusive missing transverse energy trigger ( $\cancel{E}_T$ ) which required a Level 2  $\cancel{E}_T \geq 35 \text{ GeV}$ . In Run-II, with a ten-fold increase on the instantaneous luminosity ( $\mathcal{L} = 1 \cdot 10^{32} \text{ cm}^{-2}\text{s}^{-1}$ ) the threshold on the trigger  $\cancel{E}_T$  should be raised up to 45 GeV in order to keep acceptable trigger rates, with a considerable loose in signal efficiency. In this thesis we have studied the feasibility of a new dedicated trigger for the  $H + Z \rightarrow b\bar{b}\nu\bar{\nu}$  process with lower  $\cancel{E}_T$  trigger thresholds and additional Level 2 tracking requirements. The final optimized trigger conditions at each level are:

- Level 1 Trigger:** Single trigger tower  $E_T^{\text{tow}} \geq 10 \text{ GeV}$
- Level 2 Trigger:**  $N_{\text{clus}} \geq 1$  ( $E_T^{\text{clus}} \geq 20 \text{ GeV}$ ) and  $\cancel{E}_T \geq 15 \text{ GeV}$   
(calorimeter)
- Level 2 Trigger:** At least 2 SVT tracks with impact parameter  $d_0 \geq 100 \mu\text{m}$  and  
(tracking)  $d_1 \geq 80 \mu\text{m}$

With this trigger the final rates are  $\sim 2$  Hz, with signal trigger efficiencies of  $\sim 35\%$  ( $M_H = 120 \text{ GeV}/c^2$ ). The total efficiency to select  $H + Z \rightarrow b\bar{b}\nu\bar{\nu}$  events where both b-jets are identified by the CDF offline algorithms is  $\sim 7\%$ , an improvement by a factor of 1.5 with respect to the Run-I trigger.

We have studied the impact of this trigger in the sensitivity of this channel as reported by the Tevatron Higgs Working Group, using the same offline optimization.

The Tevatron Higgs Working Group study assumes 100% trigger efficiencies with thresholds on the offline missing transverse energy of  $\cancel{E}_T \geq 35$  GeV, motivated by the inclusive  $\cancel{E}_T$  triggers used in Run-I. In our study we found that taking into account the trigger efficiency, the signal acceptance is reduced by  $\sim 50\%$ . However, our study indicates that the loose requirements on  $\cancel{E}_T$  of the new trigger can be used to lower the  $\cancel{E}_T \geq 35$  GeV requirement, and eventually significantly enhance the sensitivity in this channel.



# Appendix A

## ISL Sensors Specifications

### A.1 Hamamatsu Sensors Electrical Specifications

Initial full depletion voltage ( $V_F$ ):	$40 < V_F < V_F^{max}, V_F^{max} < 100\text{V}$
Initial leakage current: (bulk, surface and edge contribution)	$< 4\mu\text{A}$ at $V_b = V_F^{max} + 10\text{ V}$ ( $T = 20^\circ - 25^\circ$ )
Junction breakdown <sup>1</sup> with open readout electrodes:	$V_F^{max} + 50\text{ V}$
Dark current slope $dI/dV$ ((nA/cm <sup>2</sup> )/V):	$dI/dV < 0.2$ with bias voltage ( $V_b$ ) ranging from $V_F$ to $V_F^{max} + 50\text{ V}$ ( $V_b = 2V_0$ when p and n sides are at $\pm V_0$ ) <sup>2</sup>
coupling capacitor breakdown voltage: (n-side and p-side)	$> 100\text{ V}$ (200 V typical)
Interstrip resistance:	$> 2\text{ G}\Omega$
Poly-silicon resistor:	
mean value:	41.5 M $\Omega$
Variation within one detector:	$\pm 10\%$
Resistance of Al electrode: (n and p-sides)	$< 20\Omega/\text{cm}$
Capacitance of coupling capacitor: (n and p sides)	$> 14\text{ pF}/\text{cm}$ (20 pF/cm typical)
Interstrip capacitance (full length) <sup>3</sup> :	
p-side:	$< 10\text{ pF}$
n-side:	$< 12\text{ pF}$ (10 pF typical)

Table A.1: Electrical specifications for ISL Hamamatsu sensors (4" technology).

<sup>1</sup>Junction breakdown voltage is defined as  $I_{break} > 10 \times I_{break} \times (V_F + 10)\text{ V}$ .

<sup>2</sup>p and n-side balanced bias, such that all read-out electrodes are at ground.

<sup>3</sup>The interstrip capacitance is measured at  $V_b = 1.2 \times V_F$  with neighbor strips grounded.

No anomalous behavior should be observed at bias voltages up to  $V_F^{max} + 50$  V. Anomalous behavior is here defined as micro-discharges, steeply rising total current similar to breakdown behaviour, individual strip currents in excess of 100 nA, or any other behavior that would typically compromise the long term and stable operation of the sensors.

## A.2 Hamamatsu Sensors Mechanical Specifications

Sensor type:	double-sided, both sides AC-coupled p-side stereo at 1.207°
Bulk:	
type:	n-type
thickness:	$300 \pm 15 \mu\text{m}$
flatness:	$60 \mu\text{m}$ (any detector shall fit between two parallel plates which are separated by $375 \mu\text{m}$ )
Biasing method: (both sides)	poly-silicon resistors
n-side strip direction:	strips run parallel to the long edge
p-side strip direction:	strips run at 1.207° with respect to the n-side strips
n-side isolation method:	$\text{p}^+$ stop channel surrounding n-strip.
Passivation thickness:	$0.5 - 1.0 \mu\text{m}$
p-stop implant density:	$\geq 10^{14}$ borons/ $\text{cm}^2$
Implant plus diffusion depth:	$\sim 1.5 \mu\text{m}$ for p, n-strips, and $\text{p}^+$ stop
Dead channels: (p and n side each)	$< 2\%$ dead per detector. $< 3\%$ per side
Dimensions:	
Sensitive area:	$5.723 \text{ cm} \times 6.750 \text{ cm}$
Outer size:	$5.926 \text{ cm} \times 6.902 \text{ cm}$
Number of strips:	p-side: 512 readout and 1 + 13 dummy strips n-side: 512 readout and 1 + 1 dummy strips Dummy strips are also biased
Strip pitch:	p-side $112 \mu\text{m}$ n-side $112 \mu\text{m}$
Implant strip width:	p-side $22 \mu\text{m}$ n-side $22 \mu\text{m}$
Al electrode width:	p-side $16 \mu\text{m}$ n-side $16 \mu\text{m}$
Bonding pads:	physical width $60 \mu\text{m} \times 200 \mu\text{m}$ one row of pads, one pad per strip at each end
Alignment marks:	8 alignment marks (crosses of $140 \mu\text{m}$ long per $10 \mu\text{m}$ wide along the sides of the detector). Mark points at every 10 bonding pads and print of the corresponding strip number near the bias ring. Detector ID number printed on the detector.

Table A.2: Geometrical specifications for ISL Hamamatsu sensors (4" technology).

### A.3 Radiation Damage Specifications for Pilot Hamamatsu Sensors

Ten days after irradiation of 200 krad gamma-ray:	
Leakage current at 20°:	$< 3 \mu\text{A}/\text{cm}^2$
Bias resistor change:	$< 20\%$
p-strip and n-strip isolation resistance:	$> 1 \text{ G}\Omega$
Junction breakdown voltage:	$> V_F^{max} + 50 \text{ V}$
Onset voltage of micro breakdown:	$> V_F^{max} + 50 \text{ V}$
Interstrip capacitance :	
p-side:	$< 11 \text{ pF}$
n-side:	$< 13 \text{ pF}$

Table A.3: Radiation specifications for ISL Hamamatsu sensors (4" technology).

## A.4 Micron Sensors Specifications

Sensor type:	double-sided, both sides AC-coupled n-side stereo at 1.207°
Bulk:	
type:	n-type
flatness:	each detector must fit between two parallel planes whose distance does not exceed by more than 20 $\mu\text{m}$ the thickness of the silicon crystal
Strip linearity:	max deviation less than 2 $\mu\text{m}$
Front back alignment:	the mask alignment between the two sides must be better than $\pm 10 \mu\text{m}$
Biasing:	polysilicon 4 – 10 M $\Omega$ Wafer to wafer variation < 15% than variation on single wafer
Implant strip:	18 $\mu\text{m}$
Implant depth:	> 1 $\mu\text{m}$
Width of Al strips:	14 $\mu\text{m}$
p-stop width:	32 $\mu\text{m}$
gap between p stops and n-strips:	10 $\mu\text{m}$
Total strip current (guard excluded):	< 100 nA/cm <sup>2</sup> at 80 V
Total detector current (with guard):	< 15 $\mu\text{A}$
Single strip current (at 80 V):	< 15 $\mu\text{A}$
Uniformity of $V_b$ :	< 20% over the detector area
Junction breakdown:	> 150 V
Micro Brekdown:	> 150 V
Coupling Capacitor breakdown:	> 120 V
Coupling Capacitor Value:	> 20 pF/cm at 1 kHz
Coupling Capacitor leakage:	< 10 nA at 100 V
Interstrip Resistance:	> 1 G $\Omega$ at 80 V > 100 M $\Omega$ after 1 MRad photons (Co <sup>60</sup> )
Resisitvity of implant:	< 150 K $\Omega$ /cm
Resistivity Al strips:	< 30 $\Omega$ /cm
Total interstrip capac.:	< 1 pF/cm on p side < 1.2 pF/cm on n side
(to both adjacent strips)	
Bad strips:	< 3% on each side, < 2% overall

Table A.4: Specifications for ISL Micron sensors (6" technology).

Bad strip is:

1. non isolated strip (less than 1 GOhm resistance)
2. strip coupling: any coupling capac. draining more than 10 nA @100 V is defined as bad
3. strip open: any interrupted strip is BAD
4. single strip current: Any strip draining more than 100nA at 80 V is defined BAD.

# Appendix B

## DAQ During Production

In this Appendix we describe a custom Data Acquisition system (DAQ) specifically developed for electrical testing and characterization of SVX II and ISL ladders. The motivation for the development of such a system was:

- Although only the final DAQ system (Section 3.2.5) can provide the most extensive and close to real conditions testing, at the time when ladder production started the number of final DAQ test stands was not enough to perform all tests at each ladder construction stage.
- In the CDF collaboration ladder construction and testing had to be carried in different laboratories all over the world (INFN at Italy, Liverpool and Glasgow Universities at UK, Karlsruhe University in Germany, Fermilab at USA and KEK at Japan), and in conditions where the reliability and simplicity of the system was the main concern. Due to the complexity of the final DAQ system, the fragility of some of their components and their high cost, the use of a more robust, simple, and less expensive system was highly desirable.
- The electrical characterization and test of production ladders often requires to test a great quantity of devices in a short time depending on the production schedule, which involves non-expert users. Therefore, a high reliable and easy to maintain system which allowed the simultaneously testing of numerous devices was necessary. This system was initially designed to simply exercise and readout the SVX II and ISL ladders without external trigger. Later on it was modified to allow external triggering. It was used in a laser test station, and to perform measurements with a  $\beta$  source.

### B.1 System Overview

All the control and output signals of the SVX3 chip are digital. The chips can then be exercised with a pattern generator plus a logic analyzer. However, pattern generator modules are expensive and difficult to program. Furthermore, for certain

types of tests like the burn-in test (Section 4.6) where for a great number of devices large amounts of data must be monitored and recorded simultaneously, this system can not be used for obvious reasons. A more practical system was developed at the Lawrence Berkeley National Laboratory and FNAL for testing single SVX II ladders [134]. It basically consisted on a Personal Computer (PC) and two printed circuit boards, a so called *PATT* board and a scrambler board [134]. Through the PC ASCII text files reproducing the logical patterns for operational control of the SVX3 chip are coded to bitstreams and downloaded to the PATT board. In the PATT board they are stored in *First-In First-Out* chips, where all the input/output signals are single ended TTL or CMOS signals. An oscillator on the PATT board clocks the data out of the pattern FIFO's to the SVX3 chips with constant timing at the SVX3 operational frequency of 50 MHz.<sup>1</sup> The scrambler board provides the differential lines to generate the clock signals needed by the SVX3 chip and the differential line receivers for the readout data coming from the SVX3 chips. The readout data from the SVX3 chips are stored in another FIFO of the PATT board, denoted here as the DAQ FIFO. After an entire pattern cycle is run (at least one SVX3 chip initialization, and patterns for signal acquisition, charge digitization and data readout), the data stored in the DAQ FIFO is transferred back to the PC computer for further analysis.

The use of such system was limited to only one output port in the scrambler board, thus allowing the test of only a single SVX II or ISL ladder once at a time. However, for burn-in tests, where all the SVX II and ISL ladders ( $\sim 1000$  devices) had to be exercised during 72 hours, a system allowing the simultaneous operation of several ladders was necessary. For this purpose, a new system based in the same principles as the PATT system was designed (Figure B.1). It consists on a PC running the Linux operating system, a *Multiplexer First-in First-Out* board (MUX/FIFO board) able to simultaneously handle up to five ladders, and new scrambler boards. The necessary software for the system operation, on-line monitoring, data recording and offline analysis was also developed. In the following we describe in more detail each of these components.

## B.2 DAQ Personal Computer and Low Level Software

For the control of the MUX/FIFO boards and data readout a PC running the Linux operating system is used. The core of the software for the SVX3 chip operation consists in a set of low level routines written in standard C language. These routines are a modified version of the software developed for the *PATT* system [134]. They are divided in three groups, depending on their functionality:

---

<sup>1</sup>The internal clock of the PC can not provide at such frequency the necessary timing accuracy for all the control lines.

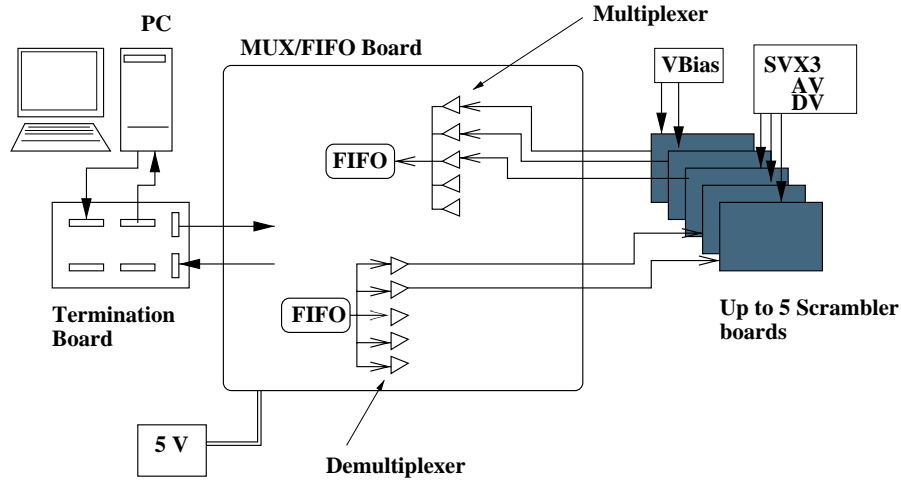


Figure B.1: Silicon DAQ system for production tests.

- Bitstream decoding. The different patterns for the SVX3 chip operation (initialization, charge acquisition, charge digitization and data readout) can be designed in the form of ASCII text files (Figure B.2). A set of routines decode these files into a series of bitstreams<sup>2</sup> (one per each input signal) which are stored in common memory arrays.
- FIFO bitstream download and data readout. Once the bitstreams are built and stored in the PC memory, they can be downloaded to the FIFO chip of the MUX/FIFO board (the pattern FIFO) by calling the appropriate routines. With the bitstreams stored in the pattern FIFO, a complete SVX3 working cycle (Section 3.2.3) consisting in charge acquisition, charge digitization and data readout operations can be issued. The patterns are clocked out from the pattern FIFO to the SVX II or ISL ladders at 50 MHz,<sup>3</sup> where the demultiplexing logic of the MUX/FIFO board allows to select one or several ports to which the patterns are routed. In this way several ladders can be exercised at the same time. The output data is stored in the output FIFO of the MUX/FIFO board (DAQ FIFO), and can be uploaded to the PC memory. Note that although all the ports can be exercised simultaneously, only the data from one of the currently active ports can be stored in the DAQ FIFO.

For each SVX3 chip the output data usually contain a number identifying each chip in the ladder (set at initialization time), the number of the pipeline capacitor where the digitized charge was stored, and the channel number followed

<sup>2</sup>A bitstream is here an array of *unsigned char* words containing only 1's or 0's.

<sup>3</sup>Note that for every SVX3 chip working cycle, a routine call must be issued (usually inside a loop). Therefore, effectively the SVX3 chip is exercised in *burst* mode (not in continuous mode like with the final DAQ system), with a frequency limited by the maximum output rate of the PC ISA bus which was found to be  $\sim 100$  Hz.



```

raw data dump at 11:41:05, machine cdfbu2.fnal.gov : 1 chips
  0: 255 255 255 255 255 255 0 129 20 0
 10: 227 1 117 2 114 3 117 4 117 5
 20: 118 6 117 7 119 8 231 9 117 10
 30: 116 11 116 12 119 13 117 14 118 15
 40: 119 16 230 17 117 18 119 19 117 20
 50: 117 21 119 22 117 23 116 24 229 25
 60: 124 26 118 27 117 28 119 29 119 30
 70: 118 31 116 32 231 33 119 34 117 35
 80: 119 36 115 37 118 38 118 39 116 40
 90: 231 41 119 42 124 43 117 44 117 45
100: 117 46 117 47 116 48 225 49 119 50
110: 116 5 116 52 119 53 117 54 116 55
120: 116 56 231 57 117 58 125 59 116 60
130: 116 61 117 62 117 63 91 64 198 65
140: 75 66 80 67 116 68 116 69 119 70
150: 117 71 119 72 230 73 117 74 116 75
160: 116 76 116 77 117 78 117 79 117 80
170: 230 81 119 82 117 83 116 84 117 85
180: 119 86 117 87 116 88 228 89 116 90
190: 117 91 124 92 117 93 114 94 114 95
200: 90 96 203 97 116 98 116 99 124 100
210: 124 101 116 102 116 103 117 104 228 105
220: 117 106 117 107 117 108 117 109 124 110
230: 117 111 124 112 231 113 116 114 116 115
240: 124 116 119 117 95 118 81 119 74 120
250: 220 121 117 122 124 123 117 124 116 125
260: 119 126 117 127 230 230 247 255 255 255

```

Figure B.3: SVX3 chip data output. They consist of 8-bit words. Initial words with 0 or 255 are words with dummy content from the FIFO. Chip identifier is coded as 128+chip identifier. The next word is the pipeline cell number (from 0 to 49). For every channel that has been readout, the channel number (from 0 to 127) together with the digitized charge in ADC counts (expressed in gray code) is sent to the output. The data from the next chip is simply placed immediately after.

multiplex/demultiplex logic to simultaneously operate several ladders. A simplified schematic view of the operation of the MUX/FIFO board is shown in Figure B.1. Figure B.4 shows a view of the MUX/FIFO board.

The MUX/FIFO board consists of 2 input connectors (a 60-pin and a 40-pin seen in Tables B.1 and B.2) to receive and send data to the DAQ PC, and 10 output connectors (five 50-pin connectors and five 34-pin connectors, Tables B.3 and B.4) to attach the scrambler boards together with the SVX II or ISL ladders. As described in Section B.2, the control and readout of the attached ladders is done through TTL I/O cards (64-channel) with a PC personal computer.

Figure B.5 shows the parts layout of the MUX/FIFO board. Table B.5 shows the parts list. Power to the MUX/FIFO board is provided by an external +5 V input

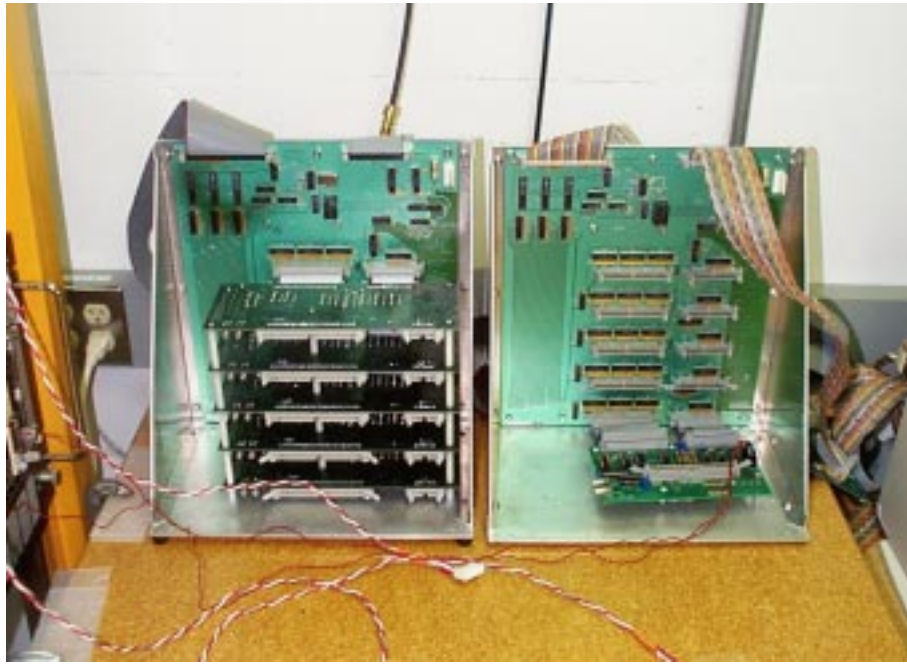


Figure B.4: A view of two MUX/FIFO boards. The MUX/FIFO board on the left side shows five instrumented scrambler boards, while the one on the right-side shows an original scrambler board from the PATT setup [134].

line which also distributes the power to the scrambler boards through two pins in the 50-pin and 34-pin connectors. The total current driven by the MUX/FIFO board with 5 attached scramblers boards is less than 5 A. The low power analog and digital voltages (AV and DV in Figure B.1) needed by the ladders attached to the scrambler boards are provided through the scrambler boards by external power supplies. High voltage power to bias the ladders is also provided through Lemo connectors on the scrambler boards by external power supplies (denoted as VBias in Figure B.1).

A termination board is also used to properly terminate the lines between the MUX/FIFO board and the I/O TTL card in the DAQ PC computer. This allows flexibility in the length of the flat ribbon cables for these lines without compromise the performance at high frequencies.

PC I/O card (CN3)	60-pin MUX/FIFO board connectors	Function
pin 1	pin 55	WRITE
pin 3	pin 1	input data 1
pin 5	pin 3	input data 2
pin 7	pin 5	input data 3
pin 9	pin 6	input data 4
pin 11	pin 9	input data 5
pin 13	pin 11	input data 6
pin 15	pin 13	input data 7
pin 17	pin 15	input data 8
pin 19	pin 17	input data 9
pin 21	pin 19	input data 10
pin 23	pin 21	input data 11
pin 25	pin 23	input data 12
pin 27	pin 25	input data 13
pin 29	pin 27	input data 14
pin 31	pin 29	input data 15
pin 2	pin 31	input data 16
pin 4	pin 33	input data 17
pin 6	pin 35	input data 18
pin 8	pin 37	input data 19
pin 10	pin 39	input data 20
pin 12	pin 41	input data 21
pin 14	pin 43	input data 22
pin 16	pin 45	input data 23
pin 18	pin 49	CONTROL
pin 20	pin 53	RUN
pin 22	pin 51	RETRANSMIT
pin 24	pin 59	BIT 9 SELECT
pin 32	pin 57	STROBE
	pin 47	not used
pins 26,28,30		not used
pin 33,34		GND

Table B.1: Correspondence between the PC I/O card 34-pin connector (CN3) and the 60-pin MUX/FIFO board input connector. This connector is specifically used to clock-in data patterns (through the WRITE input line) into the pattern FIFO's of the MUX/FIFO board.

Each MUX/FIFO board FIFO is 9 bit wide. Therefore, to download the patterns and control commands from the DAQ PC computer to the MUX/FIFO board, 3 FIFOs are put in parallel to provide up to 27 parallel input lines, where 17 of them are necessary for the operational control of the SVX3 chip (Figure B.2 and Table B.1). The data from the DAQ PC TTL card is strobed into the MUX/FIFO pattern FIFO with the WRITE signal (Table B.1). The data must be present at the FIFO input together with a high state of the WRITE signal. A high to low transition of

PC I/O card (CN 2)	40-pin MUX/FIFO board connectors	Function
pin 2	pin 37	output data 1
pin 4	pin 35	output data 2
pin 6	pin 33	output data 3
pin 8	pin 31	output data 4
pin 10	pin 29	output data 5
pin 12	pin 27	output data 6
pin 14	pin 25	output data 7
pin 16	pin 23	output data 8
pin 18	pin 21	bit 9
pin 20	pin 19	EF Flag
pin 17	pin 1	input SEL5
pin 19	pin 3	input SEL4
pin 21	pin 5	input SEL3
pin 23	pin 6	input SEL2
pin 25	pin 9	input SEL1
pin 27	pin 15	decoder input RSEL1
pin 29	pin 13	decoder input RSEL2
pin 31	pin 11	decoder input RSEL3
pin 33,34		GND
pin 1,3,5,7,9,11,13,15		not used
pin 22,24,26,28,30,32		not used
	pin 17	not used
	pin 39	V <sub>CC</sub>

Table B.2: Correspondence between the PC I/O card 34-pin connector (CN2) and the 60-pin MUX/FIFO board input connector. This is a dual purpose connector used to control the operation of the MUX/FIFO board (through the CONTROL, RUN, RETRANSMIT, RSEL and SEL input lines), and clock-out/read the data from the DAQ FIFO.

the WRITE signal writes the data into the FIFO. This procedure is repeated for each bit to be stored in the FIFO.<sup>6</sup> The CONTROL signal is kept high for normal operation. Lowering it resets the FIFO contents. The RUN signal is used to run a pattern stored in the FIFO. It must be kept high for a time at least equal to the length of the pattern times the oscillator period. The RETRANSMIT signal is usually kept low. When set to high after a RUN signal the patterns are placed in a position to be run again. The BIT-9 SELECT signal is not used and has been kept for backward compatibility with the PATT boards.

Data coming from the ladders are stored in a set of two FIFOs (referred here as the DAQ FIFOs). They were implemented as a replacement of the original single DAQ FIFO in order to keep a reliable readout performance.<sup>7</sup> Among other signals,

<sup>6</sup>The FIFOs are 4096 bit deep.

<sup>7</sup>In the original design the data coming from the ladders were stored in the DAQ FIFO synchronized with a STORE signal generated by the MUX/FIFO clock. At 50 MHz, and taking into account that the Cypress CY7C433-10 FIFO requires the STORE signal to be low for at least 10

Pin Number	Function
pin 1	V <sub>CC</sub>
pin 3,5,7,9,11	not used
pin 13	input data 1 (TRG)
pin 15	input data 2 (BUS 3)
pin 17	input data 3 (BUS 2)
pin 19	input data 4 (BUS 1)
pin 21	input data 5 (BUS 0)
pin 23	input data 6 (CH_MODE)
pin 25	input data 7 (CAL_STR)
pin 27	input data 8 (L1A)
pin 29	input data 9 (PRD2)
pin 31	input data 10 (PRD1)
pin 33	input data 11 (PA_RST)
pin 35	input data 12 (TN)
pin 37	input data 13 (BE_MODE)
pin 39	input data 14 (FE_MODE)
pin 41	input data 15 (BE_CLK)
pin 43	input data 16 (CLK_SEL)
pin 45	input data 17 (FE_CLK)
pin 47	Raw Clock
pin 49	not used
pins 2,4,6,8,10,12,14,16,18,20,22,24	GND
pins 26,28,30,32,34,36,38,40,42,44,46,48	GND
pin 50	not used

Table B.3: Pin layout of the MUX/FIFO board 50-pin connectors. Some of the SVX3 chip functions associated to the input data connector are shown in brackets.

Pin Number	Function
pin 1,3,5,7,9	not used
pin 11	output data 1
pin 13	output data 2
pin 15	output data 3
pin 17	output data 4
pin 19	output data 5
pin 21	output data 6
pin 23	output data 7
pin 25	output data 8
pin 27	not used
pin 29,30	bit 9
pin 31	V <sub>CC</sub>
pin 33	not used
pin 2,4,6,8,10	not used
pin 12,14,16,18,20,22,24,26,28	GND
pin 32,34	not used

Table B.4: Pin layout of the MUX/FIFO board 34-pin output connectors.

ns and high for at least 10 ns, the system was very sensible to imperfections in the clock waveform, different cable lengths and the different chip multiplicity devices used during readout.

Item	Quantity	Part Name	Reference	Description
1	4	C43310	U1 U2 U3 U4 U18	FIFO Buffer Memory
2	15	74AC244	U44 U21 U20 U28 U27 U22 U32 U31 U26 U33 U39 U38 U43 U42 U37	Octal Buffer/Line Drivers with TRI-STATE Outputs
3	3	74AC374	U5 U6 U4	Octal D Flip-Flop with TRI-STATE Outputs
4	3	74AS00	U8 U19 U11	Quad 2-Input NAND Gate
5	1	74AS08	U9	Quat 2-Input AND Gate
6	1	74AS10	U13	Triple 3-Input NAND Gate
7	4	74AS32	U30 U36 U41 U25	Quad 2-Input OR Gate
8	10	74AC244	U24 U15 U23 U29 U35 U34 U45 U40 U46 U16	Octal Buffer/Line Driver with TRI-STATE Outputs
9	1	74LS00	U7	Quad 2-Input NAND Gate
10	3	74LS138	U10	Dual Negative-Edge-Trigger J-K Flip-Flop
11	1	74S112	U10	Dual Negative-Edge-Trigger J-K Flip-Flop
12	1	CTS50MHZ	U12	50 MHz Clock
13	1	DDU39LS	U14	Digital Delay Unit
14	33	R10A1K	R20 R21 R22 R23 R24 R33 R30 R32 R31 R40 R35 R36 R37 R39 R38 R43 R46 R53 R45 R44 R50 R47 R51 R49 R52 R42 R54 R5 R29 R6 R7 R28 R25	
15	3	RSIP6E	R55 R61 R26	
16	10	RSIP10E	R41 R56 R27 R2 R3 R17 R1 R48 R4 R34	
17	15	R400	R8 R14 R13 R12 R11 R19 R9 R10 R16 R15 R71 R70 R72 R73 R18	
18	54	C100	C42 C46 C2 C47 C43 C22 C24 C23 C15 C16 C17 C12 C9 C4 C7 C8 C5 C14 C6 C20 C10 C21 C49 C45 C48 C25 C29 C50 C51 C52 C30 C53 C54 C55 C38 C34 C33 C37 C36 C35 C39 C40 C31 C32 C27 C28 C26 C1 C11 C3 C18 C44 C13	
19	1	POLC1300	C41	
20	5	34PIN3M	J10 J12 J4 J6 J8	Connector
21	1	40PIN3M	J2	Connector
22	5	50PIN3M	J7 J9 J11 J3 J5	Connector
23	1	60PIN3M	J1	
24	1	MOLEX6	J13	
25	8	SKTPIN	P1 P4 P6 P3 P2 P5 P8 P7	
26	7	FUSE	F2 F3 F4 F5 F6 F7	1A Pico
27	1	FUSE	F1	10A Pico

Table B.5: Parts list for the MUX/FIFO board.

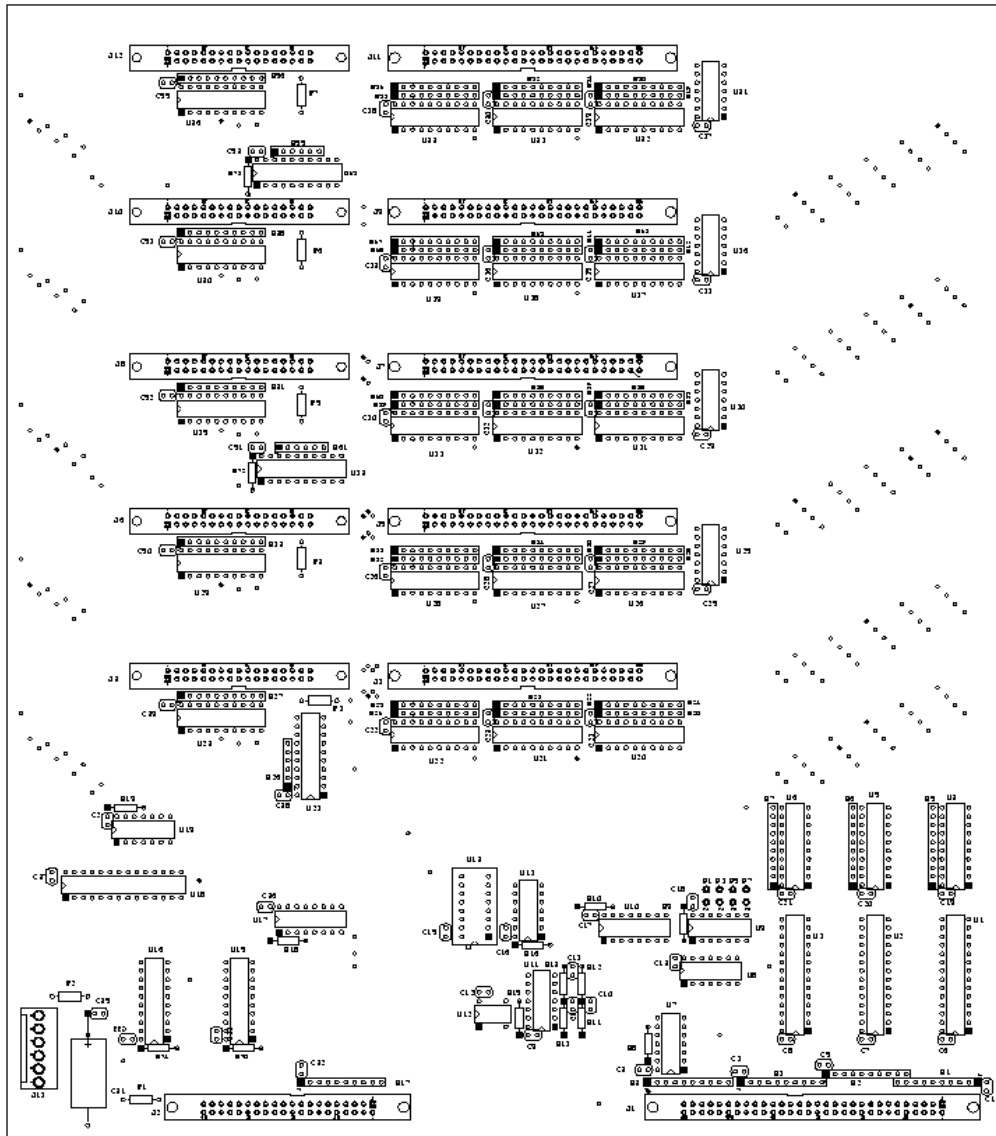


Figure B.5: Parts layout of the MUX/FIFO board.

the output of the SVX3 chip consists of 8-bit wide data words together with a signal called *Odd Byte Data Valid* (OBDV). The OBDV signal is synchronized with the output of the data bus and is used as a STORE signal to clock the data inside the FIFOs. The two FIFOs take turns reading the data words. One FIFO reads the

data when the OBDV signal is high, while the second FIFO reads the next data word when an inverted OBDV signal is high. In this way both FIFOs are effectively running at a half the readout frequency (25 MHz) necessary when multiple chips are readout. Figure B.6 illustrates the situation.

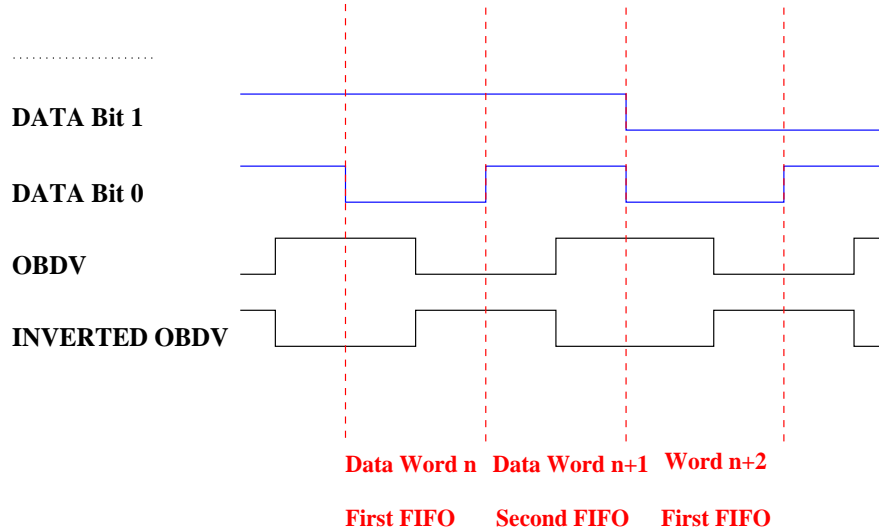


Figure B.6: DAQ FIFO timing for the MUX/FIFO board.

## B.4 Burn-in Test High Level Software

For the burn-in of the SVX II and ISL ladders the devices under test were continuously exercised for 72 hours, with readout data constantly monitored and periodically saved to a file in binary format. Due to the large number of devices ( $\sim 1000$ ) to be tested simultaneously, the great variety of ladder types (5 different SVX II ladders plus one type for the ISL) and the extensive period of testing with the required bookkeeping, a relatively complex software package was developed. It consisted of a Graphical User Interface (GUI) to allow an effective operation and on-line monitoring of the system. A binary format data handling system for the storage and analysis of the data was also developed. For the SVX3 chip operational control the software described in Section B.2 was used.

The general specifications for the software design were:

- The software must allow the handling of a practically unlimited number of boards from a single program. For each board, the software must completely handle up to 5 attached ladders, independently of their chip multiplicity.
- The software must allow the disconnection at any time of any ladder without interruption of the burn-in test of the remaining devices.

- Online monitoring of the attached ladders together with simple error diagnostics.
- Control and operation of the system must be design in a *user-friendly* way, allowing the operation by non-expert users.
- A data handling system for readout data, consisting in the definition of a binary data format and the necessary software for data packing/unpacking must be provided. Error recovery procedures in case of software crash must be defined.
- The software must be completely portable and GNU compliant.

### B.4.1 Software Architecture

To accomplish all these requirements a software based on a client/server architecture was developed. The server program was completely written in standard C and designed as *Finite State Machine* (FSM), with an infinite loop initiated by the start of the burn-in program, and finished when the corresponding command issued by the client was received. The client part was implemented as an independent Linux process. The communication between the client and the server was implemented using the standard Linux *shared memory* utilities, with a semaphore as arbitration system. The shared memory was mapped as a C structure.

On the client side, the number of active boards, the number of connected/disconnected ports in each board, and the type of ladder attached in each port were controlled through a GUI (Figures B.7, B.8 and B.9). The GUI was written with the freeware package TCL/Tk v8.0.

The server program is automatically initiated as a Linux child process when the client is started. Every time the status of a board is changed (*e.g.* a port is connected/disconnected), the client program transfers the related information to the server side through the shared memory. On the server side, the FSM first checks commands referring to the general program performance (*CONTINUE*, *FREEZE*, or *STOP* the overall program execution). Next, for every declared board each port is checked according to the declared status (type of attached ladder, active or non active). Depending on the burn-in test parameters, the corresponding action is then issued. Since the complete status of each board is stored in a memory array and continuously updated, a ladder can be disconnected in each port without disturbing the testing process in other ports.

### B.4.2 Burn-In Data Readout and Online Monitoring

When a port is activated through the GUI, the information about the port (type of ladder and burn-in test parameters) is transferred to the server process. The first time the port is found to be active by the server loop, the ASCII pattern files

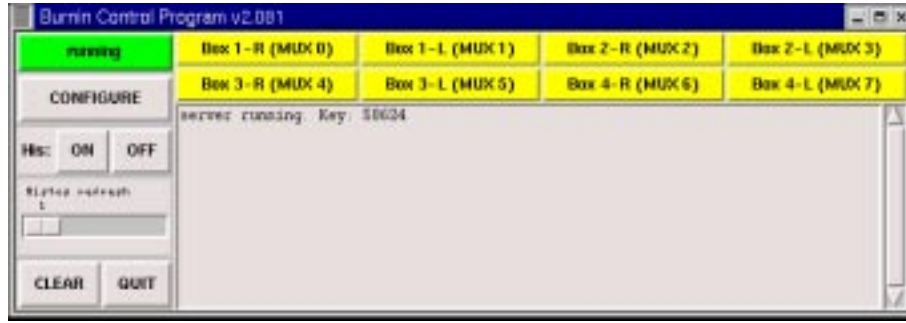


Figure B.7: Control panel for the burn-in test stand program.

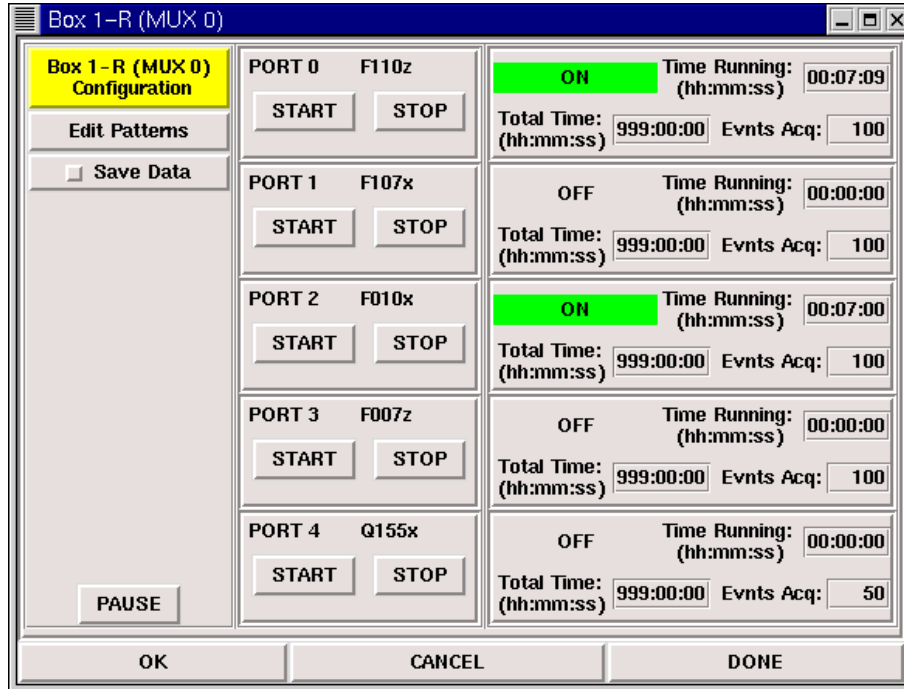


Figure B.8: MUX/FIFO control panel for the burn-in test stand program.

corresponding to SVX3 chip initialization, acquire, digitization and read-out modes are decoded and the built bitstreams stored in memory arrays (independent for each port). The attached ladder is then initialized. Afterwards, at each cycle of the server loop, the ladder is exercised and the read-out data saved to a binary file according to the burn-in test parameters in the following way:

- At each server cycle the SVX3 chips of the attached ladder are exercised through a full acquire-digitize-readout pattern bitstream. The readout data stored in the DAQ FIFO is uploaded and automatically decoded. Instantaneous pedestals, average pedestals, noise, differential noise and a basic error

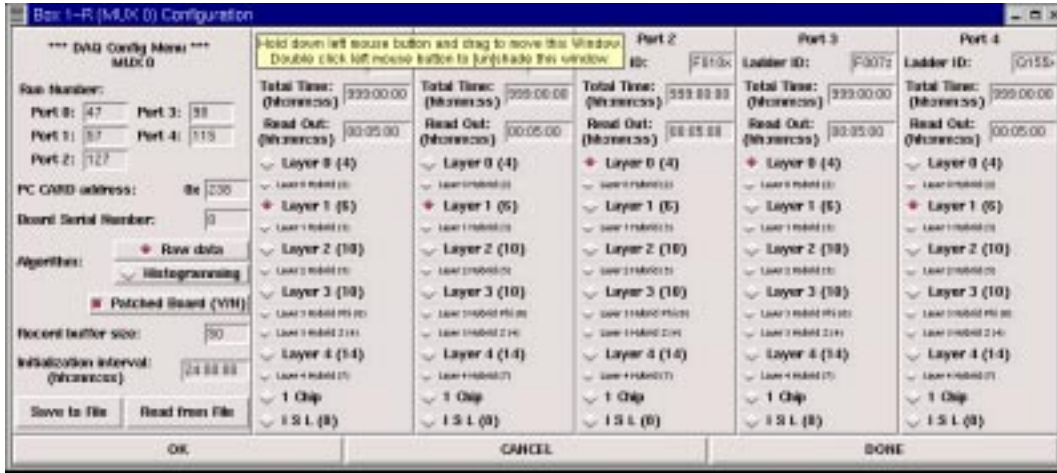


Figure B.9: MUX/FIFO configuration panel for the burn-in test stand program.

Figure B.10:

diagnostic are calculated. The results are displayed online using the HISTOSCOPES utility (Figure B.10) [136].<sup>8</sup> If the correspondent option is active, this histograms can be saved to a file.

- For each ladder, a time interval (record) is set such that at each elapsed time interval a configurable number of events are readout and saved to a binary file format (See Section B.4.3).
- Once the burn-in test time has expired, the ladder is reinitialized and the port is declared as inactive.

### B.4.3 Binary Data Format

To minimize the space for data storage, a binary format for the readout data was designed. The burn-in readout data for a particular port is divided in records stored at regular time intervals in a binary file (Figure B.11). Each record has a header with some log information (Table B.6), followed by the data corresponding to each

<sup>8</sup>The HISTOSCOPES utility is a package specially designed to monitored data produced by different Unix processes. When the server is initiated, a call to a HISTOSCOPE routine creates a pipe. When a port is initialized, the histoscope histograms (*e.g.* pedestal *versus* channel number) are created and every time the data is readout, filled. From the client side, a HISTOSCOPE display can be started. The HISTOSCOPE display is automatically attached to the pipe created by the server and the histograms displayed with the contents continuously refreshed.

event of the record. Each event is separated by an event flag. For each port a unique data file name must be provided by the test operator through the GUI.

A set of user routines to provide the inverse functionality (from a binary format file retrieve each record and the event data stored in memory arrays) were also developed.

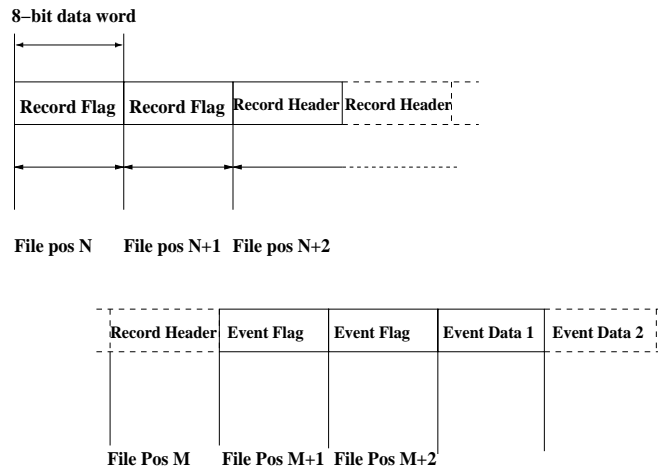


Figure B.11: Binary file data format for the raw data of the burn-in test.

## B.5 Modifications for the Laser Test Station

To use the burn-in DAQ system for the Laser Test Station (Section 4.7) two modifications were needed. A special pattern file for the acquisition mode of the SVX3 chip, and the addition of an output Lemo connector to the TRIG signal line on the MUX/FIFO board (Table B.3).

As described in Section 3.2.3, in the acquisition mode of the SVX3 chip the charge present in each input channel is integrated and stored in a 42 cell deep pipeline every time the *Front End Clock* is low (Figure B.12).<sup>9</sup> Once all the capacitors on the pipeline have been used, the pipeline contents are overwritten. If a *Level 1 Accept* signal is received, the corresponding cell capacitor is marked and its content not overwritten.<sup>10</sup>

In the MUX/FIFO board a signal line called *TRIG* (see Table B.3 and Figure B.12) was used to pulse a laser diode through a NIM delay unit, as described in

<sup>9</sup>In normal operational conditions the low window of the *Front-End Clock* will be synchronized with the Tevatron bunch crossing.

<sup>10</sup>The time delay between the *Level 1 Accept* signal and the pipe line capacitor can be set at initialization time with a time resolution equal to the *Front End Clock* signal frequency.

**Record Header**

(8-bit word)

WORD 0	run number
WORD 1	board number
WORD 2	port number
WORD 3	detector ID
WORD 4	month
WORD 5	year
WORD 6	MUX/FIFO clock frequency (MHz)
WORD 7	bias voltage (V)
WORD 8	elapsed time from the beginning of the test
WORD 9	number of events in the record
WORD 10	number of chips in the ladder
WORD 11	total number of acquired events
WORD 12	total number of events exercised
WORD 13	hour
WORD 14	minute
WORD 15	second

Table B.6: Record header content.

Section 4.7. The *TRIG* signal is not connected to the input of the SVX3 chip, and its only purpose is to serve as a synchronization signal. Adjusting the delay of the *TRIG* signal with respect to the falling edge of the *Front End* clock, one can appropriately set the coincidence between the laser pulse and the *Front-End* clock window, where the charge is integrated.

## B.6 Modifications for the $\beta$ Source Test Setup

The modifications for the  $\beta$  source setup include a special pattern file for the acquisition mode of the SVX3 chip, and the addition of output Lemo connectors for the *Level 1 Accept* and the *Front End Clock* signals, both on the MUX/FIFO board.

As explained in Section 3.2.3, the charge present in each input channel of the SVX3 chip when the *Front-End Clock* signal is low is continuously integrated and stored in one of the 42 capacitors of the pipeline. When a *Level 1 Accept* signal is received the corresponding pipeline capacitor is marked, and its contents transferred for digitization and readout.

```

!*****
!Clock beam crossings, inject charge and trigger
!*****
fe_mode:      ffffffffffffffffffffffffffffffffffffffffff
fe_clk:       43____44____45____46____47____48____49____
cal_inject:   -----
L1A:         11111111111111111111_111111111111111111111111
prd1:        -----
prd2:        -----
pa_reset:     -----
!*****
!* BE idle
!*****
trig:         __TT-----
TN:          -----
chmod:        -----
be_mode:      bbbbbbbbbbbbbbbbbbbbbbbbbbbbbbbbbbbbbbb
clk_sel:      XXXXXXXXXXXXXXXXXXXXXXXXXXXXXXXXXXXXXXXX
be_clk:       -----
comp_rst:     XXXXXXXXXXXXXXXXXXXXXXXXXXXXXXXXXXXXXXXX
rref_sel:     sssssssssssssssssssssssssssssssssssssssss
ramp_rst:     XXXXXXXXXXXXXXXXXXXXXXXXXXXXXXXXXXXXXXXX
cntr_rst:     XXXXXXXXXXXXXXXXXXXXXXXXXXXXXXXXXXXXXXXX
store:        XXXXXXXXXXXXXXXXXXXXXXXXXXXXXXXXXXXXXXXX

```

Figure B.12: Example of a modified acquire mode pattern file. A trigger signal (*trig*) is issued to pulse the laser diode, synchronized with the *Level 1 Accept (L1A)*. In this case, the charge integrated when the *Front-End Clock* is low between pulses denoted as 43 and 44 is acquired and the corresponding pipeline capacitor marked.

For the  $\beta$  source test setup, patterns for acquisition, digitization and data readout were continuously sent to the device under test (Figure 4.23). The *Front-End Clock* signal was sent through a Lemo connector to one of the inputs of a NIM coincidence unit. From a photomultiplier attached to a scintillator placed under the ladder, signals generated by the  $\beta$  particles were sent to the other input of the coincidence unit. For signals arriving in coincidence, the output signal is sent to a NIM-TTL converter, and through a Lemo connector on the MUX/FIFO board to the *Level 1 Accept* input of the SVX3 chip. The time delay between the *Level 1 Accept* signal and the corresponding capacitor on the pipeline can be set digitally when the SVX3 chip is initialized.

In case the coincidence between the photomultiplier signal and the *Front-End Clock* signal does not occur, no *Level 1 Accept* signal is issued. In this case, the output data shows an invalid pipeline capacitor number (see Section B.2). Such events are automatically rejected with a software filter on the DAQ PC.





# List of Figures

1	Extrapolació al Run-II . . . . .	ix
1.1	Running of the gauge coupling constants at the first order in the Standard Model . . . . .	8
1.2	Quark confinement . . . . .	10
1.3	Spontaneous Symmetry Breaking for a ferromagnet . . . . .	14
1.4	Total width and branching ratios of the Standard Model Higgs boson . . . . .	19
1.5	Higgs boson production cross sections at Tevatron . . . . .	21
1.6	Feynman diagrams for Higgs boson production at Tevatron . . . . .	22
1.7	Theoretical bounds on the SM Higgs boson mass . . . . .	24
1.8	Electroweak precision data constrains to the Higgs boson mass . . . . .	26
1.9	Dijet mass distribution for $HW \rightarrow b\bar{b}\nu l$ backgrounds in the Run-I analysis . . . . .	29
1.10	Dijet mass distribution for $H + Z \rightarrow b\bar{b}\nu\bar{\nu}$ backgrounds in the Run-I analysis . . . . .	29
1.11	Dijet mass distribution for $HZ \rightarrow b\bar{b}ll$ backgrounds in the Run-I analysis . . . . .	31
1.12	Dijet mass distribution for $H + W/Z \rightarrow b\bar{b}jj$ backgrounds in the Run-I analysis . . . . .	32
1.13	CDF Run I exclusion limits for the SM Higgs Boson . . . . .	33
2.1	General view of the Fermilab accelerator complex . . . . .	37
2.2	CDF detector elevation view . . . . .	40
2.3	CDF isometric view . . . . .	41
2.4	CDF Cherenkov Luminosity Monitor . . . . .	42
2.5	CDF tracking system . . . . .	43
2.6	COT view . . . . .	45
2.7	Time of flight as a function of particle type . . . . .	46
2.8	CDF muon system . . . . .	49
3.1	Bhete-Block formula for energy losses of particles traversing a material medium . . . . .	52
3.2	Donors and Acceptors impurities energetic levels . . . . .	55
3.3	The p-n junction . . . . .	55

3.4	I-V diode characteristic . . . . .	58
3.5	Microstrip detector scheme . . . . .	60
3.6	Microstrip detector manufacturing . . . . .	62
3.7	Double sided microstrip detector . . . . .	63
3.8	p-implant stops . . . . .	63
3.9	Guard ring structure . . . . .	65
3.10	ISL sensors masks . . . . .	66
3.11	ISL assembled ladders and modules . . . . .	67
3.12	SVX3 chip channel diagram . . . . .	68
3.13	ISL hybrid . . . . .	70
3.14	ISL data acquisition system . . . . .	72
3.15	ISL overview . . . . .	73
3.16	ISL Space Frame . . . . .	73
3.17	$I$ - $V$ curves for Hamamatsu ISL sensors . . . . .	75
3.18	Radiation effects on ISL Hamamatsu sensors . . . . .	76
3.19	Radiation effects on ISL Micron Sensors . . . . .	77
3.20	ISL Radiation Length . . . . .	77
4.1	DAQ system for the production tests . . . . .	82
4.2	SVX3 chip single channel pedestal distribution . . . . .	83
4.3	SVX3 chip pedestal and noise distribution . . . . .	84
4.4	Nominal depletion voltage of ISL Micron sensors . . . . .	84
4.5	Broken coupling capacitors of ISL Micron sensors . . . . .	85
4.6	Typical failures from a hybrid readout test . . . . .	86
4.7	ISL ladder assembly fixture . . . . .	87
4.8	ISL ladder reference marks . . . . .	88
4.9	ISL sensors position residuals . . . . .	89
4.10	Schematic representation of a pin-hole . . . . .	90
4.11	ISL ladder pin-holes . . . . .	91
4.12	ISL ladder gain scan . . . . .	92
4.13	ISL ladder operational voltage . . . . .	93
4.14	Failure rate as a function of time for microelectronics devices . . . . .	94
4.15	SVX II Burn-in box . . . . .	95
4.16	Pin hole creation during the Burn-in test . . . . .	97
4.17	SVX II pin-hole rate creation . . . . .	99
4.18	ISL laser test station . . . . .	100
4.19	ISL ladder alignment for the laser test . . . . .	100
4.20	ISL ladder laser scan . . . . .	101
4.21	ISL ladder charge collection efficiency as a function of the bias voltage	102
4.22	Charge collection efficiency from a laser pulse <i>versus</i> the preamplifier bandwidth . . . . .	104
4.23	ISL $\beta$ -source test station . . . . .	105
4.24	Signal synchronization for the $\beta$ -source test setup . . . . .	105

4.25	ISL $\beta$ -source events . . . . .	106
4.26	ISL cluster charge distribution for $\beta$ -source signals . . . . .	107
4.27	ISL cluster charge correlation for the junction and ohmic sides . . . . .	107
4.28	ISL cluster $x$ - $y$ distribution of $\beta$ -source hits . . . . .	108
4.29	ISL $S/N$ ratio for $\beta$ -source signals . . . . .	108
4.30	ISL $S/N$ distribution as a function of the preamplifier bandwidth . . . . .	109
4.31	ISL ladder grading . . . . .	111
4.32	ISL ladder production schedule . . . . .	112
5.1	Production cross sections for typical processes in $p\bar{p}$ collisions . . . . .	114
5.2	Run-II CDF trigger system, trigger paths and data sets . . . . .	115
5.3	COT track view . . . . .	118
5.4	Level 2 calorimetric cluster isolation sums . . . . .	120
5.5	SVT architecture . . . . .	122
5.6	Impact parameter distribution of Run-II SVT tracks . . . . .	123
5.7	CDF event reconstruction . . . . .	125
5.8	CDF track conventions and track reconstruction with SVX II data . . . . .	128
5.9	Schematic representation of the <i>Jet Vertexing Algorithm</i> . . . . .	131
5.10	SVX' b/c/fakes tagging efficiency . . . . .	131
6.1	Average number of interactions per bunch crossing as a function of the instantaneous luminosity . . . . .	137
7.1	Higgs boson pseudorapidity distribution for $H + W/Z \rightarrow b\bar{b}jj$ . . . . .	141
7.2	b-quark $p_T$ distribution for the $H \rightarrow b\bar{b}$ decay . . . . .	142
7.3	Highest $E_T$ trigger tower distribution for $H + W/Z \rightarrow b\bar{b}jj$ and <i>minimum bias</i> events . . . . .	144
7.4	Level 1 trigger rate and trigger efficiency for $H + W/Z \rightarrow b\bar{b}jj$ events <i>versus</i> the $E_T$ threshold on the highest $E_T$ trigger tower. . . . .	144
7.5	Level 1 $\sum E_T$ trigger rates and trigger efficiencies for $H + W/Z \rightarrow b\bar{b}jj$ events . . . . .	146
7.6	Level 2 cluster multiplicity and $\sum E_T^{clus}$ distribution for $H + W/Z \rightarrow b\bar{b}jj$ and <i>JET-20</i> events . . . . .	148
7.7	Level 2 $E_T^{clus}$ distribution for $H + W/Z \rightarrow b\bar{b}jj$ and <i>JET-20</i> events . . . . .	149
7.8	Level 2 calorimetric trigger efficiencies for $H + W/Z \rightarrow b\bar{b}jj$ events . . . . .	150
7.9	Level 2 calorimetric rates . . . . .	151
7.10	Level 2 $\sum E_T^{clus}$ trigger efficiency for $H + W/Z \rightarrow b\bar{b}jj$ events . . . . .	152
7.11	Level 2 $\sum E_T^{clus}$ rates . . . . .	152
7.12	SVT tracks multiplicity for $H + W/Z \rightarrow b\bar{b}jj$ and <i>JET-20</i> events . . . . .	155
7.13	Level 2 SVT trigger efficiency for $H + W/Z \rightarrow b\bar{b}jj$ events . . . . .	156
7.14	Level 2 SVT trigger rates . . . . .	156
7.15	Largest impact parameter distribution of SVT tracks for $H + W/Z \rightarrow b\bar{b}jj$ and <i>JET-20</i> events . . . . .	157

7.16	Second largest impact parameter distribution of SVT tracks for $H + W/Z \rightarrow b\bar{b}jj$ and $JET-20$ events . . . . .	157
7.17	$p_T$ distribution of SVT tracks with the highest impact parameter for $H + W/Z \rightarrow b\bar{b}jj$ and $JET-20$ events. . . . .	158
7.18	$p_T$ distribution of SVT tracks with the second highest impact parameter for $H + W/Z \rightarrow b\bar{b}jj$ and $JET-20$ events. . . . .	158
7.19	Level 2 trigger rates and $H + W/Z \rightarrow b\bar{b}jj$ trigger efficiency <i>versus</i> $\sum E_T^{clus}$ threshold . . . . .	160
7.20	Reconstructed Track multiplicity <i>versus</i> the event $z$ coordinate . . . . .	163
7.21	$z_0$ coordinate distribution of tracks reconstructed in the SVX' and CTC detectors . . . . .	163
7.22	Probability for a CTC track to have one hit in the four innermost layers of the SVX' . . . . .	164
7.23	Jet multiplicity and jet $E_T$ spectrum for $H + W/Z \rightarrow b\bar{b}jj$ events . . . . .	165
7.24	Level 3 trigger rates and $H + W/Z \rightarrow b\bar{b}jj$ trigger efficiency <i>versus</i> $\sum E_T^{clus}$ threshold . . . . .	166
8.1	Transverse energy distribution of the $\nu\bar{\nu}$ system for $H + Z \rightarrow b\bar{b}\nu\bar{\nu}$ events . . . . .	172
8.2	Highest $E_T^{tow}$ calorimeter trigger tower distribution for $H + Z \rightarrow b\bar{b}\nu\bar{\nu}$ and <i>minimum bias</i> events . . . . .	174
8.3	Level 1 trigger efficiency <i>versus</i> the threshold on the highest $E_T^{tow}$ calorimeter trigger tower for $H + Z \rightarrow b\bar{b}\nu\bar{\nu}$ events . . . . .	174
8.4	Level 2 calorimetric cluster multiplicity and $E_T^{clus}$ spectrum for $H + Z \rightarrow b\bar{b}\nu\bar{\nu}$ events . . . . .	176
8.5	Level 2 $\cancel{E}_T$ distribution for $H + Z \rightarrow b\bar{b}\nu\bar{\nu}$ and $JET-20$ events . . . . .	176
8.6	Level 2 trigger $\cancel{E}_T$ <i>versus</i> the $E_T^{clus}$ of the highest $E_T^{clus}$ cluster for $H + Z \rightarrow b\bar{b}\nu\bar{\nu}$ , QCD and $JET-20$ events . . . . .	177
8.7	Level 2 trigger efficiency for $H + Z \rightarrow b\bar{b}\nu\bar{\nu}$ events . . . . .	179
8.8	Impact parameter distribution of the SVT track with the largest impact parameter for $H + Z \rightarrow b\bar{b}\nu\bar{\nu}$ and $JET-20$ events . . . . .	179
8.9	Level 2 trigger rate . . . . .	180
8.10	Run-I data $\cancel{E}_T$ trigger turn-on curves . . . . .	183
8.11	Run-II data $\cancel{E}_T$ trigger turn-on curve . . . . .	184
9.1	$\cancel{E}_T$ distribution for $H + Z \rightarrow b\bar{b}\nu\bar{\nu}$ and QCD heavy flavor events . . . . .	190
9.2	Feynman diagrams for QCD multijet heavy flavor production . . . . .	192
9.3	Feynman diagrams for $t\bar{t}$ multijet production . . . . .	193
9.4	Feynman diagrams for $W/Z + b\bar{b}/c\bar{c}$ production . . . . .	194
9.5	b-quark $p_T$ distributions for several backgrounds . . . . .	194
9.6	Feynman diagram for single top production . . . . .	195
9.7	Statistical significance of the jet multiplicity requirement . . . . .	197
9.8	Statistical significance of the $\sum E_T^{jets}$ requirement . . . . .	198

9.9	Level 2 Trigger $\sum E_T^{jets}$ efficiency . . . . .	198
9.10	Invariant mass distribution for the b-tagged and untagged jets . . . .	199
9.11	Invariant mass and $p_T$ distribution of the b-tagged and jets for H + W/Z $\rightarrow$ $b\bar{b}jj$ and QCD events . . . . .	200
9.12	Invariant mass and $p_T$ distribution of the remaining jets for H + W/Z $\rightarrow$ $b\bar{b}jj$ and QCD events . . . . .	200
9.13	Statistical significance of the $M_{jj}$ and $M_{b\bar{b}}$ requirements . . . . .	201
9.14	$p_T$ and invariant mass distributions of the $b\bar{b}$ system for QCD heavy flavor production and H + W/Z $\rightarrow$ $b\bar{b}jj$ signal . . . . .	202
9.15	Invariant mass distribution of the two b-tagged jets <i>versus</i> its trans- verse momentum for H + W/Z $\rightarrow$ $b\bar{b}jj$ and QCD events . . . . .	203
9.16	Invariant mass distribution of the two untagged jets <i>versus</i> its trans- verse momentum for H + W/Z $\rightarrow$ $b\bar{b}jj$ and QCD events . . . . .	204
9.17	Run-II extrapolation of Run-I limits for the H + W/Z $\rightarrow$ $b\bar{b}jj$ channel . . . . .	207
B.1	DAQ system for production tests . . . . .	221
B.2	SVX3 chip control patterns . . . . .	222
B.3	SVX3 chip data output . . . . .	223
B.4	MUX/FIFO board view . . . . .	224
B.5	Parts layout of the MUX/FIFO board . . . . .	229
B.6	MUX/FIFO DAQ patch . . . . .	230
B.7	Control panel for the burn-in test stand program . . . . .	232
B.8	MUX/FIFO control panel for the burn-in test stand program . . . . .	232
B.9	MUX/FIFO board configuration panel for the burn-in test stand pro- gram . . . . .	233
B.10	Event display for the burn-in test stand program . . . . .	233
B.11	Binary file data format . . . . .	234
B.12	Acquire mode pattern file for the laser test station . . . . .	236
B.13	Acquire mode pattern file for the $\beta$ source test setup . . . . .	237



# List of Tables

1	Eficiències de senyal per al segon nivell de <i>trigger</i> per a diverses masses del bosó de Higgs al procés $H + W/Z \rightarrow b\bar{b}jj$ . . . . .	v
2	Freqüència, secció eficaç i factors de rebuig per al nivell 2 de <i>trigger</i> per al procés $H + W/Z \rightarrow b\bar{b}jj$ amb els requeriments del SVT . . . . .	vi
3	Eficiència d'identificació d'un o dos <i>jets</i> <i>b</i> per a esdeveniments $H + W/Z \rightarrow b\bar{b}jj$ . . . . .	vii
4	Eficiències de <i>trigger</i> per a esdeveniments $H + Z \rightarrow b\bar{b}\nu\bar{\nu}$ . . . . .	viii
5	Freqüència de <i>trigger</i> per al procés $H + Z \rightarrow b\bar{b}\nu\bar{\nu}$ . . . . .	x
6	Eficiència d'identificació d'un o dos <i>jets</i> <i>b</i> per a esdeveniments $H + Z \rightarrow b\bar{b}\nu\bar{\nu}$ . . . . .	x
1.1	Standard Model fundamental matter particles . . . . .	6
1.2	Gauge and Higgs bosons properties . . . . .	9
1.3	Standard Model particles properties for the electroweak interaction . . . . .	12
1.4	Z, W and Higgs boson branching ratios . . . . .	27
1.5	Run-I expected number of Higgs boson events . . . . .	27
1.6	CDF Run-I $\mathbf{WH} \rightarrow l\nu \mathbf{b}\bar{\mathbf{b}}$ Search . . . . .	28
1.7	CDF Run-I $\mathbf{ZH} \rightarrow \nu\bar{\nu} \mathbf{b}\bar{\mathbf{b}}$ Search . . . . .	30
1.8	CDF Run-I $\mathbf{ZH} \rightarrow l\bar{l}, \mathbf{b}\bar{\mathbf{b}}$ Search . . . . .	30
1.9	CDF Run-I $\mathbf{W/ZH} \rightarrow jj \mathbf{b}\bar{\mathbf{b}}$ Search . . . . .	31
2.1	CDF operational periods . . . . .	35
2.2	Tevatron operational parameters . . . . .	36
2.3	Mechanical specifications of the SVX II sensors . . . . .	44
2.4	CDF II calorimeter parameters . . . . .	48
2.5	CDF II calorimeter segmentation . . . . .	48
2.6	CDF muon systems parameters . . . . .	49
3.1	Si physical properties at room temperature . . . . .	54
3.2	Thermal conductivity of common hybrid substrats . . . . .	70
4.1	ISL ladder mechanical tolerances . . . . .	87
4.2	SVX II ladders burn-in bias voltage . . . . .	96
4.3	Pin-hole identification loose parameters . . . . .	96

5.1	Run-II CDF nominal trigger bandwidth . . . . .	115
5.2	Run-II XFT performance parameters . . . . .	117
5.3	Level 2 calorimeter clustering thresholds. . . . .	120
5.4	Impact parameter resolution of CDF reconstructed tracks . . . . .	129
6.1	Run-I multiple interactions as a function of the instantaneous luminosity	137
7.1	Expected event yield for the $H + W/Z \rightarrow b\bar{b}jj$ process . . . . .	140
7.2	CDF Run-I multijet trigger efficiency for $H + W/Z \rightarrow b\bar{b}jj$ events . .	140
7.3	Level 1 $\sum E_T$ and $E_T^{tow}$ trigger efficiencies for $H + W/Z \rightarrow b\bar{b}jj$ events	146
7.4	Level 1 $\sum E_T$ and $E_T^{tow}$ trigger rates and trigger efficiencies for $H + W/Z \rightarrow b\bar{b}jj$ events . . . . .	147
7.5	Level 2 calorimetric trigger efficiencies for $H + W/Z \rightarrow b\bar{b}jj$ events .	151
7.6	Level 2 calorimetric trigger rates . . . . .	152
7.7	Level 2 calorimetric and SVT trigger rates, cross section and rejection factors . . . . .	159
7.8	Level 2 calorimetric SVT trigger efficiencies for $H + W/Z \rightarrow b\bar{b}jj$ events . . . . .	159
7.9	Level 2 trigger efficiencies for $H + W/Z \rightarrow b\bar{b}jj$ <i>versus</i> the number of primary interactions . . . . .	161
7.10	Run-II scale factor for triggers requiring two SVT tracks . . . . .	162
7.11	Level 3 trigger efficiencies for $H + W/Z \rightarrow b\bar{b}jj$ . . . . .	165
7.12	Level 3 trigger rates . . . . .	165
7.13	Single and double $b$ -tag rates for $H + W/Z \rightarrow b\bar{b}jj$ events . . . . .	167
8.1	Expected event yield for the $H + Z \rightarrow b\bar{b}\nu\bar{\nu}$ process . . . . .	172
8.2	Level 1 trigger efficiencies for $H + Z \rightarrow b\bar{b}\nu\bar{\nu}$ events . . . . .	175
8.3	Level 2 trigger efficiencies for $H + Z \rightarrow b\bar{b}\nu\bar{\nu}$ events . . . . .	180
8.4	Level 2 trigger rates . . . . .	181
8.5	Level 3 trigger efficiencies for $H + Z \rightarrow b\bar{b}\nu\bar{\nu}$ events . . . . .	181
8.6	Level 3 rates . . . . .	182
8.7	Single and double $b$ -tag rates for $H + Z \rightarrow b\bar{b}\nu\bar{\nu}$ events . . . . .	185
9.1	Expected number of events for the $H + Z \rightarrow b\bar{b}\nu\bar{\nu}$ channel after the offline selection . . . . .	188
9.2	Expected number of events for the $H + Z \rightarrow b\bar{b}\nu\bar{\nu}$ channel after the offline selection . . . . .	189
9.3	$H + W/Z \rightarrow b\bar{b}jj$ signal and background efficiency . . . . .	196
9.4	Statistical significance of the multijet requirement . . . . .	196
9.5	Statistical significance of the $\sum E_T^{jet}$ requirement . . . . .	199
9.6	Statistical significance of the $M_{jj}$ requirement . . . . .	201
9.7	Statistical significance of the $M_{b\bar{b}}$ requirement . . . . .	202
9.8	$H + W/Z \rightarrow b\bar{b}jj$ signal and background efficiency for the kinematical selection . . . . .	205

9.9	Statistical significance of the counting experiment analysis . . . . .	205
9.10	Signal, background and cross section exclusion limit in the fully hadronic channel for the Run-I and Run-II analysis . . . . .	207
A.1	ISL Hamamatsu sensors electrical specifications . . . . .	213
A.2	ISL Hamamatsu sensors geometrical specifications . . . . .	215
A.3	ISL Hamamatsu sensors radiation specifications . . . . .	216
A.4	ISL Micron sensors specifications . . . . .	217
B.1	PC I/O card and MUX/FIFO board pin connectors assignment . . .	225
B.2	PC I/O card and MUX/FIFO board pin connectors assignment . . .	226
B.3	Pin layout of the MUX/FIFO board 50-pin connectors . . . . .	227
B.4	Pin layout of the MUX/FIFO board 34-pin output connectors . . .	227
B.5	Parts list for the MUX/FIFO board . . . . .	228
B.6	Record Header . . . . .	235



# Bibliography

- [1] S. Weinberg, *Phys. Rev. Lett.* **19** (1967) 1264;  
Salam, A., *Proceedings of the 8th Nobel Symposium* (Stockholm), edited by N. Svartholm (almqvist and Wiksell, Stockholm, 1968) p. 367.
- [2] S. Glashow, *Nucl. Phys.* **22** (1961) 579.
- [3] C. Rubbia *Rev. Mod. Phys.* **57** (1985) 699-722.
- [4] P.W. Higgs, *Phys. Lett.* **12** (1964) 132, *Phys. Rev. Lett.* **13** (1964) 508, *Phys. Rev.* **145** (1996) 1156.  
F. Englert and R. Brout, *Phys. Rev. Lett.* **13** (1964) 321  
G.S. Guralnik, C.R. Hagen and T.W.B. Kibble, *Phys. Rev. Lett.* **13** (1964) 585  
T.W.B Kibble, *Phys. Rev.* **155** (1967) 1554.
- [5] The LEP working group for Higgs boson searches, CERN-EP/2001-055 (July 11, 2001).
- [6] M. Sher, *Phys. Rev.* **179** (1989) 273.
- [7] The LEP Collaborations, the LEP Electroweak Working Group and the SLD Heavy Flavour and Electroweak Groups. *CERN-EP/2001-021*, Feb. 28, 2001.
- [8] M. Spira, Preprint DESY 98-159, hep-ph/9810289.
- [9] M. Kruse *et al.*, CDF Internal Note No 4985.
- [10] The CDF II Collaboration, *The CDF II Detector Technical Design Report*, Preprint FERMILAB-Pub-96/390-E.
- [11] A. Sill, *Nucl. Instrum. and Meth.* **A447**, 1 (2000).
- [12] S. Belforte *et al.*, *IEEE Trans. on Nucl. Sci.* **42**, 860 (1995).
- [13] The Tevatron Higgs Working Group. Preprint hep-ph/0010338, 2000.
- [14] Kane, G. L. *Modern elementary particle physics: the fundamental particles and forces?*, Addison-Wesley Publishing Company, 1993.

- [15] C. Caso *et al.*, Review of Particle Physics. *The European Physical Journal* **C3**, 1 (1998).
- [16] U. Amaldi, W. de Boer and H. Fürstenau, *Phys. Lett.* **B260** (1991) 447.
- [17] Leslie S. Groer, Ph. D. Thesis, Rutgers, The State University of New Jersey, unpublished, 1998.
- [18] G. 't Hooft. *Nucl. Phys.* **B33** (1971) 173; **B35** (1971) 167.
- [19] S.L. Glashow, *Nucl. Phys.* **22** (1961) 579;  
S. Weinberg, *Phys. Rev. Lett.* **19** (1967) 1264;  
A. Salam, *Elementary Particle Physics* (Nobel Symp. No 8), Edited by N. Svartholm, Almquist and Wiksells, Stockholm (1968), p. 367
- [20] G. Arnison *et al.*, *Phys. Lett.* **B122**, 103 (1983); *Phys. Lett.* **B126**, 398 (1983).
- [21] T. P. Cheng and L. F. Li, *The Theory of Elementary Particle Physics*, Oxford University Press, 1991 (reprinted).
- [22] P.W. Higgs, *Phys. Rev. Lett.* **12**, 132 (1964);  
F. Englert and R. Brout, *Phys. Rev. Lett.*, 321 (1964);  
G.S. Guralnik, C. R. Hagen and T. W. B. Kibble, *Phys. Rev. Lett.*, **13** 585 (1964);  
P.W. Higgs, *Phys. Rev.* **145**, 1156 (1966).  
T.W.B Kibble, *Phys. Rev.* **155**, 1554 (1967).
- [23] M. Herrero *The Standard Model*, Lectures of the NATO ASI 98 School, Techniques and Concepts of High Energy Physics; St. Croix, Virgin Islands, USA, June 18-29, 1998. Preprint *hep-ph/9812242*.
- [24] V.L. Ginzburg and L.D. Landau, *J. Expl. Theoret. Phys. USSR*, **20** 1064 (1950).
- [25] Y.Nambu, *Phys. Rev. Lett.* **4**, 380 (1960);  
J. Goldstone, *Nuovo Cimento* **19**, 154 (1961);  
J. Goldstone, A. Salam, S. Weinberg, *Phys. Rev.* **127**, 963 (1962).
- [26] M. Spira, *QCD Effects in Higgs Physics*, Preprint No hep-ph/9705337 (1997).
- [27] U. Egede, Ph. D. thesis, Lund University (1997). Preprint No LUNFD6/(NFFL-7150).
- [28] L.R. Surguladze, *Phys. Lett.* **341**, 60 (1994).
- [29] K. Riesselmann, *Limitations of a Standard Model Higgs Boson*, Preprint No hep-ph/9711456 (1997).

- [30] M. Sher, Phys. Lett. **B331**, 295 (1994);  
G. Altarelli and G. Isidori, Phys. Lett. **B357**, 141 (1994);  
J. A. Casas *et al.*, Phys. Lett. **B342**, 171 (1995).
- [31] The LEP Collaborations ALEPH, DELPHI, L3, OPAL and the LEP Electroweak Working Group, and the SLD Heavy Flavor and Electroweak Groups, *A combination of Preliminary Electroweak Measurements and Constraints on the Standard Model*, Preprint CERN-EP-2001-21, hep-ex/0103048.
- [32] The LEP Collaborations ALEPH, DELPHI, L3, OPAL and the LEP Higgs Working Group, *Search for the Standard Model Higgs Boson at LEP*, Preprint CERN-EP-2001-055, hep-ex/0107029.
- [33] W. Bokari *et al.*, Internal CDF Note No 4663.
- [34] F. Abe *et al.*, Phys. Rev. Lett. **79**, 3819 (1997).
- [35] F. Abe *et al.*, Phys. Rev. Lett. **81**, 5748 (1998).
- [36] M. Kruse *et al.* CDF Internal Note No 4827.
- [37] M. Krues *et al.* CDF Internal Note No 4985.
- [38] Tevatron RUN-II Handbook. Unpublished. Available from Internet at <http://www-bd.fnal.gov>.
- [39] Fermilab Visual Media Services.
- [40] S. van der Meer. *An Introduction to Stochastic Cooling*, AIP Proceedings 153, SLAC Summer School, 1985; Fermilab Summer School, 1984; pp 1628-1649.
- [41] F. Abe *et al.*, Nucl. Instrum. and Meth. **A271**, 387 (1998).
- [42] D. Acosta *et al.*, Preprint FERMILAB-PUB-01/031-E. Submitted to Nucl. Instrum. and Meth. Section **A**.
- [43] The CDF II Collaboration, *Proposal for Enhancement of the CDF II Detector*, Preprint Fermilab-Proposal-909 (1998).
- [44] The CMS Collaboration. *CMS, the Tracker System Project : Technical Design Report* Preprint CERN-LHCC-98-006 (1998).
- [45] M. Garcia-Sciveres *et al.*, Nucl. Instrum. and Meth. **A435**, 58 (1999).
- [46] A. Affolder *et al.*, Nucl. Instrm. and Meth. **A453**, 84 (2000).
- [47] F. Bedeschi *et al.*, Nucl. Instrum. and Meth. **A268**, 50 (1988).
- [48] L. Balka *et al.*, Nucl. Instrum. and Meth. **A267**, 272 (1988).

- [49] S. Bertolucci *et al.*, Nucl. Instrum. and Meth. **A267**, 301 (1988).
- [50] K. Byrum *et al.*, Nucl. Instrum. and Meth. **A364**, 144 (1995).
- [51] F. Abe *et al.* Phys. Rev. Lett. **73**, 2662 (1994).
- [52] G. Ascoli *et al.*, Nucl. Instrum. and Meth. **A268**, 33 (1998).
- [53] K. Byrum *et al.* Nucl. Instrum. and Meth. **A268**, 46 (1998).
- [54] K.G. McKay, Phys. Rev. **84**, 829 (1951).
- [55] J. Kemmer, Nucl. Instrum. and Meth. **A169**, 499 (1980).
- [56] H. Bethe and J. Ashkin. *Passage of radiation through matter*. In E. Segre, editor *Experimental Nuclear Physics*. volume 1, chapter 2. John Wiley & Sons, New York, 1959.
- [57] S. Ahlen, Rev. Mod. Phys. **52**, 121 (1980).
- [58] C. Caso *et al.*, Eur. Phys. Jour. **C3**, 1 (1998).
- [59] R. M. Barnett *et al.*, Phys. Rev. **D54** (1996).
- [60] H. Bichsel, Rev. Mod. Phys. **60**, 663 (1988).
- [61] S. M. Sze, *Semiconductor Devices: Physics and Technology*, John Wiley & Sons, 2001. Second Edition.
- [62] S. Wolf and R. N. Tauber, *Silicon Processing for the VLSI Era*. Lattice Press, Sunset Beach, 1986.
- [63] W. S. Ruska, *Microelectronic Processing*, McGraw-Hill, Singapore, 1988.
- [64] G. Bolla *et al.*, Nucl. Instrum. and Meth. **A435**, 51 (1999).
- [65] K. Hara *et al.*, Nucl. Instrum. and Meth. **A435**, 437 (1999).
- [66] M. Caccia, L. Evensen *et al.*, Nucl. Instr. Meth. **A260**, 124 (1987).
- [67] T. Ohsugi *et al.*, Nucl. Instrum. and Meth. **A342**, 22 (1994).
- [68] T. Ohsugi *et al.*, Nucl. Instrum. and Meth. **A383**, 116 (1996).
- [69] A. Basti *et al.* CDF Internal Note No 5034 (1999).
- [70] M. Bishai *et al.*, CDF Internal Note No 5063 (1999).
- [71] Carl Haber private communication.
- [72] K. Hara *et al.*, CDF Internal Note No 5306 (2000).

- [73] K. Hara *et al.*, CDF Internal Note No 4518 (1998).
- [74] T. P. Ma, Paul V. Dressendorfer, *Ionizing radiation effects in MOS devices and circuits*. John Wiley and Sons, Inc.
- [75] A. Chilingarov *et al.*, Nucl. Instrum. and Meth. **A360** 432 (1995).
- [76] D. Sjögren *et al.*, CDF Internal Note No 4461 (1998).
- [77] D. Stuart. CDF Internal Note No 5268 (2000).
- [78] A. Basti CDF Internal Note No 5046.
- [79] Micron Semiconductor Ltd., 1 Royal Buildings, Marlborough Road, Churchill Industrial Estate, Lancing, Sussex BN158UN, England.
- [80] Finn Jensen, Niels Erik Petersen, *Burn-In: An Engineering Approach to the Design and Analysis of Burn-In Procedures*, John Wiley & Sons, 1995.
- [81] E. Bartz *et al.*, CDF Internal Note No 5164 (1999).
- [82] M. Kruse *et al.*, CDF Internal Note No 5101 (1999).
- [83] Steve Worm private communication.
- [84] I. Abt *et al.*, Nucl. Instrum. and Meth. **A423**, 303 (1999).
- [85] A. Affolder *et al.*, Nucl. Instrm. and Meth. **A461**, 216 (2001).
- [86] D. Stuart *et al.*, CDF Internal Note No 4784 (1998).
- [87] D. Stuart *et al.*, CDF Internal Note No 5180 (1999).
- [88] Giorgio Chiarelli private communication.
- [89] F. Abe et al. Phys. Rev. **D 50** (1994) 5550.
- [90] T. Sjöstrand, Comp. Phys. Commun. **82**, 74 (1994).
- [91] Review of Particle Physics (Particle Data Group), *Eur. Phys. J. C* **3** (1998) 1-794.
- [92] F. Abe *et al.*, Phys. Rev. Lett. **68**, 1104 (1992).
- [93] F. Abe *et al.* CDF Collaboration, Phys. Rev. Lett. **68** (1992) 3403.
- [94] R. Frühwirth *et al.*, *Data Analysis Techniques for High Energy Physics*, Cambridge University Press, 2000. Second Edition.
- [95] Evelyn Thomson private communication.

- [96] A. Bardi *et al.*, Nucl. Instrum. and Meth. **A413**, 367 (1998).
- [97] S. Belforte *et al.*, IEEE Trans. on Nucl. Sci. **3**, 1810 (1996).
- [98] S. Belforte *et al.*, IEEE Trans. on Nucl. Sci. **43** 1810 (1996).
- [99] H. Wenzel, CDF Internal Note No 1790 (1998).
- [100] R. Frühwirth, Nucl. Instrum. and Meth. **A262**, 444 (1987).
- [101] The CDF II Collaboration *Proposal for Enhancement of CDF II Detector: An Inner Silicon Layer and A Time of Flight Detector.*, Fermilab-Proposal-909 (1998).
- [102] T. Affolder *et al.*, CDF Internal Note No 5425 (2001).
- [103] F. Abe *et al.*, Phys. Rev. Lett. **73**, 220 (1995).
- [104] Weiming Yao private communication.
- [105] D. Cronin-Hennessy *et al.*, Nucl. Instrum. and Meth. **A443**, 37 (2000).
- [106] F. Abe *et al.*, Phys. Rev. D **50**, 5550 (1994).
- [107] CDF QCD working group private communication.
- [108] F. Abe *et al.*, Phys. Rev. Lett. **70**, 1376 (1993).
- [109] CDF Trigger working group private communication.
- [110] *QQ - The CLEO Event Generator*, <http://www.lns.cornell.edu/public/CLEO/soft/qq>, unpublished.
- [111] F. Snider *et al.*, Nucl. Instrum. and Meth. **A268**, 75 (1988).
- [112] A. Beretvas *et al.*, CDF Internal Note No. 3599 (1996).
- [113] C. Bigongiari, Ph. D. thesis, University of Pisa, unpublished, 1998;  
C. Bigongiari, CDF Internal Note No. 4824;  
C. Bigongiari, CDF Internal Note No. 4945.
- [114] F. Abe *et al.*, Phys. Rev. Lett. **81**, 5748 (1998).
- [115] R. Vidal, Ph. D. thesis, Universidad de Cantabria, unpublished, 1999.
- [116] C. Campagnari *et al.*, CDF Internal Note No. 1180 (1990).
- [117] D. Saltzberg, M. Sochet *et al.*, CDF Internal Note No. 4178 (1998).
- [118] Wasiq M. Bokhari, Ph. D. Thesis, Massachusetts Institute of Technology, unpublished, 1997.

- [119] Luciano Ristori private communication.
- [120] S. Donati, G. Punzi. CDF Internal Note No 3780 (1996).
- [121] J. Valls, *Higgs Searches at the Tevatron in Run I*, Pub. Proceedings International Europhysics Conference on High-Energy Physics (EPS-HEP 99), Tampere, Finland, July 15-21, 1999. Preprint FERMILAB-CONF-99/263-E.
- [122] M. Spiropulu, CDF Internal Note No 4143 (1997).
- [123] G. Marchesini *et al.*, Comp. Phys. Comm. **67** 465 (1992).
- [124] T. Affolder *et al.*, Phys. Rev. **D64**, 32002 (2001).
- [125] F. Abe *et al.*, Phys. Rev. Lett. **70**, 4042 (1993).
- [126] F. Abe *et al.*, Phys. Rev. Lett. **77**, 448 (1996).
- [127] P. Azzi *et al.*, CDF Internal Note No 3428 (1995).
- [128] T. Kikuchi *et al.*, *Search for Single-Top-Quark Production in  $p\bar{p}$  Collisions at  $\sqrt{s} = 1.8$  TeV*. Submitted to Phys. Rev. Lett.
- [129] T. Stelzer, Z. Sullivan, and S. Willenbrock, Phys. Rev. **D56**, 6696 (1996).
- [130] M.C. Smith, S. Willenbrock, Phys. Rev. **D54**, 6696 (1996).
- [131] J. Ohnemus *et al.*, Phys. Rev. **D43**, 3626 (1991);  
J. Ohnemus, Phys. Rev. **D44**, 1403 (1991);  
J. Ohnemus, Phys. Rev. **D44**, 3477 (1991).
- [132] J. Conway, Proceedings of the Workshop on Confidence Levels, CERN, Geneva, Switzerland, January 17-18, 2000. Preprint FERMILAB-CONF-00/048-E.
- [133] S. Abachi *et al.*, Nucl. Instrum. and Meth. **A338** 185 (1994).
- [134] M. Garcia-Sciveres, D. Roy, *Documentation for PATT02 Pattern Generator Board*, LBNL, unpublished.
- [135] P. J. Bryant and K. Johnsen. *The Principles of Circular Accelerators and Storage Rings* Cambridge University Press, 1993.
- [136] M. Eldel *et al.*, *Histo-Scope User's Guide*, Fermilab Computing Library, Fermilab, Batavia, IL, USA. Available also as *anonymous user* at ftp.fnal.gov.